Developing a theranostic silica nanoparticle for fluorescent imaging and therapy of colorectal cancer.

Yazan Sulaiman Khaled

201032549

Submitted in accordance with the requirements for the degree of

Doctor of Philosophy

The University of Leeds

School of Medicine and Health

Leeds Institute of Clinical and Biomedical Sciences

Submitted for examination March 2020

Declaration

I confirm that the work submitted is my own and that appropriate credit has been given where reference has been made to the work of others.

Publications and presentations

Presentations

Chapter 3:

York Medical Society prize for best oral research presentation 2016.

Chapter 4:

Ronald Raven prize winner for best oral research presentation, British Association of Surgical Oncology, Liverpool, 2017.

Patey Prize finalist, Society of Academic Research Surgeons, Nottingham, 2017.

Runner-up, Yorkshire & Humber Deanery Academic Prize Session: Best Oral Presentation 2017.

Chapter 5:

Association of Coloproctology of Great Britain and Ireland, Birmingham, 2018.

John of Arderne travel fellowship winner, Royal Society of Medicine, Leicester, 2019.

Acknowledgment

My deepest thanks go to my supervisor, Professor David Jayne for his continuous support during my academic surgical training and supervision throughout my study in Leeds. I would like to thank my co-supervisors Prof. Paul Millner and associate Prof. Thomas Hughes for their tremendous effort and exceptional supervision during my PhD. Without my supervisors, I would not have been able to complete my research.

I would like to thank the following people for their support, time and patience whilst I took this work: Louise Coletta, Sarah Perry, Thomas Massey, Debra Evans, Jan Bilton, Shazan Shamsuddin and E. Al-Enezi. I gratefully acknowledge the Medical Research Council for funding this project and the University of Leeds for providing all the necessary facilities.

I am indebted to my mother Khadejah and father Naief, for their continuous sincere support and advice without which I would not have reached this stage. I would like to express my heart-felt gratitude to my precious wife Hayat and my daughters Khadejah, Maryam and Shaam for their encouragement and patience while I have been completing this research. I am also grateful to my brothers Ahmad and Sari and my sister Ruba for their thoughts and encouragement. I dedicate this work to all patients who have suffered from colorectal cancer, the courageous Syrian people in honour for their struggle for freedom and to those who have been infected with Corona virus.

Abstract

Background

Treatment of colorectal cancer (CRC) fails in 50% of cases, as evidenced by cancer deaths, and treatment itself can be associated with substantial morbidity and mortality. Residual micro-metastases are associated with increased risk of relapse while developing targeted strategies to treat advanced stages remains a clinical need. Laparoscopic resection of colorectal cancers has gained wide acceptance amongst surgeons and the platform for using fluorescent guided surgery has become appealing. The development of theranostic nanoparticles as a dye and drug delivery system is a promising strategy for colorectal cancer imaging and therapy. Carcinoembryonic antigen (CEA) can be utilised for the development of CEA-targeted nanotechnologies since it is overexpressed in most colorectal cancers. Targeted fluorescent imaging and therapy of primary colorectal tumours and lymph node metastases would aid stratification of the radicality of surgical resections and eradication of residual tumour cells. I aimed to develop a theranostic nanoparticle to facilitate fluorescent imaging and therapy of colorectal cancer.

Methods

Affimers, non-antibody binding proteins, against carcinoembryonic antigen (CEA) were expressed and purified to be used as targeting bioreceptors. Dye-doped (NIR664) and photosensitiser-encapsulated (Foslip) silica nanoparticles were fabricated using a water-in-oil microemulsion technique. Anti-CEA or control Affimers were conjugated to nanoparticles using different chemical linkage strategies. CEA-specific fluorescent imaging and photodynamic cytotoxicity of

functionalised nanoparticles was quantified in colorectal cancer cells *in vitro*. LS174T murine xenograft animal model was used to assess the binding specificity of the particles *in vivo*.

Results

Anti-CEA Affimer functionalised silica nanoparticles exhibited CEA-specific fluorescence in three colorectal cancer cell lines ($p<0.0001$) when compared to control particles. Cellular uptake of CEA-targeted nanoparticles was time and dose dependent. Following photo-irradiation after treatment with Foslip containing nanoparticles, significant cell death rate was observed in LoVo (70%), LS174T (80%) and HCT116 (65%) when compared to HEK293 (0%); $p<0.0001$ via ROS generation. In LS174T xenografts, fluorescence in the CEA-targeted tumours was significantly greater than controls from 6 to 48 h ($p<0.0001$) in 6 mice.

Conclusions

Anti-CEA Affimer functionalised nanoparticles allow CEA-specific imaging and photodynamic therapy of colorectal cancer cells and have the potential to be used as an intra-operative theranostic probe. This is the first study to demonstrate live tumour-specific fluorescent imaging of colorectal cancer using Affimer -targeted nanoparticle *in vivo*.

Table of contents

List of tables

List of figures

Abbreviations

ATCC	American type culture collection
APTES	(3-Aminopropyl) triethoxysilane
5-ALA	5-Aminolevulinic acid-induced fluorescence
Apo A-1	Apolipoprotein A-1
AISPc	Sulphonated aluminium phthalocyanine
BSTG	BioScreening Technology Group
CRC	Colorectal cancer
CLASSIC	Conventional versus laparoscopic-assisted surgery in patients with colorectal cancer trial
CT	Computed tomography
CEA	Carcinoembryonic antigen
CD95/Apo-1	Fas receptor
Cy	Cyanine
COX	Cyclooxygenase
C-PDT	Cellular-PDT
CDR	Complementarity-determining region
DCFDA	2’,7’–Dichlorofluorescin diacetate
DR-5	Death receptor-5
DAMP	Damage-associated molecular pattern
DMEM	Dulbecco’s Modified Eagle Media
DMSO	Dimethyl sulfoxide
EpCAM	Epithelial cell adhesion molecule
EPR	Enhanced permeation and retention

EGFR	Endothelial growth factor receptor
EDTA	Edetate disodium
ELISA	Enzyme-linked immunosorbent assay
EDC	N-(3-dimethylaminopropyl)-N′-ethylcarbodiimide
FD	Fluorescence diagnosis
FBS	Foetal bovine serum
Fmoc-Cl	Fluorenylmethyloxycarbonyl chloride
FDA	Food and drug administration
^{18}F-FDG	^{18}F-2-fluoro-2-deoxy-D-glucose
FRα	Folate receptor alpha
FEG-SEM	Field emission gun scanning electron microscopy
GLiSten	Next Generation intraoperative Lymph node staging for Stratified colon cancer surgery
HAL	Hexylaminolevulinate
HRP	Horseradish peroxidase
IOB	Irregular outer border
ICG	Indocyanine green
IL	Interleukin
IO	Intra-operative
IPTG	Isopropyl β-D-1-thiogalactopyranoside
IND	Investigational new drug
LB	Luria-Bertani
LN	Lymph node
MRI	Magnetic resonance imaging
MSN	Mesoporous silica nanoparticle
MUC-1	Mucin-1

mTHPC	m-Tetrahydroxyphenylchlorin
MPTES	3-Mercaptopropyl-triethoxysilane
MES	2-(N-Morpholino) ethanesulfonic acid
MTT	3-[4,5-dimethylthiazole-2-yl]-2,5-diphenyltetrazolium bromide
NBCSP	National Bowel Cancer Screening Programme
NIR	Near-infrared
NOTES	Natural orifice transluminal endoscopic surgery
Ni2+-NTA	Ni^{2+}-nitrilotriacetic acid
OSNA	One-step nucleic acid
$^1O_2$	Singlet oxygen species
OD	Optical density
PET	Positron emission tomography
PpIX	Protoporphyrin IX
PLGA	Polylactide-co-glycolic acid
PDD	Photodynamic diagnosis
PDT	Photodynamic therapy
PS	Photosensitiser
PBS	Phosphate buffered saline
PAMAM	Polyamidoamine
QDs	Quantum Dots
RIGS	Radioimmunoguided surgery
ROS	Reactive oxygen species
SILS	Single incision laparoscopic surgery
SLN	Sentinel lymph node
scFv	Single chain Fv antibody

siRNA	Small interfering RNA
SR-B1	Scavenger receptor type-B1
SOB	Super optimal broth
SDS-PAGE	Sodium dodecyl sulphate polyacrylamide gel electrophoresis
SMCC	Succinimidyl 4-N-maleimidomethylcyclohexane
TAG-72	Tumour-associated glycoprotein-72
TMT	Meso-Tetra(N-methyl-4-pyridyl) Porphine Tetra Tosylate
TCEP	Tris (2-carboxyethyl) phosphine
TMB	3,3′,5,5′-tetramethylbenzidine
TBS	SuperBlock T20
TEOS	Tetraethyl orthosilicate
TBST	SuperBlock T20 + Tween-20
VEGFR2	Vascular endothelial growth factor receptor 2
V-PDT	Vascular-PDT
VR	Variable region

Chapter One

Introduction

1 Introduction

1.1 Colorectal cancer incidence

Colorectal cancer (CRC) is a major health problem in the United Kingdom as it is the fourth most common cancer with 110 new cases diagnosed daily (CRUK, 2011). Worldwide, it is the third most common form of cancer found in men and the second in women, and is associated with overall incidence of about 6% (UK, 2011, Torre et al., 2015, Siegal et al., 2014). The incidence of colorectal cancer is rising, although five year survival rates have doubled to 50% over the last 3 decades (Office for National Statistics, 2010). The incidence in the UK shows a wide variation with age as shown in **Figure 1.1** (CRUK, 2011). Colorectal cancer affects individuals in middle to later life, with a peak number of cases in the 70-80 age groups.

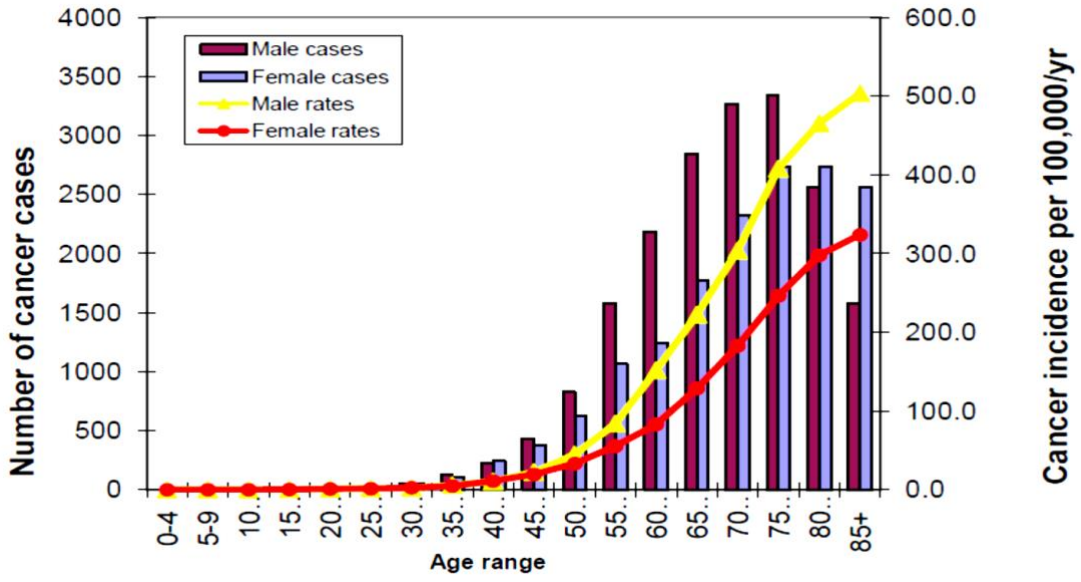

Figure 1. 1. Colorectal cancer incidence by age in the UK.

Histogram illustrating the number of cancer cases in both genders and in different age groups.

Improvement in CRC outcomes are attributed to improved surgical techniques, aided with neo-adjuvant and adjuvant therapies. However, the current treatment protocols are challenged by a number of different clinical factors, which necessitates a stratified approach to CRC management.

1.2 The clinical need in CRC surgery

Residual micro-metastases are associated with increased risk of relapse. Many patients are frail and at risk of complications from cancer surgery. Around one-third of patients operated on for colorectal cancer will suffer a complication, with 5% dying as a result of surgery (Guillou et al., 2005b, Jayne et al., 2010a). These statistics are likely to increase as the population demographic changes, with an increasing number of elderly people developing the disease. For over 100 years, surgery for colorectal cancer has been performed according to the same oncological principles, namely to resect the primary cancer with its draining lymphatic basin (radical surgical resection) so as to minimise the risk of locoregional cancer recurrence. Colorectal cancer surgery commonly involves a ‘D2 lymphadenectomy’ whereby the second tiers of draining lymph nodes are removed, whereas a high, central vascular ligation, also known as ‘D3 lymphadenectomy’ is not routinely practiced (West et al., 2008b). This is a technically challenging procedure as these intra-abdominal lymph nodes are located in close proximity to major blood vessels, which supply the colorectum. It is through this lymphovascular route that colorectal cancer cells typically metastasise distantly. Hence it is necessary that the entire anatomical territory of the artery supplying the tumour is resected en-bloc along with the tumour. Strong evidence suggest that the status of the nodal involvement is a major prognostic factor and dictates the need for adjuvant chemotherapy following curative surgery (ACPGBI, 2007).

This principle is being challenged with the shift in population demographic and the introduction of the National Bowel Cancer Screening Programme (NBCSP). Historically, some 10% of colorectal cancers were early stage (Dukes' A) with 30% of patients having lymph node disease. Radical surgery, with lymphadenectomy, was therefore justified, accepting that 70% of patients without lymph node disease would have been cured by removal of the cancer alone. With the introduction of the NBCSP there has been a sizeable shift in the stage of disease presentation, with ~50% of cancers now being Dukes' A with only a 10% risk of lymph node disease. This change in disease presentation, coupled with the increasing elderly population, presents an opportunity to re-think the surgical management of CRC. Up to 23-30% of CRC patients develop locoregional recurrence or distant metastases following curative resection for stage I or II disease (Figueredo et al., 2008, Faerden et al., 2011, Rahbari et al., 2012). Undetected lymph node micrometastases in combination with residual tumour cells are thought to be the main contributing factors for locoregional recurrence and can be easily missed during routine histopathological examination (Hermanek et al., 1999). A recent meta-analysis by Rahbari *et al* (Rahbari et al., 2012) has shown micrometastases are associated with poor overall, disease specific, and disease free survival. Although, additional immunohistochemistry combined with serial sectioning can aid in identifying micrometastases and isolated tumour cells more accurately, this is prohibitively expensive and time consuming. The treatment for patients with locoregional recurrence is palliative and hence accurate identification of positive lymph nodes could provide a solution.

1.3 Strategies to improve colon cancer surgery

The recent advancement in surgical technologies has allowed the delivery of

complex cancer surgery through minimally invasive procedures, including single incision laparoscopic surgery (SILS) and natural orifice transluminal endoscopic surgery (NOTES) (Cahill, 2010). These procedures offer significant advantages to patients when compared to traditional open surgery in the form of faster recovery, and shorter hospital stay by minimising surgical access trauma. Laparoscopic colectomy has gained wide acceptance amongst colorectal surgeons in the last decade with proven short-term benefits and oncological safety according to the “Conventional versus laparoscopic-assisted surgery in patients with colorectal cancer” (CLASSIC) trial (Guillou et al., 2005a, Jayne et al., 2010b, Nelson H, 2004, Fleshman et al., 2007). However, an important disadvantage of laparoscopic surgery is the loss of tactile feedback that is available at open surgery. The implication of such limitation is that it becomes difficult for the operating surgeon to locate early tumours, which tend to be small, or to accurately identify the tumour margins and the resection planes. Colonic tattooing has been employed by some surgeons in order to overcome the above problems and enhance small tumours location during surgery (Conaghan et al., 2010). The tumour is labelled with a permanent dye at endoscopy prior to surgery, but the location of tattooing can be variable and unreliable (Conaghan et al., 2010). Hence, a stratified approach is required, where the surgery is tailored to the fitness of the patient and the biology of the underlying cancer.

1.4 Strategies for pre-operative lymph node staging and their limitations

Stratified surgical resection relates significantly to accurate identification of pre-operative lymph node staging. The clinical challenge is to distinguish those patients with early stage (lymph node negative) disease from those patients with locally advanced (lymph node positive) disease. Patients with early stage disease will be cured by resection of the primary cancer alone, and spared the additional

morbidity of lymphadenectomy, whilst those patients with locally advanced disease will require radical resection with lymphadenectomy for cure. The problem is that there is currently no reliable means of distinguishing these two subgroups of patients. Post-operative histopathological examination of the surgical specimen is the only reliable way to ascertain if colon cancer has metastasised to the lymph nodes, by which time it is too late to 'personalise' surgery.

1.4.1 Computed tomography (CT)

The Association of Coloprocotologists of Great Britain and Ireland recommend that, ideally, all patients with CRC undergo a colonoscopy with tissue taken for histology, a staging thoracic and abdominal computed tomography (CT) scan, and in the case of rectal tumours a magnetic resonance imaging (MRI) scan with endoanal ultrasound if necessary (ACPGBI, 2007). Although the ability of CT to identify nodal status is poor, CT remains the preferred imaging modality for CRC staging (Dighe et al., 2010b, Bipat et al., 2004b). Inconsistency in the definition of a malignant lymph node appearance is the main factor for CT's poor detection accuracy. To date, single criterion or a combination of criteria including size and/or morphology (Keeney et al., 1989, Thompson et al., 1986) (lymph node size >1 cm), contrast enhancement above 100 hounsfield units (HU) (Hundt et al., 1999b), short-long axis diameter ratio, irregular outer border (IOB) and cluster of three or more normal sized lymph nodes, have all been used to improve the pre-operative diagnostic profile of CT (Smith et al., 2007, Hundt et al., 1999a). Although, the new generation of CT scanners are configured with multiple rows of detectors that facilitate more detailed assessment of size and morphology of pathological lesions (Rollvén et al., 2017), there remains a lack of validated CT

imaging criteria for the assessment of lymph node metastases in colon cancer. A meta-analysis showed CT to have a sensitivity of 70% (95% confidence interval: 65-73%) and specificity of 78% (95% confidence interval: 73-82%) in detecting nodal disease in colonic cancer (Dighe et al., 2010b). In another study of 84 patients with colon cancer undergoing pre-operative CT scanning, the accuracy, sensitivity and specificity for detection of lymph node metastasis were ~50%; no better than tossing a coin (Dighe et al., 2010a).

1.4.2 Magnetic Resonance imaging (MRI)

Despite advanced MRI technologies, prediction of nodal involvement in CRC remains difficult. MRI has a sensitivity of 66–85% and specificity of 41–97% in nodal staging for rectal cancer (Kim et al., 2000, Bipat et al., 2004a, Brown et al., 2003, Li et al., 2015). The assessment of lymph node status for colon cancer within the abdomen is limited due to the motion artefact and therefore it is primarily used for rectal cancer in the pelvis where the structures are fixed (Kijima et al., 2014). The colon is a greater challenge for MRI compared to the rectum due to anatomical considerations, peritoneal coverage, motility, and tortuosity. Few studies have assessed MRI diagnostic accuracy in colon cancer. In a retrospective comparative study of 28 patients with 29 tumours, high resolution MRI was compared to CT for pre-operative local staging of colon cancer (Kijima et al., 2014, Rollven et al., 2013). Two independent radiologists accurately predicted N stage in 72% and 69% of cases, yet the inter-observer agreement was poor: κ value 0.10. Conversely, for CT the corresponding results were 72% and 72%, with much better inter-observer agreement: κ value 0.66.

1.4.3 Positron emission tomography (PET)

Positron emission tomography (PET) scanning combined with CT colonography increases the diagnostic accuracy of lymph node metastases when compared to CT alone (Veit-Haibach et al., 2006, Sun et al., 2008). Veit-Haibach *et al* (2006) combined PET with CT colonography and found it to be significantly more accurate in detecting lymph node metastases when a 1 cm threshold was used for the size of metastatic node (p=0.003), yet when the threshold was reduced to 0.7 cm there was no statistical difference (p=0.13). As the majority involved nodes are < 5 mm in diameter, this has limited diagnostic value, although, due to the higher overall specificity PET/CT may play a role in ruling out gross nodal metastases. Cohade *et al* (2003) reported in their retrospective series of 45 patients with colorectal cancer PET/CT improved staging and restaging accuracy from 78% to 89% (Cohade et al., 2003). However, determining the precise location of lesions by PET can be challenging because bowels have variable uptake of ^{18}F-2-fluoro-2-deoxy-D-glucose (^{18}F-FDG) while urinary activity can be a confounding factor too, leading to misinterpretation of lymph node activity. In another study, Kwak *et al* (2012) retrospectively analysed 473 patients who underwent pre-operative PET/CT and curative surgery and found that PET /CT had a lower sensitivity, but a higher specificity than CT for regional nodal metastases (Kwak et al., 2012). PET is still not sensitive enough to detect micro-metastases ranging from 0.2 -2mm (Mehes et al., 2000).

1.5 Intra-operative lymph node staging

The majority of involved nodes are < 5 mm in diameter, and therefore are neither visible nor palpable intra-operatively (Markl et al., 2012, Rodriguez-Bigas et al., 1996). The ideal solution to the problem of inaccurate pre-operative lymph node

staging is to develop a reliable means of intra-operative staging. This would facilitate a real time assessment of lymph node status, thus enabling a personalised operative strategy. Although, adjuvant chemotherapy is dictated by several prognostic factors such as venous invasion, peri-neural invasion, tumour perforation, serosal involvement and incomplete resection (Fang et al., 2014, Dienstmann et al., 2015); lymph node status remains the main factor. The development of a reliable means of intraoperative lymph node (LN) staging offers the ideal solution to the problem of accurate pre-operative staging in order to allow real-time assessment and hence personalised surgery. The concept of intraoperative LN staging is not new and has proven validity in some cancers, most notably breast cancer. In CRC, early series reported sentinel LN detection rates of 58–98%, sensitivity rates of 40–100% and false-negative rates between 0% and 60% (Mulsow et al., 2003). In a more recent meta-analysis, the results were not encouraging as LN metastases identification rate was reported to be with a pooled sensitivity of 69.6% (range 33.3–100%) and a false-negative rate of 30.4% (van der Zaag et al., 2012). Of clinical importance, it is not clear whether metastases from colon cancer follow a traditional spread through tiers of LNs, or rather metastasise in a skip-manner (West et al., 2008a). It is reported that in 48% of cases with CRC, the first metastatic LNs were not adjacent to the tumour or was 5 cm beyond the longitudinal tumour margin in 18% of cases (Tan et al., 2010). Hence, it is unclear if the poor results are explained by technical problems, sub-optimal implementation of the technique or whether the concept is fundamentally flawed because of the inherently unpredictable pattern of lymph node involvement. Further evaluation of these techniques is required to determine whether they should be generally adopted. A summary of intraoperative staging techniques for colorectal cancer is presented in **Table 1.1.**

Table 1. 1. Summary of clinical intra-operative tumour detection techniques for CRC.

Technology	System design	Detection technique	Tumour targeted	Tumour target	Study design	Clinical outcome	Drawbacks
One-step nucleic acid (OSNA)+ indocyanine green (ICG) (Yeung et al., 2018)	Indocyanine green photosensitive dye combined with OSNA assessment	Dye injected Subserosally followed by OSNA assessment	No	-	Feasibility studies	Poor fluorescent diagnosis of lymph nodes	False negatives, variable sensitivity in detecting the sentinel node, technical difficulties
Radioimmunoguided surgery (RIGS) (Sun et al., 2007)	Radionuclide loaded Antibody	Hand held gamma probe	Yes	CEA TAG-72	Case series	Significant prognostic value long-term survival advantage	Radioactive material (handling, disposing) Variable sensitivity Operator dependent Delay between administration and surgery
Near-infrared laparoscopic sentinel lymph node mapping (Cahill et al., 2012b, Lieto et al., 2018)	Indocyanine green photosensitive dye	Dye injected Subserosally or laparoscopically to detect the fluorescent signal	No	-	Case series/ feasibility studies	Penetrates tissue more deeply and does not distort the view of the surgical field	False negatives, variable sensitivity in detecting the sentinel node, technical difficulties

5-Aminolevulinic acid-induced fluorescence (Andrew et al., 2016)	5-ALA pro-drug	Laparoscopic Fluorescence detection	No	-	Phase I clinical trail	Potentially sensitive Safe	Lack of specificity
Carbon nanoparticles (Yang et al., 2015)	Carbon nanoparticles	Laparoscopic direct visualisation	No	-	Case series	Safe can increase the retrieved number of lymph	No data concerning tumour margins

1.5.1 Combined Fluorescence imaging with rapid one-step nucleic acid (OSNA) pathological assessment

A facility to confidently assign nodal status intraoperatively independent of the performance of the radical resection could allow stratification of operative extent by disease stage, without compromising prognostic or therapeutic value. Yeung *et al* (2018), were the first to combine indocyanine green (ICG) fluorescence imaging with rapid OSNA in a prospective feasibility trial (n=16) (Yeung et al., 2018). One-step nucleic acid amplification (OSNA) is a rapid mRNA assay that can detect colorectal micrometastases in lymph nodes based on cytokeratin 19 (CK19) levels within 20 min of their removal. Only 9 fluorescent lymph nodes were identified intra-operatively out of 78 which were retrieved for both histological and OSNA assessment. OSNA analysis of the ICG-labelled node matched the final histological nodal stage in 3/6 patients (two being N0 and one N1). Although OSNA sensitivity was 1 (0.81–1, 95% CI) and specificity 0.98 (0.91–1, 95% CI) for the remaining retrieved lymph nodes, improving fluorescence node detection rates is the first step towards the elegant concept for OSNA identification of node negative patients during surgery.

1.5.2 Antigen-Directed Cancer Surgery

Antigen-directed surgery/Radioimmunoguided surgery (RIGS) is considered as one of the earliest intra-operative tumour detection systems (Aitken et al., 1984). This system is designed based on three main components which include: an antibody to a specific antigen expressed by the targeted tumour tissue; radiolabel to the antibody; and a hand-held gamma detector used intra-operatively to detect the bound antibody/radionuclide complex to the tumour cells. Carcinoembryonic antigen (CEA) or tumour-associated glycoprotein 72 (TAG-72) were used as the

target antigens. Povoski *et al* (2012), reported that absence of detectable TAG-72 antigen within the surgical field at completion of antigen-directed cancer surgery for primary colorectal cancer was associated with significantly improved median survival (8.8 versus 2.5 years; P = 0.005) and time-dependent survival (45.4% versus 22.0% at 10 years; P = 0.002 and 39.4% versus 20.3% at 15 years; P = 0.003) when compared with TAG-72-positive subgroup (Povoski et al., 2012). The difference in survival between the TAG-72-positive and TAG-negative groups reached significance only for advanced-stage (III and IV) disease and only at the 10- and 15-year intervals. In the absence of precise data describing which patients had extra tissue removed or a change in operation as a direct result of TAG-72 detection, it cannot be concluded that RIGS was the causal factor of this difference. It may simply have identified those patients with tumour cells remaining but not affected the outcome (Tiernan and Jayne, 2017). Others reported the sensitivity of RIGS in detecting colorectal cancer to range from 20-100% (Hamy et al., 1995, Kim et al., 2005) and 63-97% (Cohen et al., 1991, Arnold et al., 1992) for primary cancer and recurrent disease respectively. The heterogeneity between studies and difficulties associated with handling and disposing radiolabelled material have made it difficult to use RIGS as a routine intra-operative detection system for colorectal cancer surgery in the last decade.

1.5.3 Sentinel lymph node mapping

The model of intraoperative lymph node (LN) staging is not new but has attracted great interest since the introduction of sentinel lymph node (SLN) mapping techniques. Sentinel lymph node is defined as the first regional LN encountered by metastasising tumour cells (Bara et al., 2011). The concept is well established in the management of breast cancer (Baso, 2009) and melanoma (Marsden et al., 2010) and proposes that if a sentinel lymph node is free of tumour cells, then

the remaining lymph nodes would also be tumour free and therefore, stratified surgical resection can be tailored to the stage of the disease (Reintgen et al., 1994, Morton et al., 1992). In colorectal cancer surgery, SLN mapping (using a blue dye injected subserosally around the tumour prior to surgery) was first introduced in 1999 (Joosten et al., 1999). Evidence from several studies including systematic reviews and meta-analyses highlighted serious limitations such as false negatives (30.4%) and variable sensitivity in detecting the sentinel node (33.3-100%) and technical challenges particularly in rectal cancer (van der Zaag et al., 2012, Mulsow et al., 2003, van der Pas et al., 2011). The variability in anatomical site of the first metastatic LN can be explained by the fact that colon cancer metastasises as skip lesions and not necessarily follow a traditional spread through tiers of LNs. Tan *et al* (2010), reported that in 48% of cases of colon cancer, the first metastatic LN was not adjacent to the tumour while in 18% of cases it was 5 cm beyond the longitudinal tumour margin (Tan et al., 2010). The concern regarding the high false-negative detection rates meant SLN mapping is not in routine practice in colorectal cancer surgery today. Despite the limitations of SLN mapping, this concept has led to the emphasis of shifting strategies from a post-operative staging to a reliable means of intraoperative staging with potential role in selective lymphadenectomy, using advanced technologies such as near-infrared laparoscopy and intraoperative photodynamic diagnosis.

1.5.4 Near-infrared laparoscopy

Near-infrared laparoscopy is a promising technology that enhances specific light wavelength beyond that of white light illumination (Cahill et al., 2012b). NIR energy is characterised by deep fatty tissue penetration without causing collateral heat damage and facilitates excitation of certain molecules to allow real-time

fluorescence imaging. Indocyanine green (ICG) is one good example of photosensitive tricarbocyanine dye with a peak spectral absorbance at approximately 780 nm (Landsman et al., 1976, Haritoglou et al., 2003), in the near-infrared region. The small molecular weight of ICG (775 g/mol) (Alander et al., 2012) allows the dye to rapidly and passively diffuse into the lymphatic channels and travel to the first anatomical draining lymph nodes surrounding the colon cancer. It can be injected subserosally (intra-luminal via a colonoscope or laparoscopically) and a modified laparoscope can be used to detect the fluorescent signal. To date, NIR fluorescence-guided SLN mapping using ICG has been extensively studied in colorectal cancer and proved to outperform blue V dye assays due to increased tissue penetration and reduced background fluorescence (Cahill et al., 2012b, Hirche et al., 2012, Ankersmit et al., 2011, van der Pas et al., 2013). The technology is not tumour-specific, but it is foreseeable that in combination with intra-operative, morphological sentinel node assessment, it has the potential to allow intra-operative staging and surgical stratification.

1.5.5 Photodynamic diagnosis (GLISTEN Trial)

A potentially neat solution to intra-operative staging involves the use of photosensitisers. 5 aminolevulinic acid (5-ALA), which is present in virtually all human cells, has been extensively examined for photodynamic diagnosis in cancers. 5-ALA is a pro-drug, taken up into cells, where it is metabolised via the heme biosynthesis pathway to protoporphyrin IX (PpIX). Usually, 5-ALA synthesis is regulated by negative feedback due to high intracellular concentrations of heme. However, this negative feedback system is overridden when exogenous 5-ALA is administered and PpIX accumulates in malignant cells with reported selectivity (Krammer and Plaetzer, 2008b). PpIX is a fluorescent

molecule, with absorption and emission wavelengths of 405 nm and 630-700 nm respectively. This property lends itself very well to laparoscopic surgery where the light from the laparoscope can easily be modified. Therefore, 5-ALA could readily be used for in vivo fluorescence diagnosis (FD) (Krammer and Plaetzer, 2008a, Kennedy and Pottier, 1992). To evaluate the capacity of 5-ALA FD against CRC lymph node metastases, Harada et al (Harada et al., 2013) applied 15 mg/kg orally 2 hours prior to surgery. Using fluorescence microscopy and a spectral unmixing method to prevent collagen autofluorescence in 87 excised, fresh, bisected lymph nodes, the fluorescence intensity in metastatic lymph nodes was 10.2-fold greater than non-metastatic lymph nodes. The GLiSten (Next Generation intraoperative Lymph node staging for Stratified colon cancer surgery) study was the first human clinical trial using 5-aminolevulinic acid (5-ALA) in laparoscopic colorectal cancer resection, using photosensitiser for intraoperative fluorescence of LN staging in colon cancer (Andrew et al., 2016) as shown in **Figure 1.2**. Andrew *et al* (Andrew et al., 2016) (University of Leeds) reported a distinct difference has been observed in the fluorescence of the primary colon cancers, with around only 30% of cancers exhibiting fluorescence and 70% showing no fluorescence. Although the results from the GLISTEN trial proved that 5-ALA has poor sensitivity for detecting lymph node metastases and cannot be recommended for intraoperative staging, the use of photosensitiser remains as a viable option. The advantage with the clinical use of any photosensitising agent is the potential theranostic functionality. Photosensitisers have cytotoxic effect on cancer cells via the photodynamic effect and hence will not only allow fluorescent intraoperative staging of cancer and lymph nodes, but will also help eradicating residual micrometastases.

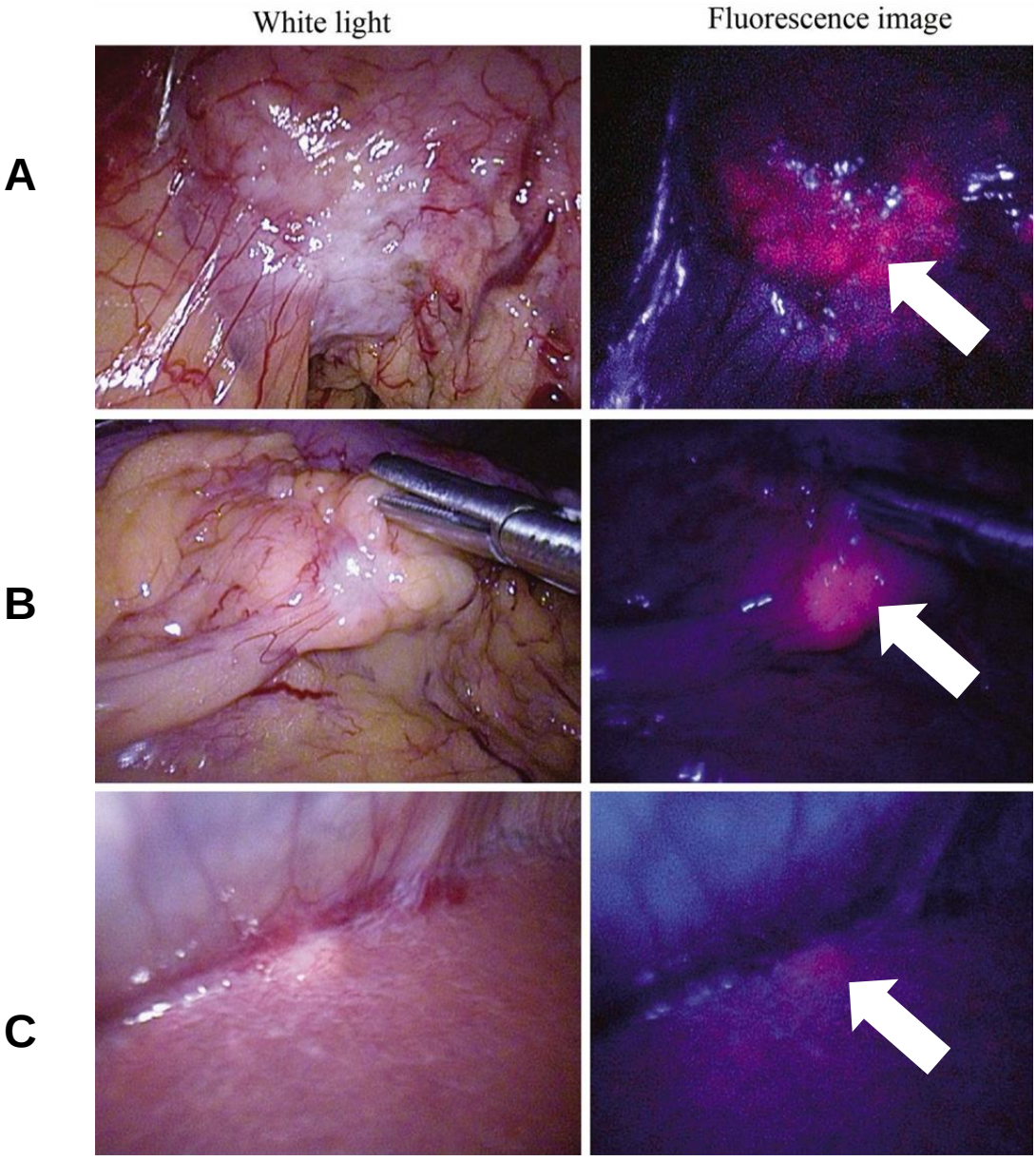

Figure 1. 2. Fluorescence diagnosis of colorectal cancer using 5-ALA.

Figures illustrate the laparoscopic images taken intra-operatively from the GLiSten trial to show the enhanced intraoperative location of colorectal cancer in a patient undergoing resection. White light is the normal laparoscopic view in contrast with the fluorescent view after 5-ALA administration. White arrows are pointing at the (A) primary CRC; (B) positive lymph node and (C) metastatic deposit in the liver. Images were taken by Prof David Jayne at St. James's University Hospital in Leeds with permission to be used in this chapter.

1.6 Nanomedicine

Recent advances in nanotechnology have aimed to overcome the limitations of current colorectal cancer treatments, by offering safer, more effective and affordable nano-vehicles for targeted diagnostic and therapeutic approaches. For such systems to be effective in laparoscopic colorectal cancer surgery, three important criteria must be fulfilled. The fluorescent nanoparticles' signal must be of adequate magnitude to pass through the muscular bowel wall and the fatty mesentery. The tumour-to background ratio must be large enough to allow sensitive and specific detection and the fluorophore must be relatively resistant to photobleaching. This is of significant clinical importance due to the sometimes-extended duration of operations for colorectal cancers. A potential solution to intra-operative staging involves the use of fluorescent nanoparticles. Nanomaterials possess unique physical and chemical features that enhance their applications in cancer therapy and imaging. They are characterised by many features such as ease of synthesis, small size (1–100 nm), resistance to oxidation, fluorescent properties, surface modification/functionalisation and mass production at cost effective levels (Fortina et al., 2007, Grobmyer et al., 2010, Hartman et al., 2008). Other features such as solubility, diffusivity, drug release capabilities and immunogenicity can all be modified based on changing the chemical structure of the nanoparticle (Fortina et al., 2007, Grobmyer et al., 2010, Hartman et al., 2008). Nanoparticles can be manufactured and fabricated in many different structures (solid, core, dendrimers), shapes (rod, sphere, prism) or composite materials (metals, semiconductors, polymers) all of which allow diverse applications of nanotechnology in cancer therapy and imaging (Fortina et al., 2007).

1.6.1 Colorectal cancer and nanomedicine

The application of nanotechnology to the diagnosis and treatment of colorectal cancer is an exciting field of research that can potentially enhance the existing therapeutic and diagnostic methods as well as advancing the development of novel staging approaches. The development of in vivo imaging agents has resulted in higher sensitivity and better tumour resolution. Nanoparticles can be used for direct visual detection and multiplexing capabilities for specific proteins or detecting surface marker (Seydack, 2005). Although, there are few examples of the application of nanotechnology to the imaging of CRC, a recent study by Tiernan *et al* (2015), showed promising results for *in vivo* imaging in a xenograft model of CRC (Tiernan et al., 2015). In addition, nanoparticles have the potential to enhance the diagnostic power of imaging modalities using contrast agents such as gadolinium, or imaging agents, such as iron oxide (Farokhzad and Langer, 2006, Saito et al., 2005, Mulder et al., 2005). These nano-enhanced imaging systems have the potential to significantly improve the features of traditional MRI and offer a better chance for CRC detection and treatment. Systemic chemotherapy for CRC is challenged by the non-specific distribution of the drugs, suboptimal concentrations of the agents to tumour sites and adverse side-effects, all of which have a negative impact on the patient's quality of life (Shabaruddin et al., 2013). Toxicity is a particularly critical matter for the elderly population that constitute the majority of the patients diagnosed with colorectal cancer (Maddams et al., 2012), and the introduction of less toxic and more effective drugs delivery would greatly benefit this cohort. Targeted nanomaterials offer potential solutions to the limitations of standard chemo and radio-therapeutic modalities in CRC. For example, the food and drug administration (FDA) has approved the use of liposomal encapsulated doxorubicin for treatment of

metastatic ovarian cancer that is resistant to paclitaxel- and platinum-based agents (Muggia et al., 1997). These liposomal nanostructures have also been investigated for the treatment of breast cancer, non-Hodgkin's lymphoma and small-cell lung cancer. Paclitaxel has also been delivered using nanoparticles for the treatment of patients with metastatic breast cancer who have failed standard chemotherapy (O'brien et al., 2004). A summary of targeted nanotechnological methods for CRC detection and treatment is presented in **Table 1.2**. Targeted nanoparticles delivery (using antibodies, proteins and small-molecule ligands) has enhanced drug delivery to specific tumour sites. This yielded greater pharmacological and clinical effectiveness and was associated with lower side effects in animal cancer models. Antibody-targeted liposomes effectively accumulated in colorectal cancer cells in mouse xenograft models (Fortina et al., 2007, Kukowska-Latallo et al., 2005, Viswanath et al., 2016). Similarly, antibody-targeted silica nanoparticles allowed specific *in vivo* imaging of CRC in a mouse xenograft model (Tiernan et al., 2015). The application of targeted delivery of these nanostructures using bioreceptors offers a real opportunity to overcome problems of untargeted delivery systems.

Table 1. 2. Summary of nanotechnological methods in the detection and treatment of CRC.

Nanosystem	Structure	Target	Bioreceptor	Applications	Ref
QDs	Nanocrystals	VEGFR2	Antibody	*In vivo* fluorescent imaging	(Carbary-Ganz et al., 2015)
Iron oxide nanoparticle	Gold coated superparamagnetic iron oxide nanoparticles	MUC-1	Aptamer	*In vivo* MRI and photothermal therapy	(Azhdarzadeh et al., 2016)
	Dextran coated iron oxide nanoparticle	VEGFR	Antibody	*In vivo* MRI	(Hsieh et al., 2012)
	Dextran coated superparamagnetic iron oxide nanoparticles	CEA	scFv	*In vitro* MRI	(Huang et al., 2013)
PLGA nanoparticles	Camptothecin loaded PLGA nanoparticles	CD95/Apo-1	Antibody	*In vitro* therapy	(McCarron et al., 2008)
	Curcumin-loaded nanoparticles	EpCAM	Aptamer	*In vitro* therapy	(Li et al., 2014)
	Epirubicin loaded PLGA	MUC-1	Aptamer	*In vivo* fluorescent imaging and therapy	(Taghavi et al., 2017)

Liposomes	Oxaliplatin loaded liposomes	VEGFR	Antibody Fab fragment	*In vivo* therapy	(Zalba et al., 2015)
	Doxorubicin and vinorelbine loaded liposome	α -enolase	pHCT74 peptide	*In vivo* therapy	(Wu et al., 2015)
Silica nanoparticles	Dye-doped silica nanoparticles	CEA	Antibody	*In vivo* fluorescent imaging	(Tiernan et al., 2015)
	Magneto-fluorescent silica nanoparticles	VEGFR	Antibody Fab fragment	*In vivo* fluorescent imaging	(Cho et al., 2010)
	(Owens Iii and Peppas)(Owens Iii and Peppas)(Owens Iii and Peppas)(Owens Iii and Peppas)(Owens Iii and Peppas)(Owens Iii and Peppas)Doxorubicin-loaded MSN	EpCAM	Aptamer	*In vivo* therapy	(Xie et al., 2016)
Lipoprotien nanoparticles	siRNA loaded nanoparticles	SR-B1	Apo A-1	*In vivo* therapy	(Shahzad et al., 2011)
Gold nanoparticle	Gold and iron oxide hybrid nanoparticles	A33 antigen	scFv	*In vivo* fluorescent imaging and therapy	(Kirui et al., 2010)

Chitosan/Alginate Nanoparticles	TMT loaded nanoparticles	DR5	Antibody	*In vitro p*hotodynamic therapy	(Abdelghany et al., 2013)
	5-ALA loaded nanoparticles	Folate receptor	Folic acid	*In vitro p*hotodynamic therapy	(Yang et al., 2010)
	Oxaliplatin loaded nanoparticles	Hyaluronic acid receptor	Hyaluronic acid	Therapy	(Jain et al., 2010)

Abbreviations: *(CRC), colorectal cancer; (QD), quantum dots; (VEGFR2), Vascular endothelial growth factor receptor 2; (MUC-1), Mucin-1 receptor; (MRI), magnetic resonant imaging; (CEA), carcinoembryonic antigen; (scFv), recombinant single chain Fv antibody fragments; (PLGA), polylactide-co-glycolic acid; (CD95/Apo-1), Fas receptor; (EpCAM), epithelial cell adhesion molecule; (MSN), mesoporous silica nanoparticle; (siRNA), small interfering RNA; (SR-B1),* scavenger receptor type B1; *(Apo A-1), a*polipoprotein A-1; *(TMT), meso-Tetra(N-methyl-4-pyridyl) Porphine Tetra Tosylate*; *(DR5), death receptor 5; (5-ALA), 5-aminolaevulinic acid.*

1.7 A proposed solution for intra-operative fluorescent imaging

Identification of better fluorescent photosensitisers and their delivery in targeted manner for intraoperative visualisation of primary colon cancers and LN disease is required and this is effectively a precursor to this project. A proposed solution to the limitations of existing staging strategies is to develop a targeted tumour-specific fluorescent system characterised by the following attributes:

I. Specifically binds to colorectal cancer tissue at a molecular level;

II. Safe and feasible to be administered to a patient prior to laparoscopic surgery;

III. Easily identified at laparoscopic surgery using specific light source;

IV. Allows surgeons to accurately delineate the primary tumour margins and detect metastatic disease;

V. Allows an intra-operative assessment of the stage of the tumour and hence stratify surgical resection to disease stage.

The build-up of such probe will require: a) CRC-specific targeting biomarker; b) theranostic visualisation component and c) nanoparticulate scaffold to combine the two; all of which will optimise the fluorescent signal at surgery. Nanomedicine is an expanding area of research and appears to offer a potential platform to build up the ideal intraoperative staging system.

1.7.1 Tumour specific targeting biomarkers

Tumour targeted delivery relies on the availability of specific tissue biomarkers to enhance the selectivity and efficacy of imaging and therapies. In colorectal

cancer, a variety of tissue biomarkers have been investigated including: carcinoembryonic antigen (CEA) (Heine et al., 2011, Yazaki et al., 2008, Campos-da-Paz et al., 2018, Boogerd et al., 2018), tumour-associated glycoprotein 72 (TAG-72) (Zou et al., 2009b, Chen et al., 2011), endothelial growth factor receptor (EGFR) (Shinozaki et al., 2018, Sartore-Bianchi et al., 2018, Dankner and Rose, 2018) and folate receptor alpha (FRα) (Hentzen et al., 2018, Yang et al., 2013). A summary of these biomarkers and their expressions is shown in **Table 1.3**. Tiernan *et al* (2013), evaluated the sensitivities and specificities of the former four (most commonly used markers); CEA, TAG-72, FR*α* and EGFR (Tiernan et al., 2013). Biomarkers were evaluated in matched mucosal and colorectal cancer tissues from 280 patients using immunohistochemistry. They also examined matched positive and negative lymph nodes from 18 patients with colorectal cancer. Of clinical interest, CEA showed the greatest differential expression, with tumours scoring a mean of 10.8 points higher than normal tissues (95% CI 10.31–11.21, $P<0.001$). Similarly, CEA showed the greatest differential expression between positive and negative lymph nodes with an overall sensitivity and specificity of 93.7% and 96.1% respectively for colorectal cancer detection. Carcinoembryonic antigen has the greatest potential to allow highly specific tumour targeted imaging and therapy and will be the first choice for the build-up of the proposed system in this project. CEA, which is the main focus of this study, is a highly N-glycosylated oncofetal antigen that was originally found in gastrointestinal cancer tissues (Gold and Freedman, 1965, Thomas et al., 1990). After undergoing post-translational modification, the molecular weight of full-length CEA protein is 180-200 KDa (Hatakeyama et al., 2013). It is comprised of an N-terminal sequence, three highly conserved repeat domains of 178 amino acids and an anchored hydrophobic C-terminal domain

(Bjerner et al., 2002). CEA is unique compared to the other CEACAMs protein because it is comprised of A3 and B3 domains that mediates the intercellular adhesion process (Blumenthal et al., 2005).

Table 1. 3. Most commonly used tissue biomarkers for CRC and their expression levels.

Biomarker	Location	CRC Tissue expression	Expression in other cancers	Other tissue expression
CEA	Membrane-bound glycoprotein	+++	++	+
TAG-72	Membrane-bound glycoprotein	+++	+++	+
EGFR	Tumour vessel protein	++	++	++
FRα	Membrane-bound protein	+	+++	-

Abbreviations: CEA, carcinoembryonic antigen; TAG-72, tumour-associated glycoprotein 72; EGFR, endothelial growth factor receptor; FRα, folate receptor alpha. + denote: (+++), high expression; (++), moderate expression; (+), low expression and (-), no expression.

1.7.2 Fluorescent visualisation component

A fluorophore is a chemical compound that absorbs light leading to electrons being excited to a higher quantum state. When they return to their ground state they emit photons at longer wavelengths to those that were absorbed. Non-specific auto-fluorescence from normal tissues is well recognised and can potentially interfere with the proposed imaging system (Monici, 2005). Accordingly, the selected visualisation dye should have an emission wavelength within the near infra-red spectrum (wavelength > 700 nm) to overcome auto-fluorescence, penetrate tissues deeply without damaging them, and be suitably bright (Weissleder and Ntziachristos, 2003, Hilderbrand and Weissleder, 2010, Muller et al., 2001). Several clinical studies have evaluated near-infrared cyanine (Cy) dyes (absorption wavelength 650-900 nm) for the purpose of mapping lymph nodes, bile ducts, ureters and anastomotic perfusion during laparoscopic surgery (Ashitate et al., 2012, Soltesz et al., 2006, Kusano et al., 2008, Hutteman et al., 2010, Cahill et al., 2011, Matsui et al., 2011, Cahill et al., 2012a, Boogerd et al., 2018, Lamberts et al., 2017). In all studies, the fluorophore was injected into the anatomical area of interest and showed localised fluorescence. The results were less impressive when the tumour-to-background ratio were considered. Most importantly, none of these studies used targeted delivery of fluorophores. Since laparoscopic surgery is gaining wide acceptance amongst colorectal surgeons, resistance to photobleaching due to the sometimes-prolonged duration of operations is also critical for such a system to be practically applicable.

1.7.3 Photosensitisers as theranostic visualisation component

Photodynamic diagnosis (PDD) is an emerging technology for the diagnosis of cancers. Following administration of a photosensitiser, it preferentially accumulates in malignant tissue and fluoresces when photo-irradiated. This can potentially enable distinction between normal and cancer tissue. When a photosensitiser is excited, it can return to its ground state with the emission of fluorescence and it can also become de-excited allowing the transfer of energy to an oxygen molecule, yielding singlet oxygen species ($^1O_2$). These reactive oxygen species are responsible for the photodynamic cytotoxic effect. Integrating PDD and photodynamic therapy (PDT) using one active agent is an interesting area to explore, which brings both diagnostics and therapeutics (theranostics) into a single intervention. In regard to colorectal cancer surgery, PDD can be initially performed by exciting a specific photosensitiser intraoperatively to assess the disease and guide treatment then, PDT is performed to kill any residual cancer by shining a light of maximum excitation. These characteristics make photosensitisers ideal visualisation components for the build-up of the planned imaging system. To date, PDD has proven to be an effective intra-operative diagnostic tool in solid cancers such as bladder and brain tumours with 5-ALA being the most studied agent in this respect (Mowatt et al., 2011, Stummer et al., 2006, Eljamel, 2008). 5-ALA is a pro-drug, taken up into cells, where it is metabolised via the heme biosynthesis pathway to protoporphyrin IX (PpIX). Usually, 5-ALA synthesis is regulated by negative feedback due to high intracellular concentrations of heme; however, this negative feedback system is overridden when exogenous 5 ALA is administered and PpIX accumulates in malignant cells with reported selectively. PpIX is a fluorescent molecule, which when exposed to blue-violet light of excitation wavelength 405 nm, emits a

characteristic red fluorescence at a wavelength of 630 to 700 nm. This property lends itself very well to laparoscopic surgery where the light from the laparoscope can easily be modified; therefore 5-ALA could readily be used for *in vivo* fluorescence diagnosis (FD).

A summary of photosensitiser induced fluorescence in colorectal cancer is shown in **Table 1.4**. Regula *et al* (1995), were the first to examine colorectal PpIX accumulation microscopically (Regula et al., 1995). High tumour/normal mucosa selective uptake was observed with a ratio of 5:1 following oral administration of 5-ALA in seven patients with colorectal cancer. Interestingly, the selectivity appeared to be dose dependent. In another clinical study, using *ex vivo* laser fluorescence spectroscopy, Moesta *et al* (2000), identified PpIX as the predominant endogenous fluorophore in 32 primary colorectal carcinomas and 1053 palpable mesenteric nodes (Moesta et al., 2000). Even in the absence of 5-ALA administration this technique was able to distinguish metastatic from uninvolved nodes with a sensitivity and specificity of 62% and 78% respectively. To evaluate the capacity of 5-ALA to diagnose CRC lymph node metastases Harada *et al* (2013), applied 15 mg/kg orally 2 hours prior to surgery (Harada et al., 2013). Using fluorescence microscopy and a spectral unmixing method to prevent collagen autofluorescence in 87 excised, fresh, bisected lymph nodes, the fluorescence intensity in metastatic lymph nodes was 10.2-fold greater than non-metastatic lymph nodes. The GLISTEN trial (University of Leeds) on the other hand, was the first human clinical trial of 5-ALA-mediated fluorescence for diagnosis of LNs in colon cancer. Although a distinct difference has been observed in the fluorescence of the primary colon cancers, only around 30% of cancers exhibited fluorescence and 70% showed no fluorescence. This might suggest a tumour related underlying difference in 5-ALA accumulation and

metabolism indicating a possibility of prognostic benefit. The only study that examined the efficacy of photodynamic therapy in colorectal cancer was conducted in 1995 by Regula *et al* (Regula et al., 1995). Two patients (1 colorectal cancer and 1 malignant polyp) received PDT after oral 5-ALA administration using a bare fibre light source (50 J/cm^2) during colonoscopy. The authors reported evidence of tumour site necrosis on microscopic examination of the specimens. The study reported no data on patients' demographics, disease stage or follow up outcomes.

The main drawbacks for using PDT in the treatment of various cancers is associated with photosensitiser distribution and local and deep tissue irradiation. To date, there are over a dozen photosensitisers that have desirable features which can benefit patients, but none is completely satisfactory. Photosensitisers are non-specific as they can be retained in normal tissue. Targeting photosensitiser to tumours using a nanoparticles formulation offers a potential solution to the limitations of conventional PDT.

Table 1. 4. Photodynamic diagnosis for colorectal cancer.

PS	Tissue/Examined specimen	Detection mode	Study design	Results	Ref
5-ALA	Primary colon cancer and lymph nodes	IO fluorescence blue light laparoscopy	*In vivo*	30% cancer fluorescence, 36.8% LN fluorescence	(Andrew et al., 2016)
5-ALA	Adenocarcinoma/adenoma	Fluorescence microscopy	*Ex vivo*	Fluorescence intensity ratio between microscopy adenoma tumour and normal mucosa of approx. 5:1	(Regula et al., 1995)
5-ALA	Dysplasia (ulcerative colitis)	Imaging and fluorescence microscopy	*In vivo*	Differentiation of inflamed fluorescence (ulcerative colitis) from normal mucosa microscopy (PS: intensity ratio 4:1)	(Eker et al., 1999)
5-ALA	Dysplasia	Endoscopy imaging	*In vivo*	Fluorescence intensity ratio (633 nm: 599 nm): discrimination between dysplastic and inflamed lesions: sensitivity 81.6%, specificity 88%, positive predictive value 75.6%, negative predictive value 91%	(Ortner et al., 1997)
5-ALA	Dysplasia	D-Light Imaging	*In vivo*	Fluorescence detection of low-grade (380–420 nm) (adenoma, dysplasia, 2 out of 3 adenomas ulcerative colitis) fluorescence positive	(Messmann et al., 1998)

5-ALA	Adenomatous and hyperplastic polyps	Nitrogen laser (337 nm) and dye laser (405 or 436 nm)	*In vivo*	Multivariate linear regression analysis: differentiation between polyps' normal mucosa and adenomas: with 405 nm excitation: sensitivity 89%, specificity 94%; 436 nm excitation: sensitivity 86%, specificity 100%	(Eker et al., 1999)

Abbreviations: PS: photosensitiser; 5-ALA, 5-aminolevulinic acid; IO, intra-operative; LN, lymph node; Ref, reference.

1.7.4 Mechanism of action of PDT on cancer cells and tissue

PDT aids tumour ablation via the production of reactive oxygen species and acts via three different mechanisms. These are; direct cell death (necrosis, apoptosis or autophagy), blood vessel constriction, and the initiation of an immune response. The mechanisms of action of PDT in the light of the most recent evidence is reviewed and discussed in more detail below.

1.7.4.1 Direct cell damage

Reactive oxygen species created by the activation of the photosensitiser by light cause direct photo-damage to biological molecules including proteins, lipids and nucleic acids. This induces cell destruction via necrosis, apoptosis or autophagy (Yoo and Ha, 2012) depending on the availability of required components for PDT; which are O2 and PS concentration and the intensity and duration of light applied (Zeng et al., 2013). The process of cell death that occurs, whether it is apoptosis, necrosis or autophagy, is determined by the intracellular localisation and accumulation of the photosensitiser which can be different depending on the molecule used and the genomic characteristics of the cancer cells as well (Allison and Sibata, 2010). Sites of accumulation of different photosensitisers and the resultant mechanism of action upon illumination is shown in **Table 1.5**. The accumulation site depends on the net ionic charge of the photosensitiser, its hydrophobicity and the asymmetry of the molecule (Castano et al., 2004). Increasing concentrations of photosensitiser in the mitochondria caused apoptotic cell death upon light exposure whereas cell death via necrosis is usually due to accumulation within the plasma membrane or lysosomes (Vrouenraets et al., 2003, Kessel et al., 1997, Hoi et al., 2012). However, some studies have found that lysosomal accumulation can also lead to apoptosis. An *in vitro* study

in 2011, found that the use of the N-aspartyl chlorin e6, a photosensitiser which preferentially accumulated in lysosomes, lead to initiation of the mitochondrial apoptosis pathway via Bcl-2-associated X protein activation in human lung carcinoma cells rather than necrosis (Liu et al., 2011). Another *in vitro* study, associating photosensitiser concentration in lysosomes with apoptosis, involved using human MCF-7c3 breast cancer cells to test the newer water soluble phthalocyanine derivative, 3-aminopropyloxy phthalocyaninato zinc II. It was found that photo damage to lysosomes occurred on light exposure, which was suggested to be the primary site of action (Vittar et al., 2010) .

Table 1. 5. Photosensitisers families and their members.

The site of accumulation and mechanism of action for different photosensitisers are shown in the table.

PS Type	Examples of PS	Site of Accumulation	Mechanism of Action
Hematophorphyrin derivates	Photofrin, Photosan, Photofrin II	Plasma membrane and mitrochondria	Apoptosis
Porphyrin based pthalocanines	Sulphonated aluminium phthalocyanine (AISPc), 3-aminopropyloxy phthalocyaninato zinc II	Mitochondria and/or Lysosomes	Apoptosis
Chlorin e6	m-tetrahydroxyphenylchlorin (mTHPC), N-aspartyl chlorin e6	Lysosomes	Apoptosis
Benzophorphyrin	Verteprofin	Golgi apparatus and/or mitochondria	Necrosis
Aminolevulinic acid (ALA)	ALA, Methyl-aminolevulonic acid (M-ALA), Hexaminolaevulinate (H-ALA)	Cell membrane and Mitochondria and Lysosomes	Apoptosis
Chlorophyll	9-hyroxypheophorbide alpha, Pheophorbide	Mitochondria	Apoptosis
Bacteriochlorin	Palladium-metalated complex of bacteriopheophorbide (Tookad®)	Blood vessels	Inflammatory reaction and necrosis

1.7.4.2 Tumour vascular constriction

The indirect destruction of tumour cells during PDT treatment is believed to be a result of hypoxia and/or deprivation of nutrients to the tumour. Blood vessel constriction and platelet aggregation occurs very early during the application of PDT, followed by damage to blood vessel walls (Star et al., 1986).

Padoporfin (Tookad) is a pure palladium (Pd) substituted with bacteriochlorophyll derivative. It is a second-generation photosensitiser with a peak absorption wavelength at 763 nm. Tookad works as a vascular targeted photodynamic therapy by damaging vasculature and altering blood supply. Padeliporfin vascular-targeted photodynamic therapy has entered recently into phase-III clinical trial versus active surveillance in men with low-risk prostate cancer. At 24-month follow up, 28% (58/206) of participants had cancer progression in the vascular-targeted photodynamic therapy group compared with 58% (120/207) in the active surveillance group (adjusted hazard ratio 0·34, 95% CI 0·24–0·46; p<0·0001). Importantly, the vascular-targeted photodynamic therapy was well tolerated with low complication rate of 2% such as prostatitis, urinary retention and erectile dysfunction (Taneja, 2017, Azzouzi et al., 2017).

In an animal model using male rats, Fingar *et al* (Fingar et al., 1992), showed PDT with Photofrin increased tissue interstitial pressure, arteriole constriction, as well as venular constriction (at the highest PS concentration used), and increased vessel permeability to albumin. Increased adherence of polymorphonuclear leukocytes to vessel walls was also seen and thought to result in the increased vessel permeability observed, leading to treated tissue oedema. Rats given the non-selective cyclooxygenase inhibitor, indomethacin, in conjunction with PDT did not produce the same responses. Hence, the vascular effects were thought

to be due to cyclooxygenase products as a result of PDT (Fingar et al., 1992). A 2006 study (Busch, 2006), showed that severe murine tumour cell hypoxia were as a consequence of the photochemical oxygen consumption and/or reduced vascular perfusion. More recent studies have reported on the fine balance between PDT's need for oxygen vs the vasoconstriction it causes. Nine out of fifteen mice treated with topical 5-ALA showed a decrease in vessel diameter to below 80% of their original diameter and 5 mice had total vessel occlusion immediately after PDT (van Leeuwen-van Zaane et al., 2014). A similar *in vivo* study investigating topical hexylaminolevulinate (HAL) as well as 5-ALA reported complete arteriole occlusion in 64% with HAL and 60% with 5-ALA due to the related PpIX concentration in the vessel wall (Middelburg et al., 2013). An explanation for the whole tumour not being destroyed via apoptosis or necrosis is that PDT induced hypoxia results in less oxygen which is an essential component required for cell eradication during PDT in tissues (Tromberg et al., 1990). Therefore, less oxygen based free radicals are formed as the PDT treatment is administered and cell death rate is reduced. However, a contrasting study highlighted the importance of the PDT effects on the vasculature on tumour abolition, noting that the persistent strong local hypoxia induced by vascular targeted PDT (V-PDT) rather than cellular targeted PDT (C-PDT) produced greater tumour growth inhibition, and consequent survival in mouse melanoma cancer models (Krzykawska-Serda et al., 2014).

1.7.4.3 Immune response

It is proposed that damage of tumour cells during PDT causes release of inflammatory mediators and cytokines such as Interleukin 1 (IL-1) and Interleukin 6 (IL-6) (Gollnick et al., 1997). This in turn triggers an immune response to the tumour cells, resulting in infiltration of lymphocytes and macrophages (Gollnick

et al., 1997). Adaptive immune response has been found to be of particular importance both in the initial therapeutic effect and in the long-term control of tumours using PDT. Lower therapeutic effect from PDT has been shown in immunodeficient mice compared to normal (Korbelik et al., 1996). Both groups of mice experienced the same level of PS accumulation, light absorption and initial tumour ablation following PDT. However, immunodeficient mice lacked the long-term tumour reduction seen in the control mice which was suggested to be due to the absence of the immune-related mechanism of tumour cell death. PDT has the ability to activate both the innate and adaptive immune responses (Korbelik et al., 2005) due to the release of acute phase response mediators from the site of treatment and complement activation (Barathan et al., 2013). Infiltration of the area with neutrophils can be seen due to the trauma inflicted by the PDT, as well as the PDT activation of dendritic cells causing them to phagocytose necrotic tumour tissue and present antigens to lymphocytes (Cecic et al., 2006). The activation of the host immune system is largely thought to be due to the PDT induction of damage-associated molecular pattern (DAMP) molecules on the tumour cell surface.

A more recent study found evidence of systemic antigen β-galactosidase specific immune response in result of PDT (Mroz et al., 2010). Mice with antigen positive colon adenocarcinomas were cured of their tumours and were resistant to re-challenge. In addition, 70% of otherwise untreated metastases were destroyed in these mice. The T lymphocytes isolated from cured mice could successfully recognise and destroy antigen positive tumour cells. This was not the case for mice with antigen negative tumours or mice without adaptive immune response (Mroz et al., 2010). This study demonstrated the future potential of using PDT for curing metastases.

1.8 Nanoparticles scaffold

Nanoparticles have attracted great interest for both therapeutic and diagnostic biomedical applications. Their distinctive optical properties make them ideal candidates for cellular imaging and biosensing. Their applications were also extended to include fluorescent and colorimetric detection (Storhoff et al., 2004, Tiernan et al., 2015), photothermal and photodynamic therapy (O'Neal et al., 2004, Chatterjee et al., 2008) and multimodal techniques (Melancon et al., 2011). Passive drug loaded nanoparticles have been recognised as a potential solution to improve poor tumour tissue delivery of traditional cancer chemotherapy (Danhier et al., 2010, Cho et al., 2008). Inherent 'leaky' vasculature and impaired lymphatic drainage of solid tumour tissue allow nanoparticulate formulations to selectively access and accumulate into tumours, the so-called the enhanced permeation and retention (EPR) effect (Peer et al., 2007b, Matsumura and Maeda, 1986). Organic nanoparticles (including liposomes, lipoproteins, and polymersomes) are good examples of the EPR effect-driven tumour targeting of nanoparticles with human therapeutic applications (Peer et al., 2007a, Gabizon, 2001). The fluorescent signal could be concentrated by providing many more fluorophore molecules per nanoparticle while multiple antibodies or synthetic binding bioreceptors could theoretically be conjugated to the surface to maximise targeting sensitivity (Tiernan et al., 2015). The small size of nanoparticles enables deeper tissue penetration while their surface can be functionalised with a variety of chemical groups to be hydrophilic, minimally antigenic and with prolonged circulation time (Owens Iii and Peppas, 2006, Gaur et al., 2000).

Exploitation of the EPR effect may also be suitable for selective delivery of photosensitiser loaded nanoparticles. Unlike drug loaded nanoparticles where a higher encapsulation of chemotherapy drug correlates with higher cellular toxicity

effect, the ideal dose of PS for effective PDT is not necessarily dose dependent. Extensive PS molecules within the nanoparticulate formulation may lead to self-quenching when photo-irradiated yielding reduced photodynamic efficacy (Master et al., 2012). The photosensitiser-nanoparticle complex has to be stable while in the circulation and with minimal leakage of PS molecules to avoid premature drug loss into the plasma. Photosensitiser encapsulation strategy has also to be carefully considered when designing the system. Unlike chemotherapeutic drugs, where the cytotoxic effects may be hindered due to slow release kinetics of the drug from the nanoparticle core, for PDT the physical release of the PSs from the nanoparticle may not be essential. The cytotoxic effect of PDT is mediated via reactive oxygen species which can easily diffuse out of the vehicle core to cause cellular damage. Therefore, nanoparticle vehicles that allow encapsulation of PSs within the core may offer a better solution to early drug loss into the plasma, while facilitating PSs accumulation within the tumour tissue for subsequent PDT (Torchilin, 2008, Figueiredo et al., 2018). For this purpose, nanoparticle designs where the PS is physically embedded within the core or chemically conjugated to the vehicle will be considered in this project.

1.9 Targeting bioreceptors for CRC

For any bioreceptor to be used for targeted delivery it has to possess high stability and resistance to proteolytic activity. Bioreceptors should also be small in size and highly soluble to allow efficient tissue penetration. Importantly, they should be able to bind selectively to target proteins with strong affinity and avidity. Although antibodies have been successfully conjugated to the surface of nanoparticles for different applications including imaging and drug delivery, they are not without limitations. Hence, alternative binding proteins have been developed over the last two decades. To date, there are over 50 novel non-antibody protein scaffolds that can be divided into two categories (Sha et al., 2017a). The first is based on scaffold mediated binding via amino acids on surface-exposed side chains of secondary structural elements. The second category is based on scaffold mediated binding via amino acids in one or several exposed loops on a rigid protein structure, which imitate the antibody binding site the paratope.

1.9.1 Antibody

Antibodies have been exploited by researchers in biological science for decades. They are one of the most frequently used bioreceptors for therapeutic and diagnostic applications. Antibodies are clinically approved as therapeutic agents for treatment of cancer, and autoimmune and inflammatory diseases (Slamon et al., 2001, Dankner and Rose, 2018). However, there are a number of disadvantages regarding antibodies. Antibodies are large molecules (150 KDa in molecular weight and 14x8 nm in size), which limit their tissue penetration and may reduce targeted delivery or therapy. Their complex structure of the light and heavy chains leads to unstable domain association in the production of small Fv

fragments. Complicated cloning steps are required for the development of recombinant antibodies, and the manufacture of antibodies is also expensive and time-consuming and depends on use of live animals which is undesirable. Batch-to-batch heterogeneity is another major concern for antibody use. This is a common problem encountered when using commercial antibodies. This issue was highlighted by recent publications suggesting that batch-to-batch variability and poor characterisation of antibodies are the main contributing factors for reproducibility problems in life sciences research; accounting for ~50% of globally invested funds being wasted (Baker, 2015, Bradbury and Plückthun, 2015). Although monoclonal antibodies have no batch variability, their production is much more complex, time consuming and expensive. Therefore, several alternatives have been proposed to replace antibodies. Antibody fragments can offer a potential replacement for whole antibodies in solving the problems mentioned. However, their use has not gained wide acceptance due to their instability and restricted applications (Binz and Plückthun, 2005). A lot of attention has turned to non-antibody binding proteins and these will be discussed in the next section.

1.9.2 Affimer (Adhiron)

The procedure of generating synthetic non-antibody binding proteins usually starts with building a combinatorial library onto a preferred protein scaffold. The library is built by selective random mutagenesis of unprotected surface residues of the scaffold, typically unstructured loops. After this, a range of binding affinities are produced by careful selection of variants using phage display. The degree of mutagenesis and the selection conditions are the two most important factors for determining biomolecular properties of the binding molecules. Ideally, the binding protein should have sufficient affinity and specificity to a target. Also, it should

exhibit thermodynamic, chemical and enzymatic stabilities (Skerra, 2007; Hamzeh-Mivehroud et al., 2013). The Affimer, initially known as Adhiron (Tiede et al., 2014b), is a very recent protein scaffold developed by Tiede *et al* (2014) and commercialised under collaboration between the University of Leeds, the Leeds BioScreening Technology Group (BSTG) and Avacta Life Sciences Ltd. It is based on a consensus phytocystatin sequence derived from protein inhibitors of plant cysteine proteases. This scaffold consists of a single alpha helix and four anti-parallel- β -strands and contains two unique variable regions, consisting of nine random amino acids in each variable region, located between the first and second β strands (VR1) and between the third and fourth β strands (VR2) (Figure 4). The variable regions are where the molecular recognition takes place in similar fashion to the complementarity-determining region (CDR) loops of antibodies. Affimer's molecular weight is ~13 KDa and it contains 92 amino acids. Randomisation takes place within nine residues of each loop to generate the Affimer library. The absence of cysteine residues in the scaffold is another advantage, which allows the introduction of cysteine for site-specific coupling of biotin, fluorescent labels, or other linkers. Moreover, lack of disulphide bridges in most alternative binding proteins allows them to be employed as excellent reagents in intracellular assays and structural biology applications. Affimers are thermostable, with denaturing temperature of up to 100°C. This enables long-term storage at ambient temperature (Tiede et al., 2014b, Tiede et al., 2014a). In recent studies, Affimers have been used as a biorecognition elements for electrochemical biosensors (Raina et al., 2015) and as a targeting agents in diabetes to reduce cardiovascular disease (King et al., 2015).

To date, Affimers have proved to be as effective as antibodies in standard laboratory techniques including Western blotting, Enzyme-linked immunosorbent

assay (ELISA), super-resolution microscopy, affinity histochemistry, inhibiting extracellular receptor function and modulating ion channel activity (Tiede et al., 2017, Tiede et al., 2014a). Affimers against colorectal cancer marker tenascin C. were also used for *in vivo* imaging and demonstrated similar staining specificity when compared to their respective antibodies (Tiede et al., 2017). The advantage of using non-antibody binding proteins in building a nanoparticle delivery system for colorectal cancer is that a uniform protein can be produced by a cheaper and less complicated process, which enables long-term availability. In addition, because of their compact size, they can be packed on to the surface of nanoparticle more densely as compared to larger antibodies, which may enhance the sensitivity of targeting colorectal cancer tissue. Affimers appear to fulfil many of the criteria required for targeting CRC intra-operatively and are the preferred choice as a bioreceptor in this project.

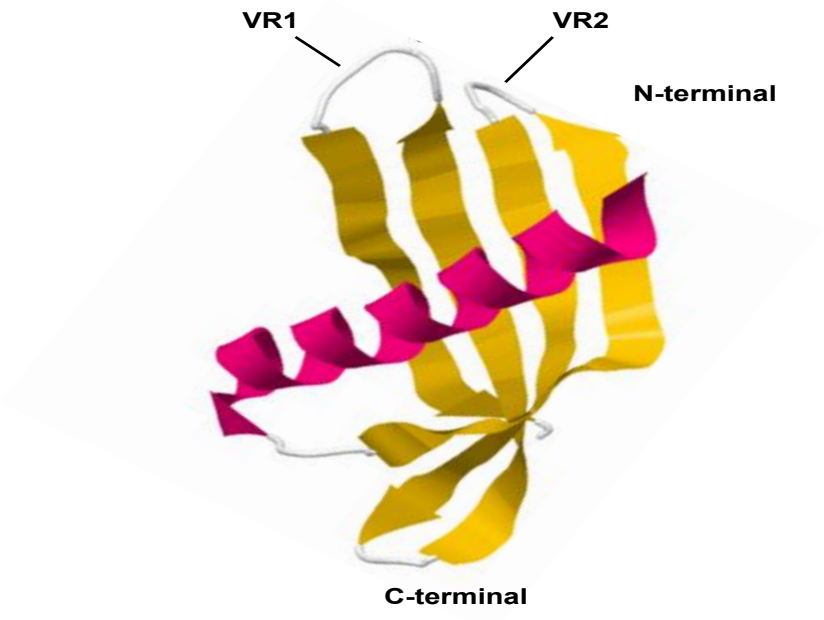

Figure 1. 3. Molecular structure of an Affimer.

Four anti-parallel β strands are shown in yellow and one α helix strand in pink. VR: Variable region. Protein data base (PDB) file was obtained from RCSB protein data bank (http://www.rcsb.org/pdb/home/). PDB ID: 4N6T.

1.10 Hypothesis and aims

1.10.1 Hypothesis

The hypothesis for this study is that a multi-functional nanoparticle which is functionalised with anti-CEA Affimer would allow specific fluorescent imaging and cytotoxic effect on colorectal cancer cells.

1.10.2 Aims

I. To manufacture dye-doped silica nanoparticle;

II. To functionalise silica nanoparticle with an anti-CEA Affimer (antibody mimetic);

III. To incorporate a photosensitiser into silica nanoparticle to enable theranostic capability;

IV. To examine the sensitivity and specificity of these fluorescent nanoparticles for colorectal cancer cells using model systems including cell lines and xenograft mouse models.

Chapter Two

Methods

2 Methods and materials

2.1 Affimer production

All Affimers employed in this project were produced following phage display screening, DNA sequencing while the Affimer coding sequences were subcloned into the expression vector *pET*11 by Mrs. Shazana Shamsuddin (anti-CEA Affimer) and Mrs. Eiman Al-Enezi (anti-myoglobin Affimer) at the University of Leeds. The plasmid DNA was extracted using a QIAGEN® miniprep kit according to the manufacturer's instruction. For each Affimer, I received *pET11a* DNA (10 µl/ml) in Eppendorf tubes from Mrs Shamsuddin and Mrs Al-Enezi and I am very grateful for their gifts to this project.

2.1.1 DNA minipreps

Unless otherwise stated, all chemicals were purchased from Sigma (Sigma Aldrich, St Louis, USA). DNA miniprep was performed as the following. The XL1-Blue super competent cells were slowly thawed on ice; whilst 1 µl/ml of *pET11a* DNA was aliquoted into a 1.5 ml low protein binding Eppendorf tube and pre-chilled on ice. Then, 10 µl of the competent cells were added to the pre-chilled DNA and incubated on ice for 30 min. The cells were heat shocked in a 42 ºC water bath for 45 s before incubating on ice again for 2 min. Then, 180 µl of super optimal broth (Hermanek et al.) medium was added to the above mixture and incubated at 37°C for 1 h with shaking at 230 rpm. Luria-Bertani (LB) carbenicillin (100 µg/ml) plates were then inoculated with 100 µl of the transformation mixture and incubated at 37°C overnight.

A single colony was then picked and inoculated into 5 ml of LB carbenicillin (100 µg/ml) broth and allowed to grow overnight at 37°C and 230 rpm until the cells

reached an optical density at 600 nm (OD_{600}) of 0.7-0.8. A QIAprep ® Spin Miniprep Kit (Qiagen, Germany) was used to purify the plasmid DNA using a mixture of buffers provided within the kit. Plasmid DNA was then sent out to GENEWIZ UK, LTD, UK for sequencing. A Thermo Scientific NanoDrop Lite Spectrophotometer was used at 260 nm to measure the concentration of the purified DNA plasmids.

2.1.2 DNA Sequencing

One hundred µg/ml of the purified plasmid DNA samples were resuspended in phosphate buffered saline (PBS) solution in 1.5 microcentrifuge tubes then posted to GENEWIZ UK, LTD, UK. Expasy Translate Tools was used through an online portal to translate the sequencing data into amino acid sequence. All anti-CEA Affimers were reported to have matching amino acids sequences when compared with the original plasmid sequence. This is in keeping with the results of Mrs Shamsaddin and Mrs Al-Enezi. The clones were subsequently sequenced and 3 distinct binders termed anti-CEA Affimer I, II, and III were named with the amino acid sequences of the variable regions as shown in **Table 2.1**.

Table 2. 1. The amino acid sequences of the binding loops from the three anti-CEA binding Affimers.

Anti-CEA Affimers	Loop1	Loop2
Anti-CEA Affimer I	W I V G W R Q P D	N W I K N N M E L
Anti-CEA Affimer II	W V S G H M Q V D	N P W G D Q Y P R
Anti-CEA Affimer III	D Y Q K D N I K H	W F H L I S P I M F

2.1.3 Expression of Affimer

The expression of Affimer protein was induced using 0.1 mM isopropyl β-D-1-thiogalactopyranoside (IPTG). A protocol for expression of Affimers was established previously using an IPTG induction method by BSTG. The expression was based on the pET expression system for recombinant proteins. Some optimisation was carried out in order to increase the yield for each Affimer, after plasmid DNA containing anti-CEA Affimers were transformed into BL21-Gold (DE3) competent cells. Originally single colonies from each binder were picked and a start-up culture was inoculated in 2 ml LB media + 1% (w/v) glucose. However, it was found out that using 2 TY media as a start-up culture instead could increase the yield by 0.5-1 mg/ 50 ml culture. Also, a final IPTG concentration of 0.1 mM with a longer incubation time (16 h) provided a better yield when compared to 0.5 mM incubated for 6 h was used. *pET*11a vector was transformed into BL21 Star™ (DE3) *E.coli* using heat shock protocol as described in the miniprep protocol. On the following day, 100 µl of 50 mg/ml carbenicillin was added to the pre-warmed media, followed by 625 µl of the overnight culture. The culture was grown until OD_{600} reached ~0.8. IPTG was then added to a final concentration of 0.1 mM. The culture was incubated for an additional 16 h at 25 ºC on the shaker at 150 rpm. The cells were harvested following centrifugation at 3,220 xg for 30 min using an Eppendorf centrifuge, (5810R). The supernatant was discarded and the cell pellet was stored at -20 ºC for purification the following day.

2.1.4 Purification of Affimer

First, frozen cell pellet was thawed and resuspended in 1 ml mixture of lysis buffer Bugbuster® protein extraction reagent (100 µl, 1X), Benzonase® nuclease (0.4

µl, 10 U/ml) and protease inhibitor cocktail (10 µl, 1X). The mixture was transferred into a 2 ml microcentrifuge tube and incubated at room temperature for 20 min on a rotator followed by an incubation at 50 ºC in a water bath for 20 min to denature non-specific proteins. The mixture was then centrifuged at 16,000 xg for 20 min to pellet cell debris and insoluble proteins. Meanwhile, 300 µl of Ni^{2+}-nitrilotriacetic acid (Ni2+-NTA) resin, which would bind to his-tag on the Affimer, was resuspended in 1 ml lysis buffer in a 2 ml tube and washed one time by centrifugation at 1,000 xg for 1 min to sediment the resin and the buffer was carefully removed using a pipette. Then, the soluble fraction of the cell mixture was transferred to the tubes containing Ni^{2+}-NTA resin and incubated for 2 h on a rotator at room temperature. After incubation, the mixed solution was centrifuged at 1,000 xg for 1 min to sediment the Affimer-bound resin. A Pierce disposable 2 ml column was used to facilitate the purification. The Affimer-bound resin was resuspended in 1 ml wash buffer and moved to the equilibrated column. The resin was washed with wash buffer several times until the absorbance at 280 nm of the wash buffer was consistently lower than 0.09. If the absorbance at 280 nm was higher than 0.09 another 3 washes were applied. The Affimers were eluted with 500 µl of elution buffer and the flow-through fractions were collected. The concentration of purified Affimers were measured using a Nanodrop spectrometer at 280 nm. Affimer were then either stored at -20 ºC or biotinylated immediately.

2.1.5 Affimer reduction and biotinylation

All reagents used for Affimer dimers reduction of -s-s- links and biotinylation were purchased from Thermo scientific UK. This step was needed as the Affimer clones were expressed bearing a C-terminal Cysteine residue. Pierce®

Immobilised tris (2-carboxyethyl) phosphine (TCEP) reducing gel was used to reduce Affimer disulphide bonds to free all thiol (Souris et al.) groups for subsequent maleimide coupling chemistry. TCEP gel (150 µl) was washed with PBS containing 1 mM edetate disodium (EDTA) three times followed by 4 µl of PBS containing 50 mM EDTA, followed by adding of 150 µl of 0.5 mg/ml Affimer. The mixture was incubated for 1 h at room temperature on a rotator at 20 rpm. The mixture was centrifuged at 1,000 xg for 1 min and the supernatant containing the reduced Affimer was recovered.

For biotinylation, EZ-Link® NHS-SS-Biotin (0.8µl) was dissolved in 1 ml of dimethyl sulfoxide (DMSO) stock solution (5 mg/ml). Then, a 6 µl aliquot was immediately mixed with 45 µl of 0.1 mg/ml of reduced Affimer to make a total volume of 100 µl PBS. This was incubated at room temperature for 2 h. After that the free biotin maleimide was removed by using a Zepa spin desalting column (7K MWCO). The biotinylation was confirmed by ELISA.

2.1.6 Enzyme-linked immunosorbent assay (ELISA) for Affimer biotinylation

ELISA was used to confirm the biotinylation of Affimers. Nunc-Immuno™ MaxiSorp™ strips were coated with 50 µl of PBS per well then mixed with 1, 0.1 and 0.01 µl of biotinylated Affimers. The plate was incubated over night at 4°C then washed 3 times with 300 µl per well of phosphate-buffered saline/Tween 20 (PBST) using a plate washer (TECAN HydroFlex). Diluted high sensitivity streptavidin-HRP (1:1000 in 2x Blocking Buffer) was added at 50µl per well then incubated for 1 h at room temperature on a vibrating platform shaker (Heidolph VIBRAMAX 100; speed setting 3). Six washes with 300 µl per well of PBST were performed using the plate washer prior to developing in 50 µl of 3,3′,5,5′-

tetramethylbenzidine (TMB)/substrate solution. The absorbance was measured at 620 nm in an Ascent^{TM} microplate reader (Thermo scientific).

2.1.7 Sodium dodecyl sulphate polyacrylamide gel electrophoresis (SDS-PAGE)

SDS-PAGE was used to determine the molecular mass of purified Affimers and in pull-down assays. Ten μg of total protein samples were mixed with 10 μl of 2x Laemmli sample buffer (95%) and 2-mercaptoethanol (5%, w/v) and heated immediately at 95°C for 10 min. Then, the mixed solutions were centrifuged at 16,000 xg for 5 min. After that, 10 μl of the supernatants were loaded into Mini-PROTEAN® TGX™ 4-15% precast gels (4-15% (w/v)) along with 5 μl of protein ladder. The gel was run at 100V for 75 min with 1X Tris-glycine running buffer and developed with Generon quick Coomassie stain for 1h at room temperature. A protein ladder (10 to 260 KDa) was used as a standard molecular weight guide. SDS gels were washed overnight with deionised water to destain the gels. Images were captured using Syngene G-Box imager.

2.2 Affimer characterisation

2.2.1 Immunoprecipitation (pull down assay)

All selected anti-CEA Affimers and CEA protein were dialysed in 1X PBS (pH 7.4) before pull-down assay. Ni^{2+}-NTA resin (40 μl) was washed three times with wash buffer followed by centrifugation then resuspended in 40 μl wash buffer. Then, 200 μg of Affimer was added to the washed resin and incubated on rotator for 2 h at 4^{o} C. The Affimer loaded resin was centrifuged at 1000 xg for 15 min to remove unbound Affimer followed by a single wash using wash buffer. Affimer loaded resins were then mixed with 40 μl of 1 mg/ml purified CEA from Abcam

(Abcam Plc), cell lysates of LoVo and CEA secreted into the LoVo medium as described in **section 2.2.3**. These mixtures were incubated overnight at 4 ˚C on a rotator. The resins were washed 3x times with 1X PBS and proceed with SDS-PAGE analysis and western blotting to determine the success of the pull-down assay. SDS-PAGE was run including all fractions collected from the pull down including unbound Affimer, washed Affimer, unbound CEA, washes to remove free CEA and the lysate. The supernatants were aspirated carefully (10 µl) and loaded into the precast gel (4-15% (w/v)) along 5 µl of protein ladder. The gel was then run at 100 V for 75 min with 1X Tris-glycine running buffer and developed using quick Coomassie stain dye for 1 h at room temperature.

2.2.2 Western blotting

Following electrophoresis, as for SDS-PAGE analysis, proteins were transferred using wet electroblotting onto 0.2 µm PVDF membranes under a constant voltage of 100 V for 90 min with cooling. Then, the membranes were soaked in SuperBlock T20 (TBS) blocking solution for 30 minutes on a rocking platform then washed 3× with 0.1 % (v/v) TBST for 5 min each time. The membranes were then probed with anti-CEA or anti-His tag antibody diluted 1:1000 in TBS blocking solution followed by incubation for 1 h at room temperature on a gentle rocking platform. Membranes were washed 3x for 5 min with 1X PBS after each incubation and then incubated with appropriate secondary antibody HRP conjugated (1:2000) for 1 h at room temperature. Three final washes were carried out in 0.1% TBST followed by three washes in 1xTBS. Pierce™ ECL substrate was added and images were captured using a Syngene G-Box imager.

2.2.3 CEA protein isolation

2.2.3.1 Cell culture

LoVo cells (ATCC® Cat. No. 8706010), were grown in media containing F-12 Nutrient Mixture with GlutaMAX™-I (Ham) 1X (Gibco® by Life technologies; Cat. no. 31765-027) and 10% (v/v) Foetal Bovine Serum (FBS), 50 U/ml of penicillin and 50 µg/ml of streptomycin in a 150 cm^2 flask at 37 ˚C inside 5% CO_2 humidified incubator. Then culture medium was aspirated on day-3 and day-6 then stored for CEA protein isolation. Cells were grown as monolayer until reaching confluency at day 7.

HEK 293 cells (ATCC® Cat. No. 85120602), were grown in Dulbecco's Modified Eagle Media (DMEM) containing GlutaMax™-I (Gibco® by Life Technologies; Cat. No. 31966-021) supplemented with 10% (v/v) heat-inactivated FBS (Sigma life Science; Cat no. F7524). Culture media was aspirated and stored in a similar manner as for LoVo cells.

2.2.3.2 CEA protein isolation

Culture medium for LoVo and HEK293 cells was centrifuged at 3220 × g for 5 min at 4˚C to remove cell debris followed by careful aspiration of the supernatant. The supernatant was then concentrated using an Amicon® Ultra Centrifugal Filter (15 ml, 50 KDa device, Millipore) for 10 min at 5000 × g and 4˚C. The supernatant was then centrifuged at 16,000 × g for 30 min at 4˚C and stored at -20 ˚C.

2.2.3.3 Direct ELISA

Neutravidin-coated 96-well plate was prepared as the following: A stock solution of 1 mg/ml Neutravidin was prepared using 100 mM PBS then 50 µl of Neutravidin at a concentration of 5 µg/ml in 100 mM PBS was added into each well of a Nunc-

ImmunoTM MaxisorpTM 96-well plate. The plates were incubated overnight at 4 ºC then 200 µl of 2x blocking buffer was added into each well and incubated overnight at 37 ºC. As a final step, the plate was washed one time with PBS before further use.

Biotinylation of target protein CEA or human-myoglobin as a control was performed using biotin N-hydroxysuccinimide (NHS). Biotin NHS was dissolved in DMSO at concentration of 5 mg/ml while proteins were dissolved in 1X PBS buffer (pH 7.4) at a concentration of 1 mg/ml. Then, 10 µl of 1 mg/ml CEA or myoglobin solution was mixed with 0.8 µl of biotin NHS in 100 µl of PBS buffer followed by incubation for 1 h at room temperature. Zeba Spin Desalting Columns (7K MWCO) were then used to remove unbound biotin. Next, 100 µl of 80% (v/v) glycerol was added to the mixture and the solution was stored at -20 ˚C or used for direct ELISA.

For direct ELISA, 1 mg/ml of biotinylated protein was diluted in 2x blocking buffer (1:1000) and aliquoted 50 µl into each well followed by incubation for 1 h at room temperature on a plate shaker platform at 400 rpm. The plates were washed 3x with PBS then 10 µl of 10x blocking buffer was aliquoted into each well then 40 µl of 0 – 100 µg/ml Affimers were added. The plates were then placed on a shaking platform at 400 rpm for 1 h at room temperature. Following 3x washing steps with PBS, 50 µl of diluted anti-His6-HRP (1:1000) in 2x blocking buffer were added as a secondary antibody into each well and plates were further incubated for 1 h on a plate shaker (400 rpm) at room temperature. Finally, six washing steps were performed using PBS before 50 µl of TMB substrate was added per well. Colour change was allowed to develop for 5 min before measuring absorbance at 620 nm.

2.2.3.4 Affimer immunofluorescence staining

The binding specificity of Affimers was assessed in fixed LoVo and HEK 293 cells. Cells were seeded in a 6-well plate at $3x10^6$ cells per well for 3 days on cover slips (Cellpath, Newtown Powys, UK) and cultured in the same condition as described in **section 2.2.3.1**. At 70% cells' confluency, the medium was aspirated, then each well was washed 3x with PBS (pH7.4) buffer with incubation for 5 min at room temperature. Next, cells were fixed in 4% (w/v) paraformaldehyde solution for 10 min at room temperature before fixative solution was discarded. Fixed cells were washed 3x times with PBS then blocked in TBS blocking buffer (pH7.4) and incubated for 30 min at room temperature. Biotinylated Affimers at 10 µg/ml in blocking buffer were added and incubated overnight at 4 ˚C. As a positive control, 1 µg/ml of mouse anti-human CEA antibody (Thermo Scientific) was used as a primary antibody on separate coverslips. Next, the coverslips were washed 3x times with PBS and incubated with Streptavidin DyLight 488 conjugate (1:1000) for cells probed with biotinylated Affimers or Goat anti-mouse IgG secondary antibody conjugated with Alexa Fluor® 488 (Invitrogen) (1:1000) for positive control coverslips. Incubation with secondary reagents was carried out for 1 h at room temperature in the dark. Coverslips were washed 3× with PBS then mounted with ProLong® gold antifade reagent with DAPI and left to cure overnight then stored at 4°C in the dark. As a negative control, biotinylated Affimers or primary antibodies were omitted. Immunofluorescence staining was visualised using an AxioObserver Z.1 microscope equipped with an ApoTome system of structured illumination (Zeiss, Germany).

2.3 Silica nanoparticles

Dye-doped silica nanoparticles were synthesised according to recently published methods (Tiernan et al., 2015, Santra et al., 2001, Huang et al., 2009, Gubala et al., 2010). The linkage chemistry for conjugating the antibodies and Affimers to the surface of the silica nanoparticles was assessed while confocal microscopy was used to quantify tumour specific cell targeting across the colorectal cancer cell lines. Unless otherwise stated in the following sections, 'Wash' steps refer to the nanoparticles being pelleted via centrifugation, resuspended in the wash solution using ultrasonication, re-pelleted by centrifugation and the supernatant discarded.

2.3.1 Fluorophore (NIR664)-doped silica nanoparticle manufacture

Dye doped silica nanoparticles were manufactured in batches as shown in **Figure 2.1.** For each batch, 5 mg of near infra-red (Master et al.) 664-iodoacetamide (4,5-Benzo-5′-(iodoacetaminomethyl)-1′,3,3,3′,3′-pentamethyl-1-(4-sulfobutyl)indodicarbocyanine) dye was dissolved in 6.25 ml of 1-hexanol followed by mixing with 3.25 µl of 3-mercaptopropyl-triethoxysilane (MPTES). The final dye: MPTES molar ratio of this mixture was 1:2. Next, the mixture was stirred at room temperature under N_2 for 4 h to ensure conjugation of the dye and organosilane. Then, 2 ml of the conjugated dye was added to the following mixture in a plastic tube covered in aluminum foil: 3.78 g (4.045 ml) of the non-ionic surfactant Triton X-100, 15 ml of cyclohexane, 1.6 ml of 1-hexanol and 960 µl of distilled water. The mixture was further stirred for 5 min to form a microemulsion. Tetraethyl orthosilicate (TEOS) was added (200 µl) and the tube was stirred for 30 min at room temperature. One hundred and twenty microliters of 28% [w/w] ammonia hydroxide was added and the mixture was stirred for 24

h at room temperature. This was followed by addition of 150 µl of TEOS, and the tube was further stirred for 30 min at room temperature. Ethanol (20 ml) was added to break the microemulsion and the mixture was resuspended in 30 ml Corex centrifuge tubes (Corning) with equal volumes. Each tube was then centrifuged at 11,000 xg for 25 min at room temperature and supernatant was discarded and the particles were resuspended in ethanol using sonication. The particles were washed 4x times with ethanol. Tubes were stored at 4°C or immediately functionalised.

2.3.2 Amination of silica nanoparticles

Dye doped silica nanoparticles (4 ml of 2 mg/ml) were suspended in ethanol plus 4% [v/v] (3-aminopropyl) triethoxysilane (APTES) for 3 h at room temperature while stirring in a 15 ml Falcon tube. The aminated particles were then transferred to a centrifuge tube (Corex) followed by 2x washes with ethanol and centrifuged at 11,000 xg for 25 min. The contents were then washed once using 2-(*N*-morpholino) ethanesulfonic acid (MES) buffer (pH 7.0) then resuspended in MES buffer at final concentration of 2 mg/ml.

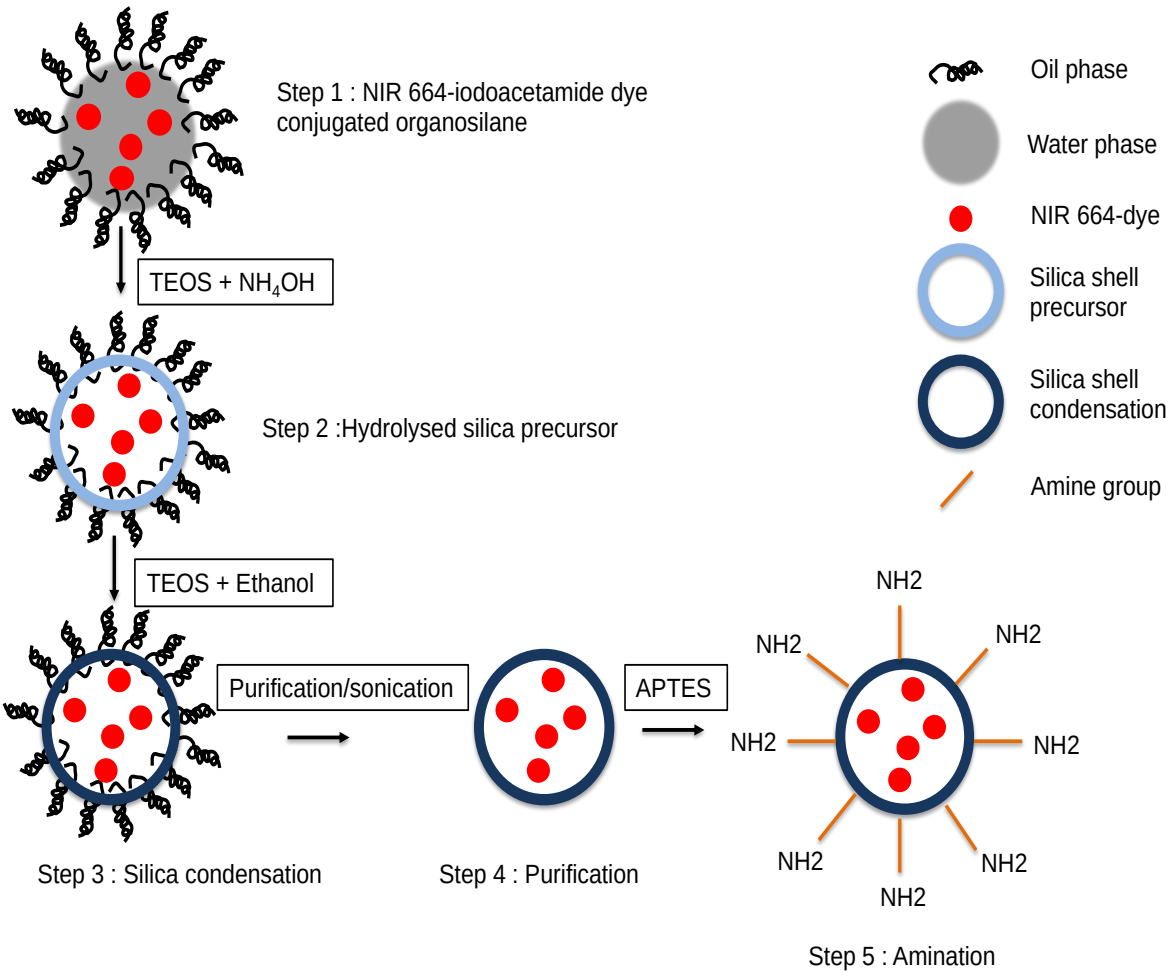

Figure 2. 1. Schematic of NIR 664- dye doped silica nanoparticles synthesis using water in oil microemulsion technique.

Water in oil phase was created by dissolving NIR 664-iodoacetamide dye in 1-hexanol followed by mixing with 3-mercaptopropyl-triethoxysilane (MPTES) followed by mixture with Triton X-100, cyclohexane, 1-hexanol and distilled water. Hydrolysis step was achieved by addition of Tetraethyl orthosilicate (TEOS) and ammonia hydroxide. Silica shell condensation was achieved by addition of TEOS then ethanol to break the emulsion. Purification step involved centrifugation and sonication followed by amination step. (NH_4OH) : ammonia hydroxide; (*APTES): 3-aminopropyl) triethoxysilane.*

2.3.3 Quantification of amine on silica nanoparticles

The fluorenylmethyloxycarbonyl chloride (Fmoc-Cl) assay was used to quantify the number of free amine groups on the surface of the nanoparticles (Chen and Zhang, 2011). Fmoc-Cl is a chloroformate ester and used to introduce FMOC group as the FMOC carbamate. The FMOC carbamate is often used as a protecting group for amines and may be cleaved by bases such as piperidine. The assay involves binding the fluorenyl group, which is highly fluorescent, to free amine groups on silica nanoparticles surface (King et al., 1990). The Fmoc-Cl assay is ideal for the dye-dope silica nanoparticles, since the quantification step of the Fmoc-Cl fluorescent assay takes place independent of the presence of the nanoparticles. Fmoc-Cl fluorescence was measured at various concentrations in a borate buffer (0.1 M, pH 8.0) containing 10% [v/v] piperidine in order to create a standard calibration curve (Chen and Zhang, 2011). The dye-doped silica nanoparticles were suspended in borate buffer (0.1 M, pH 8.0) at a concentration of 60 mg/ml then 435 µl of the suspension was mixed with 15 µl of Fmoc-Cl solution (0.01 M in acetonitrile). The mixture was incubated at room temperature for 40 min with continuous mixing then washed twice with 10 ml of 1% Tween-20 and four times with distilled water. The particles were resuspended in 450 µl of borate buffer and 50 µl of piperidine was added at 10% [v/v] solution for 10 min. The mixture was centrifuged at 10,000 xg for 15 min. The supernatant was aspirated and its fluorescence measured using fluorimeter at an excitation wavelength of 267 nm.

2.4 Silica nanoparticle-antibody conjugation

2.4.1 Conjugation of dendrimer onto the silica nanoparticles

Polyamidoamine (PAMAM) dendrimer (1 µmol) generation 4.5 (Dentritech, Midland, USA) was dissolved in distilled water then 41.7 mg of N-hydroxysulfosuccinimide (sulfo-NHS) and 71.6 mg of N-(3-dimethylaminopropyl)-N′-ethylcarbodiimide (EDC) were added to the mixture and made up to a 1 ml volume using MES buffer (pH 6.0) and stirred for 25 minutes at room temperature. Nanoparticles (1 ml of 2 mg/ml) were suspended in MES pH 7.0 then added to the reaction mixture and stirred at room temperature for 25 min. The mixture was centrifuged at 16,000 xg for 8 min, unbound dendrimer was removed in the supernatant and the particles were washed twice and resuspended in MES buffer pH 7.0.

2.4.2 Conjugation of antibody onto silica nanoparticles

The dendrimer functionalised silica nanoparticles mixture was split into two equal volumes and 10 µg of anti-CEA IgG or 10 µg of anti-digoxin IgG antibody, as a negative control, were added to each sample and incubated at room temperature for 4 h with gentle stirring. Sodium hydroxide (100 µl [4.5 mM], pH 9.0) was added to stop the reaction. The functionalised nanoparticles were washed twice in 0.1 M sodium phosphate, 0.15 M sodium chloride, pH 7.2 (referred to subsequently as 0.1 M PBS) and centrifuged at 11,000 X g for 25 min to remove unbound IgG. The functionalised nanoparticles were resuspended in 0.1 M PBS at 2 mg/ml. Bovine serum albumin (BSA) (2%, w/v) was added before the nanoparticles were stored at 4°C in the dark.

2.5 Silica nanoparticle-Affimer conjugation

2.5.1 Polyethylene glycol (PEG)-linked nanoparticle-Affimer conjugates

Bifunctional PEG linkers are capable of conjugating amine groups to sulfhydryl groups and therefore offer oriented conjugation. NHS-PEG-Maleimide $(SM(PEG))_4$ was prepared as a stock solution of 250 mM by dissolving 100 mg in 680 µl of dimethyl sulfoxide (DMSO). Next, 8 µl of 250 mM $SM(PEG)_4$ solution was added to 5 ml of NIR-664 dye-doped nanoparticles (2 mg/ml) and incubated with gentle mixing for 30 min at room temperature. Particles were washed twice with PBS (pH 7.2, 10000g x 15 minutes) to remove unbound $SM(PEG)_4$ then particles were resuspended in PBS at 2mg/ml. The sample was divided into two and 60 µl (1 mg/ml) of anti-CEA or anti-myoglobin (control) Affimer were added for each 1 mg of nanoparticles then incubated for 2 h at room temperature with gentle mixing. The functionalised nanoparticles were then washed 2x with PBS and resuspended at 2 mg/ml. Bovine serum albumin (BSA) 0.1% [w/v] was added to the suspended particles and stored in the dark at 4°C.

2.5.2 EDC-linked nanoparticle-Affimer conjugation

NIR-664 dye-doped nanoparticles were first carboxylated as the following. The nanoparticles were washed 2x in dimethylformamide (DMF) (10000g x 15 minutes) then resuspended at 1 mg/ml in 15 ml of 10% succinic anhydride dissolved in DMF. Particles were then gently stirred under running argon gas for 4 hours at room temperature. Since there were no oxygen sensitive functional groups present, argon gas was used as a protective gas at this step. The particles were then washed 3x times with distilled water.

Then, 10mg of carboxylated nanoparticles were suspended in 5 ml mixture of 0.1M MES, 0.5 M NaCl (pH 6.0) and 1.92 mg of EDC. Then 5.43 mg of sulfo-NHS

was added to the mixture and incubated for 15 min at room temperature with gentle mixing. The reaction was quenched by adding 20 mM of 2-MEA while unreacted molecules were removed by washing the particles 2x with PBS (6000g x 10 minutes). Particles were resuspended at 2 mg/ml in 0.1M PBS then 60 µg (1 mg/ml) of anti-CEA or anti-myoglobin Affimer was added for each 1 mg of nanoparticles. The reaction mixture was incubated at room temperature for 2 h with gentle mixing. The functionalised nanoparticles were then washed 2x with PBS and resuspended at 2 mg/ml. Bovine serum albumin (BSA) 0.1% [w/v] was added to the suspended particles and stored in the dark at 4°C.

2.5.3 sSMCC-linked nanoparticle-Affimer conjugates

Fresh sulfo-succinimidyl 4-(maleimidomethyl) cyclohexane-1-carboxylate (SMCC) (6 mg) was mixed with 60 µg (1 mg/ml) of anti-CEA or anti-myoglobin Affimers and stirred gently at room temperature for 20 min. The reaction mixture was then added to 4 ml of 1 mg/ml aminated nanoparticles and stirred at room temperature for 2 h then washed twice with PBS (6,000 xg for 15 min) to remove unbound sulfo-SMCC. The nanoparticles were resuspended at 2 mg/ml and finally 0.1% (w/v) BSA was added. The nanoparticles were either stored in the dark at 4°C or used immediately for *in vitro* experiments.

2.6 Photosensitiser encapsulated silica nanoparticle

2.6.1 Foslip® encapsulated silica nanoparticle

Water soluble meta-tetra (hydroxyphenyl) chlorin (mTHPC) Foslip® photosensitiser (20 mg/mL DPPC/DPPG, 2.2 mM mTHPC, 50 mg/mL glucose) was kindly provided by Biolitec AG (Jena, Germany) with molecular weight of 680.764 g/mol. It was supplied as a powder and stored at -20 ^{o}C as per the manufacturer's instructions. The powder was dissolved in PBS to make a stock

solution of 100 µM and filtered through a syringe filter (0.1 µm pore size; TPP, Trasadingen, Switzerland). One mL aliquots of the stock solution were then stored in the dark. The stock solution was used to assess Foslip® PDT-mediated cellular toxicity on colorectal cancer cell lines before it was encapsulated inside silica nanoparticles. Foslip powder (20 mg) was dissolved in 25 ml of hexanol-1-water (50%:50% v/v) solution then mixed with 6.5 µl of 3-mercaptopropyl-triethoxysilane (MPTES). MPTES is an organosilane which prevents nanoparticles aggregation. The mixture was stirred at room temperature under N2 for 4 h then 2 ml of the mixture was added to 7 g (8.09 ml) of the non-ionic surfactant Triton X-100, 30 ml of cyclohexane, 3.2 ml of 1-hexanol and 1.92 ml of distilled water. The mixture was further stirred for 5 minutes then TEOS was added (400 µl) and the tube was stirred for 30 minutes at room temperature. 240 µl of 28% [w/w] ammonium hydroxide was added and the mixture was stirred for 24 h at room temperature. This was followed by addition of 300 µl of TEOS, and the tube was stirred for 30 minutes at room temperature. Ethanol (40 ml) was added to break the microemulsion and the mixture was resuspended in 30 ml Corex centrifuge tubes (Corning) with equal volumes. These underwent centrifugation 3x times at 15,000 xg for 25 min at room temperature. The liquid was discarded and the particles were resuspended in 0.1 M PBS at a concentration of 1 mg/ml using sonication then stored at 4°C. Foslip loaded silica nanoparticles were then functionalised with either anti-CEA or anti-myoglobin Affimer on the following day using sSMCC as described in **section 2.5.3**.

2.7 Silica nanoparticles characterisation

2.7.1 Spectrofluorometer measurements of silica nanoparticles

The fluorescence intensity of dye or photosensitiser doped silica nanoparticles

was quantified on a spectrofluorometer (Berthold Technologies Mithras LB 940 multimode microplate reader with Mikro Win 2000 software) with a halogen lamp intensity of 23,000 and excitation and emission spectra of 405 nm +/- 10 nm and 645 nm +/- 30 nm corresponding to NIR665 dye and Foslip. Thirty-six separate readings were recorded for each well. The values corresponding to outer areas of each well were discarded from further analysis in order to negate the effects of increased cell density at the edge of each well.

2.7.2 Dynamic light scattering (DLS)

The DLS measurement for nanoparticles was made using a Zetasizer Nano series, Nano-ZS DLS system with a red (633 nm) laser (Malvern Instruments Ltd) at room temperature and in a small volume disposable cuvette. Data analysis was performed using DTS Applications 5.10 software. Data acquisition was performed following 10 measurement runs with 10 s/run for each sample and the average value was reported. For characterisation of functionalised silica nanoparticles, 100 µl of each sample was used in the measurement.

2.7.3 Scanning electron microscopy imaging (SEM)

SEM images were captured using field emission gun scanning electron microscopy (FEG-SEM, LEO 1530 Gemini FEGSEM) fitted with an Oxford Instruments 80 mm X-Max SDD detector, Carl Zeiss. Silica nanoparticles were dispersed in water and a drop of the particle suspension was placed on a piece of micro glass slide fixed to a metal grid coated with carbon film. The drop was dried gradually at room temperature then sputter coated with gold and observed using the SEM to assess the particle size and shape.

2.8 Cell culture

The human embryonic kidney (HEK) 293 epithelial cell line (Cat. No. 85120602) as a control, and the human colorectal cancer cell lines: LoVo (Cat. No. 8706010, metastatic left supraclavicular lymph node from a primary colon adenocarcinoma), HCT116 (Cat. No. 91091005, colonic adenocarcinoma), and LS174T (Dukes' B human colorectal adenocarcinoma) were obtained from the American Type Culture Collection (ATCC). Cells were passaged when they were 70 to 80% confluent. HEK 293 cells were maintained in Dulbecco's Modified Eagle Medium (DMEM) (1X) with GlutaMAX™-I (Gibco® by Life Technologies; Cat. No. 31966-021) and 10% (v/v) foetal bovine serum (FBS) (Sigma life Science; Cat no. F7524). LoVo cells were maintained in F-12 Nutrient Mixture with GlutaMAX™-I (Ham) 1X (Gibco® by Life technologies; Cat. no. 31765-027) and 10% (v/v) FBS. LS147T cells were maintained in minimum essential media (MEM) with 10% (v/v) FBS. HCT116 cell lines were maintained in Roswell park memorial institute medium (RPMI 1640) with GlutaMAX™-I (Gibco® by Life Technologies; Cat. no. 61870-044) and 10% (v/v) FBS. Cells were grown on tissue culture treated non-pyrogenic polystyrene culture plates (Corning® Costar®) at 37 ^{o}C in a humidified atmosphere, in the presence of 5% CO_2.

2.8.1 Cell counting

Cell number was assessed using an improved Neubauer haemocytometer, by introducing 10 µl of cell suspension. Cells were counted in four large corners (x10 magnification) on each of the grids and an average number was calculated. This value was multiplied by 10^4 to give the total number of cells per ml of cell suspension.

2.9 Nanoparticle *in vitro* fluorescence imaging assay

2.9.1 Cell lines

Colorectal cancer LoVo, LS174T, and HCT116 ($9x10^4$) cells were seeded onto three sterile glass coverslips (Cellpath, Newtown Powys, UK) in a six-well plate (Corning) and grown for 24 h. Next, culture media was discarded and the cells were washed 2x with PBS followed by addition of paraformaldehyde (4%, v/v) for fixation. The cells were incubated at room temperature for 30 min. then the fixative was discarded and cells were washed 3x times with PBS. BSA (0.1% (w/v), (EMD chemicals, San Diego, USA)) was added to each well and incubated for 30 min at room temperature. The BSA was removed and the cells underwent 3x washes with PBS. Antibody or Affimer functionalised (NIR665 or Foslip loaded) nanoparticles (suspended in PBS at 1 mg/ml) were added to the wells and incubated at room temperature in the dark for 1 h. The nanoparticle suspension was discarded and the cells were washed 3x times with PBS then coverslips were mounted onto glass slides using Depex (Waltham, Massachusettes, USA). The slides were left to cure overnight then stored at 4 °C in the dark then imaged using confocal microscopy. For each experiment, three biological replicates were performed and results were discarded if the cell monolayer was disrupted.

2.9.2 Confocal microscopy

A Nikon A1R-A1 confocal microscope (Nikon, Tokyo, Japan) with NHS Elements software (version 4.0) was used for all imaging. The microscope was calibrated and settings were saved and used for all subsequent image capturing. Each slide was divided into 4 quadrants, each of which was examined systematically. For each slide, five z-stack files were captured including an image from approximately

the centre of each quadrant and one from the centre of the entire coverslip. For each quadrant, a phase/Cy7 z-stack image (distance between stacks: 0.5 µm, 0.2 µm and 0.4 µm for LS174T, LoVo and HCT116 cells respectively, chosen to produce a similar number of z-stack images) was captured. The whole depth of at least one cell was included during imaging by setting up the upper and lower limits of the z-stack. The microscope stage was then moved to the next quadrant and a z-stack captured. The fluorescent image was not examined during image location selection in order to eliminate the potential selection bias.

2.9.2.1 Nanoparticle image analysis: single z-stack slice

The analysis strategy was adopted from Tiernan *et al* 2015. A fluorescence value per µm of membrane for the image was calculated using the following equation and as shown in **Figure 2.2**:

$$Membrance\ fluorescence\ per\ \mu m = \left\{ \frac{RawIntDen_{membrane} - \left[\left(\frac{RawIntDen_{background}}{Area_{bacground}} \right) \times Area_{membrane} \right]}{Circumference} \right\}$$

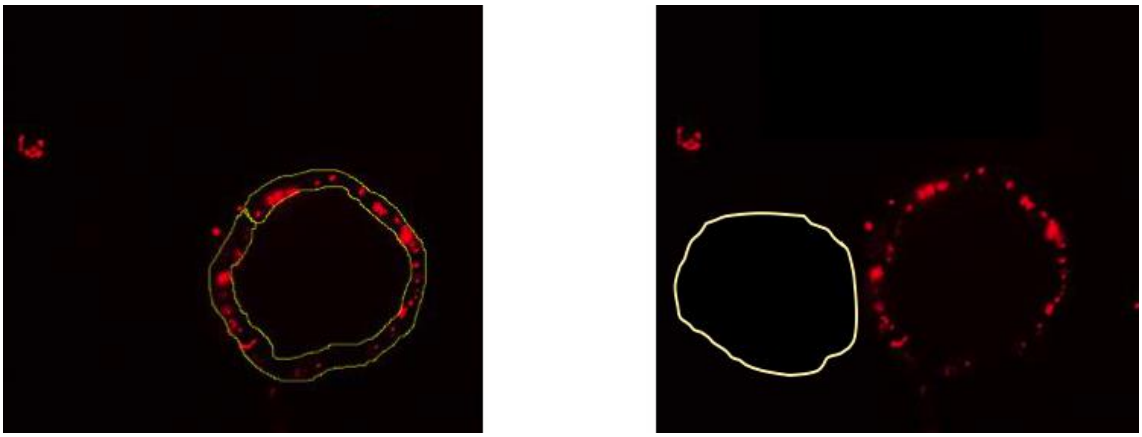

Figure 2. 2. Quantification method of membrane fluorescence.

The cell membrane was traced (left) of the fluorescent image and measurement was taken. The mean background was then subtracted (right). Confocal images of LoVo cells incubated with anti-CEA Affimer functionalised dye-doped silica nanoparticles.

Two analysis strategies were employed to quantify the fluorescence signal intensity for each cell line. First, a single slice from each z-stack was selected approximately half way between the base and top of the cell. These distances were 5 µm, 1.4 µm and 4.8 µm for LS174T, LoVo and HCT116 cells respectively. These slices were saved as fluorescent, phase and combined '.tiff' images, then fluorescence was quantified using ImageJ software version 1.42q (NIH Freeware, Maryland, USA). Using the phase image, the inner and outer boundaries of the cell membrane were traced then applied to the fluorescent only image and the raw integrated density (RawIntDen, the sum of the pixel values in the selected area) were recorded. A background area was also selected (ie. an area with no cell fluorescence) and the same measurements were taken. The circumference of the cell being examined was also measured. The above fluorescence

measurement protocol was used for five z-stacks per cell line, in all three cell lines including test and control nanoparticles.

2.9.2.2 Nanoparticle image analysis: maximum image projection

The second image analysis was performed using the maximum image projection (MIP) function according to the following equation:

$$Mean\ cell\ fluorescence = \left(\frac{RawIntDen_{cell}}{Area_{cell}}\right) - \left(\frac{RawIntDen_{background}}{Area_{background}}\right)$$

NHS Elements software offers this function where all of the z-stack images are constructed to give a new single image by taking the brightest pixel from all of the z-stacks. This is not a true cumulative image but can be used to verify the results of the single z-stack slice analysis. MIP images analysis was performed in a similar manner as described in the single z-stack analysis.

2.9.3 Image analysis: statistical methods

The mean fluorescence and standard error were compared for CEA-targeted nanoparticles and control nanoparticles for in all cell lines using unpaired t-test and Mann-Whitney test.

2.10 Nanoparticle photodynamic therapy *in vitro* assay

All experiments were conducted in subdued lighting to prevent the photodynamic effects of photosensitisers.

2.10.1 Photodynamic treatment of cell lines

LoVo, LS147T, HCT116 and HEK293 cells were grown as described previously (**section 2.9.1**) in two identical 6 well plates. Anti-CEA Affimer functionalised nanoparticles and their respective controls with various concentrations (1-5 mg/ml) were added to the wells and incubated at room temperature in the dark for 24 h. The nanoparticle suspension was removed after 24 h and the cells were washed 3x times with PBS. Cells were checked again to ensure no disruption of the monolayer. Cell culture plates were placed on top of the diffuser surface of a light-radiating device and treated with a light dose of 0.225 - 0.675 J/cm^2 then kept in the dark. Light dose was calculated based on treatments which lasted for 10-45 min at 0.25 mW/cm^2. The light-radiating device comprised of a series of LEDs (Avago Technologies, California, USA), with peak wavelength of 600-700 nm and a spectral half-width of 12 nm. Control plates were kept in the dark with no light irradiation. Three biological replicates were performed for each experimental condition. Results were discarded if the cell monolayer was incomplete or disrupted and the experiment was repeated.

2.10.2 Viable cell counts with trypan blue

At 24 h following light irradiation, cells were detached from the 6-well plate with trypsin 0.05 % (v/v) and 0.5 % ethylenediaminetetraacetic acid (EDTA), (Gibco® by Life Technologies™ Cat no. 15400-054) in sterile Dulbecco's phosphate buffered saline (DPBS) (1X), (Gibco® by Life Technologies™; Cat. no. 14190-094), for 5 minutes at 37 ^{o}C in a humidified atmosphere, in the presence of 5% CO_2. The plates were visualised under x10 magnification to ensure cells were no longer adherent to the plate. Cell specific media with phenol red and FBS was added to each well to inactivate the trypsin and the contents of each well were

aspirated and transferred to an individual 15 ml centrifuge tube (Corning® Costar® Cat. No. 430790). Each well was washed with 1 ml DPBS and the wash was added to the 15 ml centrifuge tube. Tubes were centrifuged at 400 g for 5 minutes at 21 ^{o}C, the supernatant was removed and the cell pellet was re-suspended in 0.5 ml of cell specific media. The cell suspension was transferred to a 4 ml vicell cup (Beckman Coulter Cat. No 10192147) and viable cell counts were performed via an automated cell counter incorporating Trypan Blue staining, (Vi-cell® Beckman Coulter) to obtain the number of viable cells per well.

2.10.3 Cell viability assay

The 3-[4,5-dimethylthiazole-2-yl]-2,5-diphenyltetrazolium bromide (MTT) tetrazolium salt (yellow) is reduced into a blue/purple formazan dye via the mitochondria of the cells. If the mitochondria are not viable or have reduced activity then there will be very little or none precipitate formed. Stock solution of MTT (Sigma,Cat. No. M-2128) was prepared at 5 mg/ml in PBS and wrapped in foil to protect from light. The media, in which the seeded cells were grown, was replaced with 50 µl of 1 mg/ml working MTT solution and incubated in the dark for 3 hours. MTT solution was then removed and the dark blue formazan dye formed was dissolved in 100 µl of propan-1-ol. Optical density was measured using a microplate reader (Opsys MR^{TM}, Dynex technologies ltd, UK) at 570 nm.

2.10.4 Cellular reactive oxygen species detection assay

Effect of Foslip on the intracellular Reactive Oxygen Species (ROS) levels was estimated using 2',7' –dichlorofluorescin diacetate (DCFDA). DCF is a highly fluorescent compound which can be detected by fluorescence spectroscopy with maximum excitation and emission spectra of 495 nm and 529 nm respectively. Cells were seeded on a 96 well plate 2.5 x 10^4 cells/well and incubated for 24 h.

Cells were then washed once using 1X Buffer then stained with 25 µM DCFDA in 1X Buffer for 45 min at 37 °C. Cells were then washed once with PBS then incubated with functionalised silica nanoparticles for 24 h in the dark then illuminated for 30 min. Immediately after illumination, nanoparticles suspension was then discarded and 10 µM DCF-DA (Merck, New Jersey, USA) in Hank's balance salt solution (Merck, New Jersey, USA) was added for 30 min and incubated in a CO_2 incubator then washed with PBS. DCF fluorescence was observed using confocal microscope.

2.11 Animal model of colorectal cancer

2.11.1 General considerations

All *in vivo* experiments were approved and licensed by the Home Office (animal licence holder Dr Louise Coletta, current licence number P93AOF172 and expired licence number 70/7965) and carried out in keeping with the University of Leeds ethical review committee. Personal animal licence was obtained from Home Office with reference number 41683 after I successfully completed the licensee training course. All reasonable efforts were made to reduce the number of mice required and to minimise any likely suffering. The animals were inspected daily by a qualified technician while their weight and tumour dimensions were measured twice per week. Mice were housed in a polypropylene cage with a 12 h day/night cycle while food and water were provided. Mice were euthanised at the end of each experiment following standard regulations. I am very grateful to Mr Thomas Maisey and Ms Debra Evans at St. James Biomedical Services (SBS), University of Leeds who purchased the animals, developed the xenograft model and helped with the tail vein injections for this part of the project.

2.11.2 Colorectal cancer mouse xenograft model

Four to 6-week-old BALB/c nu/nu female mice were injected subcutaneously to the right flank with 1.5 x 10^6 LS174T cells. When the tumours reached approximately 8-10 mm in diameter (approximately 10-12 days), the mice were injected with nanoparticles through the tail vein then imaged using an IVIS small animal molecular imaging system (Perkin Elmer, Waltham, USA) with excitation and emission filters set at 652 nm and 684 nm respectively.

2.11.3 Nanoparticles in vivo fluorescence imaging

Foslip-loaded nanoparticles were suspended in Eppendorf tubes and imaged using Living Image (version 4.3.1, Caliper Life Sciences, Massachusetts, USA) before they were injected into mice to ensure that they were fluorescent and active. Mice were randomised into 4 groups. Mice were injected with 100 µL of 1 mg/ml concentration of nanoparticles (suspended in PBS) as the following: anti-CEA Affimer Foslip-loaded silica nanoparticles, anti-myoglobin Affimer Foslip-loaded silica nanoparticles, anti-CEA Affimer Foslip-negative silica nanoparticles and anti-myoglobin Affimer Foslip-negative silica nanoparticles. The mice were imaged at 1 h, 6 h, 30 h and 48 h post injection. For each mouse at every single time point, three images were captured. The animals were then sacrificed under anaesthesia and organs tissues were harvested and imaged again using the IVIS imaging system. All organs including xenografts were halved and one half was snap frozen while the other half was embedded in 4% (w/v) paraformaldehyde for future analysis. Fluorescence measurements were taken using Living Image (version 4.3.1, Caliper Life Sciences, Massachusetts, USA) as the following. The tumour was traced as a ‘region of interest’ and a mean quantum efficiency measurement taken. A second region of interest was drawn on the opposite flank

and another mean quantum efficiency measurement taken (background fluorescence) and subtracted from the tumour measurement.

2.11.4 Fresh frozen tissue

Archived sample of freshly frozen fluorescence positive xenograft and matched control (fluorescence negative) from mice were cryosectioned (Leica LM3050, Leica Biosystems, Newcastle, UK) into 5 µm thick sections and mounted directly onto SuperFrost Plus slides. They were left to dry at room temperature for 60 min and rehydrated with TBS. They were then mounted, viewed and captured as per the fixed cells using confocal microscopy.

2.11.5 Nanoparticles in vivo photodynamic therapy

This experiment has been postponed due to the ongoing corona virus pandemic. We plan to perform this part of the project in the near future as the following. LS174T xenograft bearing mice will be randomised into three groups. Mice will then be injected with the following: anti-CEA Affimer Foslip loaded silica nanoparticles followed by light illumination, anti-CEA Affimer Foslip loaded silica nanoparticles but will be kept in the dark and finally anti-myoglobin Affimer Foslip loaded silica nanoparticles followed by light illumination. Xenograft's size and volume will be measured for a period of 2 week then mice will be sacrificed. Organs will be harvested and treated as described in **section 2.11.4**.

Chapter Three

Anti-CEA Affimer targeted, dye-doped silica nanoparticles for imaging of colorectal cancer cells

3 Anti-CEA Affimer targeted, dye-doped silica nanoparticles for imaging of colorectal cancer cells

3.1 Abstract

Background

Nanoparticles can offer potential solutions for targeting colorectal cancer during laparoscopic surgery, including sensitive imaging. Targeting can be achieved using a bioreceptor. Synthetic binding proteins, such as Affimer, are emerging as potential alternative to antibodies with many additional advantages. The aim of this chapter was to conjugate carcinoembryonic antigen (CEA) -specific Affimers to dye-doped silica nanoparticle and test its targeted fluorescent imaging of colorectal cancer cells *in vitro*.

Methods

Three clones of anti-CEA Affimer (I-III) were expressed and purified then tested for binding specificity to CEA using pull-down assay, ELISA and immunofluorescence. NIR664-doped silica nanoparticles were fabricated using water-in-oil microemulsion technique. Anti-CEA or control Affimers were conjugated to nanoparticles using three different chemical linkers: polyethylene glycol (PEG); 1-Ethyl-3-[3-dimethylaminopropyl]carbodiimide hydrochloride (EDC) and sulfosuccinimidyl-4-(*N*-maleimidomethyl)cyclohexane-1-carboxylate (sulfo-SMCC). The positive control anti-CEA antibody was conjugated to nanoparticle using polyamidoamine dendrimers (PAMAM). Colorectal cancer cells (LoVo, LS174T and HCT116) were incubated with CEA-

targeted or control nanoparticles for 24 h then washed. Fluorescent imaging of cell lines was quantified using confocal microscopy.

Results

Immunofluorescence staining of biotinylated anti-CEA Affimers (I-III) showed cell membrane binding specificity in LoVo cells and in a similar pattern to anti-CEA antibody. Conjugation of anti-CEA Affimers via sSMCC showed strong tumour-specific targeting, with CEA-targeted nanoparticles demonstrating 9-, 10.7- and 2.8-fold greater fluorescence than control in LoVo, LS174T and HCT116 cells respectively ($p<0.0002$). EDC and PEG-linked anti-CEA Affimer nanoparticles showed negligible tumour-specific binding in all cell lines.

Conclusion

Anti-CEA Affimer was specific to CEA and when it was conjugated to silica nanoparticles it allowed tumour-specific fluorescent imaging of colorectal cancer cells *in vitro*.

3.2 Introduction

There is a substantial clinical need to develop a system that allows accurate intra-operative staging of colorectal cancer to facilitate precision oncological surgery. Only 35% of patients who undergo colorectal cancer resection will have lymph nodes metastases, yet all of them receive radical resection that entails removal of the primary cancer, vasculature and lymphatics. This means that almost 65% of patients are over-treated with unnecessary extended resections that increase the risk of morbidity and mortality (Logan et al., 2011); **see section 1.2** . These figures are likely to increase due to the introduction of the NBCS programme, which led to increased diagnosis of small, early stage cancers, such as polyps and Dukes' A cancers. To date, there is no accurate method for pre- or intra-operative lymph nodes staging. A potential solution to this problem is to target a tumour specific biomarker using antibodies or synthetic binding proteins, such as Affimers (Hoogstins et al., 2018, Andrew et al., 2016). The recently published work by Tiernan *et al* (Tiernan et al., 2015), demonstrated that CEA antibody targeted dye-doped silica nanoparticles allow specific *in vivo* fluorescent imaging of colorectal cancer in a mouse model. Antibodies have their own limitations and alternative methods are warranted to develop a robust imaging system for colorectal cancer. This chapter focuses on anti-CEA Affimer production and a method to conjugate them to dye-doped silica nanoparticles. The proposed fluorescent nano system is a nanoparticle encapsulated fluorophore conjugated to a targeting molecule using a tumour-specific antibody or Affimer. Fluorescent signal to background ratio has to be substantial to allow translational potential; a feature that has not been achieved in colorectal cancer surgery so far. Affimers are synthetic binding proteins and proved to be match antibodies in their biorecognition characteristics (Tiede et al., 2017). In an application requiring

biorecognition, specific binding of the Affimer to its target tissue dictates the successful targeting of the fluorescent nanoparticles. In this chapter, a unique feature of the near-infrared (NIR664) dye has been exploited to improve the signal-to-background ratio compared to published studies (Heath et al., 2012, van Scheltinga et al., 2011).

The aims for this part of the project were to:

i. Assess the ability of anti-CEA Affimers to target colorectal cancer cells *in vitro;*
ii. Fabricate and characterise dye-doped silica nanoparticles;
iii. Conjugate anti-CEA and control Affimers or antibodies to the nanoparticle surface;
iv. Compare the ability of the targeted nanoparticles (Affimer or antibody) to bind to tumour cells *in vitro.*

3.3 Results

3.3.1 Affimer expression and purification

Here, the aim was to assess the binding specificity of three different anti-CEA Affimers in order to select the most specific for colorectal cancer cell targeting. Anti-myoglobin Affimer was used as a negative control because we hypothesised that colorectal cancer cells do not express this muscle-related protein. The anti-CEA and anti-myoglobin Affimers were selected and characterised for Kd value and other parameters using mass spectrometry, surface plasmon resonance and ELISA and the expression plasmids for Affimers were kindly provided for this project by Dr. S. Shamsaddin (Shamsuddin, 2019) and Mrs E. Al-Enezi respectively. Once the DNA sequence of the plasmids was confirmed, anti-CEA and anti-myoglobin Affimers were expressed and purified in order to be used for other investigations in this project. After validation of DNA sequence, the plasmids of Affimer were expressed in BL21 (DE3) *E.coli* and purified using Ni2+-NTA Affinity column chromatography; exploiting the His tag region as described in **section 2.1.4**.

Anti-CEA Affimer expression was effective for Affimer II and III with a yield of ~ 3 mg/ml whilst Affimer I yielded only 0.5 mg/ml as shown in **Table 3.1**. Next, I attempted to improve the yield of anti-CEA Affimer I by inoculating the bacterial colonies in 2TY media as a start-up culture instead of 2 ml LB media + 1% (w/v) glucose. A final IPTG concentration of 0.1 mM with a longer incubation time (16 h) was also used as an optimisation step. This method increased the expression yield substantially in anti-CEA Affimer II and III but the yield of Affimer I only showed slight increase to 0.9 mg/ml. The original protocol provided by the BSTG for Affimer purification included a heating step at 50 ^{0}C. The heating was

introduced in order to remove non-specific proteins based on the property of Affimers that they are stable at higher temperature compared to other proteins. Although we avoided this step in anti-CEA Affimer I expression, the yield did not improve beyond 0.9 mg/ml. This finding suggested that anti-CEA Affimers with different loop sequences may have unique properties.

Table 3. 1. Outcome of anti-CEA and anti-myoglobin Affimers expression and purification.

Clone	Concentration (mg/ml)	Aggregation	Volume
Anti-CEA-I	0.5	Yes	1 ml
Anti-CEA-II	3.1	No	1 ml
Anti-CEA-III	3.7	No	1 ml
Anti-myoglobin	2.9	No	1 ml

Next, purification of anti-CEA Affimers was performed using Ni^{2+}-NTA resins and their molecular size was determined using SDS-PAGE gel as shown in **Figure 3.1**. The cell lysates were centrifuged to remove insoluble proteins and only soluble fractions were transferred to the tubes containing the Ni^{2+}-NTA resin. Elutions of each Affimer were run on the gels and compared to their respective soluble fractions. For all three anti-CEA Affimer (I-III), the elution bands migrated in the range between 10-15 KDa, suggesting successful Affimer monomers purification. The intensity of the bands observed indicated that anti-CEA Affimer I was less expressed than anti-CEA Affimer II and III despite using the same volume of eluant (5 µl). Affimer dimers were seen on the gel due to the presence

of cysteine amino acid in the C-terminus. This is due to disulphide bond formation between two cysteine groups on two Affimers.

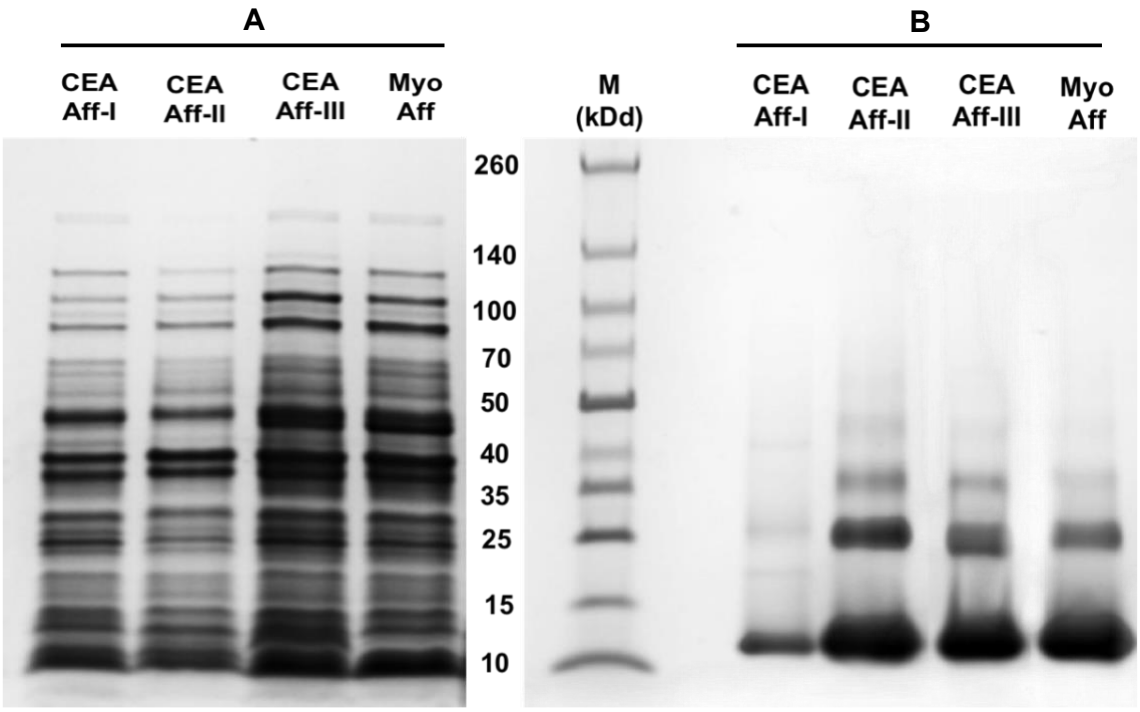

Figure 3. 1. SDS-PAGE gel of purified anti-CEA Affimers.

Gels show: (A); soluble fractions of each Affimer before Ni^{2+}-NTA resin purification; (B), purified Affimers after Ni^{2+}-NTA resin had been loaded. Five µl of each sample was added to each well and run in 4-15% (w/v) gradient gel under reducing condition. The lanes denote: (M), protein marker in KDa; (CEA Aff-I), anti-CEA Affimer I; (CEA Aff-II), anti-CEA Affimer II; (CEA-III), anti-CEA Affimer III and (Myo Aff), anti-myoglobin Affimer.

3.3.2 Anti-CEA Affimer binding specificity

Next, the aim was to assess the binding specificity of purified anti-CEA Affimers and, if they were specific, to conjugate them to silica nanoparticles for targeting colorectal cancer cells. The binding specificity of the Affimer was determined using pull down assays, immunofluorescence and ELISA.

3.3.2.1 Pull down assay of anti-CEA Affimer against CEA protein

The aim of this experiment was to determine whether purified anti-CEA Affimer could specifically bind to cellular CEA within the context of a complex protein mixture. Therefore, proteins were purified from the culture medium taken from the colorectal cancer cell line LoVo, which is known to secrete CEA into the medium (Lee et al., 2013). As controls, recombinant CEA from Abcam (positive control) and media of HEK293 cell line (negative control) were also purified. The Affimers were purified onto Ni^{2+}-NTA resin and excess Affimers were removed by centrifugation followed by two washing steps. The supernatant containing unbound Affimers (UB Aff) and from two washing steps were kept and run on SDS-PAGE gel. Then, the Affimer-loaded resins were mixed and incubated with the protein mixtures and supernatant containing unbound CEA was removed and kept to be run on SDS-PAGE gel. The result from SDS-PAGE analyses for protein recovery with Coomasie stain is shown in **Figure 3.2**. In the lane of unbound Affimer (UB Aff), there were bands migrating between 10 – 15 KDa, suggesting Affimers were still in the supernatant with reduced intensity of the band after the second wash (W2). This confirmed that the resins were saturated with Affimers before moving to the next step. Results from SDS-PAGE analysis then showed that all anti-CEA Affimers successfully pulled-down CEA from CEA secreted into the media (LoVo M) as shown by a band detected at around 200

KDa (**Figure 3.2. A-C**). The same size of band was also observed in the positive control sample whereby anti-CEA Affimers I and III, less for anti-CEA Affimer II, bound specifically to recombinant CEA (Recom CEA) that was commercially obtained. No band at this position was detected in the cell media of HEK293. Similarly, no high molecular weight protein was seen on anti-myoglobin Affimer which was used as control Affimer (**Figure 3.2. D**).

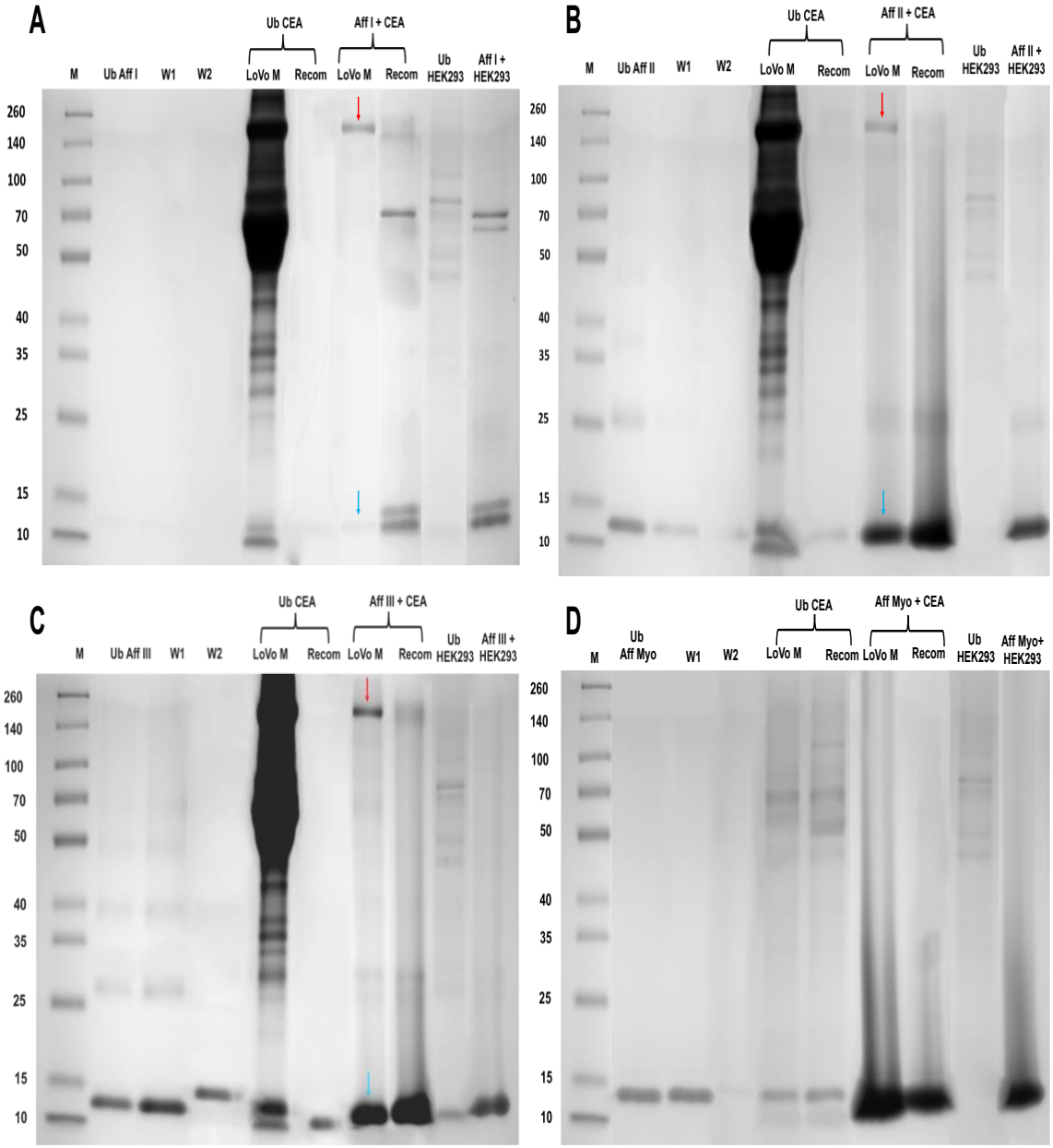

Figure 3. 2. Anti-CEA Affimers successfully bind to protein of the correct size.

SDS-PAGE gel for pull-down CEA using Affimers: (A-D), showing gels of anti-CEA I, II, III and anti-myoglobin Affimers respectively. Ten µl of each sample was added to each well and run in 4-15% (w/v) gradient gel under reducing condition. The lanes denote: (M), protein marker in KDa; (W), washed fraction; (Ub Aff) and (Ub CEA), unbound fractions of Affimer and CEA, respectively; (LoVo M), LoVo's cell media; (Recom), recombinant CEA from Abcam; (Ub HEK293) unbound HEK293 media; (Aff + CEA) and (Aff + HEK293), mixture pull down lysate. Arrows denote: (red), the pulled-down CEA; (blue), Affimers band.

Next, immunoblotting of the corresponding pull-down complex was carried out to confirm that the protein bands detected represented the actual CEA and Affimers. For western blotting, protein samples were separated following the same procedure as for SDS-PAGE analysis. Then, membranes were probed with anti-CEA or anti-His tag antibody followed by secondary antibody HRP conjugated.

Two bands from the pull-downs of LoVo media (LoVo M) and recombinant CEA (Recom) were detected at 200 KDa and represented CEA on the western blot probed with anti-CEA antibody as shown in **Figure 3.3. A**. No bands were seen from the pull-downs of HEK293 cell media or by the control anti-myoglobin Affimer. The western blot probed with an anti-His tag antibody confirmed that the protein band detected at 13 KDa represented the corresponding anti-CEA Affimers as shown in **Figure 3.3. B**.

Collectively, these findings suggested that anti-CEA Affimers were able to specifically bind to CEA in the protein complex.

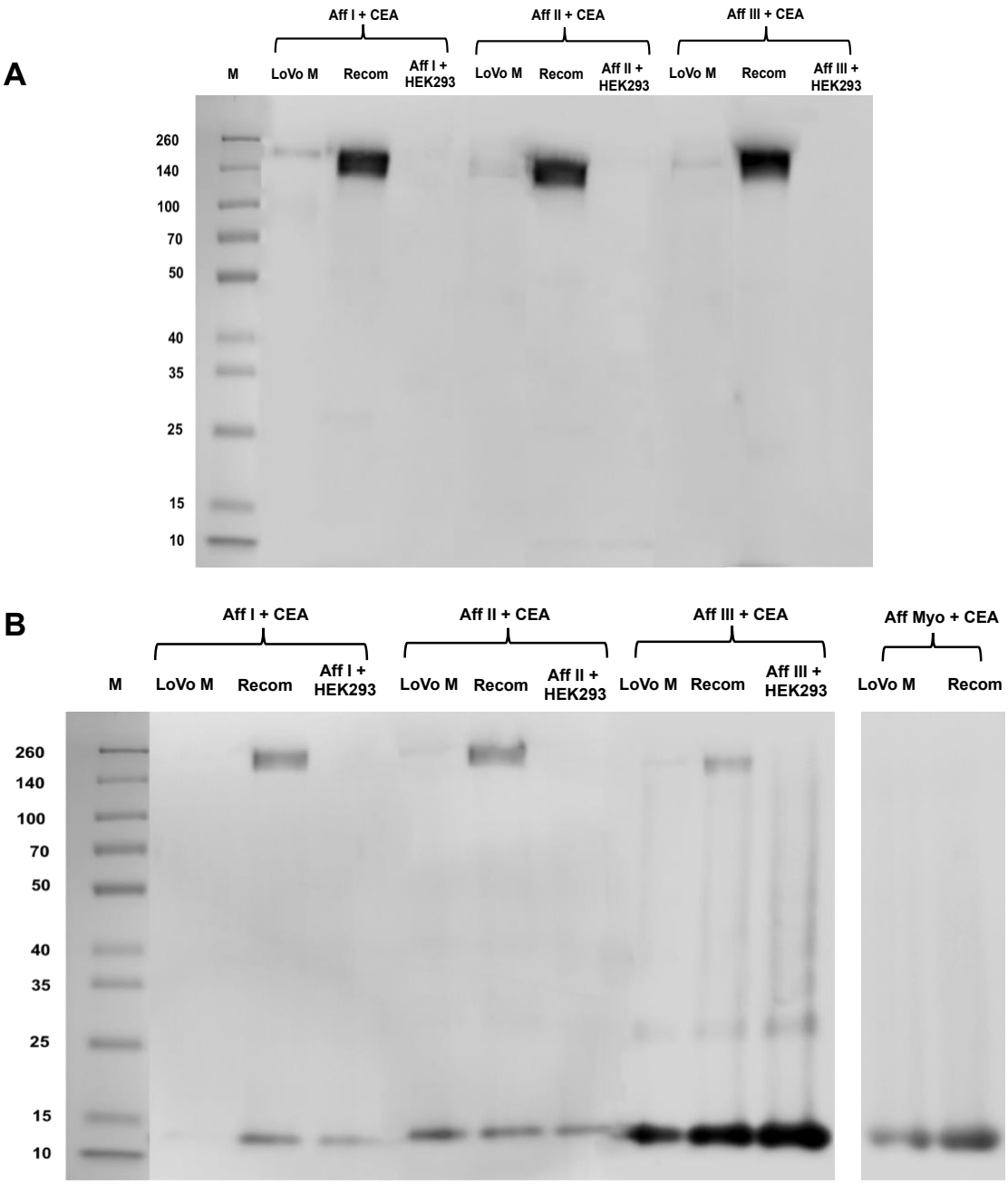

Figure 3. 3. Immunoblotting of anti-CEA Affimer bound to CEA.

Gels for immunoblotting from the pull-down complex using: (A), monoclonal anti-CEA antibody to detect CEA and (B), anti-His tag antibody to detect Affimers respectively. The lanes denote: (M), protein marker in KDa; (Aff I, II, II, and Myo) anti-CEA I, II, III and anti-myoglobin Affimers respectively; (LoVo M), LoVo's cell media; (Recom), recombinant CEA from Abcam; (Aff + CEA) and (Aff + HEK293), mixture pull down complex.

3.3.2.2 ELISA analysis of purified Affimers

To further evaluate the binding characteristics of anti-CEA Affimers against CEA, an ELISA was used. Recombinant CEA was biotinylated and immobilised onto streptavidin coated Nunc-Immuno™ Maxisorp™ 96-well plate and each Affimer was used as a primary detection agent at varying concentrations. Anti-His_6-HRP was used as secondary antibody at 1:1000 dilution. A single well of 1x PBS was used as negative control. Three 96-well plates with three replicates were carried out for ELISA and absorbance at 620 nm (A_{620}) was quantified using plate reader as shown in **Figure 3.4**. All three anti-CEA Affimers showed binding to CEA in proportion to the concentration of Affimers, whereas anti-myoglobin Affimer showed minimum response suggesting specific binding of anti-CEA Affimers to CEA.

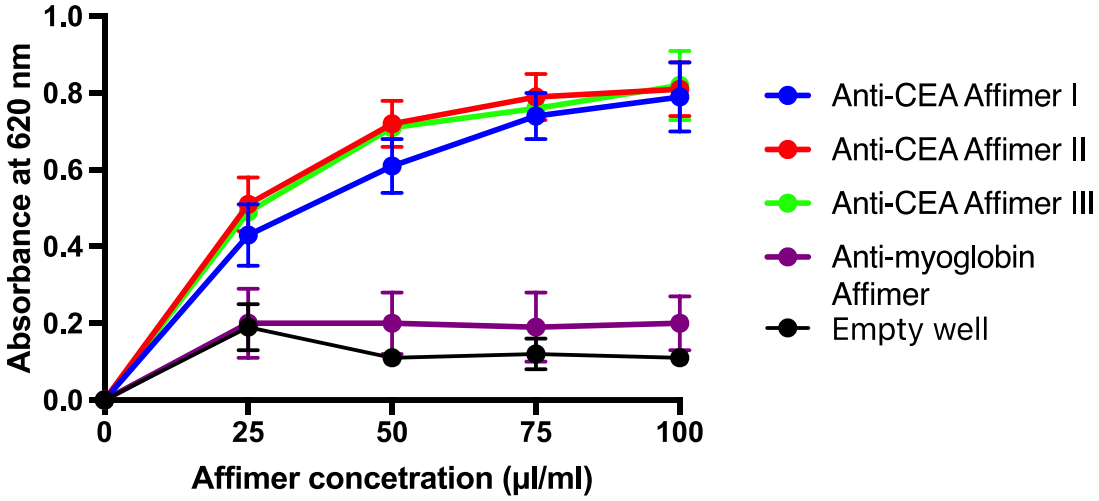

Figure 3. 4. Direct ELISA results for anti-CEA Affimers together with negative controls.

Anti-His_6-HRP conjugate was used as the secondary reagent. Data are mean A_{620} (SEM, n=3, X3). Symbol denote: (●) Anti-CEA Affimer I;(●), Anti-CEA Affimer II; (●), Anti-CEA Affimer III; (●), Anti-myoglobin Affimer and(●), empty well.

3.3.2.3 Anti-CEA Affimer immunofluorescent imaging of LoVo cells

Next, the aim was to assess the binding specificity of anti-CEA Affimers to fixed colorectal cancer cells LoVo which is known to have high expression of CEA on the cellular membrane (Ohannesian et al., 1995, Ashraf et al., 2009, da Paz et al., 2012, Fahlgren et al., 2003, Wang et al., 1999). A key step, which was Affimer biotinylation, had to be performed before immunofluorescence could be assessed in fixed cells. I aimed to biotinylate anti-CEA and control Affimers to allow Affimer-based staining when it is bound to streptavidin conjugated DyLight in the immunofluorescence staining. Affimer biotinylation was performed by mixing freshly reduced Affimer with biotin-maleimide then excess biotin was removed using Zeba spin desalting column (7 MWCO). The success of Affimer biotinylation was then confirmed using ELISA in a 96-well plate with two replicates for each Affimer. Nunc-Immuno™ MaxiSorp™ wells were aliquoted with 50 µl of PBS per well then mixed with biotinylated Affimers then incubated with streptavidin-HRP. Wells were then washed prior to developing in TMB/substrate solution. Affimers biotinylation was validated by colour change from colourless in the negative control well (omitted the biotinylated Affimer) to a blue colour as shown in the positive wells **Figure 3.5. A**. Then, absorbance at 620 nm (A_{620}) was quantified in all Affimers using plate reader **Figure 3.5. B**.

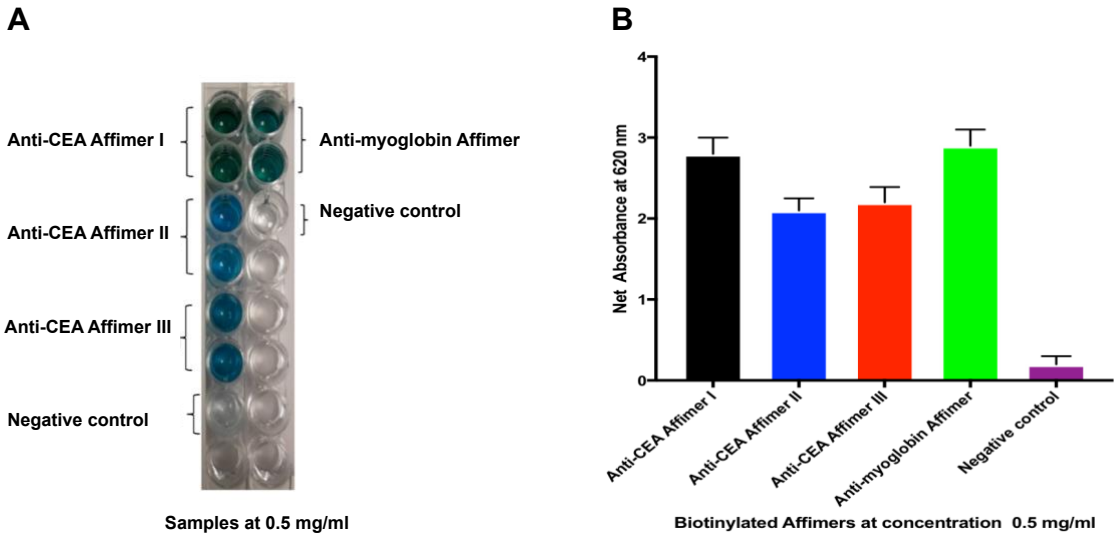

Figure 3. 5. ELISA result of biotinylated anti-CEA Affimers and control.

(A), biotinylated anti-CEA Affimers and control in the first column of wells and followed by anti-myoglobin Affimer and control in the second column of wells. Negative control wells consisted of 1x PBS and TMB. (B), comparison between biotinylated anti-CEA and anti-myoglobin absorbance measurements. Data are mean A_{620} (SEM, X2) using TMB as substrate.

Having demonstrated successful biotinylation of anti-CEA Affimer, the aim was then to assess the binding specificity of anti-CEA Affimer to LoVo cells.

LoVo and HEK293 control cells were fixed with paraformaldehyde on a 6-well plate and incubated with 10 µg/ml biotinylated anti-CEA and control anti-myoglobin Affimers. Mouse anti-human IgG CEA (1µg/ml) was also used as a primary antibody and included as a positive control on separate coverslips. Streptavidin DyLight 488 conjugate was then applied to cells incubated with biotinylated Affimers while goat anti-mouse IgG secondary antibody conjugated with Alexa Fluor® 488 was used on the positive control coverslip then images

were taken as shown in **Figure 3.6.** All anti-CEA Affimers selectively (**Figure 3.6. A-C**) targeted CEA expressing LoVo cells in a similar fashion to the staining pattern seen with anti-CEA antibody (**Figure 3.6. K**). No CEA staining in LoVo cells was seen when incubated with the control anti-myoglobin Affimer (**Figure 3.6. D**). Also, no CEA staining was seen in HEK293 cells (**Figure 3.6. E-H**) and in negative control slides of LoVo (**Figure 3.6. I**) and HEK293 (**Figure 3.6. J**) where the anti-CEA Affimer was initially omitted. Collectively, these images suggest that anti-CEA Affimers can specifically bind to CEA-expressing cell line. The immunofluorescent images suggested that CEA protein could be imaged as early as 24 h following incubation.

Considering all the results on anti-CEA Affimer binding specificity thus far, it appeared that the Affimer was worthy of being assessed as a bioreceptor for targeting silica nanoparticle against colorectal cancer which was the subject of the next part of this chapter.

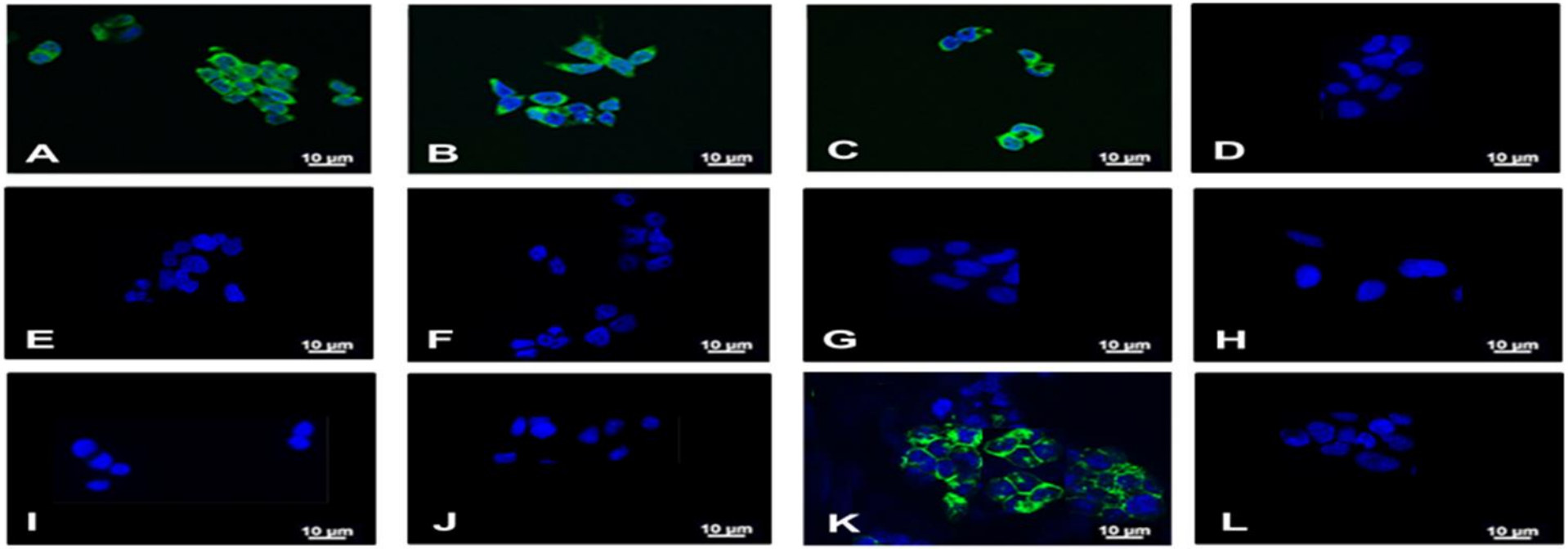

Figure 3. 6. Immunofluorescence staining of LoVo cells with anti-CEA Affimers.

Cells were incubated with Affimers or anti-CEA antibody for 24 h then imaged. Images denote: (A), (B), (C) and (D), LoVo cells incubated with anti-CEA Affimer I, II, III and anti-myoglobin Affimer respectively; (E), (F), (G) and (H), HEK293 cells incubated with anti-CEA Affimer I, II, III and anti-myoglobin Affimer respectively; (I) and (J), LoVo and HEK293 negative control cells where anti-CEA Affimer was omitted respectively; (K) and (L), LoVo and HEK293 cells incubated with anti-CEA antibody respectively. Scale bar on the images represent 10 µm.

3.3.3 Dye-doped silica nanoparticles: fabrication and characterisation

The aim of this part of the project was to synthesise dye-doped silica nanoparticles to target colorectal cancer cells using anti-CEA Affimer as a bioreceptor for selective fluorescent imaging. The NIR664 dye-doped silica nanoparticles were fabricated using an established and published protocol (Tiernan et al., 2015). The particles size, density of amine groups available on the surface and their fluorescence spectra were characterised and measured.

3.3.3.1 Particle size

To measure particle size, field emission gun scanning electron microscopy (FEG-SEM) was used. Sixty nanoparticles were randomly selected to calculate the mean diameter which was 58.62 nm (±0.96 SEM); **Figure 3.7**.

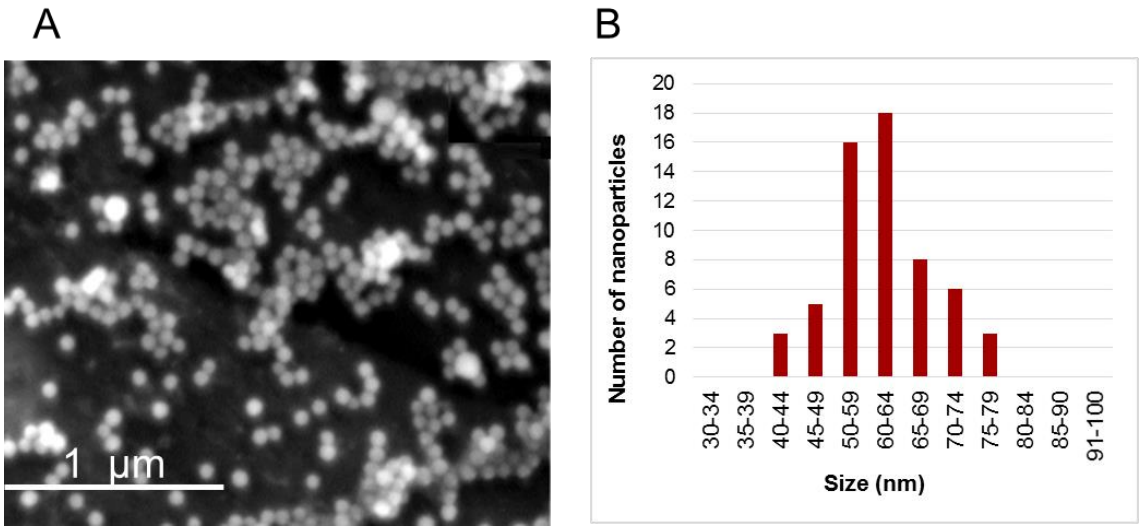

Figure 3. 7. Size distribution of NIR664 dye-doped silica nanoparticles.

(A), the particles were imaged using FEG-SEM and the diameter of 60 randomly selected particles was measured using Photoshop; (B), the size distribution is shown with particles diameter being binned into 5 nm intervals (n=60).

3.3.4 Physical characterisation of 'bare' nanoparticles

3.3.4.1 Amine group on silica nanoparticles quantification

Following the manufacturing of the dye-doped silica nanoparticle, the surface was aminated using 3-aminopropyltriethoxysilane (APTES) to add amine functional group and allow conjugation of Affimer to the surface of the nanoparticle. The efficiency of the amination process was quantified using fluorenylmethyloxycarbonyl chloride (Fmoc-Cl) (Chen and Zhang, 2011) using the absorbance of the solution containing the cleaved Fmoc-Cl molecules with reference to a standard curve for Fmoc-Cl absorbance from five batches of freshly aminated nanoparticles. The data showed that 1 mg of nanoparticles would be functionalised with 1.92 $x10^{16}$ amine groups; **Table 3.2**. Therefore, the amination process was effective when compared to other published results (Tiernan et al., 2015, Liu et al., 2007).

Table 3. 2. Quantification of amine groups on silica nanoparticles.

Batch	Fluorescence	Concetration (mM)	Sample mass (Conaghan et al.)	Mol Fmoc/mg	Amine groups/mg
1	443.0	13.9	3.3	1.50 $x10^{-7}$	8.89 $x10^{15}$
2	426.3	12.8	4	3.51 $x10^{-7}$	18.29 $x10^{15}$
3	410.5	12.9	2.5	5.11$x10^{-7}$	29.54 $x10^{15}$
4	415.5	13.8	2.5	5.24 $x10^{-7}$	30.01$x10^{15}$
5	459.0	15.1	4	1.55 $x10^{-7}$	9.20 $x10^{15}$
Mean				**3.38$x10^{-7}$**	**1.92 $x10^{16}$**

3.3.4.2 Fluorescence analysis

Excitation and emission spectra of the dye-doped nanoparticles was measured using spectrofluorometer at various concentrations. Measurements were taken from three freshly synthesised batches suspended in 1X PBS. The peak excitation (λ_{ex}) and emission (λ_{em}) wavelengths for particles loaded with NIR664 were 670 and 696 nm respectively; **Figure 3.8. A**. The fluorescent signal produced by particles increased with increasing concentration up to approximately 2 mg/ml, after which the signal reduced most likely due to internal filter effect; **Figure 3.8. B**.

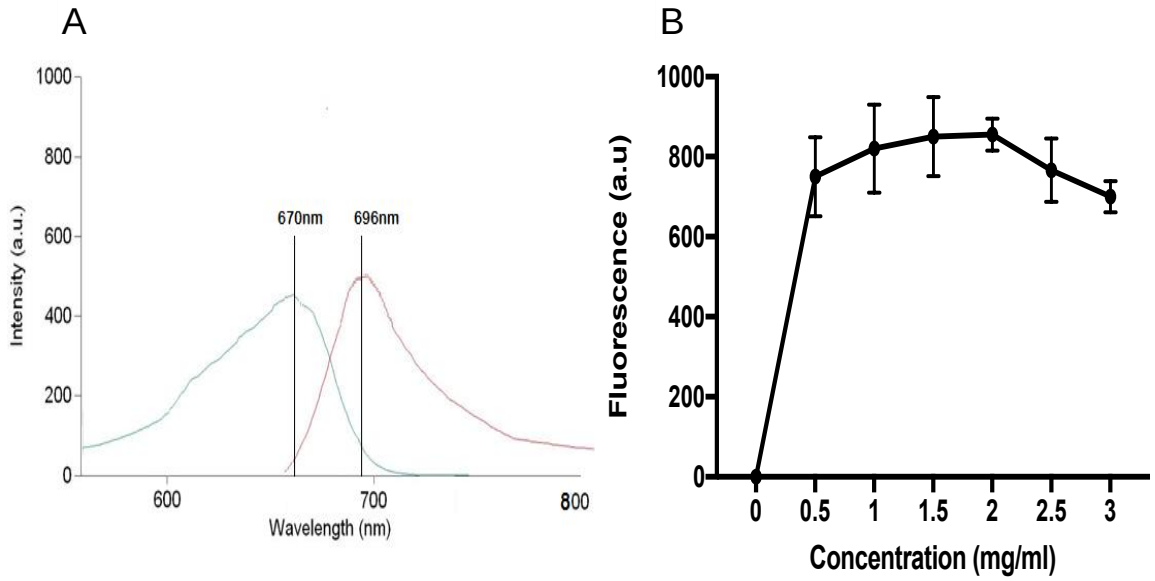

Figure 3. 8. Fluorescence spectrum of NIR664-doped silica nanoparticles.

Dye-doped silica nanoparticles were suspended in PBS. (A), peak absorption and emission wavelengths were recorded on a spectrometer. The blue and red lines represent the excitation and emission spectra. (B), the relationship between NIR664-doped nanoparticle concentration and emission fluorescence. Data denote mean (SEM, n=3).

3.3.5 Chemical linkage strategies for Affimer conjugation

The aim in this section was to target aminated NIR664-doped silica nanoparticles to CEA using anti-CEA Affimer. To do so, three chemical linking strategies were used to assess the ability of the nanoparticles to bind to tumour cells *in vitro* and quantify the specificity and fluorescent signal magnitude for each linking strategy. Amine groups on the scaffold and sulfhydryl groups on c-terminal cysteine of the Affimer were available for chemical linkage to nanoparticles. Therefore, chemical linkers that could link those functional groups were assessed. Due to the low yield of anti-CEA Affimer I as shown in **Table 2.1**, only anti-CEA Affimer II and III were assessed in nanoparticle conjugation.

3.3.5.1 Affimer linkage to nanoparticle using EDC

The nanoparticle surface was carboxylated as described and then EDC was used to link the amine groups on the Affimer scaffold as shown in **Figure 3.9**.

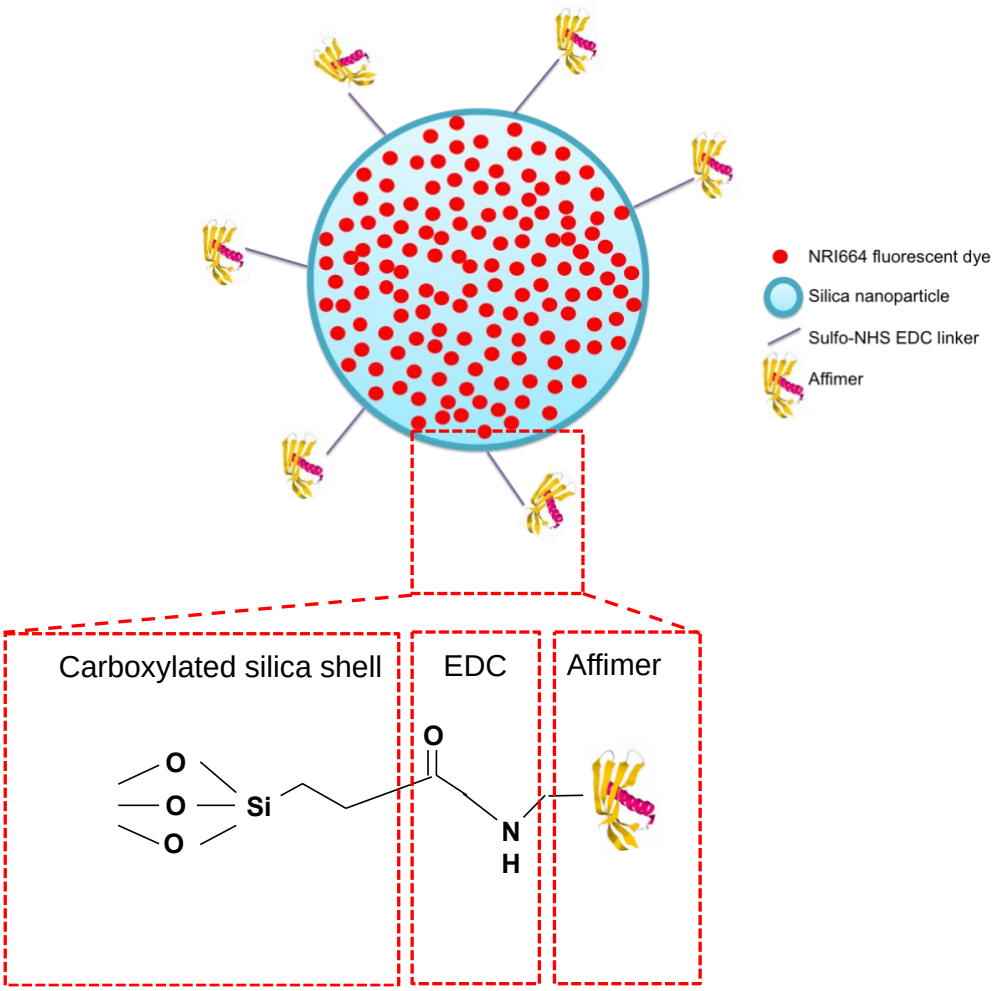

Figure 3. 9. Schematic of EDC as a chemical linker for Affimer functionalised dye-doped silica nanoparticles.

EDC and sulfo-NHS were used as a zero length crosslinker to conjugate carboxylated nanoparticles and Affimers. Four anti-parallel β strands are shown in yellow and one α helix strand in pink. PDB ID: 4N6T.

Due to the presence of lysine amine acid within the loop of anti-CEA Affimer III, which could potentially link this Affimer to the nanoparticle in manner in which would be compromised it was not used. Instead, anti-CEA Affimer II and anti-myoglobin Affimers were selected for this experiment. The nanoparticle suspension was washed 3 times to ensure that unbound Affimers were discarded following centrifugation. Removal of unbound Affimers was confirmed by measuring the absorbance corresponding to protein in the reaction mixture and each discarded supernatant. It is evident from the graph that A_{280} nm, dropped significantly following incubation and washing, showing removal of loosely bound Affimers; **Figure 3.10**. This approach was used with all other chemical linkers for Affimer conjugation. Washing unbound Affimers would allow only those conjugated to nanoparticles to target CEA on colorectal cancer cells. The mean diameter of EDC linked nanoparticles was 65 nm ($\pm$10.7 SEM, n=5) using dynamic light scattering (DLS).

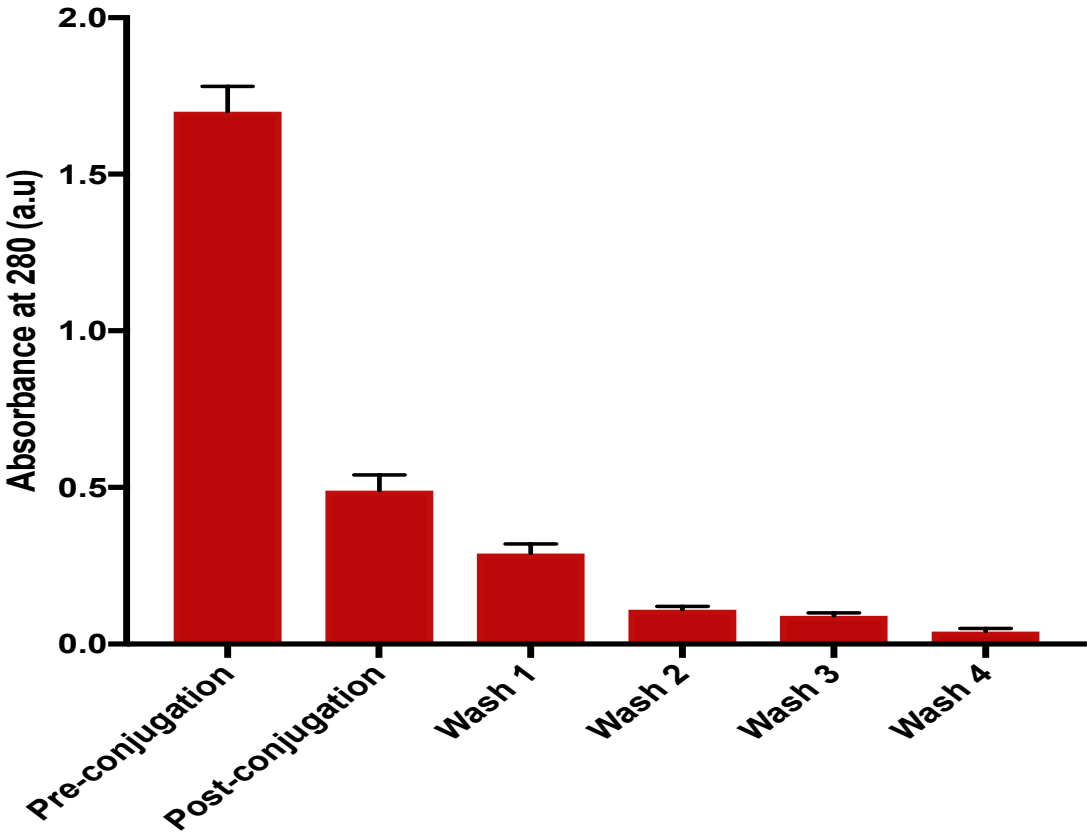

Figure 3. 10. Absorbance measurement of EDC-linked anti-CEA Affimer II to nanoparticles.

A_{280} of the reaction mixture comprising sulfo-NHS, EDC and anti-CEA Affimer II prior to the nanoparticles being added (pre-incubation), following incubation but with the nanoparticles removed, and of the supernatant following washes in ethanol. Data denote mean (SEM, n=3).

3.3.5.2 Affimer linkage to nanoparticle via bifunctional PEG

Bifunctional PEG crosslinkers, that contain an NHS ester at one end and a maleimide group at the other, were used to conjugate reduced Affimers and link free amine groups on the surface of the aminated nanoparticles to the free sulfhydryl groups on c-terminal cysteine of the Affimer; **Figure 3.11**.

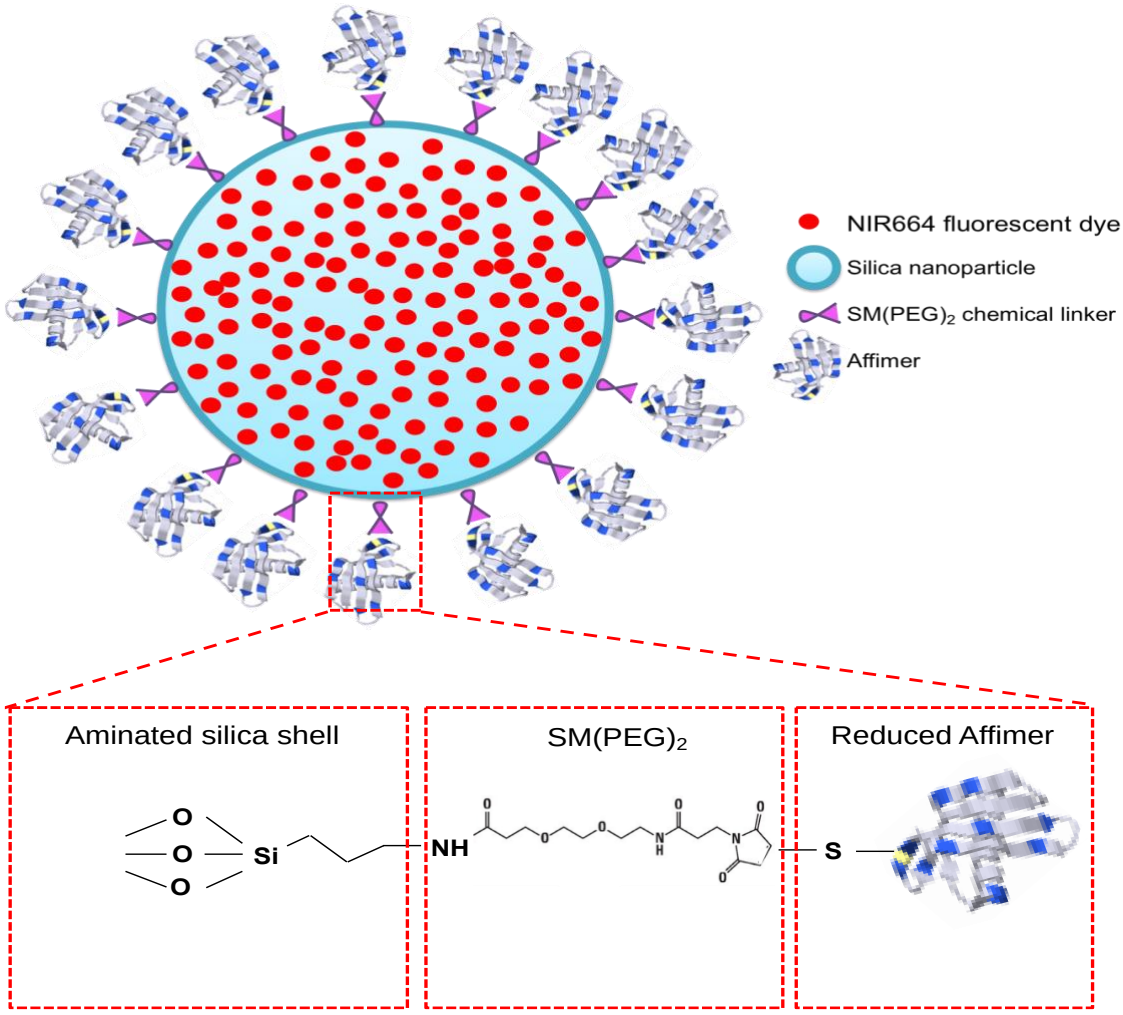

Figure 3. 11. Schematic of PEG as a chemical linker for Affimer functionalised dye-doped silica nanoparticles.

Bifunctional PEG crosslinker was used to conjugate Affimer to aminated nanoparticles. The blue colour on the reduced Affimer represents the 11 lysine residues at the surface of the Affimer scaffold whilst the yellow colour represents the cysteine at the C-terminal (pdp. 4N6T).

The nanoparticle mixture was washed 3 times to remove unbound Affimers in a similar manner to that described in section **3.5.1.** Although a prolonged (2 h) incubation was used more unconjugated Affimer remained (**Figure 3.12**); possibly due to the much larger number of amine groups available when carrying out EDC catalysed conjugation. The mean diameter of PEG linked nanoparticles was 90 nm (±18.5 SEM, n=5) using DLS.

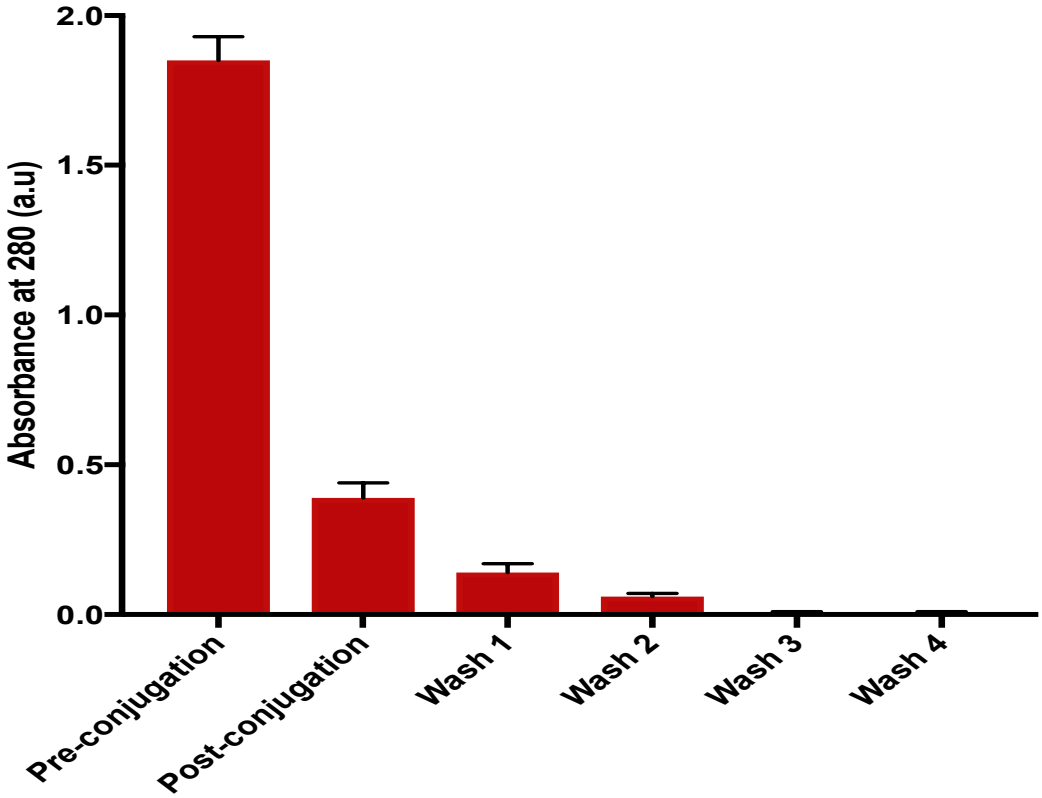

Figure 3. 12. Absorbance measurement of PEG-linked anti-CEA Affimer II to nanoparticles.

A_{280} of the reaction mixture comprising PEG and anti-CEA II Affimer prior to the nanoparticles being added (pre-incubation), following incubation but with the nanoparticles removed, and of the supernatant following washes in ethanol. Data denote mean (SEM, n=3).

3.3.5.3 Affimer linkage to nanoparticles via sSMCC

TCEP reduced anti-CEA and anti-myoglobin Affimers were prepared and linked via the free Affimer sulfhydryl group to the aminated nanoparticle surface using sSMCC; **Figure 3.13**. The mean diameter of sSMCC linked nanoparticles was 61 nm (±18.5 SEM, n=5) using DLS. In a similar manner to PEG linkage to nanoparticle, more unbound Affimers post incubation was observed when absorbance was measured at 280 nm.

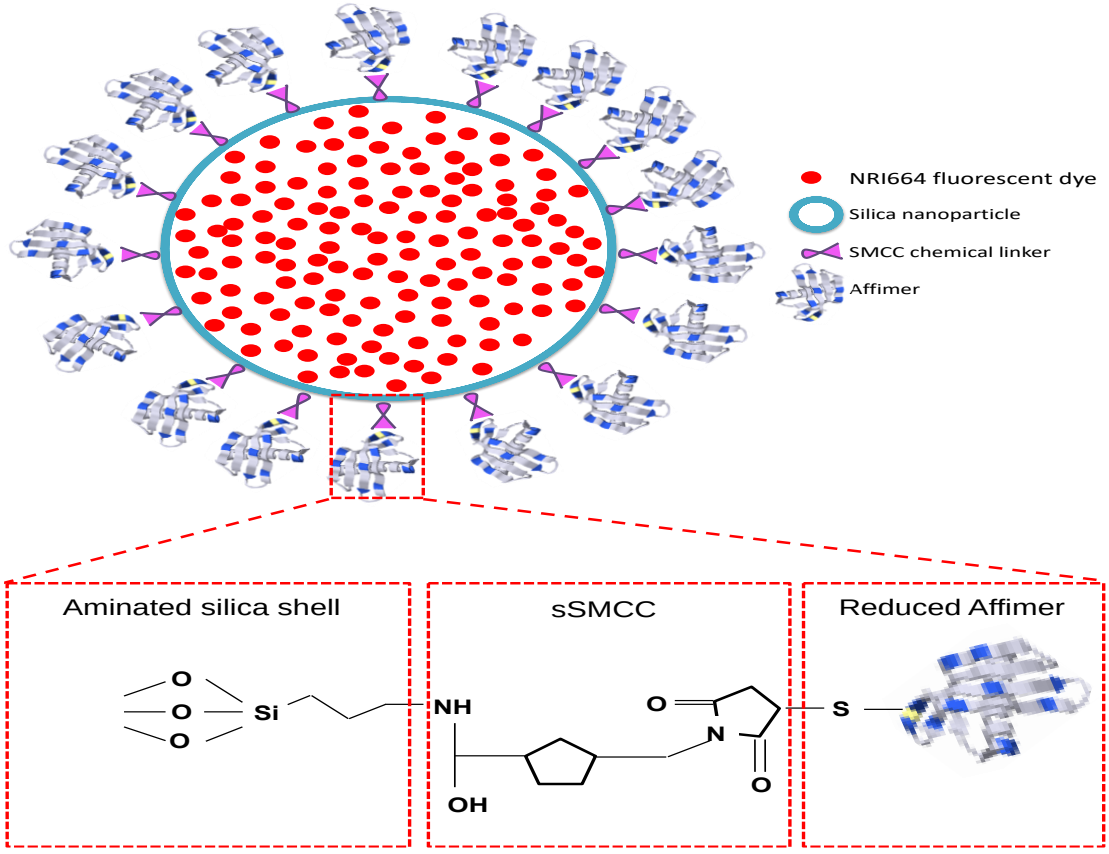

Figure 3. 13. Schematic of sSMCC as a chemical linker for Affimer functionalised dye-doped silica nanoparticles.

sSMCC reacts with the aminated nanoparticle surface to form a stable amide bond with a maleimide group that can then be conjugated to the free sulfhydryl group on a reduced Affimer. The blue colour on the reduced Affimer represents the 11 lysine residues at the surface of the Affimer scaffold whilst the yellow colour represents the cysteine at the C-terminal (pdp. 4N6T).

3.3.6 PAMAM linkage of anti-CEA antibody to nanoparticles

Next, the aim was to conjugate anti-CEA antibody to the surface of NIR664 dye-doped silica nanoparticles using an established conjugation protocol (Tiernan et al., 2015) as shown in **Figure 3.14**. Anti-CEA antibody functionalised nanoparticles acted as positive control, when compared to anti-CEA Affimer functionalised nanoparticles. PAMAM dendrimers are branched chain molecules that can be synthesised to contain a specified number of branches. PAMAM generation 4.5 carboxylate sodium salt dendrimers were used to conjugate aminated nanoparticles to whole IgG. Each 'R' group in this case has 16 available carboxyl groups, due to the increased number of branches (four versus one). PAMAM dendrimer conjugation should lead to change in nanoparticle diameter due to its size (approximately 5 nm). Therefore, the size of 'bare' nanoparticles and CEA-targeted nanoparticles were compared using DLS. The mean diameter of PAMAM linked nanoparticles was 72 nm ($\pm$11.5 SEM, n=5); compared to 58.62 nm ($\pm$0.96 SEM, n=5); for bare nanoparticles ($p < 0.0001$; unpaired t-test); **Figure 3.15**. The size of functionalised nanoparticles was still small enough for the proposed applications.

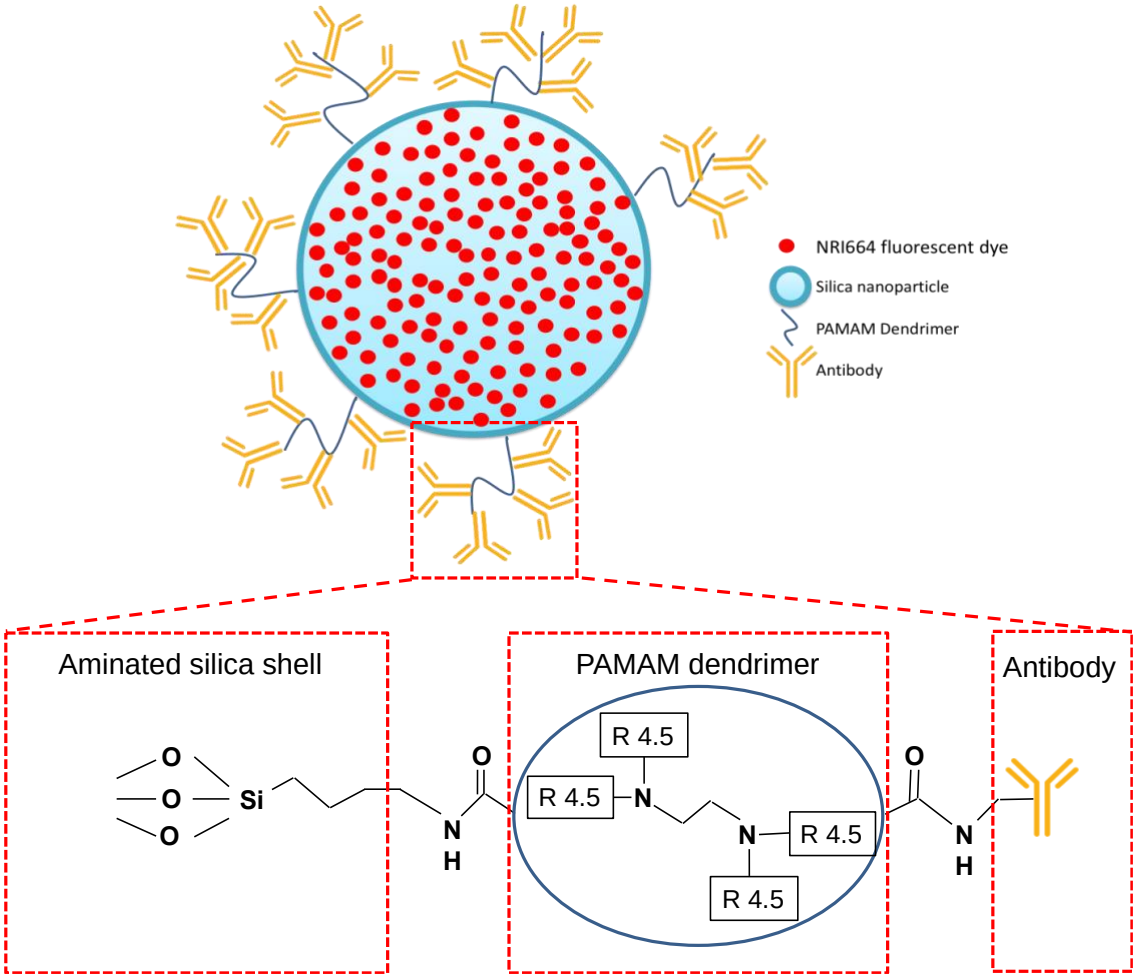

Figure 3. 14. Schematic of antibody functionalised silica nanoparticles.

PAMAM generation 4.5 carboxylate sodium salt dendrimers was used to conjugate aminated nanoparticles to whole IgG antibodies. EDC and sulfo-NHS were used as a zero length crosslinker between the dendrimer and aminated nanoparticle and between the dendrimer and whole antibody forming covalent bond. *Each 'R' group has 16 available carboxyl groups.*

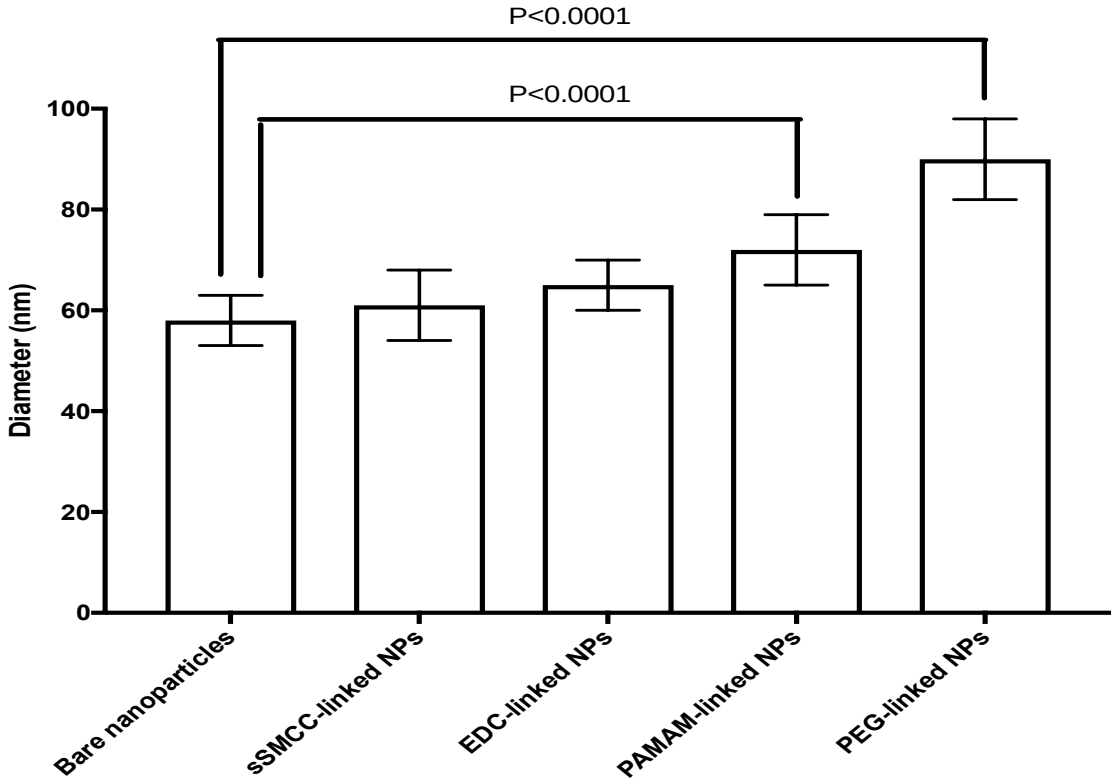

Figure 3. 15. Size difference of functionalised and bare nanoparticles.

Bare dye-doped silica nanoparticles compared to Affimer (conjugated via sSMCC, EDC and PEG) targeted nanoparticles and antibody targeted nanoparticles conjugated via PAMAM dendrimers. NP denotes: nanoparticle. Data denote diameter mean (SEM, n=5). Data are significantly different at P<0.0001.

3.3.7 In vitro analysis of binding specificity of targeted nanoparticles against colorectal cancer cells

The potential of each of the chemical linking strategies was assessed systematically and quantitatively to ascertain the success of targeted tumour-specific fluorescent imaging. The binding specificity of anti-CEA antibody was optimised previously within our group and identical methods were followed to confirm the findings. The ability of each anti-CEA Affimer functionalised

nanoparticles was then compared to anti-CEA antibody and control Affimer functionalised nanoparticles. The control nanoparticle was identical in structure and chemical properties to the anti-CEA functionalised nanoparticle and varied only in the Affimer specificity. Although bare nanoparticles have been used in other published studies as controls, their size, surface chemistry and charge are different which makes them inappropriate controls.

Confocal microscopy was used to quantify the fluorescence in two ways: a representative optical signal through the cell, and a maximum image projection (MIP) as described in **Chapter 2**. Data are expressed as the fold difference in fluorescence intensity between the cells incubated with control and anti-CEA functionalised nanoparticles.

3.3.8 Affimer functionalised fluorescent nanoparticles

First, the potential of each of the linking strategies for directing tumour-specific fluorescent imaging was quantitatively assessed. To do this, the ability of each conjugated nanoparticle type to direct binding to CEA-positive colorectal tumour cells *in vitro was compared*. In each case, binding directed by the anti-CEA Affimer was compared with a control anti-myoglobin Affimer. Anti-CEA and anti-myoglobin functionalised nanoparticles were incubated with LoVo cells to assess specific binding. PEG- and EDC-linked Affimer tagged nanoparticles failed to demonstrate significant Affimer-dependent tumour cell binding. PEG-linked particles produced poor signals whilst nanoparticles to Affimer conjugated using EDC showed very poor Affimer-dependent tumour cell binding, with only 1.1-fold greater binding of CEA-targeted nanoparticles as compared to control ($p=0.013$). Conjugation of Affimer carried out with sSMCC showed strong tumour-specific

targeting, with CEA-targeted nanoparticles demonstrating 3.2-fold greater fluorescence than control in the MIP analysis ($p<0.0003$); **Figure 3.16.**

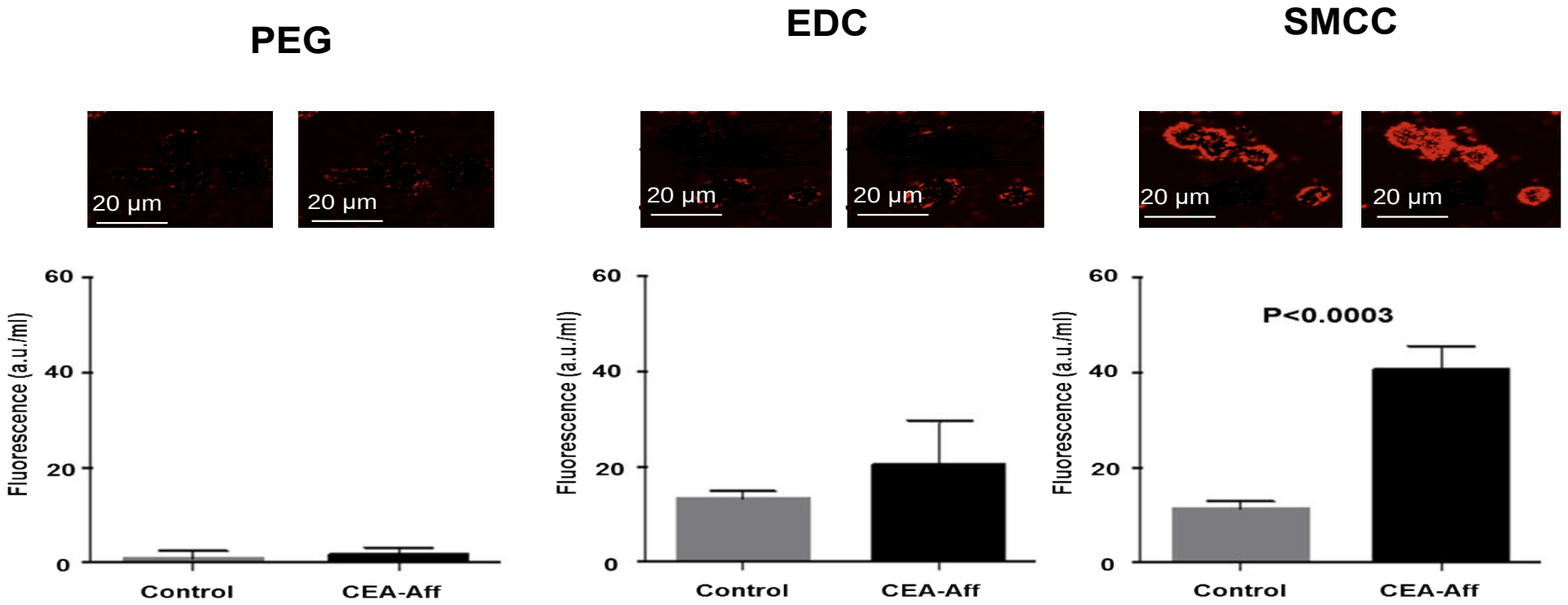

Figure 3. 16. Affimer conjugation of dye-doped silica nanoparticles using PEG, EDC or sSMCC.

LoVo cancer cells were incubated with either anti-CEA (CEA-Aff) or control anti-myoglobin Affimers II tagged nanoparticles. Images were collected using confocal microscopy and fluorescence was quantified. Representative maximum image projection images are shown. Data denote mean fluorescence (*SEM, n=5*). *Data are significantly different at p<0.0003.*

Having identified SMCC as the appropriate chemical linker to conjugate the Affimer to the surface of the nanoparticle, anti-CEA Affimer II and III, conjugated via SMCC to nanoparticles, were incubated with three different colorectal cell lines, each of which is known to express CEA at differing concentrations and HEK293 control cell line. LoVo cells show high level expression, LS174T cells moderate to high expression, HCT116 cells low expression, and HEK293 cells no expression of CEA (Ohannesian et al., 1995, Ashraf et al., 2009, da Paz et al., 2012, Fahlgren et al., 2003, Wang et al., 1999). Conjugation of Affimers via sSMCC allowed strong tumour-specific targeting, with CEA-targeted nanoparticles demonstrating 9-, 10.7- and 2.8-fold greater fluorescence than control in LoVo, LS174T and HCT116 cells respectively ($p<0.0002$) for the single slice analysis (**Figure 3.17-19**). Only data for single slice images were shown in the graphs. A similar pattern of successful CEA-targeted fluorescence was observed in the MIP analysis, with CEA-targeted nanoparticles demonstrating 3.3-, 4.4-, and 2.2-fold greater fluorescence than control particles in LoVo, LS174T, and HCT116 cells respectively ($p<0.0002$). There was no fluorescent signal seen when HEK293 cells were incubated with anti-CEA II and III or anti-myoglobin functionalised nanoparticles. The data are summarised in **Table 2 and 3**. Importantly, there were no differences in the fluorescent signal when comparing nanoparticles bearing anti-CEA Affimer II or III. Similarly, the mean fluorescence for anti-CEA Affimer functionalised nanoparticles was comparable to anti-CEA antibody functionalised nanoparticles. Anti-CEA antibody targeted nanoparticles via PAMAM dendrimer also showed high antibody-dependent tumour cell binding with 7.8-fold greater fluorescence than control in LoVo cells ($p<0.0002$) for the single slice analysis and 3.2-fold greater fluorescence than control particles in the MIP analysis ($p<0.002$).

In all three cell lines that I tested, anti-CEA Affimer targeted nanoparticles showed significantly greater fluorescence compared to non-targeted control nanoparticles. The time dependent nature of the fluorescence and the fact that it appeared to be cytoplasmic, suggests the fluorophore had been internalised by the cells.

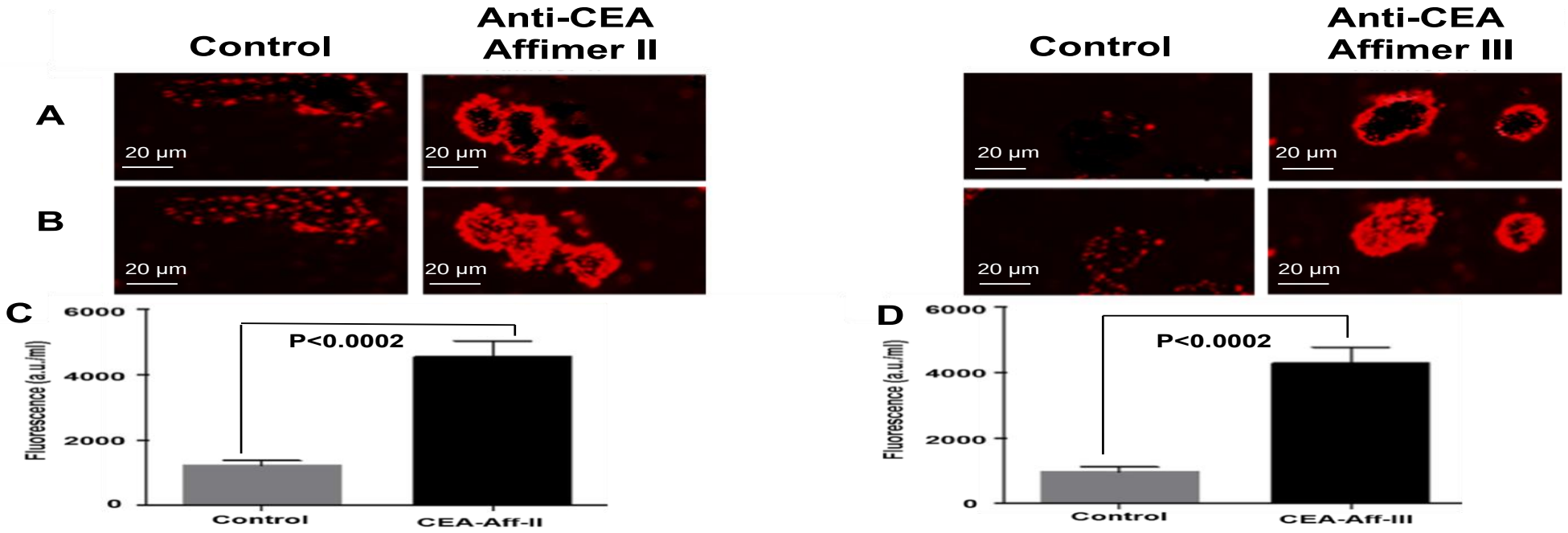

Figure 3. 17. Fluorescent imaging of LoVo cells using anti-CEA Affimer functionalised nanoparticles.

LoVo cancer cells were incubated with either anti-CEA Affimer II and III or control anti-myoglobin Affimers tagged nanoparticles. Images were collected using confocal microscopy and fluorescence was quantified. Panels A and B show single slice and maximum projection images respectively. Graphs C and D show quantification of fluorescent from single slice images (A). Data denote mean fluorescence (SEM, n=5). Data are significantly different at p<0.0002.

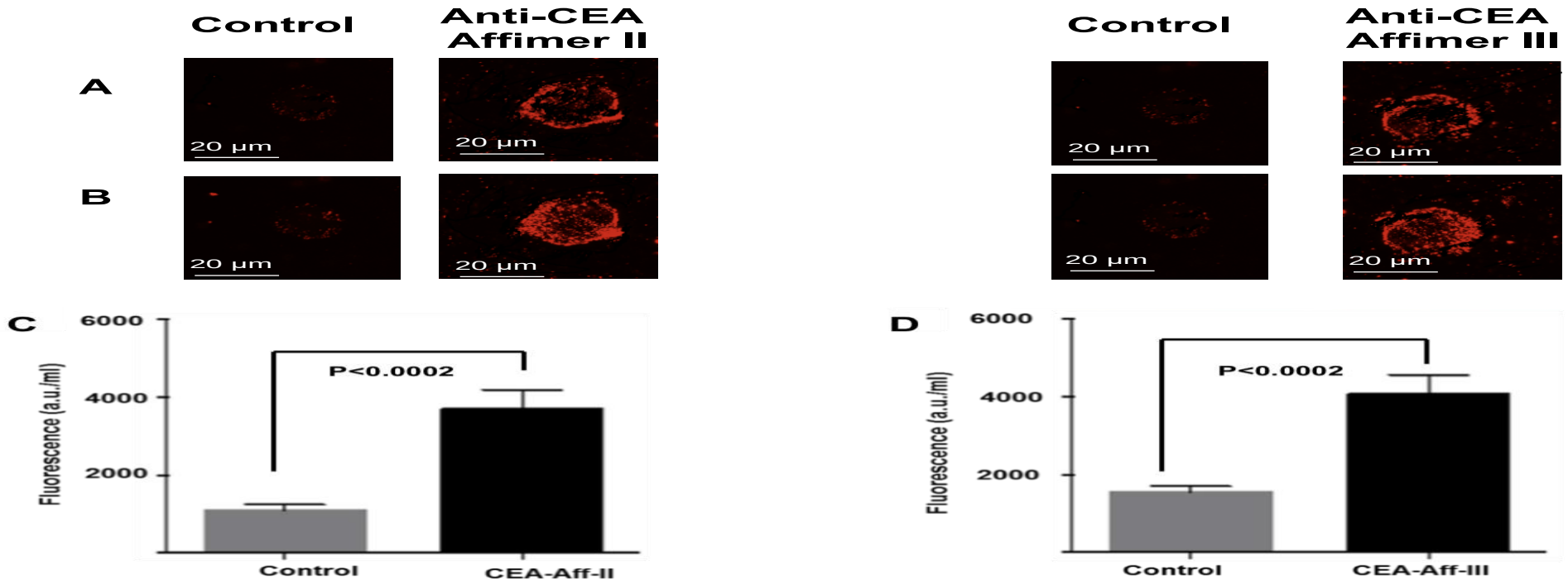

Figure 3. 18. Fluorescent imaging of LS174T cells using anti-CEA Affimer functionalised nanoparticles.

LS174T cancer cells were incubated with either anti-CEA Affimer II and III or control anti-myoglobin Affimers tagged nanoparticles. Images were collected using confocal microscopy and fluorescence was quantified. Panels A and B show single slice and maximum projection images respectively. Graphs C and D show quantification of fluorescent from single slice images (A). Data denote mean fluorescence (SEM, n=5). Data are significantly different at p<0.0002.

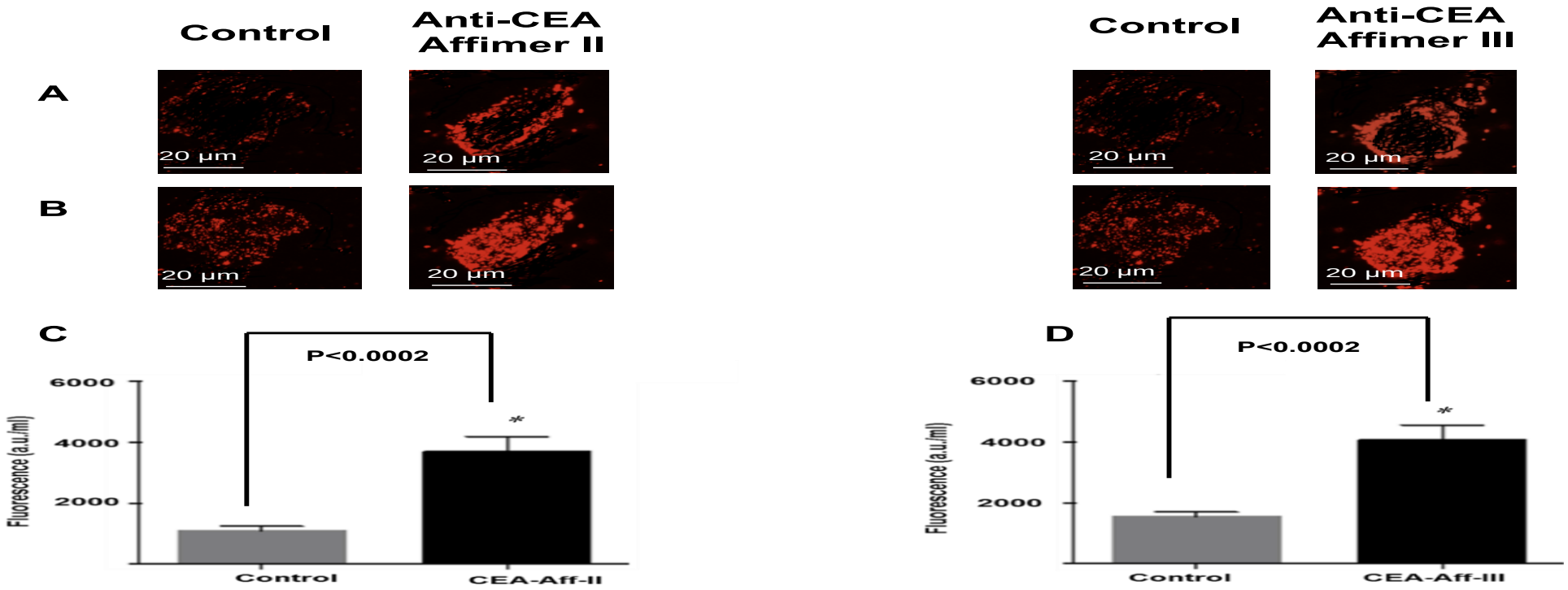

Figure 3. 19. Fluorescent imaging of HCT116 cells using anti-CEA Affimer functionalised nanoparticles.

HCT116 cancer cells were incubated with either anti-CEA Affimer II and III or control anti-myoglobin Affimers tagged nanoparticles. Images were collected using confocal microscopy and fluorescence was quantified. Panels A and B show single slice and maximum projection images respectively. Graphs C and D show quantification of fluorescent from single slice images (A). Data denote mean fluorescence (SEM, n=5). Data are significantly different at p<0.0002.

			Unpaired t-test				Mann-Whitney test			
			CEA targeted (Mean)	Control (Mean)	p value	Fold difference	CEA targeted (Median)	Control (Median)	p value	Fold difference
PEG	Single slice	LoVo	44.91	42.30	0.71	1.06	30.20	30.9	0.99	0.98
		LS174T	53.11	59.5	0.72	0.9	63.091	64.01	0.98	0.99
		HCT116	465.2	495.01	0.71	0.94	479.58	478.04	1	1
	MIP	LoVo	2.7	2.65	0.99	1.04	3.5	3.2	0.98	1.1
		LS174T	3.1	3.059	0.98	1.01	3.7	3.45	0.89	1.07
		HCT116	7.2	6.48	0.84	1.1	7.7	7.1	0.99	1.08
EDC	Single slice	LoVo	812.00	722.18	**0.013**	1.12	665.89	410.78	**0.016**	1.62
		LS174T	869.6	779.0	0.41	1.12	767.94	714.24	0.65	1.08
		HCT116	891.78	889.4	0.84	1	531.11	486.25	0.45	1.09
	MIP	LoVo	30.7	20.04	**0.013**	1.53	31.99	19.04	**0.014**	1.68
		LS174T	29.2	28.1	0.81	1.04	30.08	29.85	0.59	1
		HCT116	26.05	22.70	0.49	1.15	18.6	18.51	1	1
SMCC	Single slice	LoVo	3510.000	390.1	**0.0003**	9	3881.2	464.24	**0.0071**	8.4
		LS174T	1402.0	131.05	**0.002**	10.7	1311.5	128.03	**0.008**	10.24
		HCT116	2449.4	848.14	**0.0004**	2.8	2610.4	840.45	**0.008**	3.1
	MIP	LoVo	46.42	14.10	**0.0002**	3.3	52.4	17.61	**0.0071**	2.9
		LS174T	31.42	7.10	**0.0001**	4.4	29.22	6.56	**0.0071**	4.5
		HCT116	31.05	13.91	**0.0002**	2.2	36.74	12.89	**0.0072**	2.9

Table 3. 3. Summary of *in vitro* fluorescent quantification analysis of anti-CEA Affimer II functionalised dye-doped silica nanoparticles binding.

Data from control and test experiments were compared using both parametric and non-parametric statistical analyses. Bold numbers represent statistical significance. CEA targeted: Anti-CEA Affimer II dye-doped silica nanoparticles; control: Anti-myoglobin dye-doped silica nanoparticles.

			Unpaired t-test				Mann-Whitney test			
			CEA targeted (Mean)	Control (Mean)	p value	Fold difference	CEA targeted (Median)	Control (Median)	p value	Fold difference
PEG	Single slice	LoVo	45.11	41.00	0.694	1.1	30.97	30.87	0.98	1
		LS147T	51.45	61.2	0.78	0.84	61.89	64.44	0.88	0.96
		HCT116	441.9	486.21	0.655	0.91	480.88	478.32	0.89	1
	MIP	LoVo	2.9	2.6	0.97	1.11	3.1	3.09	0.99	1
		LS174T	3.3	3.09	0.98	1.07	3.45	3.21	0.89	1.07
		HCT116	6.5	5.87	0.765	1.11	7.45	6.99	0.78	1.07
EDC	Single slice	LoVo	845.00	768.18	**0.0127**	1.1	678.45	397.78	**0.0149**	1.71
		LS174T	877.6	798.0	0.39	1.1	779.4	678.45	0.45	1.15
		HCT116	891.78	889.4	0.79	1	542.91	389.14	0.09	1.4
	MIP	LoVo	30.9	19.80	**0.0142**	1.5	32.19	19.44	**0.0125**	1.66
		LS174T	28.9	27.9	0.49	1.04	31.15	29.72	0.419	1.05
		HCT116	26.4	19.40	0.219	1.4	18.9	17.11	0.78	1.1
SMCC	Single slice	LoVo	3502.000	389.1	**0.0003**	9	3876.4	450.74	**0.0071**	8.6
		LS174T	1380.0	125.5	**0.002**	11	1299.5	116.03	**0.0072**	11.2
		HCT116	2465.7	850.24	**0.0004**	2.9	2590.9	835.77	**0.0079**	3.1
	MIP	LoVo	47.69	14.90	**0.0002**	3.2	51.8	17.86	**0.0071**	2.9
		LS174T	30.12	6.85	**0.0001**	4.4	29.71	6.063	**0.0071**	4.9
		HCT116	31.50	13.125	**0.0002**	2.4	35.45	11.44	**0.0072**	3.1

Table 3. 4. Summary of *in vitro* fluorescent quantification analysis of anti-CEA Affimer III functionalised dye-doped silica nanoparticles binding.

Data from control and test experiments were compared using both parametric and non-parametric statistical analyses. Bold numbers represent statistical significance. CEA targeted: Anti-CEA Affimer III dye-doped silica nanoparticles; control: Anti-myoglobin dye-doped silica nanoparticles.

It is therefore concluded that anti-CEA Affimer functionalised dye-doped silica nanoparticles, using sSMCC for effective coupling, allowed tumour cell-specific fluorescent targeting *in vitro*. This is the first successful and sufficiently controlled use of targeted fluorescent nanoparticles using Affimers for *in vitro* colorectal cancer imaging.

3.4 Discussion

The data presented in this chapter are the first to demonstrate specific, *in vitro* imaging of colorectal cancer cells using Affimer-targeted fluorescent nanoparticles. A nanotechnological approach was utilised to concentrate a fluorescent dye within the core of silica nanoparticles then directed against the CEA on tumour cells using synthetic binding protein Affimer. To achieve this, a number of distinct steps were formulated that allowed a logical progression from a hypothesis to *in vitro* testing with successful outcomes.

The challenge in developing a targeted nanoparticle against a specific tissue is to produce a stable detection probe with reliable binding properties between the bioreceptor on the nanoparticle surface and the target tissue. CEA was selected as the target tissue because it has been shown to be a robust tissue biomarker for colorectal cancer (Tiernan et al., 2013). The characteristic features of dye-doped silica nanoparticles are fit for purpose here as they are sufficiently small, easy to synthesise, non-toxic, can be functionalised with targeted proteins and are cheap to mass produce (Guillou et al., 2005a, Santra et al., 2001, Tiernan et al., 2015). Silica nanoparticles can be made by a variety of routes, which may be categorised into “chemical” or “physical”. However, the main two methods are: the Stober method or the water-in-oil reverse microemulsion method. The latter was used in this project because it produces monodispersed nanoparticles with well-controlled diameter below 100 nm (Bagwe and Khilar, 2000, Bagwe et al., 1999). The silica core is hydrophilic and suitable for water-soluble dyes in order to make a stable core as the electrostatic interaction of positive dye with the negatively-charged silica molecules is an important factor for stability. Our group had a significant experience with manufacturing NIR664-doped silica nanoparticles that allowed consistent production of the optimised nanoparticles.

Having synthesised the dye-doped particle, the surface was modified through attachment of an amino-silane to make amine groups available for conjugation to antibody/Affimer. Amination of the particles was required for all of the tested linking strategies. Quantification of the number of amine groups on the surface on the nanoparticles can be achieved using several assays. Some of these traditional assays rely on absorbance or fluorescence measurement (Habeeb, 1966) but would not be ideal for the current project as the amine groups are located on a fluorescent particle that would distort the results via light scattering. Accordingly, the methodology to quantify amine groups in fluorescent nanoparticles was employed and showed effective loading of amine groups (Chen and Zhang, 2011).

3.4.1 Anti-CEA Affimer as a targeting bioreceptor

Antibodies have very high specificity to the antigens and recognise a defined molecular structure (epitope) (Haggarty et al., 1986). When considering an alternative binding protein to antibody, high affinity and specificity are key parameters. The relationship between specificity and affinity in anti-CEA antibody to CEA interactions has been investigated extensively (Muraro et al., 1985, Haggarty et al., 1986, Bosslet et al., 1985, Byers et al., 1988). Antibodies are enriched with amino acids residues containing aromatic side chains such as tyrosine, tryptophan and phenylalanine which are surrounded by short-chain hydrophilic side chains (aspartate, asparagine, serine, threonine and glycine). The highly structured amino acids organisation of antibody plays an important role in attaining the conformation which accounts for its high affinity binding (Koide and Sidhu, 2009, Peng et al., 2014). This phenomenon occurs in other synthetic binding proteins such as nanobody and monobodies as these residues present favourable interaction with the epitope surface (Sha et al., 2017b). Of

interest, all anti-CEA Affimers contain these amino acids in each variable region with approximately 44% frequency as shown in **Table 2.1**. Apart from the chemical properties of epitopes that contribute to the protein-protien interaction, Affimer has many other advantages over antibody. The advantages of using Affimers is that a uniform protein can be produced by a cheaper and less complicated process, which enable long-term availability. In addition, their compact size when compared to antibodies, allow more stable conjugation to nanoparticles which inevitably improve the binding affinity and avidity (Tiede et al., 2014b). So far, Affimers have been able to bind to around 60 target molecules, including CEA (Kyle, 2018). Affimers are expressed in *E.coli* with no animals used for production. This makes Affimers more ethically sound and in keeping with the National Centre 3Rs principles (replacement, refinement and reduction) of animals in research. The average cost for 1 ml (50 µg/ml) of human anti-CEA antibody is ~£275 whereas the cost for producing 5 ml (3 mg/ml) of anti-CEA Affimer is less than £100. On a mass scale, the Affimer offers a substantial cost effectiveness when compared to antibody, an important criterion for clinical application in the future. Since anti-CEA Affimers would be used as bioreceptors in developing a targeted fluorescent nanoparticle, extensive characterisation was crucial, particularly in regard to specificity of the Affimers against CEA.

Results from Affimer-fluorescence analysis demonstrated that all three anti-CEA Affimers were highly specific to CEA secreted on LoVo cell surface and no binding was observed in control HEK293 cells. These results matched the tumour-specific fluorescence of LoVo, LS174T and HCT116 cell lines when targeted by anti-CEA antibody functionalised silica nanoparticles (Tiernan et al., 2015) and in accordance with CEA being membrane–anchored glycoprotein (Tiernan et al., 2013). To date, no reports on anti-CEA Affimer being conjugated

to nanoparticles for fluorescent imaging in colorectal cancer. Kaushal *et al (Kaushal et al., 2008a)*, used anti-CEA antibody-AlexaFluor488 conjugate for targeted fluorescent imaging of colorectal cancer cells LoVo, HCT116, SW948, LS174T, HT29 and SW480 *in vitro*. Interestingly, only LoVo, HCT116, SW948, and LS174T cancer cell lines expressed CEA as identified by antibody staining. HT29 and SW480 cell lines were reported to be CEA-expressing negative due to weak antibody-based fluorescence above background. However, the authors did not describe a systematic method for quantification of antibody-based fluorescence and confined the definition of CEA expression in these cells to being CEA-expressing positive. In addition, their study lacked control cell line and control antibody. In sharp contrast, Boonstra *et al* (2015), showed high CEA expression in LoVo, SW480 and HT29 cancer cell lines when targeted by fluorescein-conjugated anti-CEA antibody in flow-cytometry, immunohistochemical and immunofluorescent analysis (Boonstra et al., 2015). They also found HCT116 cell line to have low CEA expression, which is in keeping with our findings. There are plethora of recombinant anti-CEA antibodies that have been engineered for imaging and therapy of colorectal cancer such as single chain Fv (scFv, ~25 kDa) (Graff et al., 2004, Pavoni et al., 2006), single chain antibody (scAb), diabody (Db, ~50 kDa) (Mølgaard et al., 2017), nanobodies (Leung, 2012) and bispecific antibody (Yazaki et al., 2012).

Anti-CEA Affimers showed specific binding to CEA in different forms including secreted CEA by LoVo cells and commercially available native protein. Collectively, these results justified using anti-CEA Affimer as an alternative bioreceptor to anti-CEA Antibody.

3.4.2 Affimer chemical linkage strategies

To covalently link two compounds, it is first necessary to understand the reactive groups that are present in each of them. Next, it is required to choose the most appropriate crosslinker to participate in the selected conjugation reaction. The selection of potential chemical linkers to conjugate the Affimer onto the nanoparticle was based on both published and novel techniques. Three linking strategies were employed including PEG, EDC and sSMCC in an effort to control the orientation of the Affimer and therefore increase sensitivity while reducing steric hindrance.

PEG is hydrophilic co-polymer that consists of repeating units and in variable range of lengths (Harrison et al., 2016). Bifunctional PEG linkers are capable of conjugating amine groups to sulfhydryl groups and therefore offer oriented conjugation hence it was tested. PEGylated gold nanoshells were one of the first models to successfully harness the potential of metallic nanoparticles for use in photothermal ablation therapy (Hirsch et al., 2003). PEG had been successfully used to conjugate tumour-necrosis-factor-alpha (TNF) antibody to gold nanoparticles with mean diameter ~ 34 nm and resulted in a significant reduction in tumour volume and enhanced survival in MC38 colorectal tumour-burdened C57/BL6 mice (Paciotti et al., 2004, Lipka et al., 2010, Libutti et al., 2010).

PEG linking failed to demonstrate any Affimer-dependent cell binding as show in the present study. Varying experimental conditions were employed in attempt to discover the cause of this. We hypothesised that some of the amine groups of the nanoparticles were not bound to the PEG linker. Two different methods were tested including: PEG to nanoparticle initially or PEG to Affimer initially before attaching the second component. Different concentrations, media pH and

solvents were also employed but all failed to produce any successful tumour specific imaging. PEG decreases the amount of attraction between nanoparticles by increasing the steric distance between them and increasing hydrophilicity via ether repeats forming hydrogen bonds with solvent. PEG linked nanoparticles measured ~100 nm in diameter. The relative size of the particles means there are likely to be unbound antigen sites between adjacent bound particles. Steric hindrance, where the size of the nanoparticle-Affimer complex, the location and orientation of the Affimers on the surface, and the relative density of the antigen on the cell membrane can all reduce binding specificity (Lu et al., 1996, Jie et al., 2011). Yoon *et al* (2005), fabricated cobalt ferrite magnetic nanoparticles coated with a shell of amorphous silica (MSN), which contained luminescent rhodamine B isothiocyanate or fluorescein isothiocyanate on the inside of the silica shell (Yoon et al., 2005). Then, they attached PEG on the outside of silica shell to compare the efficiency of uptake into MCF7 breast cancer cells the particles with and without PEG modification. Attachment of PEG did not significantly change the size of their nanoparticles, but we observed 1.8-fold increase in silica nanoparticles size when conjugated to PEG. They also reported that PEGlation of the MSN increased internalisation into lung cancer cells (A-549), and breast cancer cells (MCF-7) but also into control mammalian lung normal cells (NL-20). The unwanted internalisation into control cells is a common problem with untargeted nanoparticles despite PEG functionalisation. On the other hand, Yoo *et al* (2004), used PEG to conjugate folate as a bioreceptor to doxorubicin to form a nano-aggregates with an average size of 200 nm in diameter (Yoo and Park, 2004). Doxorubicin and folate were respectively conjugated to a- and N-terminal end group of a PEG chain. The doxorubicin nano-aggregates showed a greater extent of intracellular uptake against folate-receptor-positive cancer cells than

folate-receptor-negative cells, suggesting folate-receptor-mediated endocytosis. The nano-aggregates also exhibited more potent cytotoxic effect on epidermal nasopharyngeal carcinoma cancer cell line KB and lung cancer cell line A549 than free doxorubicin. Therefore, PEG linkers are appropriate for a liposome nanoparticle but may fail when deployed to solid, metallic nanoparticles as liposomal nanoparticles better mimic naturally circulating entities and, thus, may not require as stringent of a PEGylation protocol. Nanoparticle composition is the most important consideration when selecting a PEG conjugation approach (Jokerst et al., 2011).

EDC has been used to conjugate whole IgG antibodies to silica nanoparticles (Zhao et al., 2004, Wu et al., 2008) for tumour targeting *in vitro*. It is used to conjugate carboxyl and amine groups and is known as a zero-length cross-linker due to the 'leaving group'. However, crosslinking is essentially randomly oriented. EDC linking demonstrated tumour-specific binding, but with low effect (fold increase ~1) in LoVo cells only. Although EDC seems to have been the most popular chemical linker for conjugating antibody to nanoparticles, here it failed to demonstrate a significant tumour-specific imaging. Control EDC-linked nanoparticles produced high levels of non-specific fluorescence too. Researchers reported that EDC forms an unstable O-acylisourea ester that is prone to fast hydrolysis and regeneration of the carboxyl (Tiernan et al., 2015, Gubala et al., 2010). The unstable chemical linkage could lead to increased level of unbound anti-CEA Affimer to the surface of nanoparticle and the fluorescence observed was due to nanoparticles being very sticky to cells surface as shown in the control group. In attempt to reduce the non-specific binding of control nanoparticles and after Affimers were conjugated to the surface, succinic anhydride was used to convert remaining free amine (positively charged) groups into negatively charged

carboxylates. No difference in fluorescence was observed despite this step and attempting this prior to Affimer incubation would prevent their conjugation. In a recent study, doxorubicin-loaded mesoporous silica nanoparticles were targeted against the epithelial cell adhesion molecule (EpCAM) in colon cancer cells SW620 with aptamer (Xie et al., 2016). The aptamer functionalised nanoparticles were synthesised by EDC/NHS amide coupling reaction between carboxyl modified particles and amino modified aptamer with mean diameter ~ 180 nm. The targeted nanoparticles increased cellular uptake and increased cytotoxicity of doxorubicin in SW620 but not in Ramos human B lymphoma control cells when compared to nanoparticles without aptamer on the surface. However, the authors did not describe whether the control particles were bare nanoparticles or EDC functionalised but without aptamers. Their synthesis protocol involved 12 h incubation period of NHS, aptamer and EDC activated nanoparticles mixture and the final particles were obtained by centrifugation at 15,308 xg at 4 °C. Our incubation period was only 2 h and the centrifugation to remove unbound molecules was 10,000 xg. The shorter incubation period of the nanoparticles mixture might suggest reduced number of bound Affimers despite the low absorbance readings following the 3 washing steps. Further optimisation of the EDC linkage protocol in our study could potentially improve the efficacy of Affimer conjugation to nanoparticles.

SMCC is a heterobifunctional linker that can react with the aminated nanoparticle surface to form a stable amide bond with a maleimide group that can then be conjugated to the free sulfhydryl group on the Affimer. A number of published reports described linking a reduced antibody to a quantum dot using SMCC and iron oxide (Abdolahi et al., 2013, Tiwari et al., 2009). sSMCC linking allowed strong tumour-specific imaging across all colorectal cancer cell lines. The figures

for fluorescence fold difference correlated with the relative expression of CEA for each cell line, but importantly it is also the level of non-specific fluorescence for control nanoparticles that dictates the highest fluorescence fold change that was seen in LS174T. However, it is difficult to draw any conclusions regarding the relationship between targeted-nanoparticle-induced fluorescence and cell surface antigen density. Gubala *et al* (Gubala et al., 2010) reported successful functionalisation of dye-doped silica nanoparticles with goat anti-human IgG using sSMCC. Although they reported a significant increase in nanoparticle diameter to ~200 nm following the conjugation process, their bare nanoparticles size was ~ 100 nm when compared to ~ 50 nm in our report. In addition, Affimers are 10 times smaller than antibodies which also accounts for the size difference observed. Control sSMCC-linked particles produced low levels of non-specific fluorescence. We hypothesised that a proportion of amine groups on the particle surface may not be bound to SMCC linkers and may be creating a positive surface charge leading to non-specificity in the control group. However, there was significant difference in fluorescence between CEA-Affimer dependent cell binding and control Affimers. The conjugation process used in this chapter proved to be stable and effective for functionalising the Affimers on the surface of the nanoparticles. However, the techniques for each surface modification (amination or carboxylation) and subsequent conjugation process (PAMAM or SMCC) can be further optimised by controlling different factors such as temperature, media pH, antibody/Affimer to nanoparticles ratio and so on. For the purpose of this project this appeared to be exhaustive and infeasible where testing nanoparticles in a cellular system will yield a huge number of variables.

3.5 Conclusion

It is concluded that the purified anti-CEA Affimer is specific to CEA and when it is linked to dye-doped silica nanoparticles using sSMCC it can be targeted against CEA-expressing colorectal cancer cells for *in vitro* imaging. The successful targeted delivery of the nanoparticle to colorectal cancer cells lends itself to be an ideal vehicle to replace the dye with a molecule that can allow fluorescent imaging and cytotoxic effect simultaneously. Functionalisation of the nanoparticle with a photosensitiser is an appealing option to make it a true multi-functional theranostic nanoparticle which will be the subject of **chapter 4**.

Chapter Four

Anti-CEA Affimer targeted, Foslip-loaded silica nanoparticles successfully deliver PDT to colorectal cancer cells

4 Anti-CEA Affimer targeted, Foslip-loaded silica nanoparticles successfully deliver PDT to colorectal cancer cells

4.1 Abstract

Background

Targeted delivery of photosensitisers by functionalised nanoparticles is an appealing strategy to increase the efficacy of their photodynamic therapy and reduce side effects. Meso-tetra(hydroxyphenyl)chlorin (mTHPC) is one of the most potent photosensitisers against cancers and is clinically approved for treatment of head and neck cancer in Europe. The aim of this chapter was to encapsulate mTHPC (Foslip) inside silica nanoparticles and test its targeted fluorescent imaging and phototoxic effect on colorectal cancer cells *in vitro*.

Methods

Foslip was encapsulated inside silica nanoparticles using the water-in-oil microemulsion technique. Mixture of anti-CEA (II and III) or control anti-myoglobin Affimers were then conjugated to the surface of the particles via sSMCC. Colorectal cancer cells (LoVo, LS174T and HCT116) and control HEK923 cells were incubated with CEA-targeted or control nanoparticles for 24 h then washed. Fluorescent imaging of cell lines was quantified using confocal microscopy. Cells were also photo-irradiated with 0.45 J/cm^2 to allow photodynamic therapy while cell death post irradiation was quantified using MTT and ROS generation assays.

Results

Anti-CEA Affimer-functionalised Foslip-loaded silica nanoparticles showed strong tumour-specific targeting with 9.5, 10.2- and 3.5-fold greater fluorescence than control-Affimer targeted nanoparticles in LoVo, LS174T and HCT116 cells respectively ($p<0.0001$). Cellular uptake of anti-CEA Affimer targeted nanoparticles was time and dose dependent in colorectal cancer cells ($p<0.0001$). At 2 mg/ml of anti-CEA Affimer-functionalised Foslip-loaded silica nanoparticles concentration, significant cell death rate was observed in LoVo (70%), LS174T (80%) and HCT116 (65%) when compared to HEK293 (0%) ($p<0.0001$) following photo-irradiation. The cytotoxic effect seen in the PDT results was Foslip-mediated via ROS generation.

Conclusion

Anti-CEA Affimer-functionalised Foslip-loaded silica nanoparticles allowed tumour-specific fluorescent imaging and cellular death of colorectal cancer cells *in vitro*.

4.2 Introduction

Personalised surgery focuses on tailoring the surgical approach to the individual characteristics and needs of patients at all levels of management. Fluorescence guided surgery has the potential to offer surgeons the ability to visualise positive lymph nodes, tumour margins and distant metastasis intra-operatively. Based on the fluorescent visualisation, the surgical resection can then be stratified according to the patient's specific disease progression. Simple fluorescent molecular probes for intra-operative cancer imaging have been designed previously using fluorophores conjugated to tumour-specific antibodies. Several near infrared dyes including Oregon Green Thermo (Thermo-Fisher, Massachusetts, USA), Cy7, IRDye 800CW (Li-Cor, Nebraska, USA) and Rhodamine have been evaluated in murine models of colorectal (Kaushal et al., 2008b, Zou et al., 2009a), pancreatic (Kaushal et al., 2008b), breast (van Scheltinga et al., 2011, Wu et al., 2013) and head and neck cancers (Heath et al., 2012, van Scheltinga et al., 2011). The fluorophores were conjugated to tumour specific antibodies for fluorescent labelling of tumours. Although the probes allowed fluorescent imaging of tumour tissue, the fluorescent signal appeared to be low when non-specific background fluorescence was taken into account. Despite these initial studies in 2008, none of the probes have been translated to the operating theatre and there has been no progress beyond mouse models.

We have shown that anti-CEA Affimer functionalised dye-doped silica nanoparticles allow specific fluorescent imaging of colorectal cancer cells *in vitro* and the system warrants further evaluation in an animal model. If we can deliver the fluorescent dye to colorectal cancer cells for visualisation then there is a strong argument to deliver a therapeutic agent in a theranostic nanoparticle. The

rationale would be to kill residual tumour cells that are not removed and act as the source of local cancer recurrence following surgery with curative intent.

Photodynamic therapy (PDT) is an attractive alternative in the treatment of malignant diseases and might benefit from nanosystems to enhance drug delivery to tumour tissue (Gary-Bobo et al., 2012, Bechet et al., 2008, Chatterjee et al., 2008). Photosensitisers (PSs) are ideal candidates to be delivered as a therapeutic drug using nanoparticles, because the PDT-mediated killing of cancer cells is due to the cytotoxic reactive oxygen species (ROS) generated after its activation by an external light (Tada and Baptista, 2015, Yu et al., 2016). As a result, there is no need to release the PS from the nanoparticle to achieve the therapeutic effect, unlike chemotherapeutic agents (Abrahamse and Hamblin, 2016, Brown et al., 2004). Therefore, no controlled release mechanism needs to be designed, provided the nanoparticle is porous and transparent to allow light and molecular oxygen to reach the photosensitiser in the core and ROS to diffuse out. The majority of photosensitisers only meet some of these criteria due to their low water solubility and the difficulty in conjugation to antibodies (Agostinis et al., 2011, Dolmans et al., 2003). An ideal photosensitiser should have good efficacy (dependent upon the triplet state lifetime τT and the triplet quantum yield (ΦT) of the photosensitiser) for PDT while minimising side effects and should meet the following criteria:

I. Chemical purity; constant composition that will induce a reliable PDT treatment;

II. Tumour selectivity;

III. Fast accumulation in target tissue;

IV. Rapid clearance from circulating system;

V. Activated at NIR wavelength;

VI. No dark toxicity;

Several studies have reported the use of nanoparticles loaded with photosensitiser for photodynamic therapy such as liposomes (Buchholz et al., 2005, de Visscher et al., 2010), polymerosomes (Gao et al., 2007), gold (Cheng et al., 2008) and silica nanoparticles (Kim et al., 2007, Ohulchanskyy et al., 2007, Roy et al., 2003, Compagnin et al., 2009) to overcome the limitations of photosensitiser only systemic administration. Although these nanoparticles improved tumour specific accumulation, they still suffered from rapid up take by the phagocytic system.

Silica based nanoparticles appear to be superior to other systems for carrying photosensitisers because they are transparent to light, photochemically inert, compatible with biological systems, relatively easy to synthesise and functionalise and the porous shell allows the diffusion of ROS out of the core (Compagnin et al., 2009, Yan and Kopelman, 2003, Gary-Bobo et al., 2012). We therefore aimed to evaluate the potential of substituting the NIR664 dye used in the previous chapter with a photosensitiser and evaluate its theranostic capabilities against colorectal cancer cells.

The aims for this part of the PhD project were to:

I. Manufacture photosensitiser encapsulated silica nanoparticles;

II. Conjugate anti-CEA and control Affimers to the surface of the nanoparticle;

III. Assess the ability of the nanoparticle to bind to tumour cells *in vitro* and the specificity of fluorescent signal;

IV. Assess the efficacy of PDT-mediated cytotoxic effect of photosensitiser loaded nanoparticles on tumour cells;

V. Assess the mechanism of PDT-mediated cytotoxic effect of the nanoparticles on the tumour cells.

The photosensitiser was selected to be encapsulated inside the core of silica nanoparticle which was water-soluble meta-tetra(hydroxyphenyl)chlorin (mTHPC) Foslip. Foslip belongs to the second generation of photosensitisers and 100 times more potent than first generation such as Photofrin. Foslip produces a PDT effect with low drug concentration and low light dose, with negligible dark toxicity (Josefsen and Boyle, 2012). In clinical PDT, mTHPC is applied at a very low drug dose (0.15 mg/ kg) and light intensity (order of 10 J/cm2), resulting in a total PDT dose (light dose x PS dose) >100 times lower as compared to other clinically approved photosensitisers, such as haematoporphyrin derivatives (Savary et al., 1998, Savary et al., 1997) and Photofrin (Ball et al., 1999). Along with Photofrin, mTHPC is the only other photosensitiser approved for use in systemic cancer therapy (Yakavets et al., 2019b). In 2001, mTHPC was approved in the European Union and used as a solvent-based formulation (Foscan®; Biolitec Research GmbH, Jena, Germany) for the palliative treatment of head and neck cancers (Senge and Brandt, 2011). In addition, mTHPC has been successfully used for the treatment of early squamous cell carcinoma (de Visscher et al., 2013, Jerjes et al., 2011), basal cell carcinoma (Betz et al., 2012), biliary tract carcinoma (Wagner et al., 2015), prostate (Swartling et al., 2016),

pancreatic cancer (Huggett et al., 2014) and non-melanoma skin cancers (Horlings et al., 2015). In colorectal cancer, the application of mTHPC has not progressed beyond pre-clinical studies.

4.3 Results

4.3.1 Optimisation of experimental conditions for Foslip induced fluorescence

The aim was to optimise the experimental conditions for soluble Foslip before encapsulating it inside silica nanoparticles to confirm the fluorescence spectrum and PDT-cytotoxic efficiency against colorectal cancer cells. It would also inform the experimental conditions for Foslip encapsulation in silica nanoparticles and serve as an additional control.

4.3.1.1 Foslip concentration in colorectal cancer cells

To determine the optimum concentration of Foslip induced fluorescence, representative human colon cancer cells lines (LoVo, LS174T and HCT116) were seeded in 6-well plates in phenol red and FCS free media then incubated with various concentrations of Foslip (0 nM – 250 nM) for 24 h while control cells were incubated with media only. Fluorescence intensity was read using appropriate excitation (λ_{ex}= 420 nm) and emission (λ_{em} = 652 nm) for Foslip. **Figure 4.1** shows Foslip induced fluorescence with increasing doses of Foslip, showing a dose dependent response, seen to plateau and fall at 200 nM in all cell lines. Foslip induced greater fluorescence intensities in moderately and well differentiated cell lines, LS174T and HCT116, while poorly differentiated and metastatic cell line LoVo, showed lower fluorescence intensities. The variation in fluorescence intensities observed in colorectal cancer cell lines might be due to biological and genomic variations of colon cancer cells. Foslip at a concentration of 150 nM induced fluorescence in all cell lines in comparison to the untreated control. Therefore, this dose of Foslip was used as a baseline for further experiments.

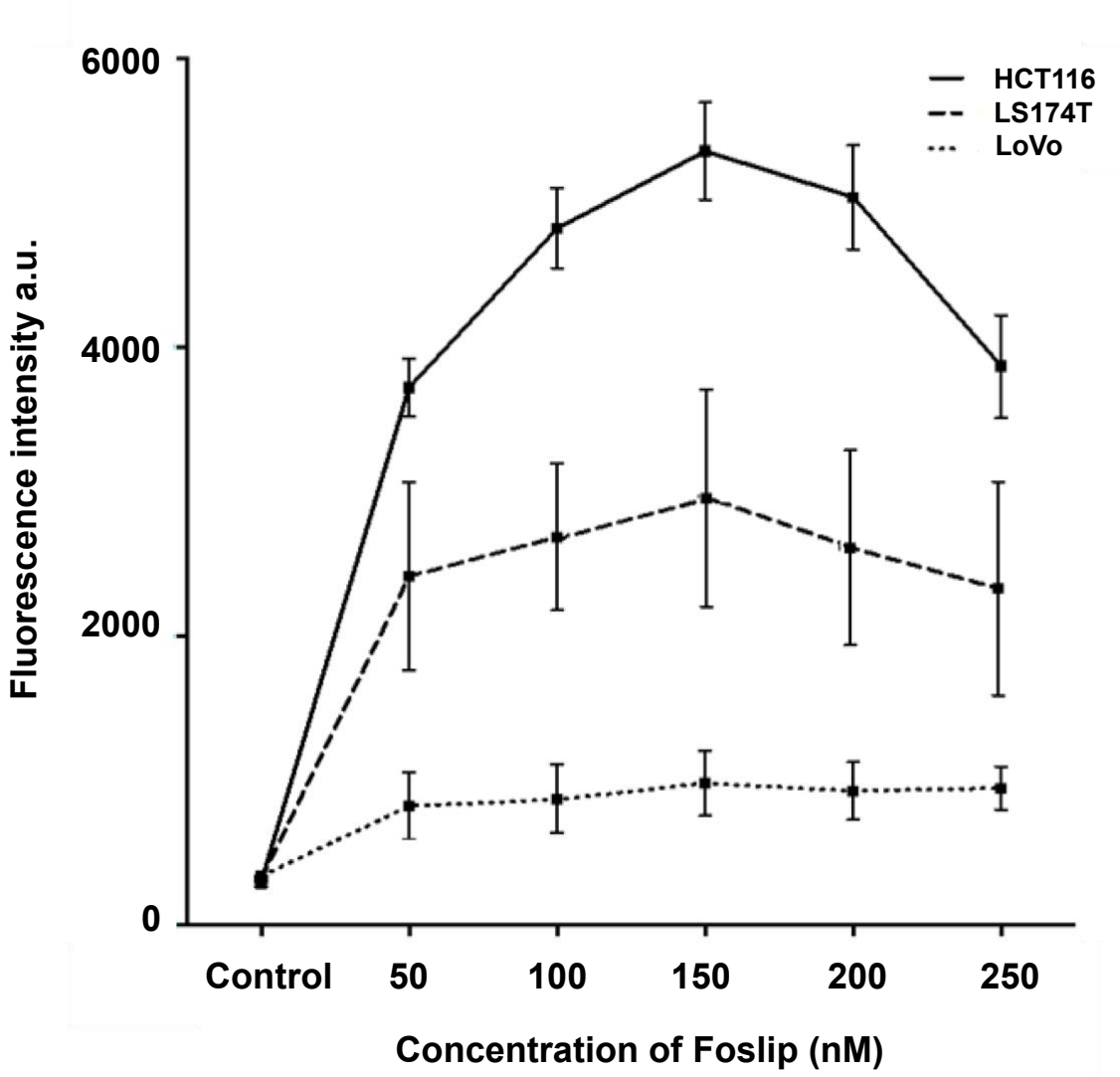

Figure 4. 1. Foslip induced fluorescence in colorectal cancer cells with optimum dose at 24 h incubation.

Foslip induced fluorescence was measured after incubating LoVo, LS174T or HCT116 cells for 24 h at Foslip concentration 0-250 nM. Data denote fluorescence mean from 3 separate biological experiments, each with 4 technical replicates, (SEM). Control represents cells treated with FBS and phenol free RPMI media.

4.3.1.2 Foslip incubation period in colorectal cancer cells

A similar method was used to determine the optimum incubation period for Foslip. Cells were incubated with 150 nM Foslip for various time periods (1 – 48 h) and then fluorescence emission was analysed. **Figure 4.2** shows Foslip induced fluorescence with increasing incubation periods in 150 nM Foslip, showing a time dependent response. LS174T and HCT116 cell lines exhibited the greatest fluorescence readings but in all cell lines incubation with 150 nM Foslip for 24 h gave the maximum fluorescence. Therefore, 24 h incubation time point was used as a baseline for further experiments. After 24 h incubation period, Foslip induced fluorescence plateaued then decreased after 30 h in all cell lines.

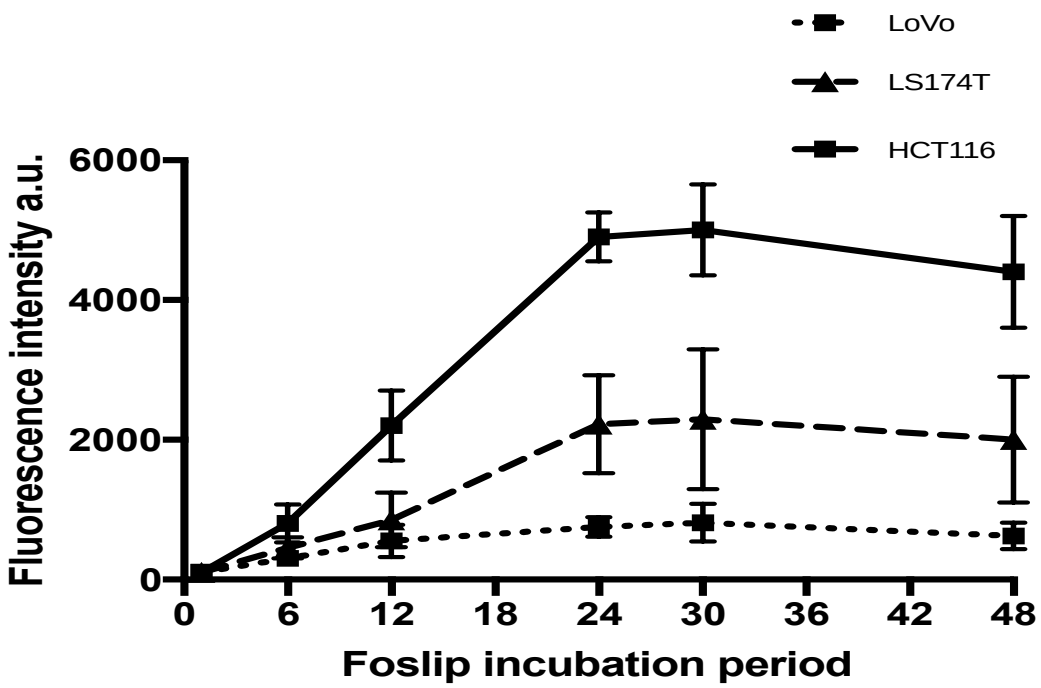

Figure 4. 2. Foslip induced fluorescence at 150 nM with optimum incubation period.

Foslip induced fluorescence was measured after incubating LoVo, LS174T or HCT116 cells with 150 nM Foslip concentration for 0-48 h. Data denote fluorescence mean from 3 biological experiments, each with 4 technical replicates, (SEM). Control represents cells treated with FBS and phenol free RPMI media.

4.3.1.3 Foslip induced fluorescence intensity in non-tumour cells

Next, the aim was to explore the potential for selective accumulation of Foslip in malignant cells. Therefore, two non-tumour cell lines including HEK293 cell line and breast cancer associated fibroblast (CAF) cell line were grown to a monolayer on collagen coated 6-well plates in phenol red and FCS free media then incubated with 150 nM of Foslip for 24 h. **Figure 4.3** showed that the non-tumour cell lines produced similar fluorescence intensities to the poorly differentiated and metastatic (LoVo) colon cancer cell line. The data suggest that higher Foslip fluorescence signals are not only observed in tumour cells *in vitro.*

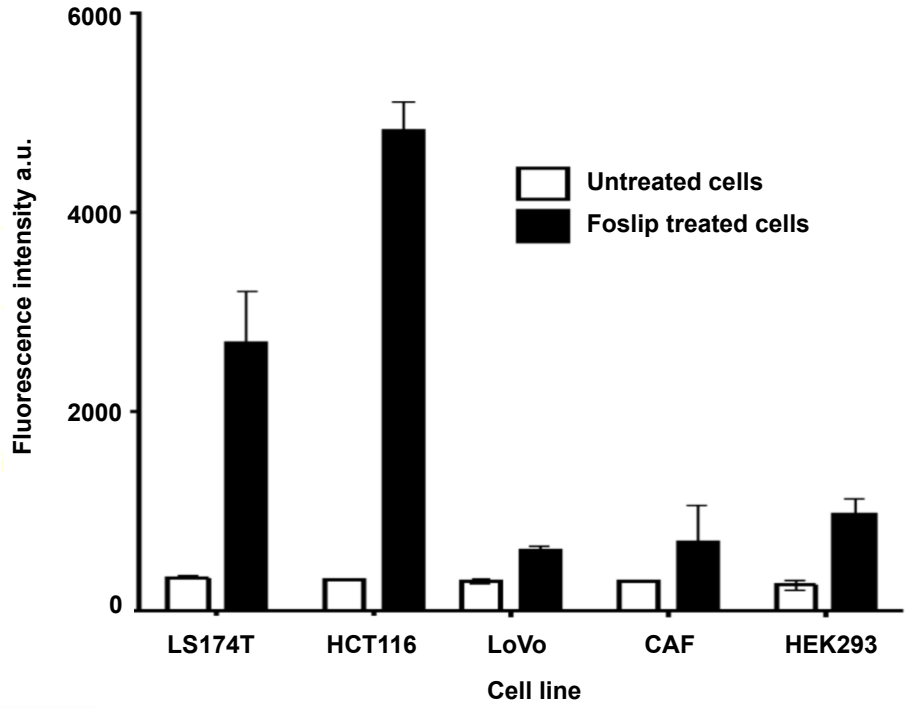

Figure 4. 3. Foslip induced fluorescence in tumour and non-tumour cell lines.

Foslip induced fluorescence in untreated and Foslip treated (150 nM Foslip, 24 h incubation) tumour (LS174T, HCT116 and LoVo) and non-tumour cells lines (CAF and HEK 293). Data denote the fluorescent mean from 3 biological experiments, each with 4 technical replicates, (SEM). Control represents cells treated with FBS and phenol free RPMI media.

4.3.1.4 Foslip induced fluorescence per 1000 viable cells

In all spectrofluorometer experiments, cells were seeded at $9x10^4$ /ml and grown to confluence in collagen coated 6-well plates over 5 days in cell specific media. However, cell lines varied in size and shape, and grew at different rates, resulting in variation in the numbers of cells per well. As the number of viable cells may impact on the overall fluorescence intensity an attempt was made to standardise this variable. Spectrofluorometer experiments were conducted in the same fashion as described previously. Immediately following fluorescence readings cells were trypsinised and stained with Trypan Blue. Viable cell counts were ascertained for each well via the Beckman Coulter vi-cell counter. The mean fluorescence intensity of each well was divided by the number of viable cells per well to calculate fluorescence per 1000 viable cells. **Figure 4.4** shows that when viable cell numbers were standardised, all colon cancer cell lines exhibited a significant increase in fluorescence intensity when incubated with 150 nM Foslip for 24 h in comparison to untreated controls ($p<0.0001$). However, the variation in fluorescence intensity between Foslip treated cells was large, and appeared to correspond to the degree of differentiation of the cell line. Moderately and well-differentiated cells (LS174T and HCT116) exhibited a 13- and 15-fold change in fluorescence intensity in comparison to untreated controls, whilst the poorly differentiated and metastatic cells (LoVo) exhibited a 3-fold change only.

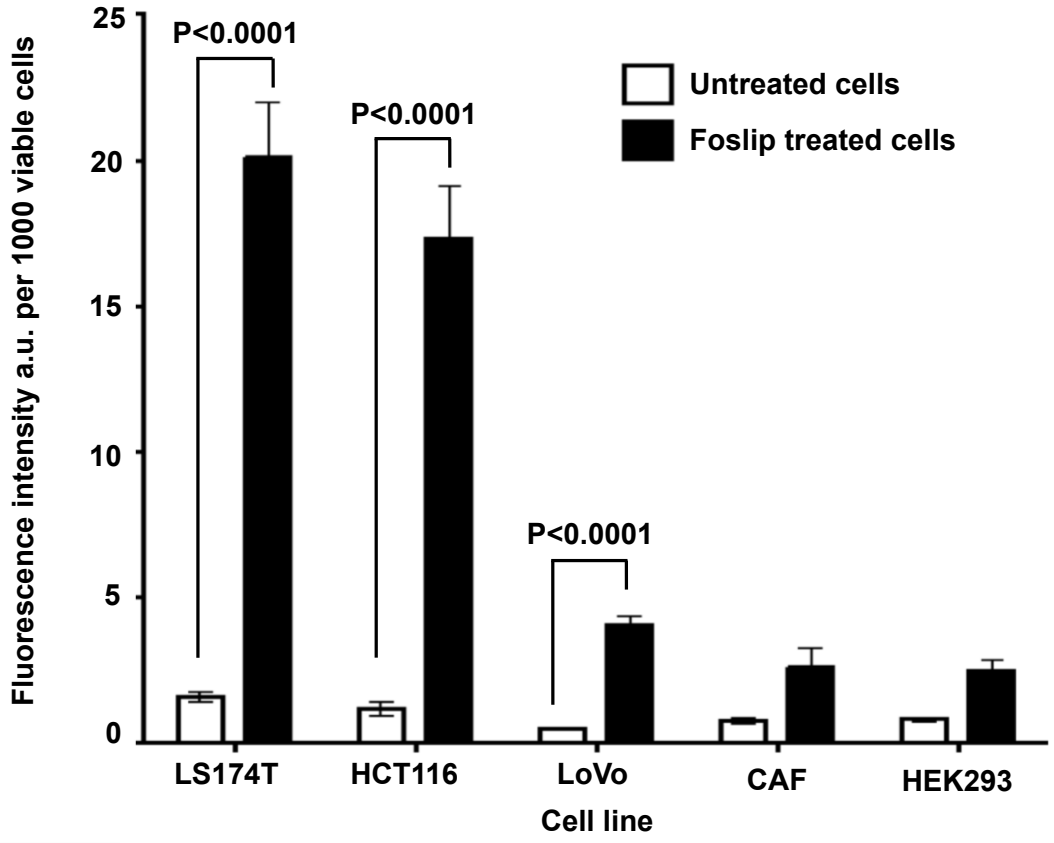

Figure 4. 4. Normalised Foslip induced fluorescence per 1000 viable cells.

Foslip induced fluorescence per 1000 viable cells in untreated and Foslip treated (150nM Foslip, 24 h incubation) cell lines. Data denote fluorescence mean from 3 biological experiments each with 4 technical replicates, (SEM). Untreated cells represent those cultured with FBS and phenol free RPMI media. Data are significantly different at p<0.0001.

4.3.2 Foslip-loaded silica nanoparticles characterisation

4.3.2.1 Nanoparticles synthesis and characterisation

Next, the aim was to encapsulate Foslip inside silica nanoparticles. The Foslip-loaded silica nanoparticles were manufactured using the water-in-oil microemulsion technique as detailed in **Chapter 2**. Their mean diameter was 92.22 nm (±10.96) using DLS for measurement. Fluorescence of the Foslip-loaded nanoparticles was measured at various concentrations and recorded using spectrofluorometer in water suspension. Encapsulation of Foslip inside silica nanoparticles was demonstrated by the absorption and fluorescence emission spectra of the synthesised nanoparticles. **Figure 4.5 A.** shows typical peak excitation and emission wavelengths for particles loaded with Foslip at 420 and 652 nm, respectively. The spectral properties of Foslip-loaded silica nanoparticles were almost equivalent to soluble Foslip and after destruction with Triton X-100, indicating that Foslip molecules were included inside the nanoparticles in a monomeric form. The fluorescent signal produced by particles suspended in PBS increased with increasing concentration up to approximately 2 mg/ml, after which the signal reduced as shown in **Figure 4.5 B**.

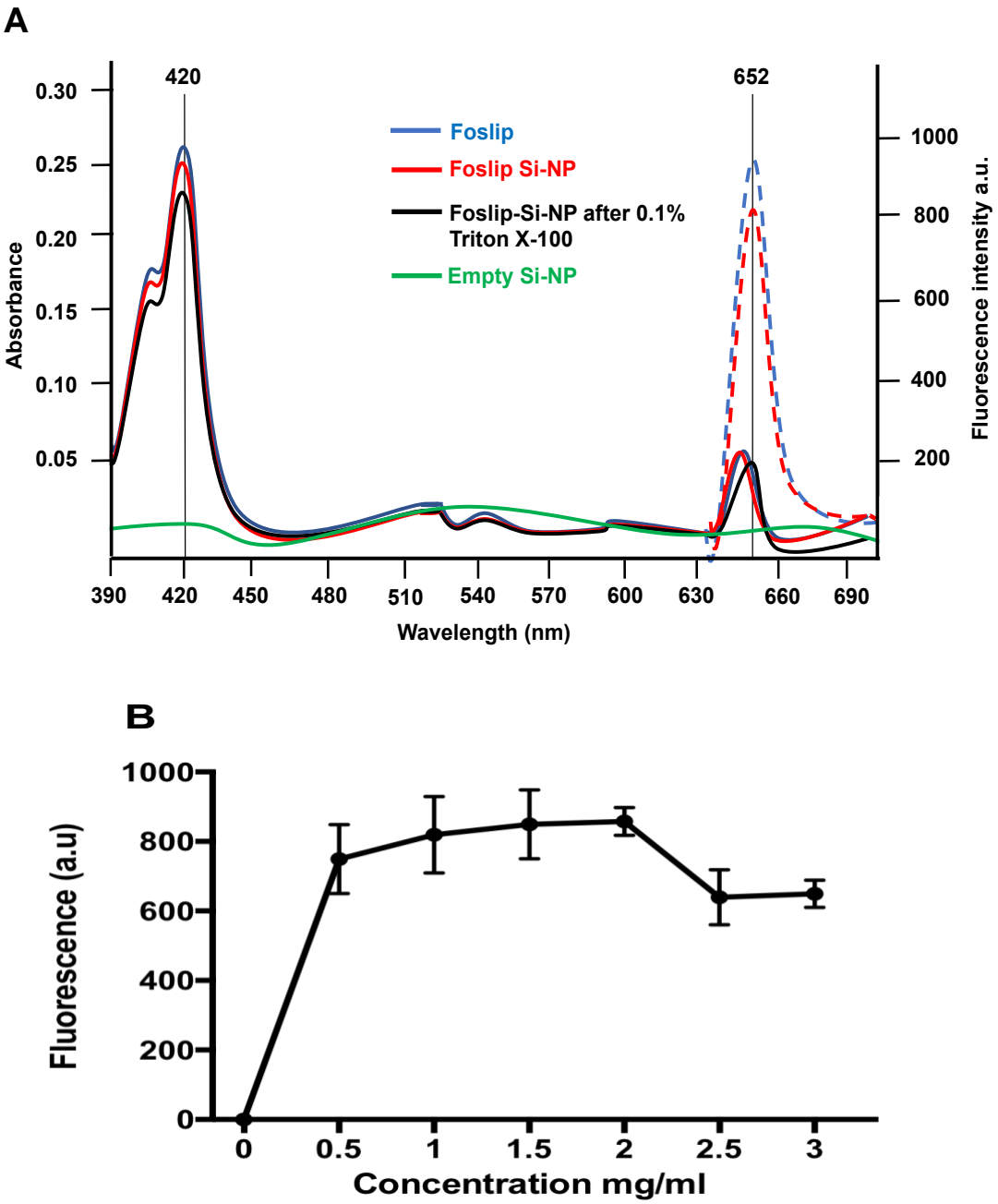

Figure 4. 5. Fluorescence spectrum of Foslip-loaded silica nanoparticles.

(A), Foslip-loaded silica nanoparticles were manufactured and suspended in PBS then peak absorption and emission wavelengths for Foslip alone (—), Foslip-loaded silica nanoparticles (—), dissolved silica nanoparticles (—) and empty silica nanoparticles (—) were measured and plotted on the same graph. (B), the relationship between Foslip-loaded nanoparticle concentration and emission fluorescence. Data fluorescence mean from 3 biological separate experiments (SEM, n=3).

4.3.2.2 Quantification of Foslip encapsulation efficiency in silica nanoparticles

Encapsulation of Foslip inside silica nanoparticles was confirmed earlier by the UV-is absorption and fluorescence emission spectra of the synthesised nanoparticles in water. Next, I aimed to quantify Foslip encapsulation efficiency in silica nanoparticles. The efficiency of the encapsulation process was quantified by measuring the absorbance of Foslip with reference to a standard curve (**Figure 4.6**) using microplate reader. Therefore, Foslip absorbance at A_{420} was measured before and after encapsulation process. The nanoparticle suspension was washed 3 times and A_{420} was also measured for each discarded supernatant. Then, Foslip encapsulation efficiency (EE) was calculated by using the following equations:

$$Ecapsulation\ efficiency\ (\%) = \frac{Amount\ of\ Foslip\ added - Amount\ of\ Foslip\ in\ supernatant}{Amount\ of\ Foslip\ added} x100$$

The results suggested that a typical nanoparticle sample contained ~ 1 mg/ml of nanoparticles and 110 nM of Foslip. These values correlated to Foslip loading of ~52.2 $\pm$ 2.1 % of the nanoparticles.

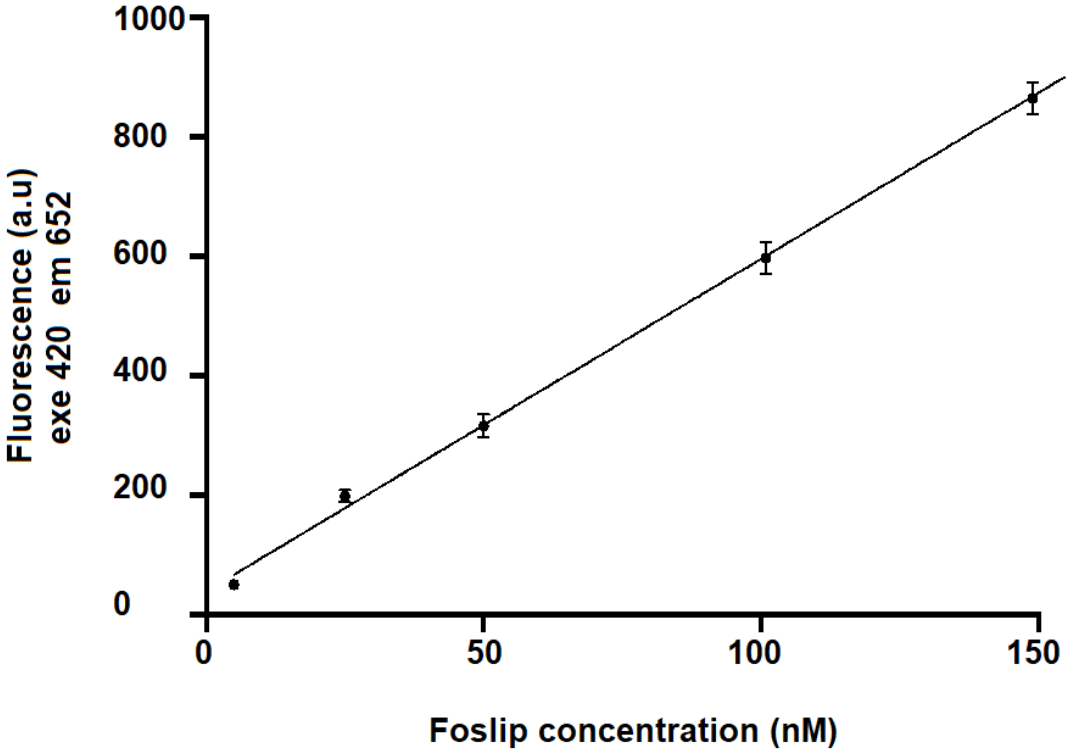

Sample	Fluorescence	Nanoparticle concentration (mg/ml)	Foslip Concentration (nM)	EE (%)
1	784.5	1	200	45
2	802.3	1	200	56.3
3	799.5	1	200	55.2
		Mean	**200**	**52.2**

Figure 4. 6. Foslip encapsulation efficiency in silica nanoparticles synthesis.

A standard curve of absorbance was plotted for soluble Foslip. Foslip-loaded silica nanoparticles were manufactured using a water-in-oil microemulsion technique and suspended in water then readings were taken for samples from three separate batches of Foslip-loaded nanoparticles.

4.3.2.3 In vitro analysis of fluorescent imaging of LoVo cells by anti-CEA Affimer targeted nanoparticles

Having identified sSMCC as the appropriate chemical linker to conjugate the Affimer on to the surface of the nanoparticle in **Chapter 3**, here we aimed to investigate whether polyclonal anti-CEA Affimer (II and III) would enhance fluorescent imaging of colorectal cancer cells when compared to monoclonal anti-CEA Affimer (II or III) tagged nanoparticles. sSMCC was mixed with 60 µg of reduced anti-CEA Affimers II and III (50/50, v/v) for 2 h then the reaction mixture was added to 4 ml of 2 mg/ml aminated nanoparticles followed by washing steps to remove unbound molecules. As controls, Foslip loaded nanoparticles were also functionalised with monoclonal anti-CEA Affimer II or III and anti-myoglobin Affimer. Next, LoVo, LS174T, HCT116 and control HEK293 cells were grown in 6-well plates then incubated with 1 mg/ml of nanoparticles for 2 h then imaged. Cell-specific fluorescence was quantified based on central optical sections analysis via confocal microscopy.

Figure 4.7 shows that polyclonal tagged nanoparticles increased the fluorescent imaging of colorectal cancer cells by 1.5-, 2.2-, 1.6- folds in LoVo, LS174T and HTC116 respectively ($p<0.06$-0.12) without increasing non-specific fluorescent imaging in the control cell line. The increased level of fluorescence in the polyclonal Anti-CEA Affimer tagged nanoparticles did not reach statistical significance in comparison to control monoclonal nanoparticles in this small number of experiments.

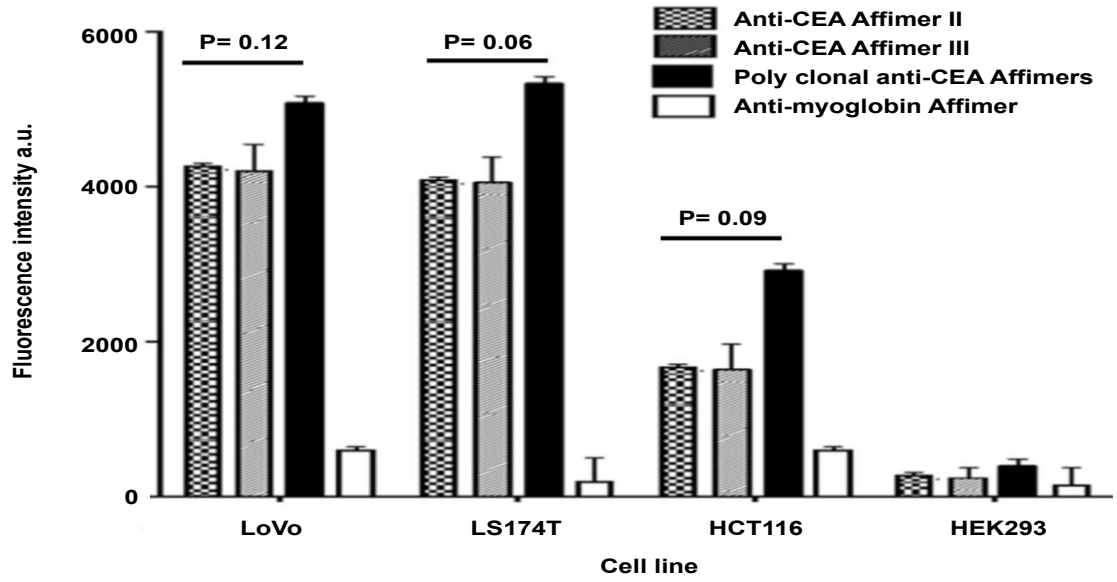

Figure 4. 7. Fluorescent imaging of colorectal cancer cells with polyclonal anti-CEA Affimer functionalisation.

Foslip-loaded silica nanoparticles were conjugated to anti-CEA Affimer II, III or to both. LoVo and HEK293 cell lines were incubated with anti-CEA Affimer or control myoglobin Affimer tagged nanoparticles then imaged. Data denote fluorescence mean for central optical sections from 3 biological experiments (SEM, n=3). Significance was tested using unpaired t-tests.

4.3.2.4 In vitro analysis of fluorescent imaging of colorectal cancer cells by polyclonal anti-CEA Affimer targeted nanoparticles

Next, the aim was to assess the fluorescent imaging of colorectal cancer cell lines when incubated with polyclonal anti-CEA Affimers tagged to Foslip-loaded silica nanoparticles. The mean diameter of the particles was ~101 nm (±2.5) using DLS for measurement. Nanoparticles (1 mg/ml) were then incubated with colorectal cancer and control cell lines for 2 h in a 6-well plate then imaged and cell-specific fluorescence was quantified based on central optical sections analysis. As positive control, cells were grown in 6-well plate then incubated with 150nM of soluble Foslip for 24 h then fluorescence was measured using spectrofluorometer. Anti-CEA Affimer-functionalised Foslip-loaded silica nanoparticles produced strong tumour-specific targeting, with anti-CEA targeted nanoparticles showing 9.5-, 10.2- and 3.5-fold greater fluorescence than control-Affimer targeted nanoparticles in LoVo, LS174T and HCT116 cells respectively ($p<0.0001$) for single slice analysis; **Figure 4.8**. Anti-CEA targeted nanoparticles also produced significant increase in fluorescence intensity across all colorectal cancer cell lines when compared to soluble Foslip. In contrast, soluble Foslip produced strong fluorescence intensity in the control cell line HEK293 when compared to anti-CEA targeted silica nanoparticles ($p<0.0002$). This is of clinical interest as it confirms that the anti-CEA Affimer targeted silica nanoparticles were specific to CEA expressing cells and likely to prevent unwanted accumulation in normal tissues, thereby reducing side effects.

A similar pattern of successful anti-CEA targeted fluorescence was observed in the maximum image projection analysis, with anti-CEA targeted nanoparticles demonstrating 3.0-, 4.1-, and 1.9-fold greater fluorescence than control particles in LoVo, LS174T, and HCT116 cells respectively ($p<0.0001$). Confocal microscopy images are shown in **Figure 4.9**.

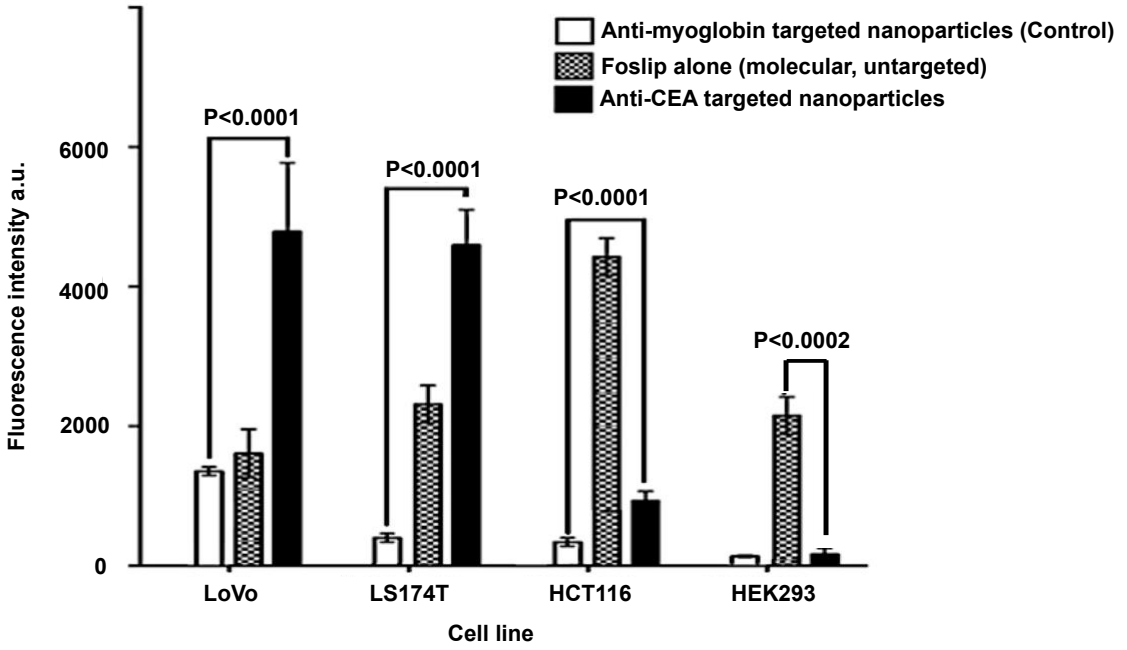

Figure 4. 8. Fluorescent imaging of colorectal cancer cells with polyclonal anti-CEA Affimer, Foslip-loaded silica nanoparticles.

Foslip-loaded silica nanoparticles conjugated to mixture of anti-CEA Affimer II and III via sSMCC in vitro. LoVo, LS174T, HCT116 and HEK293 cell line were incubated with either nanoparticles conjugated to anti-CEA, control Affimer or soluble (molecular) Foslip for 24 h. Data denote fluorescence mean for central optical sections from 3 biological experiments (SEM, n=3). Significance was tested using unpaired t-tests.

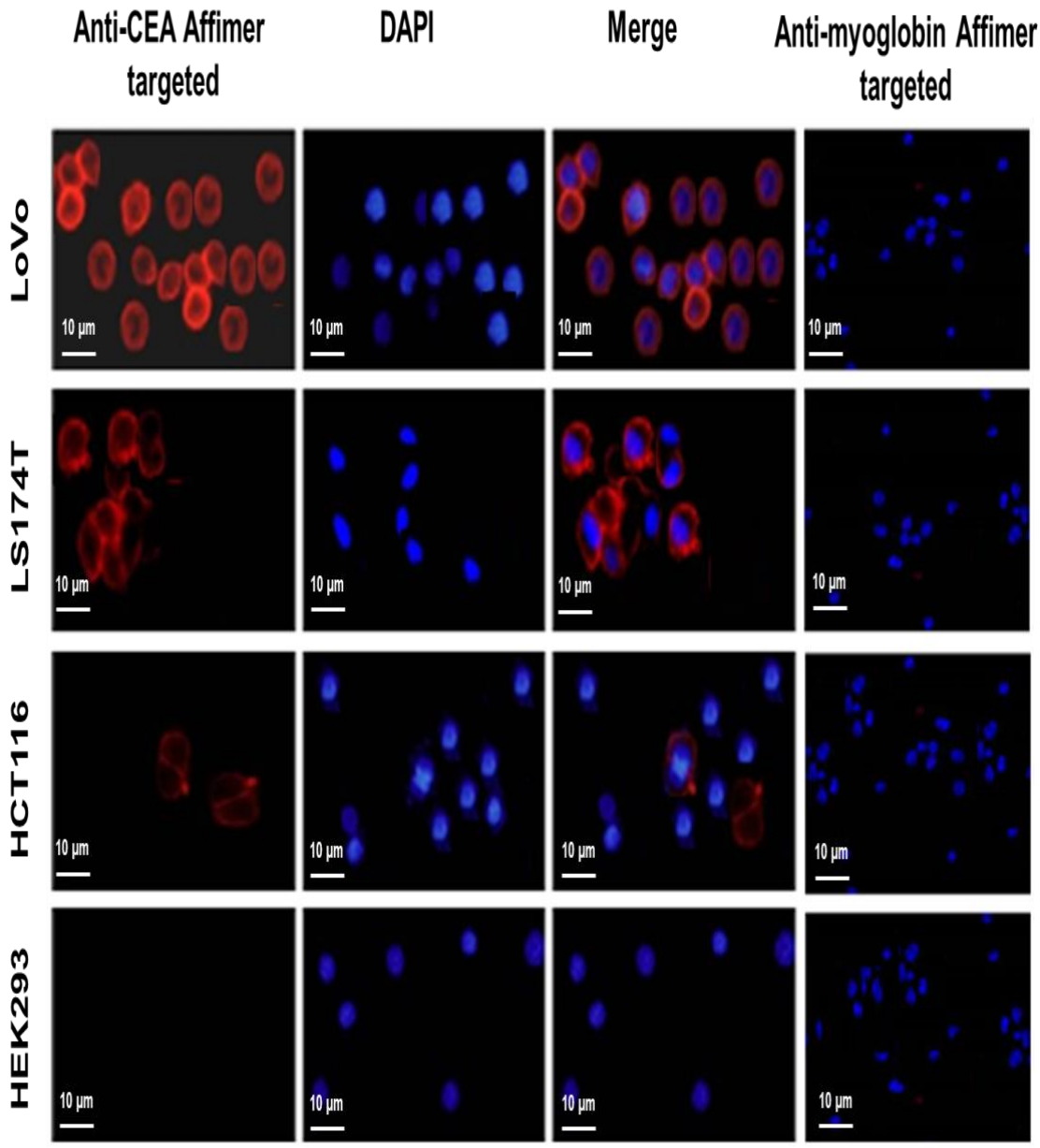

Figure 4. 9. Fluorescent imaging of colorectal cancer cells with polyclonal anti-CEA Affimer functionalised nanoparticles.

LoVo, LS174T, HCT116 and HEK293 ell lines were incubated with either anti-CEA targeted or control Affimer nanoparticles for 24 h then washed 3 times before imaging. Images were collected using confocal microscopy and fluorescence was quantified. Abbreviations denote: (Anti-CEA Affimer targeted), Anti-CEA Affimer functionalised silica nanoparticles; (Anti-myoglobin Affimer targeted), anti-myoglobin Affimer functionalised silica nanoparticles and (DAPI), 4',6-diamidino-2-phenylindole.

4.3.2.5 Cellular uptake of anti-CEA Affimer targeted nanoparticles

Next, we aimed to characterise cellular uptake of Foslip-loaded nanoparticles in colorectal cancer cells. In a similar manner to what was described in the previous experiments, colorectal cancer and HEK293 cell lines were grown on a 6-well plate then incubated with polyclonal anti-CEA Affimer-functionalised Foslip–loaded silica nanoparticles. Cells were incubated with 1 and 2 mg/ml nanoparticles for 4 and 24 h. After incubation, the cells were washed and fresh nanoparticle-free media was added for an additional 20 h (4+ 20h) and 24 h (24+24h). Fluorescent imaging using confocal microscopy was used to quantify the cellular uptake of targeted nanoparticles**.**

LoVo cells internalised larger amounts of targeted nanoparticles than other cell lines ($p<0.02$) followed by LS174T and HCT116 cells in a dose dependent manner (**Figure 4.10-I)**. Cellular uptake was seen as early as 4 h but the difference between the single time points was most obvious at 24 and 24+24 h in all cancer cell lines. Although fluorescence was still present in nanoparticles after 24 h incubation, the mean fluorescence intensity at 24+24 h was greater than 24 h time point ($p=0.01$) indicating that cellular uptake was also time dependent. The mean fluorescence caused by Foslip-loaded nanoparticles in HEK293 cell line was almost identical at 4+20 h and 24h ($p>0.9$) while in the colorectal cell lines a significant difference was observed between these two time points ($p<0.001$); highlighting the selectivity towards cancer cells was increased using the targeting anti-CEA Affimer. Such increased uptake would lead to a higher concentration of Foslip-loaded nanoparticles inside cells with a potential greater photodynamic effect. Confocal images of LoVo and HEK293 cells are shown in **Figure 4.10-II.**

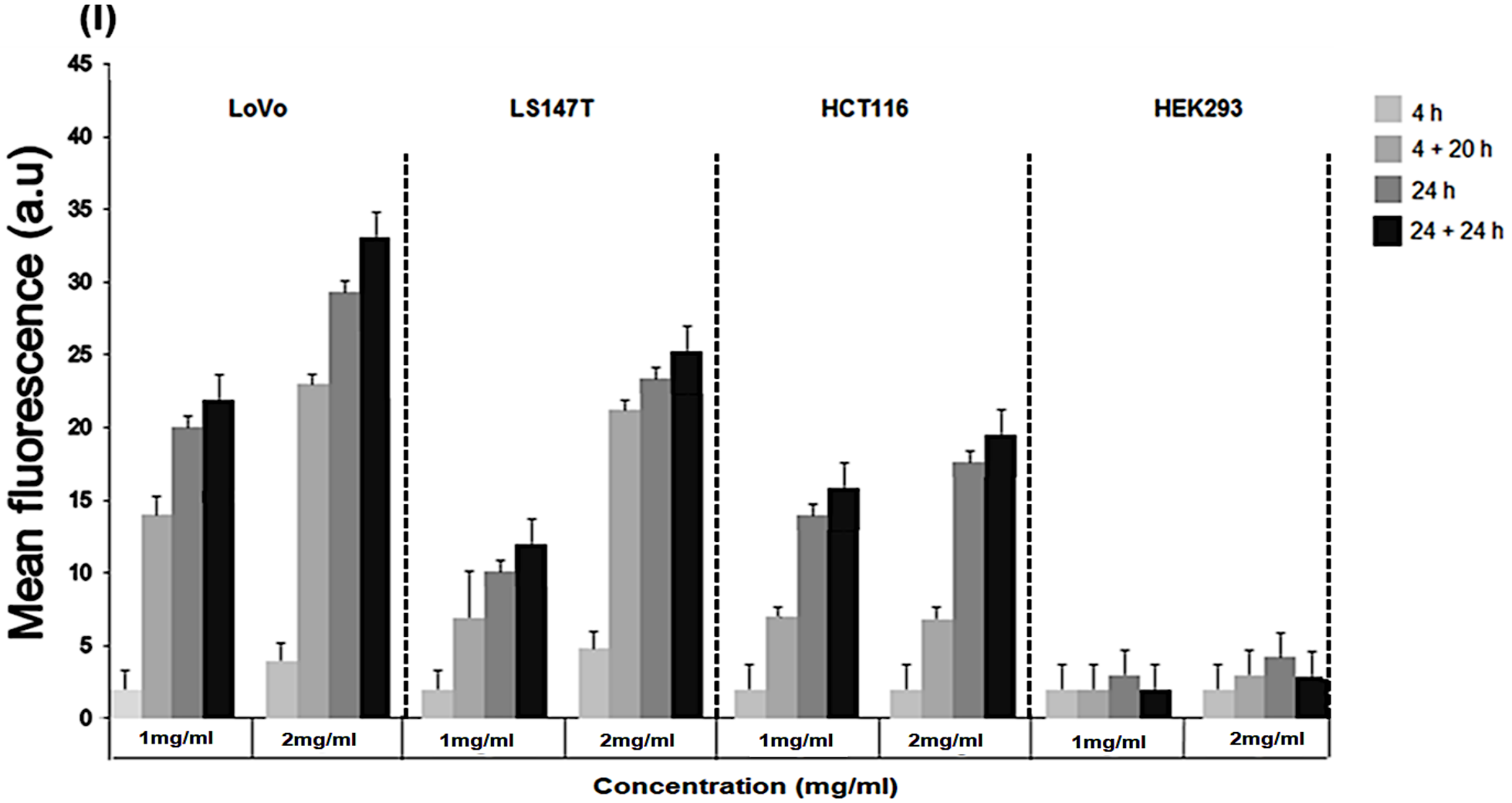
(I)
Mean fluorescence (a.u)
45
40
35
30
25
20
15
10
5
0
LoVo
LS147T
HCT116
HEK293
4 h
4 + 20 h
24 h
24 + 24 h
1mg/ml
2mg/ml
1mg/ml
2mg/ml
1mg/ml
2mg/ml
1mg/ml
2mg/ml
Concentration (mg/ml)

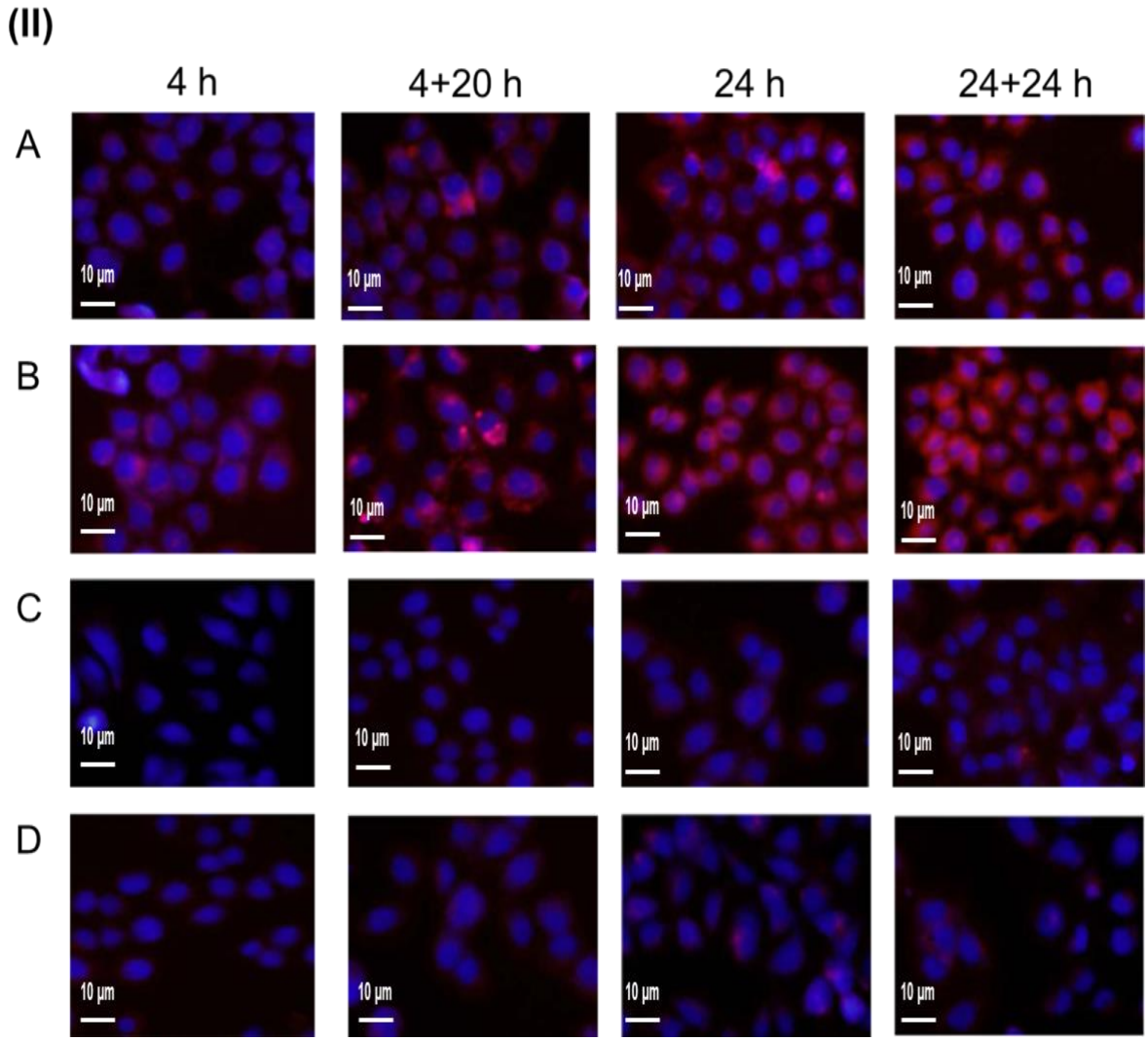

Figure 4. 10. Cellular uptake of Foslip-loaded silica nanoparticles in colorectal cancer and control cell lines at different time points and nanoparticles concentrations.

(I), cells were incubated with 1 or 2 mg/ml of anti-CEA targeted nanoparticles for 4 and 24 h. After incubation, the cells were washed and fresh nanoparticle-free media was added for an additional 20 h (4+ 20 h) and 24 h (24+24 h). Data denote fluorescence mean from 3 biological experiments (SEM, n=3). Significance was tested using unpaired t-tests. (II), confocal images represent: (A and B) LoVo cells incubated with 1 mg/ml and 2 mg/ml of anti-CEA Affimer tagged nanoparticles respectively at 4 and 24 h incubation period; (C and D) HEK293 cells incubated with 1 and 2 mg/ml of anti-CEA Affimer tagged nanoparticles respectively 4 and 24 h incubation period.

4.3.2.6 Dark cytotoxicity of Foslip-loaded silica nanoparticles

The next experiment was aimed at investigating the cytotoxic effect of anti-CEA Affimer tagged to Foslip-loaded silica nanoparticles against colorectal cancer cells. It was paramount to ensure that the nanoparticles had no dark toxicity before the cells were photo-irradiated. Here, I tested all elements of the designed nanoparticle up to the maximum concentration in the dark. Colorectal cancer and control cell lines were grown on 6-well plates then incubated with empty silica and functionalised silica nanoparticles at 4 mg/ml, poly clonal anti-CEA and anti-myoglobin Affimer at 1 mg/ml and soluble Foslip at 250 nM for 24 h. Wells were then washed and cells kept in free media for additional 24 h followed by MTT assay quantification of cellular viability. At all steps during this experiment, plates were wrapped in foil and kept in the dark during incubation periods.

High dose of empty silica nanoparticles, did not affect the survival of all cell lines when exposed to high concentrations of 4 mg/ml for 24 h which is much higher than that used to achieve cell-specific fluorescence and cellular uptake in the previous experiments. The MTT assay showed that the number of metabolically active cells at 24 h and 24+24 h after exposure to nanoparticles was not reduced relative to controls (**Figure 4.11 A-D**). Similarly, no cellular death was observed when cells were incubated with Affimers (anti-CEA or anti-myoglobin) alone at high concentration of 4 mg/ml. The dark toxicity of Foslip-loaded nanoparticles was evaluated and compared with soluble Foslip delivered in the standard solution. Foslip-loaded silica nanoparticles were highly toxic in the dark at 4 mg/ml suggesting a possibility of Foslip leakage. Similarly, soluble Foslip was highly toxic at 300 nM concentration in all cell lines with cell survival reduction to <20 % in all cell lines. Therefore, concentrations of Foslip used in our experiments are below the threshold of dark toxicity of all formulations.

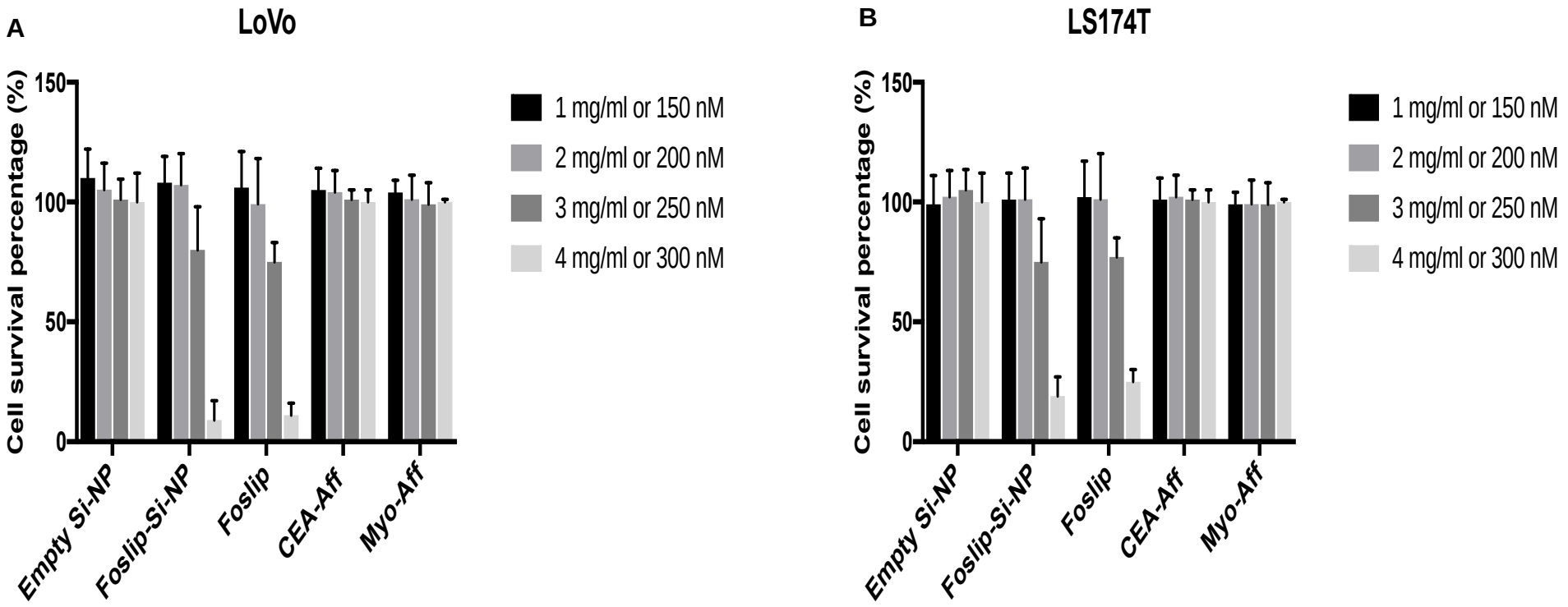
A
LoVo
Cell survival percentage (%)
150
100
50
0
Empty Si-NP
Foslip-Si-NP
Foslip
CEA-Aff
Myo-Aff
1 mg/ml or 150 nM
2 mg/ml or 200 nM
3 mg/ml or 250 nM
4 mg/ml or 300 nM
B
LS174T
Cell survival percentage (%)
150
100
50
0
Empty Si-NP
Foslip-Si-NP
Foslip
CEA-Aff
Myo-Aff
1 mg/ml or 150 nM
2 mg/ml or 200 nM
3 mg/ml or 250 nM
4 mg/ml or 300 nM

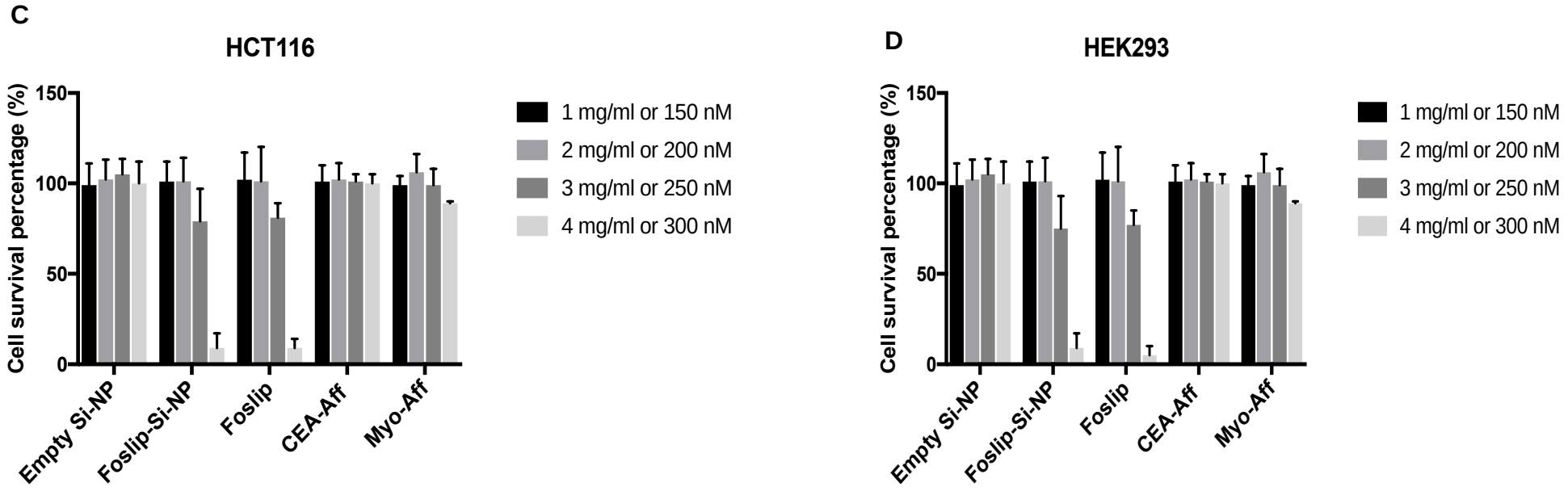

Figure 4. 11. Dark toxicity of Affimers, free Foslip, empty silica nanoparticles and functionalised silica nanoparticles in colorectal cancer cells.

Cells were incubated with empty silica and functionalised silica nanoparticles up to 4 mg/ml, poly clonal anti-CEA and anti-myoglobin Affimer up to 4 mg/ml and soluble Foslip up to 300 nM for 24 h in the dark then washed and kept in free media for additional 24 h. Cells viability was quantified using MTT assay. Data denote mean cells viability from 3 biological experiments (SEM, n=3) for: (A), LoVo; (B), LS174T; (C), HCT116; and (D), HEK293 cells. Abbreviations denote: (CEA), carcinoembryonic antigen; (Si), silica; (NP), nanoparticle; (Myo), myoglobin; (Aff), Affimer.

4.3.2.7 Photo-irradiation period cytotoxicity effect on colorectal cancer cells

Next, I aimed to investigate the effect of the light dose on cells survival in order to ensure that any cytotoxic effect to be observed was Foslip-mediated only. Colorectal cancer and control cell lines were grown on 6-well plates then incubated with anti-CEA Affimer functionalised Foslip-loaded silica nanoparticles at various concentrations for 24 h while wrapped in foil and kept in the dark. Wells were then washed and cells were incubated with fresh media then photo-irradiated immediately with a light dose of 0.15 - 0.675 J/cm^2 . Cells were then kept in free media for additional 24 h followed by MTT assay quantification of cellular viability.

At 0.45 J/cm^2 light dose, significant reduction in cell survival percentage was observed in LoVo, LS174T and HCT116 cells when compared to relative control HEK293 cells ($p<0.0001$) (**Figure 4.12 A-D**). Data showed that light dose of 0.45 J/cm^2 did not reduce cell survival percentage in the untreated cells. Photo-irradiation above 0.45 J/cm^2 appeared to be toxic to untreated colorectal cancer cells where cell survival was reduced to 80%. Cell survival in HEK293 was also reduced significantly at light does above 0.45 J/cm^2 ($p<0.0001$). Importantly, there appeared to be no additive cytotoxic effect of anti-CEA Affimer functionalised nanoparticles on cell survival in HEK293 cells before or after 30 min illumination period. Therefore, light dose at 0.45 J/cm^2 was considered as the cut-off point for safe photo-irradiation of cells and would be used for assessing the targeted photodynamic effect of Foslip-loaded nanoparticles in the next experiment.

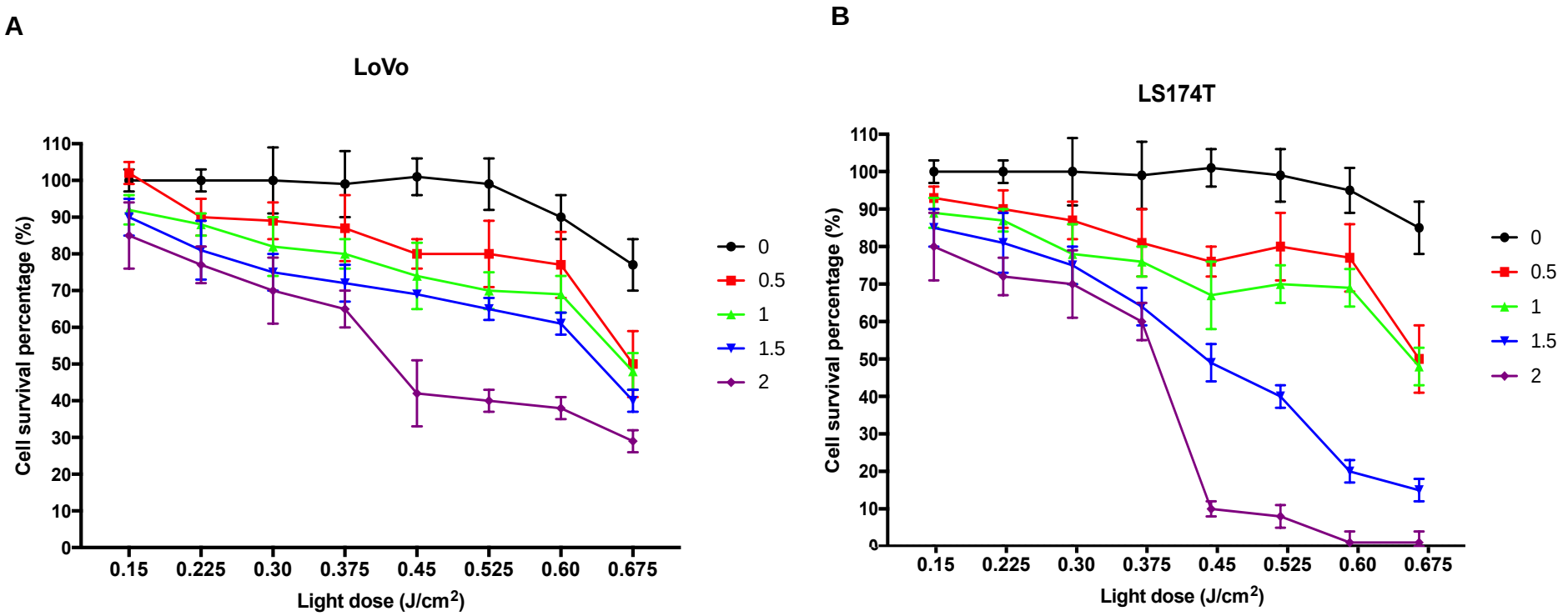
A
LoVo
Cell survival percentage (%)
110
100
90
80
70
60
50
40
30
20
10
0
0.15
0.225
0.30
0.375
0.45
0.525
0.60
0.675
Light dose (J/cm2)
0
0.5
1
1.5
2
B
LS174T
Cell survival percentage (%)
Light dose (J/cm2)
0
0.5
1
1.5
2

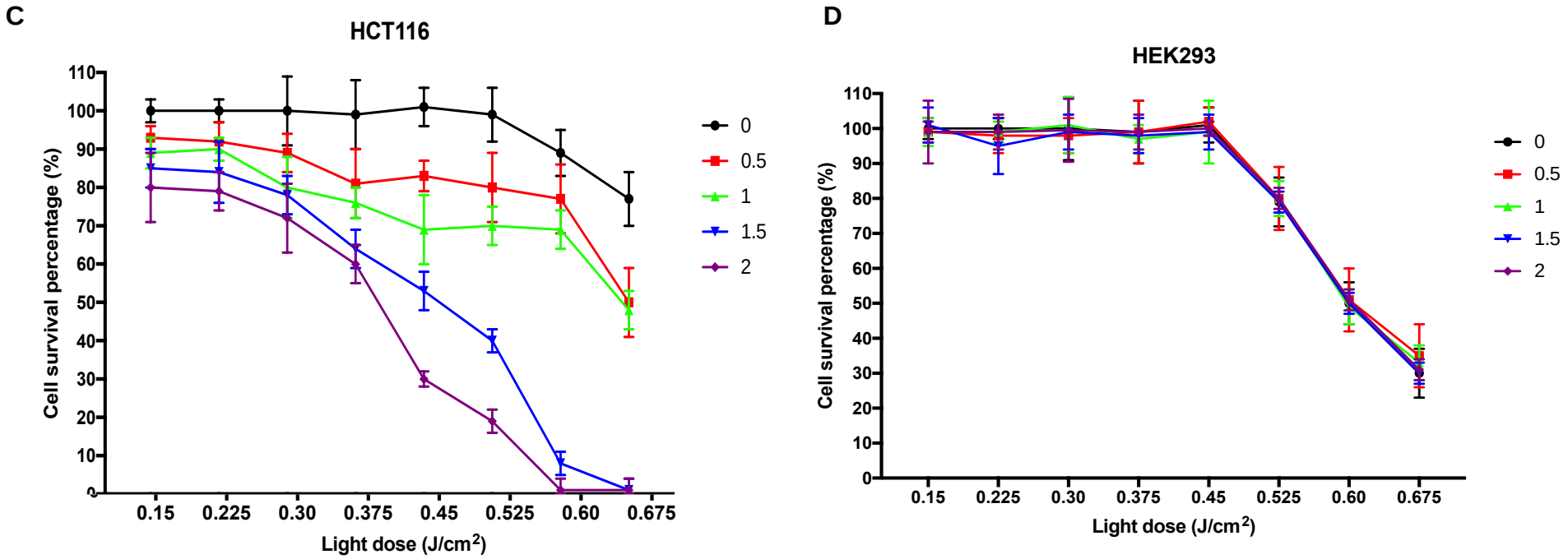

Figure 4. 12. Photo-irradiation light dose effect on colorectal cancer cells.

Cells were incubated with various concentrations of anti-CEA Affimer functionalised Foslip-loaded silica nanoparticles for 24 h then photo-irradiated with 0.15 – 0.675 J/cm^2 of 600-700 nm. Cells viability was quantified using MTT assay. Data denote mean cells viability from 3 biological experiments (SEM, n=3) for: (A), LoVo; (B), LS174T; (C), HCT116; and (D), HEK293 cells. Symbols denote nanoparticles concentration at: (●), untreated cells; (■), 0.5; (▲), 1; (▼), 1.5 and (◆), 2 (mg/ml).

4.3.2.8 Light cytotoxicity of Foslip loaded silica nanoparticles

Next, the aim was to assess the phototoxicity efficacy of Foslip-loaded silica nanoparticles in killing cancer cells *in vitro*. The experiment was carried out using anti-CEA and anti-myoglobin Affimer targeted nanoparticles against colorectal cancer cell lines and control cell line. LoVo, LS174T, HCT116 and HEK293 cells were grown on 6-well plates then incubated with various concentrations of nanoparticles for 24 h, wrapped in foil and kept in the dark. Supernatant was carefully aspirated and replaced by fresh media and immediately photo-irradiated with a light dose of 0.45 J/cm^2. After irradiation plates were covered in foil and stored in the dark in an incubator for additional 24 h before MTT assay was carried out.

As shown in **Figure 4.13 A,** the reduction in cell survival measured at 24 h after irradiation was dose dependent. At 2 mg/ml poly clonal anti-CEA Affimer-functionalised Foslip-loaded silica nanoparticles concentration, significant cell death rate was observed in LoVo (60%), LS174T (90%) and HCT116 (70%) when compared to HEK293 (0%); $p<0.0001$. However, cellular toxicity was seen in the control HEK293 cells when treated with the anti-CEA targeted nanoparticles at concentration above 2 mg/ml. Importantly, no cellular toxicity was observed when cells were treated by identical nanoparticles but functionalised with the control anti-myoglobin Affimer (**Figure 4.13 B**).

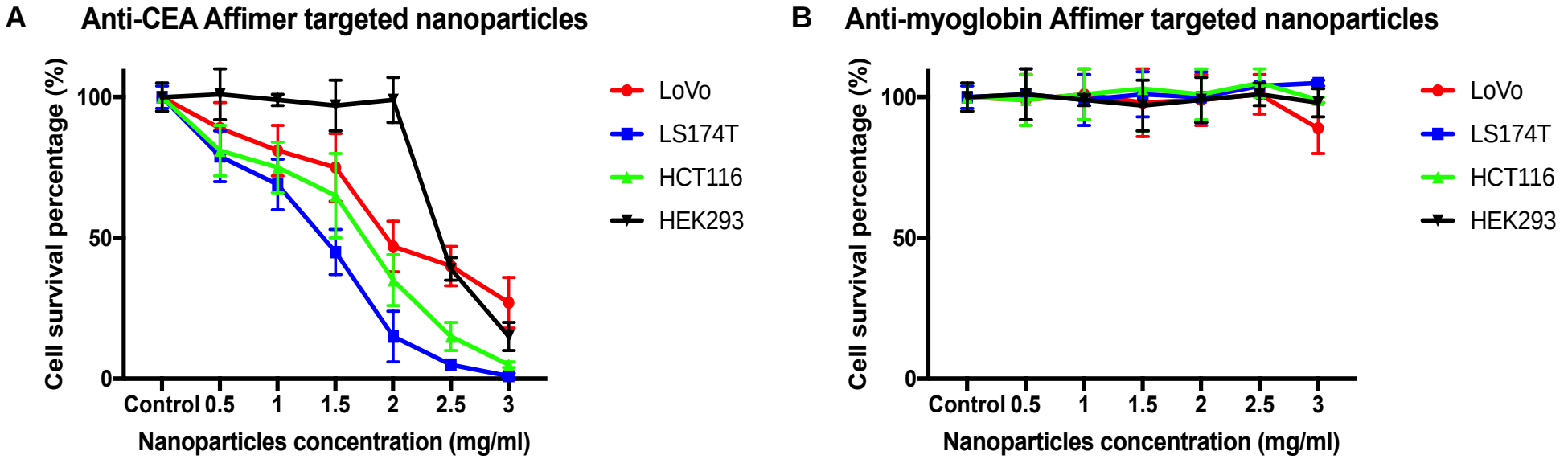

Figure 4. 13. Light cytotoxicity of CEA-targeted nanoparticles in colorectal cancer cells.

Cells were pre-incubated with increasing dose of: (A), targeted anti-CEA Affimer- or (B), anti-myoglobin Affimer-functionalised Foslip-loaded silica nanoparticles for 24 h and then photo-irradiated with light dose of 0.45 J/cm^2 . Viability was evaluated using MTT assay 24 h post irradiation. Data denote mean percentages of cells survival from 3 biological experiments (SEM, n=3) with respect to untreated and non-irradiated cells (Control).

4.3.2.9 Cellular reactive oxygen species detection in colorectal cancer cells

Having demonstrated that the optimised anti-CEA Affimer functionalised nanoparticle allowed selective cytotoxic killing of colorectal cancer cells, next we aimed to assess the mechanism of cellular death induced. The DCFDA assay was performed to study the cell death mechanism which is widely used to detect ROS. DCFDA is cell permeable redox sensitive fluorescent probe that is oxidised by ROS to yield the highly fluorescent product 2,7-dichlorofluoroscein. The DCFDA assay was performed following PDT to mimic the experiments in which cell viability was assessed using the MTT assay. Cells were incubated with PBS containing 10 mM DCFDA for 30 minutes in a CO_2 incubator then washed with PBS. DCF fluorescence was observed using confocal microscope.

The assay showed strong fluorescence in all cancer cells treated with anti-CEA targeted Foslip-loaded silica nanoparticles but not when using control nanoparticles or in control cells (**Figure 4.14)**. The results supported the hypothesis that the cytotoxic effect seen in the PDT experiment was Foslip mediated via ROS generation.

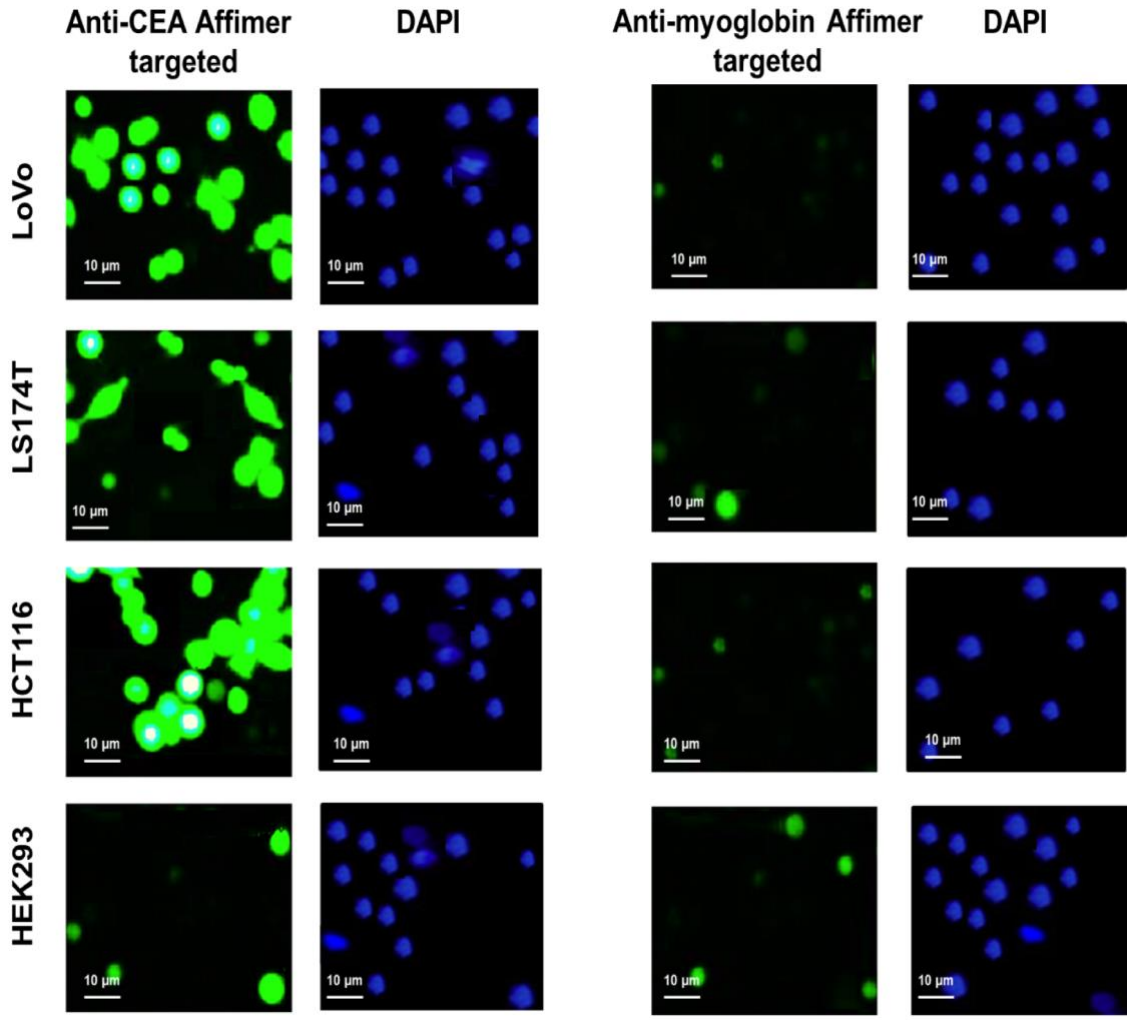

Figure 4. 14. ROS detection in colorectal cancer cells following PDT post-incubation with anti-CEA and anti-myoglobin Affimer tagged Foslip-loaded silica nanoparticles for 24 h.

Cells were incubated with PBS containing 10 mM DCFDA for 30 minutes in a CO_2 incubator then washed with PBS. DCF fluorescence was observed using confocal microscope. Abbreviations denote: (Anti-CEA Affimer targeted), Anti-CEA Affimer functionalised silica nanoparticles; (Anti-myoglobin targeted), anti-myoglobin Affimer functionalised silica nanoparticles and (DAPI), 4',6-diamidino-2-phenylindole.

It is therefore, concluded that polyclonal anti-CEA Affimer-functionalised Foslip-loaded silica nanoparticles were specific to colorectal cancer cells and allowed specific tumour fluorescent imaging and photodynamic killing *in vitro*.

4.4 Discussion

In this chapter, I used a combination of (bi-Affimer) anti-CEA Affimers to produce polyclonal bioreceptor to target Foslip-loaded silica nanoparticles to colorectal cancer cells. The nanoparticles showed significant anti-CEA specific cellular fluorescence in colorectal cancer cell lines, which appeared to be both time and dose dependent. We have also shown that the same nanoparticle allowed targeted photodynamic therapy via ROS generation. These promising results suggested that the functionalised nanoparticles were theranostic for both imaging and photodynamic therapy of colorectal cancer cells *in vitro*. Importantly, the control nanoparticles did not cause fluorescence or PDT activity in the cancer cells. These data are the first of their kind in the field of Affimer targeted nanoparticles against colorectal cancer for fluorescent imaging and photodynamic therapy.

The use of nanoparticles as drug delivery systems can significantly improve the distribution of the photosensitiser for PDT and the efficacy of the treatment in cancer patients (Rawal and Patel, 2019, Cisterna et al., 2016). The inclusion of the photosensitiser in the nanoparticle may lead to completely different pharmacokinetics and bio-distribution, and selective accumulation in the tumour tissues can be improved either by passive enhanced permeability and retention (EPR) effect or active targeting (Cho et al., 2008). In this study, we synthesised silica nanoparticles with Foslip incorporation into its core. The average particle size of ~ 100 nm would enable nanoparticles accumulation at the tumour site by the EPR effect and selective targeting via the anti-CEA Affimer. For application in photodynamic therapy, silica nanoparticles such as Stöber silica nanoparticles (Kim et al., 2010), organically modified silica (Ohulchanskyy et al., 2007,

Compagnin et al., 2009), and mesoporous silica nanoparticles (Lu et al., 2007) have been reported frequently. Silica-based nanoparticles are recognised as efficient delivery systems for mTHCP photosensitiser (Brezániová et al., 2018).

4.4.1 Interactions of Anti-CEA Affimer functionalised nanoparticles with cells in vitro

Photosensitisers entrapped inside nanoparticles were suggested to form aggregates that dissociate to monomeric forms after their release from the nanoparticles and transfer to plasma proteins (Konan-Kouakou et al., 2005, Vargas et al., 2009). Aggregation inside the nanoparticles can potentially lead to fluorescence quenching. However, we hypothesised that Foslip will not aggregate inside silica nanoparticles due it its liposomal nanoformation and encapsulation inside silica nanoparticles did not significantly change the fluorescence properties of Foslip. This was further confirmed by the targeted fluorescence seen in colorectal cancer cells when incubated with the Foslip loaded silica nanoparticles.

The subcellular localisation of the photosensitiser is one of the key factors governing the outcome of photodynamic therapy, since it determines the primary sites of photo-induced damage (Moor, 2000, Berlanda et al., 2010). Other researchers reported that Foslip was successfully internalised into cellular membranes ensuring efficient accumulation in many types of cancer cells (Gaio et al., 2016, Meier et al., 2017, Kiesslich et al., 2007, Gyenge et al., 2011b). After internalisation, the liposomal membrane is simply fused with cellular membranes and mTHPC is redistributed between cellular compartments. Although Foslip was reported to show reduced dark cytotoxicity effects when compared to mTHCP in

monolayer cells *in vitro* (Berlanda et al., 2010, Compagnin et al., 2011, Petri et al., 2012), our results suggested the contrary. We observed significant cellular uptake of free Foslip in two control cell lines. Therefore, there is an argument to encapsulate Foslip in targeted silica nanoparticle to overcome the drawbacks of non-specific cellular uptake in control cells. Silica nanoparticles are internalised by specific endocytotic processes (Gyenge et al., 2011a). Our results of Foslip intracellular uptake could be explained by two mechanisms of cell internalisation when silica nanoparticles were used as a delivery system. First, bound anti-CEA Affimers were recycled which mediated possible silica nanoparticle internalisation. Although we did not investigate the internalisation process of anti-CEA Affimer tagged nanoparticles, evidence related to anti-CEA antibodies suggested that they were internalised by colorectal cancer cells with a half-life of 10-16 hours (Schmidt et al., 2008). We therefore hypothesised that anti-CEA Affimer would internalise in a similar manner to bound anti-CEA antibody. Our results suggested cellular uptake of the nanoparticles as early as 4 h post incubation in a time and in a dose dependent manner. Second, Foslip released from silica nanoparticles prior to cell internalisation followed the same route as the internalisation of free Foslip (Compagnin et al., 2009, Rojnik et al., 2012). In support of this theory, no dark cytotoxicity for empty silica nanoparticles at high concentrations up to 4 mg/ml was seen in colorectal and control cells lines; whereas nanoparticles loaded with Foslip were highly toxic at 4 mg/ml. This suggested that Foslip might leak outside the silica shell and internalise into the cells as a free molecule. In colorectal cancer cell lines, the cytoplasmic fluorescence reduced after 48 hours suggesting that Foslip was either excreted by the cell or degraded within it. This reduction in fluorescence also suggested

that either the membrane-bound CEA molecules were recycled at a slower rate than they were bound and internalised, or the nanoparticle was processed by the cell membrane. Nonetheless, the encapsulation of Foslip into silica nanoparticles reduced its unwanted dark cytotoxicity.

4.4.2 Fluorescent imaging and photodynamic therapy with Foslip-loaded nanoparticle

In all three cell lines tested, targeted nanoparticle showed significantly greater fluorescence at each time point from 4 to 48 hours compared to non-targeted control nanoparticle. The time dependent nature of the fluorescence and the fact that it appeared to be cytoplasmic, suggested that Foslip had been internalised by the cells. Cellular fluorescence from control nanoparticles was negligible. Peak fluorescence occurred at 24 to 36 hours post incubation and decreased after 48 hours. In all three cell lines tested, the fluorescence at 48 hours was greater than at 4 h. The fold difference in mean fluorescence between anti-CEA and control Affimer conjugated nanoparticles at 36 hours was 9.5, 10.2- and 3.5-fold for LoVo, LS174T, and HCT116 respectively ($p<0.0001$). Importantly, the mean fluorescence of Foslip-loaded silica nanoparticle was comparable to that observed in NIR664 dye-doped silica nanoparticle (**Chapter 3**). The near infra-red fluorescence of Foslip-loaded silica nanoparticles is an important characteristic feature for imaging. However, this feature was hardly reported in the literature when Foslip was utilised for photodynamic therapy.

Each of the three cell lines is known to express CEA but at differing concentrations: LoVo cells have a high expression, LS174T cells a moderate/high expression and HCT116 cells a low expression (Ohannesian et al., 1995, Ashraf

et al., 2009, da Paz et al., 2012, Fahlgren et al., 2003, Wang et al., 1999). Although our results suggested a relationship between fluorescence intensity and CEA expression level, this does not reflect a true CEA expression concentration on cell surfaces. This is the case even when non-specific control binding is ignored (to consider the higher levels in LS174T cells). This is likely to be due to differing steric hindrance, where the antigen density at the cell membrane can affect Affimer binding occurring between cell lines (Kent et al., 1978). Although our results showed anti-CEA specific fluorescence, the relationship between cellular CEA concentration and fluorescence is not clear.

Reports on targeted delivery of mTHPC nanoparticulate formation to colorectal cancer cells for photodynamic therapy are very limited. Abdelghany *et al* (2013), were successful at encapsulating meso-tetra(N-methyl-4-pyridyl) porphine tetra tosylate (TMP) photosensitiser in a hydrogel-based chitosan/ alginate nanoparticle formulation (Abdelghany et al., 2013). Anti-death-receptor-5 (DR5) antibody, a cell surface apoptosis-inducing receptor up-regulated in various types of cancer and found on HCT116 cells, was then conjugated onto the particles. Although their nanoparticle elicited a more potent photocytotoxic effect than free drug, the nanoparticle diameter was prohibitively large at 560 nm. In addition, the tissue target DR5 is not specific to colorectal cancer and not known to be highly expressed. On the other hand, Yang *et al* (2010) synthesised Folic acid-conjugated chitosan nanoparticles and loaded them with protoporphyrin IX (PpIX) photosensitiser (Yang et al., 2010). They used folic acid as a bioreceptor to target high folate receptor-expressing colorectal cancer cells HT29 and Caco-2. The authors reported that PpIX accumulated in cancer cells via receptor-mediated endocytosis with significant fluorescence when compared to free PpIX but with

no report on the photodynamic effect. In addition, their experiments did not include either control nanoparticles or control cell lines. Others reported successful encapsulation of mTHPC in nanoparticles for photodynamic therapy in colorectal cancer cells but lacking a targeting molecule on the surface (Löw et al., 2011).

The photodynamic effectiveness of Foslip delivered by targeted silica nanoparticles was assessed following light (600–700 nm) irradiation of colorectal cancer cells compared to control nanoparticles. The *in vitro* photocytotoxic effect of the anti-CEA targeted and control nanoparticle was significantly different. The data showed that anti-CEA Affimer targeted nanoparticles significantly allowed Foslip-mediated photodynamic therapy in all three colorectal cancer cells when compared to control nanoparticles. This is a novel finding and we are the first to demonstrate effective PDT using anti-CEA Affimer as a targeting bioreceptor on the surface of silica nanoparticles. However, at doses above 2 mg/ml a cytotoxic effect was observed in the control cell line HEK293. The photodynamic toxicity observed in the HEK293 cells when incubated with Anti-CEA Affimer targeted nanoparticles was likely due to the non-specific binding of nanoparticles to the cells. Interestingly, such photo induced cytotoxicity was not seen in HEK293 cells when incubated with the control anti-myoglobin Affimer nanoparticles. Whether HEK293 cells express CEA at the surface or whether the polyclonal functionalised nanoparticles at high concentration mediated the unwanted cellular death is unknown. These findings necessitate further investigations including another control cell line. Taking together, the results suggested that a dose of 2 mg/ml of targeted nanoparticles is the cut-off for safe treatment *in vitro*. However, this cut-off value for safe dose of Foslip-loaded silica nanoparticle may

differ when tested *in vivo*. The mechanism of cellular toxicity was suggested to be mediated via ROS generation. Although quantification of the fluorescent signal of the ROS generation assay is feasible, it would not be a true reflection of the exact mechanism of cellular cytotoxicity induced.

The conclusion from this piece of research is that Foslip-loaded silica nanoparticles conjugated to anti-CEA Affimers allowed tumour cell-specific fluorescent and photodynamic therapy *in vitro*, with sufficient promise to justify testing in an animal model of colorectal cancer.

Chapter Five

Anti-CEA targeted, Foslip-loaded silica nanoparticles for colorectal cancer imaging *in vivo*

5 Anti-CEA targeted, Foslip-loaded silica nanoparticles for colorectal cancer imaging *in vivo*

5.1 Abstract

Aim

The aim of this chapter was to test anti-CEA Affimer-functionalised Foslip-loaded silica nanoparticles fluorescent imaging in colorectal cancer murine model.

Methods

Anti-CEA (II+III) and anti-myoglobin Affimer functionalised Foslip-loaded silica nanoparticles were synthesised and suspended in sterile PBS. Six-week-old BALB/c nu/nu female mice, bearing LS174T xenograft tumours in the right flank, were injected with either anti-CEA Affimer-functionalised Foslip-loaded nanoparticles (n=6) or control anti-myoglobin-functionalised Foslip-loaded (n=6) nanoparticles via tail vein. IVIS animal imaging system with excitation filters at 615 - 665 nm and 8 s exposure time was used for *in vivo* and *ex vivo* imaging at 6, 24, 30 and 48 h while confocal microscopy was used for histological imaging of xenografts. Wilcoxon Signed Rank Test was used for statistical analysis and $P<0.05$ was considered significant.

Results

Foslip-loaded silica nanoparticles were detectable by the IVIS system at 2 mg/ml, 200 µg/ml and 20 µg/ml. Anti-CEA Affimer-functionalised Foslip-loaded nanoparticles allowed tumour-specific imaging of LS174T xenografts in all 6 mice. Fluorescence in the CEA-targeted tumours was significantly greater than

controls at every time point after and including 6 h ($p<0.0001$). Mean tumour fluorescence increased from 6 h (mean $0.55x10^7$ $psec^{-1}cm^{-2}sr^{-1}/\mu W/cm^2$) to 30 h (mean $9.415x10^7$ $psec^{-1}cm^{-2}sr^{-1}/\mu W/cm^2$). Mice injected with control anti-myoglobin Affimer-functionalised nanoparticles showed no tumour fluorescence above background at any point. The xenograft tissue sample from the mouse injected with anti-CEA Affimer targeted nanoparticles showed fluorescent signal within the tumour microenvironment while no fluorescence was seen in the control xenograft.

Conclusion

Anti-CEA Affimer-functionalised Foslip-loaded silica nanoparticles allowed tumour-specific fluorescent imaging of LS174T colorectal cancer murine model.

5.2 Introduction

The application of antibodies to colorectal cancer targeting nanoparticles is still an emerging field, but there are already many antibodies in preclinical and clinical development (Löw et al., 2011, Conaghan et al., 2008, Oukkal et al., 2010, Douillard et al., 2010). For example, the humanized A33 monoclonal antibody has shown great promise in clinical trials as an immunotherapeutic biological agent and also as a targeting ligand for colorectal cells of polymer capsules formed by the layer-by-layer method (Chong et al., 2005, Cortez et al., 2007) . Using targeted nanoparticles as a drug delivery system based on antibodies is now one of the main approaches for colorectal cancer therapy under preclinical development. However, the major limitation of antibodies is their large size and complexity, posing a challenge to their conjugation on the surface of nanoparticles (Brennan et al., 2004, Weinberg et al., 2005). Peptides also represent a promising targeting alternative, given their small size and ease of attachment to nanoparticles. However, the use of peptides for colorectal cancer , for example, the tumor necrosis factor-related apoptosis- inducing ligand (Cao et al., 2008) , and the peptide RPMrel (CPIEDRPMC) (Kelly and Jones, 2003) as a targeting ligand, has not yet been well explored. One study has shown high cellular uptake of HPMA-copolymer-doxorubicin conjugate with the oligopeptide GE11 in colorectal cancer cells that overexpress epidermal growth factor receptor (EGFR), achieving selective release of doxorubicin (Kopansky et al., 2011). The differential expression of folate receptor-α (FRα) has been associated with several types of cancers including colorectal cancer (Shia et al., 2008). Cell lines such as Caco-2 and HT29, which overexpress the folate receptor, selectively internalise nanoparticles with folate conjugated to their surface (Li et al., 2011).

Sharma *et al* (2013), described a multifunctional nanosystem based on methotrexate-loaded guar gum nanoparticles functionalised with folic acid , which released methotrexate at colonic pH 6.8 and displayed preferential *in vivo* uptake by colon tissue (Sharma et al., 2013). A recent study reported that mesoporous silica nanoparticles, loaded with porphyrin and camptothecin, were successfully targeted against HCT116 cells using galactose on the surface as bioreceptor (Gary-Bobo et al., 2012). The combined drug delivery and photodynamic therapy of the nanoparticle showed a dramatic enhancement of cancer cell death compared to separate treatments.

Other types of nanoparticles loaded with different types of photosensitisers and functionalised with different type of bioreceptors have been described. This highlights the difficulties faced when a fluorescent, tumour-specific molecular nanoparticle, for live *in vivo* colorectal cancer imaging, and photodynamic therapy is considered. The particular challenge in this application is to construct a particle that can simultaneously fluoresce and target tumour cells. The nanoparticle must have pharmacokinetic properties that enable it to be delivered efficiently to a tumour following systemic vascular delivery; while the fluorescent signal must be of adequate magnitude to pass through the muscular bowel wall and the mesentery and must have favourable toxicity profile. In addition, the tumour-to-background ratio must be large enough to allow sensitive and specific detection of cancer cells and deliver specific photodynamic therapy in a targeted manner.

A limited number of studies have been published in which mTHPC loaded nanoparticles were targeted against colorectal cancer. In **chapter 4**, we have exploited the unique features of near-infrared fluorescence spectrum and the potent photodynamic cytotoxicity effect of Foslip encapsulated in silica

nanoparticles against colorectal cancer cells *in vitro*. In an effort to further improve those features, we aimed to test the nanoparticle in an animal model of colorectal cancer. For systemic delivery, the particles must be capable of passing out of the vasculature. Although, it is worth noting that the requirements for this are less stringent in the context of relatively permeable tumour-associated vasculature. Although dependent upon many factors including particle shape, surface chemistry and charge, it is generally accepted that for this to occur, nanoparticles must have a diameter of less than 200 nm (Matsumura and Maeda, 1986, Moghimi et al., 2012, Perrault et al., 2009).

The aims for this part of the project were to:

v. Assess the ability of polyclonal anti-CEA Affimer (II+III) tagged to Foslip-loaded silica nanoparticles to bind to colorectal cancer xenograft *in vivo*
vi. Quantify the specificity and fluorescent signal magnitude of Foslip-loaded nanoparticles
vii. Test the effectiveness of the Foslip-induced photodynamic therapy *in vivo.* This part of the project will be carried out in the near future as described in **section 2. 11. 5.**

In this chapter we show what we believe is the first successful and sufficiently controlled use of systemically delivered, anti-CEA Affimer targeted fluorescent nanoparticles for live *in vivo* colorectal cancer imaging.

5.3 Results

5.3.1 Dye-doped silica

To perform the *in vivo* analysis of binding of colorectal cancer cells by targeted nanoparticles, a series of experiments were carried out involving systemic nanoparticle delivery to a murine xenograft model of colorectal cancer.

5.3.1.1 Anti-CEA Affimer Foslip-loaded silica nanoparticles are detectable in vivo.

First, we confirmed that the IVIS small animal imaging system, which was to be used for all *in vivo* experimental imaging, was capable of detecting the fluorescent signal from the nanoparticles. The nanoparticles were suspended in PBS at 2 mg/ml, 200 µg/ml and 20 µg/ml and took fluorescent images with the appropriate wavelengths selected (**Figure 5.1**). A dose of 50 mg/kg was planned to be used in the targeting experiments, in line with other silica nanoparticle mouse experiments (Meng et al., 2011, Tivnan et al., 2012), which equates to approximately 625 µg/ml (assuming a six week old BALB/c nu/nu female mouse has a weight of 25 g and circulating blood volume of 80 ml/kg (Doevendans et al., 1998) with uniform nanoparticle distribution throughout the vascular compartment). The strong fluorescent images obtained with a 20 µg/ml suspension suggested that the IVIS system should be able to detect this concentration at the lowest threshold ~ 1×10^8 (p/sec/cm^3/sr)/(µW/cm^2)**.**

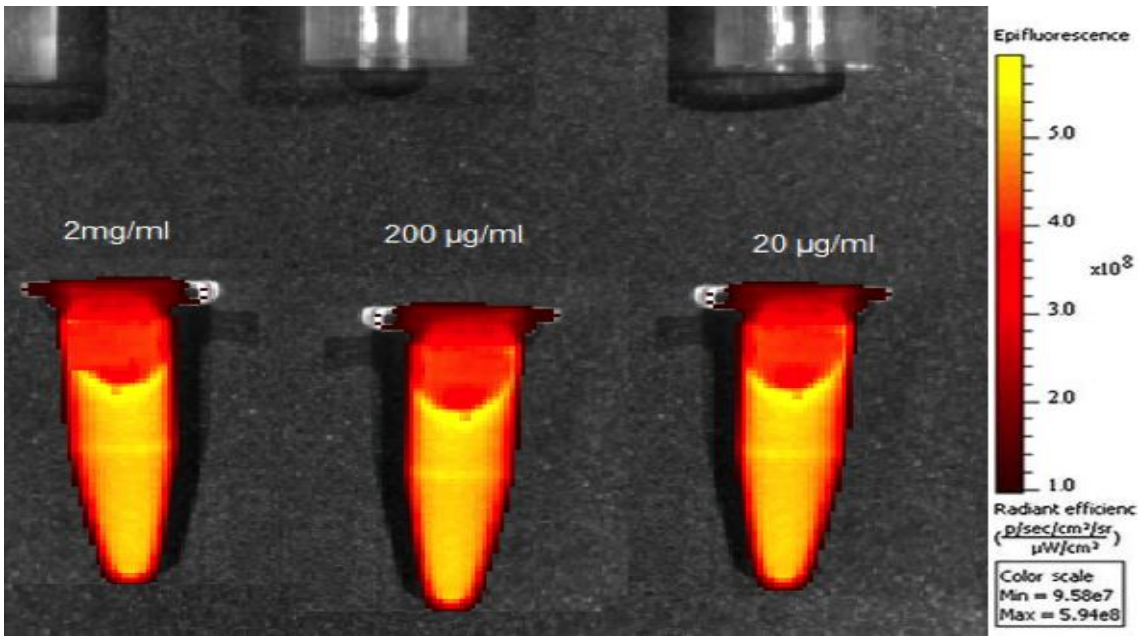

Figure 5. 1. Fluorescent signal detection from polyclonal anti-CEA (II+III) Affimer tagged nanoparticles.

Anti-CEA tagged nanoparticles suspended in PBS at 2 mg/ml, 200 µg/ml and 20 µg/ml then imaged using an IVIS small animal imaging system. Images were captured using IVIS with excitation filters at 615 - 665 nm and 8 s exposure time. Colour scale represents minimum = 9.58 x 10^7 and maximum = 5.94 x 10^8 (p/sec/cm^3/sr)/(µW/cm^2).

Next, the aim was to determine in a pilot experiment whether nanoparticles delivered systemically to mice were detectable, for how long, and their tissue location. Anti-CEA Affimer tagged nanoparticles (200 µg/ml) were injected into the tail veins of three 6-week-old BALB/c nu/nu female mice (without xenograft tumours) and live IVIS images were taken at 1, 24, and 48 h after injection (**Figure 5.2**). At 24 h post-injection, all three mice were imaged as normal,

allowing the IVIS system to auto-expose and detect more sensitively the fluorescence in the livers.

The injection in mouse-2 failed to deliver successfully to the tail vein as evidenced by the fact that particles were visible in the subcutaneous tissue of the tail at all time points. The other mice demonstrated systemic delivery of particles and accumulation in the liver within 24 h, consistent with hepatic excretion. At 24 h post-injection there appeared to be biliary fluorescence in addition to hepatic fluorescence. At 24 h post-injection, mouse -1 was sacrificed and the liver, kidneys, heart, brain and spleen were retrieved and imaged *ex vivo*. The same was done with a control mouse that had not been injected with nanoparticles. By 48 h, the hepatic fluorescence had decreased in mouse-3, leaving only biliary fluorescence. This was suggestive of hepatobiliary excretion, a feature observed previously in systemically delivered silica nanoparticles (Souris et al., 2010, Tiernan et al., 2015).

The mean fluorescence of the ex vivo liver from mouse-1 injected with nanoparticles at 24 h was 28.15 x 10^7 $psec^{-1}cm^{-2}sr^{-1}/\mu W/cm^2$, compared to a degree of natural fluorescence of 0.521 x 10^7 $psec^{-1}cm^{-2}sr^{-1}/\mu W/cm^2$ for the control mouse liver with a fold difference of 174 (Figure 3). The control mouse spleen and kidney exhibited no natural fluorescence whilst the spleen and kidney from treated exhibited low-level fluorescence (0.501 and 0.328 x 10^7 $psec^{-1}cm^{-2}sr^{-1}/\mu W/cm^2$ respectively). These findings confirmed that the nanoparticles were detectable in vivo, were deliverable systemically, and were metabolised and excreted predominately by the liver. Importantly, no photo-sensitivity reactions were observed in any of the injected mice.

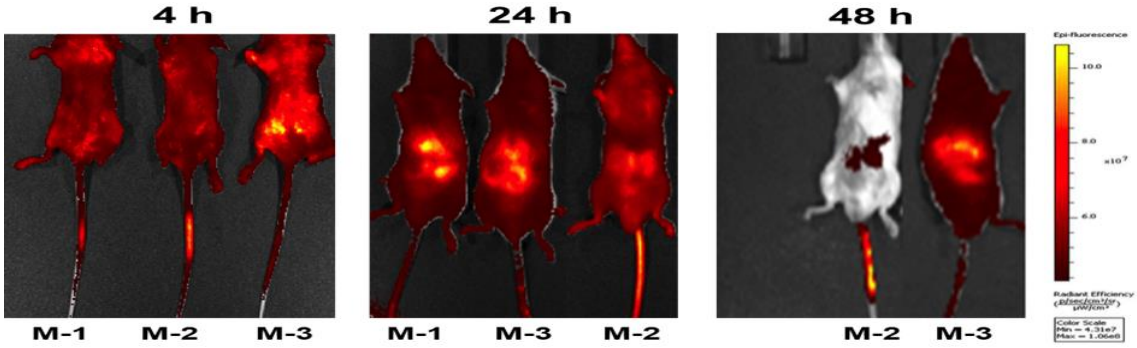

Figure 5. 2. Polyclonal anti-CEA Affimer (II+III) tagged silica nanoparticle bio-distribution.

Mice were injected with 200 µg/ml of anti-CEA Affimer tagged nanoparticles and were imaged in groups using IVIS at 4, 24 and 48 h time points as shown. Mouse-1 was sacrificed at 24 h post injection. Abbreviations denote:(M-1), mouse-1; (M-2), mouse-2; (M-3), mouse-3 and (h), hour. Images were captured using IVIS with excitation filters at 615 - 665 nm and 8 s exposure time. Colour scale represents minimum = 4.31 x 10^7 and maximum = 1.06 x 10^8 (p/sec/cm^3/sr)/(µW/cm^2).

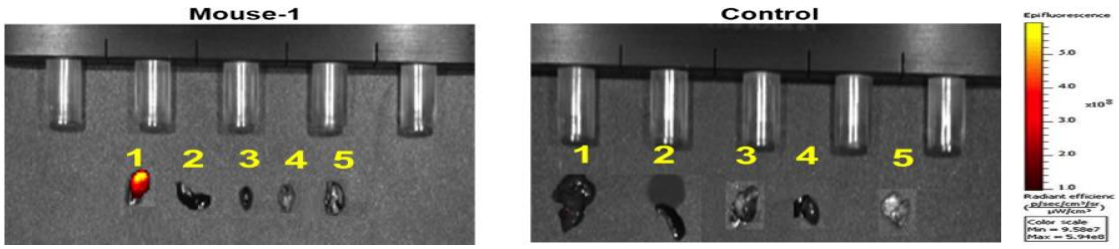

Figure 5. 3. Ex vivo imaging of nude mouse injected with polyclonal anti-CEA Affimer (II+III) tagged silica nanoparticle.

After 24 h of nanoparticles injection, organs were harvested from mouse-1 and imaged ex vivo, along with the same organs from a mouse that had not received the nanoparticles (control). Numbers denote: (1), liver; (2), spleen; (3), kidney; (4), heart and (5), brain. Images were captured using IVIS with excitation filters at 615 - 665 nm and 8 s exposure time. Colour scale represents minimum = 9.58 x 10^7 and maximum = 5.94 x 10^8 (p/sec/cm^3/sr)/(µW/cm^2).

5.3.1.2 Anti-CEA Affimer-functionalised silica nanoparticles for tumour-specific imaging in a murine xenograft model of colorectal cancer

For the next experiment, we aimed to test whether anti-CEA Affimer-functionalised nanoparticles were capable of tumour-specific labelling, as measured by fluorescence *in vivo*. Six-week-old BALB/c nu/nu female mice, bearing LS174T xenograft tumours in the right flank, were injected with 50 µl (1 mg/ml) either anti-CEA Affimer-functionalised Foslip-loaded nanoparticles (n=5) or control anti-myoglobin-functionalised Foslip-loaded (n=4) nanoparticles via tail vein. Then, fluorescent images were obtained at 1, 6 and 24 h post-injection (**Figure 5.4**). Two of the tail vein injections showed extravasation at the injection site in the anti-CEA Affimer-functionalised nanoparticles targeted group, leaving 3 test and 4 control mice. At 24 h post injection, 2 out of 3 mice demonstrated tumour-specific fluorescence in LS174T xenograft murine model of colorectal cancer. Importantly, no tumour cell fluorescence above background at any point was observed in mice injected with control anti-myoglobin Affimer-functionalised nanoparticles. Three additional LS174T tumour-bearing mice were injected with anti-CEA (n=2) and anti-myoglobin (n=1) Affimer-functionalised nanoparticles which were free of Foslip (**Figure 5.5**). No tumour cell fluorescence was observed in all three mice at lowest threshold ~ 2×10^7 *(p/sec/cm^3/sr)/(µW/cm^2)* confirming that the fluorescence seen in **Figure 5.4** was only Foslip-related. Fluorescence in other mouse tissues was not seen for either control or CEA-targeted particles, demonstrating that the particles have negligible non-specific or Affimer directed binding to host cells. The continued accumulation of tumour fluorescence with the CEA-targeted nanoparticles for up to 24 hours suggested that at least a

proportion of the conjugated particles are stable in the circulation for a minimum of 24 h.

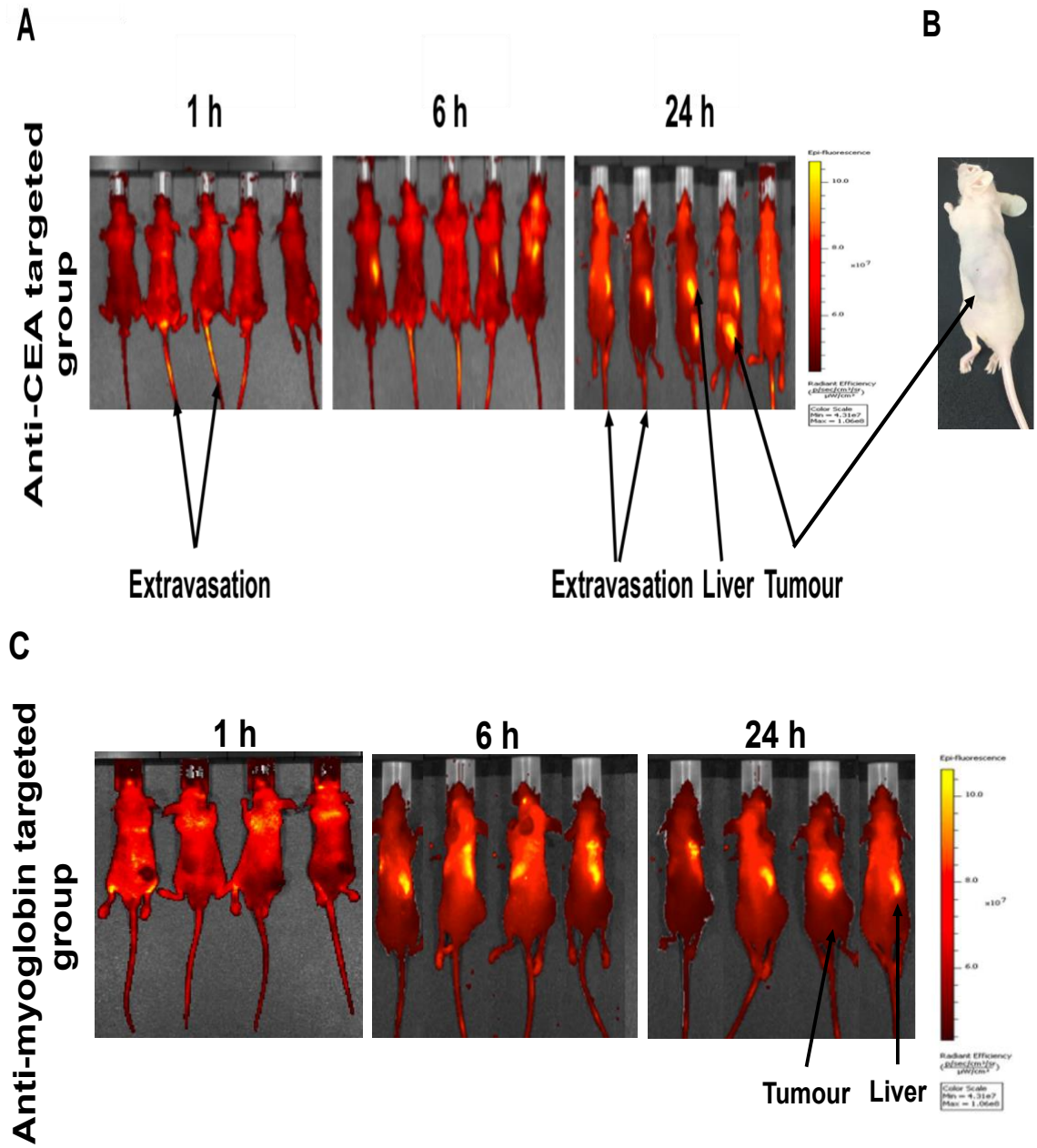

Figure 5. 4. Systemic administration of polyclonal anti-CEA (II+III) and anti-myoglobin Affimer-functionalised Foslip-loaded nanoparticles.

Mice were injected with anti-CEA Affimer tagged nanoparticles (n=5) or anti-myoglobin nanoparticles (n=4) through the tail vein. Mice were imaged at 1, 6 and 24 h post injection. Images were captured using IVIS with excitation filters at 615 - 665 nm and 8

s exposure time. Panel (A); images of mice injected with CEA-targeted nanoparticles; (B), photograph of mouse injected with anti-CEA Affimer tagged nanoparticles at 24 h showing the tumour xenograft and (C); images of mice injected with anti-myoglobin Affimer tagged nanoparticles. Note that a strong signal from anti-CEA targeted group is observed in the tumour in 2 mice. Colour scale represents minimum = 4.31 x 10^7 and maximum = 1.06 x 10^8 (p/sec/cm^3/sr)/(μW/cm^2).

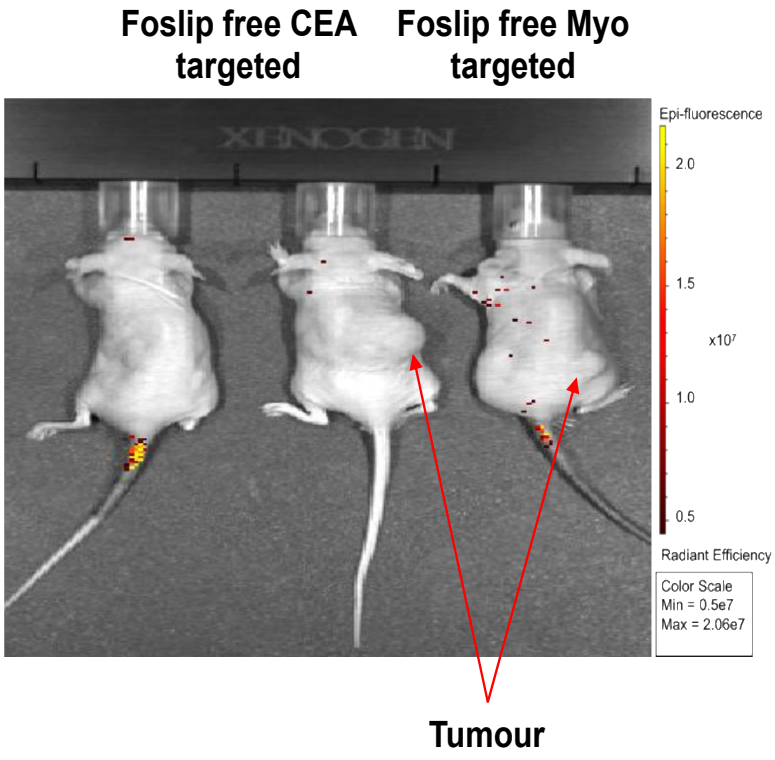

Figure 5. 5. Systemic administration of polyclonal anti-CEA (II+III) and anti-myoglobin Affimer-functionalised Foslip-free nanoparticles.

Mice were injected with anti-CEA Affimer tagged nanoparticles (n=2) or anti-myoglobin nanoparticles (n=1) through the tail vein. Mice were imaged at 24 h post injection. Images were captured using IVIS with excitation filters at 615 - 665 nm and 8 s exposure time. Colour scale represents minimum = 0.5 x 10^7 and maximum = 2.06 x 10^7 (p/sec/cm^3/sr)/(μW/cm^2).

Liver fluorescence was evident at 6 h in all mice (mean 59.1 x 10^6 $psec^{-1}cm^{-2}sr^{-1}/\mu W/cm^2$) and increased at 24 hours (85.8 x 10^6 $psec^{-1}cm^{-2}sr^{-1}/\mu W/cm^2$) (**Figure 5.6**). Hepatic localisation was confirmed by *ex vivo* imaging of isolated organs. There was no significant difference in liver fluorescence between mice injected with control particles and those injected with anti-CEA Affimer targeted particles at any time point.

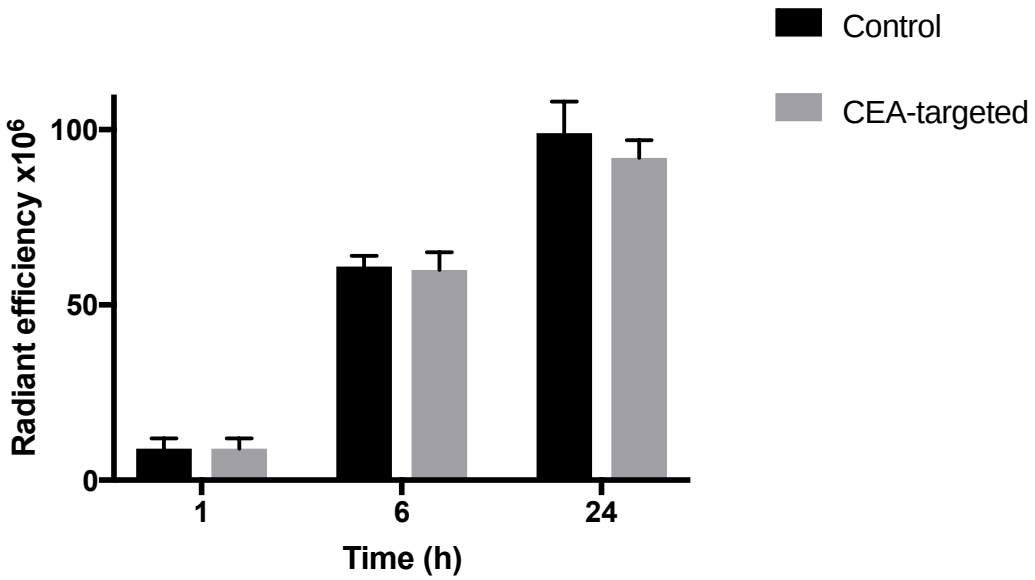

Figure 5. 6. Hepatic fluorescence following systemic delivery of control and polyclonal anti-CEA (II+III) Affimer targeted nanoparticles in vivo.

Data denote mean fluorescence (*SEM, n=3*). *Control: anti-myoglobin Affimer tagged nanoparticles.*

During this experiment, all mice had to be sacrificed at 24 h due to the tumour volume reaching the upper limit for acceptable diameter and due to skin ulceration. This has limited the understanding of the *in vivo* fluorescent imaging in our animal model and limited the conclusion that can be drawn from the presented data. One of the challenges faced in the *in vivo* experiment was the

success rate of tail vein injections. Tumour xenograft fluorescence appeared in 2 out of 3 mice injected with CEA-targeted nanoparticles but the intensity was less than what was expected when compared to Tiernan *et al* (Tiernan et al., 2015). When the background fluorescence parameter was set to eliminate the hepato-biliary fluorescence, the signal in the xenograft was weak. Therefore, we refined the protocol and repeated the experiment to better enhance the targeted fluorescent imaging in the xenograft.

5.3.1.3 Anti-CEA Affimer-functionalised Foslip-loaded nanoparticles allow tumour-specific imaging in LS174T xenograft model of colorectal cancer

In this experiment, the nanoparticles were suspended in sterile PBS at higher concentration (2 mg/ml). Xenografts were grown to ~10 mm in diameter then mice were injected with 150 µl of nanoparticles. Six mice in two groups were injected with either anti-CEA Affimer-targeted (n=6) or control anti-myoglobin Affimer-targeted (n=6) nanoparticles and imaged at 6, 24, 30 and 48 h. For better understanding of the biodistribution and fate of the nanoparticles one mouse, from each group, was sacrificed after imaging at each time point and organs were harvested then imaged *ex vivo*. The background fluorescence point was set high to eliminate the hepato-biliary fluorescence and ensure that any fluorescence to be seen in the xenograft was a real signal.

Tumour-specific fluorescence was seen in the xenograft of all mice that were injected with anti-CEA Affimer-functionalised Foslip-loaded nanoparticles as shown in **Figure 5.7**. The fluorescent signal was seen as early as 6 h, peaked at 30 h and remained in the xenograft at 48 h. Fluorescence ratio, which was defined

as the fluorescence of the tumour site over the fluorescence of normal tissue, at 6, 24, 30 and 48 h was 21, 88, 95 and 85 respectively.

In sharp contrast, no fluorescent signal was seen in any of the mice that were injected with anti-myoglobin Affimer-functionalised Foslip-loaded nanoparticles. The lateral view of the imaged mice also confirmed that the fluorescent signal was located at the xenograft tissue as shown in **Figure 5.8**. Fluorescence in the CEA-targeted tumours was significantly greater than controls at every time point after and including 6 h ($p<0.0001$, Wilcoxon Signed Rank Test). Mean tumour fluorescence increased from 6 h (mean 0.55×10^7 $psec^{-1}cm^{-2}sr^{-1}/\mu W/cm^2$) to 30 h (mean 9.415×10^7 $psec^{-1}cm^{-2}sr^{-1}/\mu W/cm^2$). Mice injected with control anti-myoglobin Affimer-functionalised nanoparticles showed no tumour fluorescence above background at any point.

The tumour tissue and other organs were harvested and imaged *ex vivo*. The tumour xenograft was halved and imaged. Tumour fluorescence was only detected in xenografts of mice injected with CEA-targeted nanoparticles as shown in **Figure 5.9.**

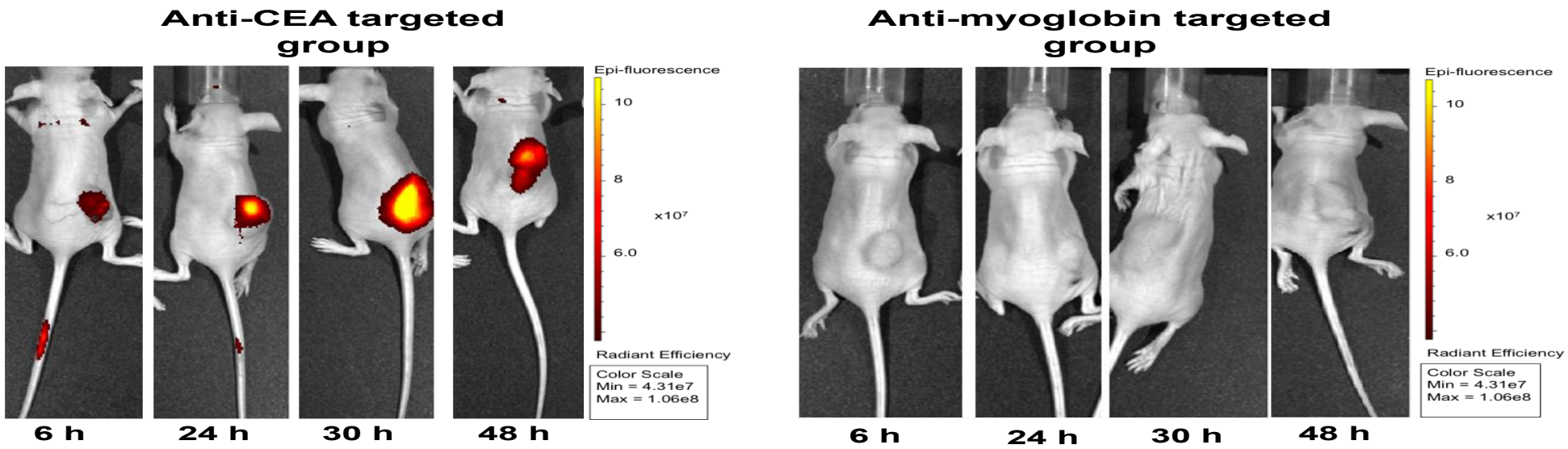

Figure 5. 7. Polyclonal anti-CEA (II+III) and anti-myoglobin Affimer-functionalised Foslip loaded nanoparticles tumour fluorescent imaging *in vivo*.

Mice were injected with 150 µl (2 mg/ml) *anti-CEA Affimer tagged nanoparticles (n=6) or anti-myoglobin nanoparticles (n=6) through the tail vein. Mice were imaged at 6, 24, 30 and 48 h post injection. An image of 1 representative mouse from both groups at each time point is shown. Images were captured using IVIS with excitation filters at 615 - 665 nm and 8 s exposure time. Note that a strong signal from anti-CEA Affimer targeted group is observed in the tumour at all time points. Colour scale bar: minimum = 4.31 x 10^7 and maximum = 1.06 x 10^8 $psec^{-1}cm^{-2}sr^{-1}/\mu W/cm^2$.*

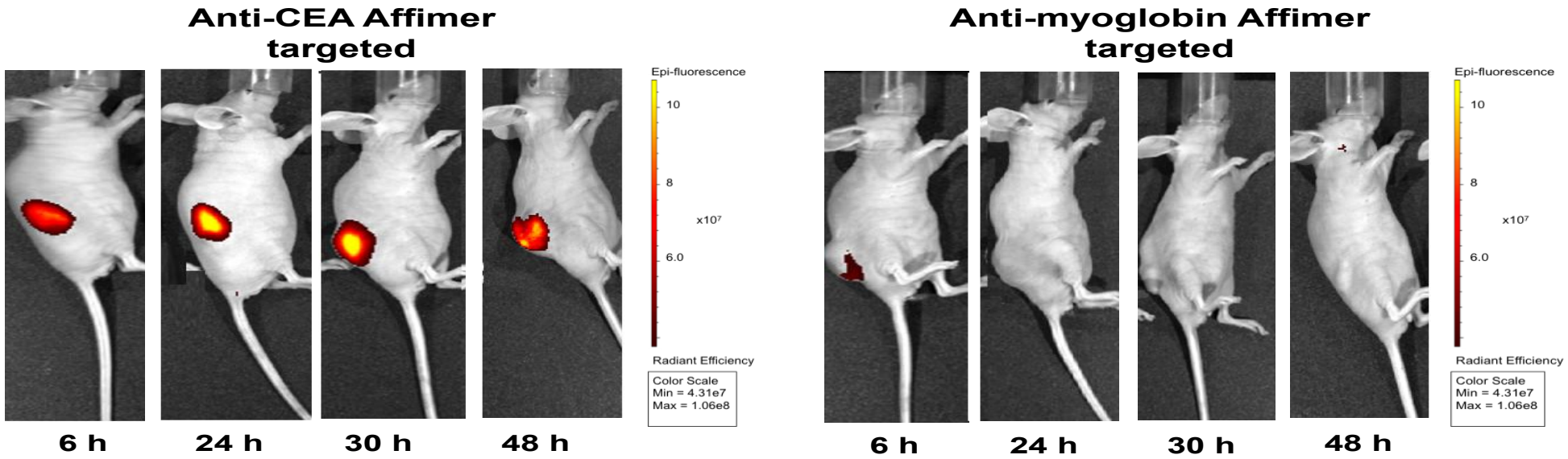

Figure 5. 8. Lateral view of polyclonal anti-CEA (II+III) and anti-myoglobin Affimer-functionalised Foslip loaded nanoparticles tumour fluorescent imaging *in vivo*.

Mice were injected with 150 µl (2 mg/ml) *anti-CEA Affimer tagged nanoparticles (n=6) or anti-myoglobin nanoparticles (n=6) through the tail vein. Mice were imaged at 6, 24, 30 and 48 h post injection. An image of 1 representative mouse from both groups at each time point is shown. Images were captured using IVIS with excitation filters at 615 - 665 nm and 8 s exposure time. Note that a strong signal from anti-CEA Affimer targeted group is observed in the tumour at all time points. Colour scale bar: minimum = 4.31 x 10^7 and maximum = 1.06 x 10^8 $psec^{-1}cm^{-2}sr^{-1}/\mu W/cm^2$.*

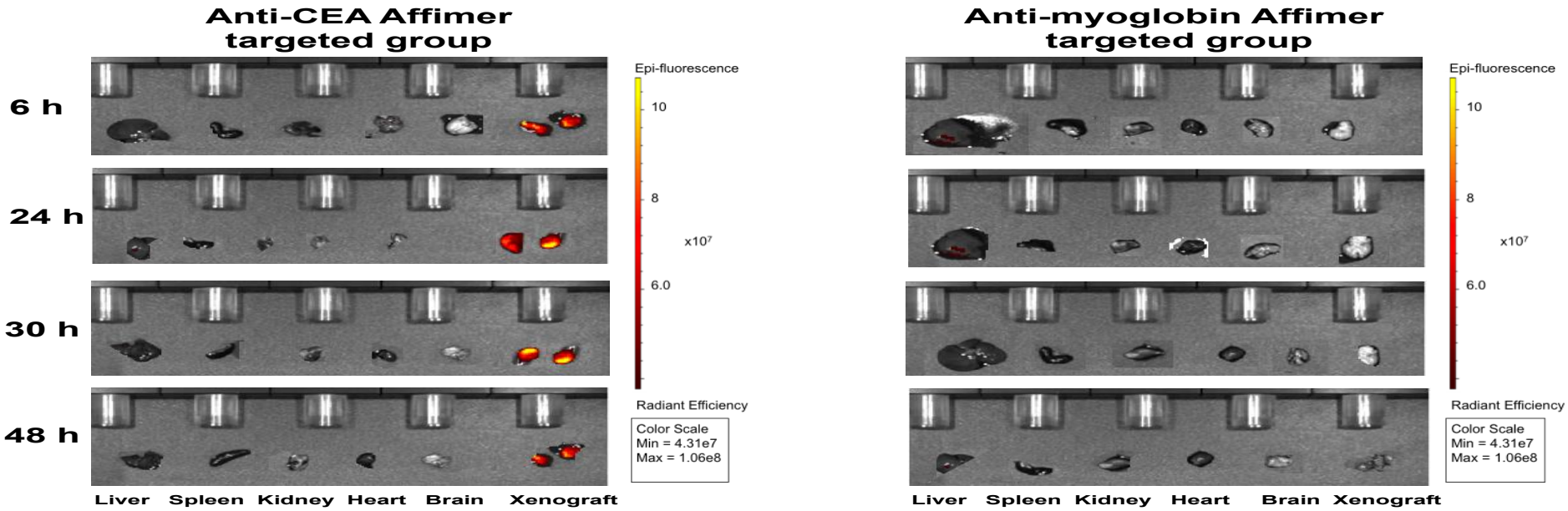

Figure 5. 9. *Ex vivo* fluorescence detection in LS174T mouse model.

Mice were injected with 150 µl (2 mg/ml) *anti-CEA Affimer tagged nanoparticles (n=6) or anti-myoglobin nanoparticles (n=6) through the tail vein. Mice were sacrificed at 6, 24, 30 and 48 h then organs were imaged. Each image represents a single mouse organs. Images were captured using IVIS with excitation filters at 615 - 665 nm and 8 s exposure time. Note that a strong signal from anti-CEA Affimer targeted group is observed in the tumour at all time points. Colour scale bar: minimum = 4.31 x 10^7 and maximum = 1.06 x 10^8 $psec^{-1}cm^{-2}sr^{-1}/\mu W/cm^2$.*

Mean fluorescence in xenografts of mice injected with anti-CEA Affimer targeted nanoparticles increased from 6 h (mean 0.65 x 10^7 p/sec/cm^2/sr/µW/cm^2) to 24 h (mean 9.9 x 10^7 p/sec/cm^2/sr/µW/cm^2) then plateaued (**Figure 5.10 A**). Importantly, the *ex vivo* imaging of the halved CEA-targeted xenografts showed fluorescence within the core of the xenograft and not only on the outer surface as shown in **Figure 5.9**. This is a very promising finding which suggested that the nanoparticles were able to accumulate within the tumour microenvironment and thereby likely to overcome the limitations of poor tissue penetration known to traditional chemotherapeutic drugs. To confirm this observation, confocal imaging was performed on histological sections from xenograft of a mouse injected with anti-CEA Affimer targeted and control nanoparticles (**Figure 5.10 B**). The xenograft tissue sample from the mouse injected with anti-CEA Affimer targeted nanoparticles showed fluorescent signal within the tumour microenvironment while no fluorescence was seen in the control xenograft. Collectively, these findings suggested a directed-nanoparticles delivery to the tumour site.

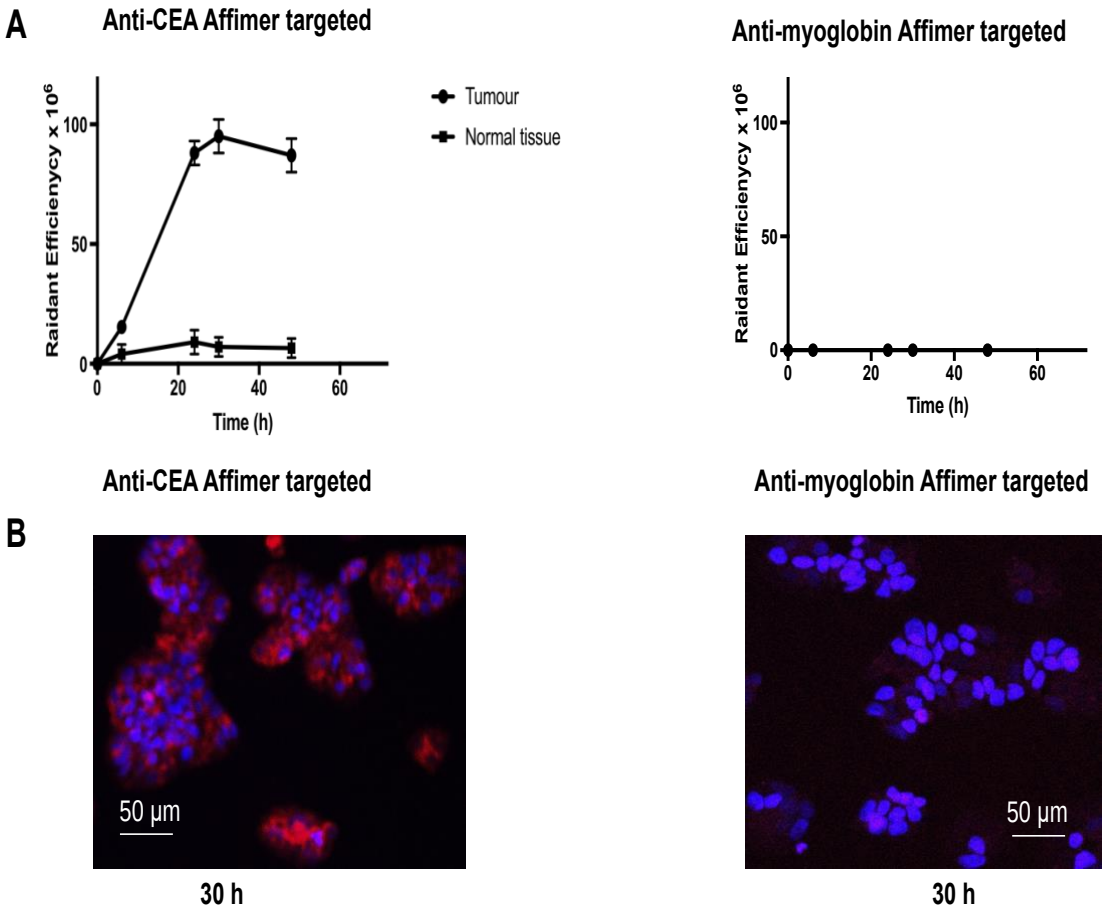

Figure 5. 10. Polyclonal anti-CEA (II+III) Affimer targeted nanoparticles fluorescent tumour detection *ex vivo*.

(*A), data are mean tumour fluorescence for ex vivo xenografts for mice injected with anti-CEA Affimer and anti-myoglobin Affimer targeted nanoparticles respectively (SEM, n=6). Normal tissue represents skin. (B), fluorescence histology images of tumour xenograft from mice injected with anti-CEA Affimer and anti-myoglobin Affimer targeted nanoparticles 30 h after injection respectively. Red and blue indicate Anti-CEA Affimer targeted nanoparticles and cell nuclei respectively.*

5.4 Discussion

In this chapter I sought to use nanotechnology to provide a concentrated fluorescent signal in an anti-CEA Affimer-mediated, tumour specific, *in vivo* imaging system. The *in vivo* experiments showed that anti-CEA tagged to the surface of Foslip-loaded silica nanoparticles successfully targeted LS174T tumour xenograft in a murine model of colorectal cancer.

The principle aim of this part of the project was to test whether the particles could reach the tumour cells following systemic delivery, and whether they showed tumour-specific binding. Tiernan *et al* were the first group to show specific tumour targeting of anti-CEA antibody- functionalised NIR669-doped silica nanoparticles in LS174T murine xenograft mouse model (Tiernan et al., 2015). Our data were comparable to their work and we have shown that the nanoparticle penetrated into the core of the xenograft. In addition, we used the photosensitiser Foslip instead of NIR669 dye which has the potential to induce photodynamic therapy. Cho *et al* (2010), synthesised magneto-fluorescent silica nanoparticles which were functionalised with cetuximab for the targeting and imaging of colorectal cancer (Cho et al., 2010). Cetuximab-conjugated magneto-fluorescent nanoparticles specifically targeted colon cancer cells that expressed EGFR on their cell membranes, and allowed specific fluorescence while the same particles produced significant MRI signal changes in a human colon cancer HCT116 xenograft mouse model. The authors did not the test the nanoparticles *in vivo* for xenograft specific-fluorescent imaging and the study lacked control nanoparticles and control cell lines. The only two other studies that have investigated specific targeting of dye-doped silica nanoparticles to tumours via systemic delivery were Tivnan *et al* (Tivnan et al., 2012) who used dendrimer-conjugated particles

targeted to neuroblastoma and Soster *et al* (Soster et al., 2012) who used PEG-conjugated particles targeted to colorectal cancer metastases, both in murine xenograft models. However, both studies used ‘bare’ nanoparticles as controls, which are potentially problematic in terms of demonstrating antigen-specific targeting, and both imaged fluorescence only on harvested organs *ex vivo*, which may relate to poor tissue penetration of the nanoparticles.

Our *in vitro* results suggested that non-specific binding could be a potential problem as normal cells can also express CEA. In an attempt to investigate this problem, non-tumour bearing mice were injected with anti-CEA targeted particles to evaluate non-specific binding to normal tissues. The data showed that significant fluorescence was only observed in the hepatobiliary system, which peaked at 24 hours and reduced by 48 h post-injection. Other studies that investigated the biodistribution and excretion of silica nanoparticles (Souris et al., 2010, Kumar et al., 2010, Park et al., 2009, Sarparanta et al., 2012), reported the same finding and found that a higher particle surface charge was associated with rapid excretion. Although LoVo cells are known to have higher level of CEA expression on the surface, LS174T cells were chosen for the xenograft model in this study because they showed the greatest fold difference in fluorescence between anti-CEA targeted and control nanoparticles *in vitro*.

Anti-CEA Affimer targeted nanoparticles showed significant time-dependent accumulation within tumours xenografts while control nanoparticles showed no tumour accumulation in tumour-bearing mice, ($p<0.0001$). Reassuringly, in all 6 tumour bearing mice injected with anti-CEA targeted nanoparticles specific fluorescence was observed and without obvious variations. This strongly suggest that anti-CEA Affimer is specific to CEA expressing cells. The 100% successful

rate at targeting tumour xenografts can also be attributed to the successful tail vein injections in the hands of experienced operators. This is supported by the fact that the fluorescent signal persisted in the tail in a number of mice during the early experiments. Therefore, these mice showed no tumour-specific fluorescence.

Although the small number of mice in this study did not allow appropriate correlation between the xenograft diameter and tumour-specific fluorescence, the greatest tumour-specific signal appeared to have the biggest xenograft diameter. *Ex vivo* examination of the xenografts at the end of the experiment, showed that the largest tumour was more vascularised and had invaded into the surrounding muscular tissue. Precise control of the depth of the subcutaneous injection of tumour cells into the flank region is technically very challenging and thereby deep injections could account for the intra-muscular tumour growth. Correlating the size of the xenograft diameter and volume with the fluorescent signal observed would be an interesting finding but in a bigger number of mice in each group.

The results of this work and to the best of my knowledge, are the first to describe successful live, *in vivo* fluorescent imaging of colorectal cancer in a murine animal model using Foslip-loaded silica nanoparticles. Despite the small number of mice in each arm of the study, the findings remain highly significant due to the lack of any detectable fluorescent signal in the xenograft tumours which were injected with control particles.

The next experiment, that is being carried out in the meantime, is to illuminate the xenograft with light in order to activate Foslip induced photodynamic therapy.

The experiment will inform the efficacy of photodynamic therapy of the targeted Foslip-loaded nanoparticle and hence its theranostic capabilities.

Our data shows great promise for clinical translation in the context of intra-operative imaging. Of clinical interest, the technology is applicable to imaging any tissue or pathology using Affimers targeting appropriate specific biomarkers and so is likely to be applicable to therapy of other solid tumours.

Chapter Six

Summary

6 Summary

I aimed to develop a multi-functional tumour-specific nanoparticle that would allow fluorescent imaging and photodynamic killing of colorectal cancer cells. The ultimate aim was to develop a real-time molecular imaging platform for laparoscopic colorectal cancer surgery to aid intra-operative staging, identify tumour margins and eradicate residual tumour cells following personalised radical resection. To achieve this, the project was divided into a series of distinct steps that progressed logically to *in vivo* testing of a theranostic nanoparticle with successful outcomes.

6.1 Anti-CEA Affimer as a novel bioreceptor

The bioreceptor component of this work was fundamental. The performance of the nanoparticle was completely dependent upon the ability of the bioreceptor to discriminate between normal colorectal tissue and CEA-expressing tumour tissue. The perfect fluorescent molecular bio-imaging system would fail if the bioreceptor was unable to recognise its respective target. Accordingly, the first aim of the project was to identify a suitable bioreceptor and ensure that it was specific to CEA. The choice of target, CEA, was based on evidence from previous publication at the University of Leeds by Tiernan *et al* (Tiernan et al., 2013). CEA has a high sensitivity and specificity in discriminating colorectal cancer cells from normal mucosal cells. The anti-CEA Affimer was chosen as the targeting mechanism for this project based on the binding specificity to CEA *in vitro* when compared to the antibody. Dr Shamsuddin's work on anti-CEA Affimer phage display, sub-cloning and purification was highly valuable to the success of this project. Although there are other novel methods of targeting membrane-bound

molecules such as aptamers and peptides (Farokhzad and Langer, 2006), an Affimer was the preferred choice in the interests of time and availability of the characterised protein at the University of Leeds. Two other anti-CEA bioreceptors from other amino-acid protein scaffolds were reported by other research teams during the time of this project, which were Affibodies and designed ankyrin repeat proteins (DARPin) (Sainz Pastor, 2008, Ahlgren, 2007).

Affibody molecules are small (molecular weight ~ 6 kDa) affinity proteins derived from the Staphylococcus aureus surface protein A. The IgG binding domain Z, consists of 58 amino acids that form three-helix bundle and is used as a scaffold (Nilsson et al., 1997). Randomisation of 13 amino acids takes place on the surface of Z domain on helix one and two resulting in a large combinatorial library which could potentially bind to any target protein (Nord et al., 1997, Nord et al., 1995).

Anti-CEA Affibody was identified by screening against A3B3 recombinant domain of CEA protein (Ahlgren, 2007). The clones of Affibody were identified and their binding specificity to A3B3 CEA was only characterised by a dot blotting assay only (Ahlgren, 2007). The expression yield for anti-CEA Affibody was low while only one out of three purified clones showed binding to full length CEA protein. The results from their dot blotting assay was further compromised by binding of the negative control to A3B3 CEA. To date, there are no reports in the literature on successful application of anti-CEA Affibody for targeted colorectal cancer imaging or therapy. On the other hand, Shi *et al* (2017), produced a dimeric Affibody with a 0.9 nM affinity against platelet-derived growth factor receptor β (PDGFRβ) (Shi et al., 2017) which is known to be overexpressed on the pericytes of many types of tumours (Paulsson et al., 2009). The photosensitiser infra-red

700DX N-hydroxysuccinimide ester (IR700) was then conjugated to anti-PDGFRβ Affibody for targeted vascular-photodynamic therapy in mice bearing LS174T tumour grafts. Systemic administration of PDGFRβ-affibody-IR700 conjugates in mice bearing LS174T tumour grafts (n=3), followed by illumination allowed IR700-mediated PDT damage to tumour blood vessels thereby reducing the average mass of tumour grafts to approximately 20–30% of that of the control (Shi et al., 2017). However, the study lacked control Affibody-IR700 conjugate while the control animals were either mice injected with PBS or mice kept in the dark. The lack of appropriate control mice rendered the *in vivo* findings questionable.

Designed ankyrin repeat proteins (DARPins) are small synthetic scaffolds (18 kDa) derived from the human ankyrin repeat domain and consist of a fixed region which represents the scaffold and a variable region which interacts with the target molecule (Binz et al., 2003, Tamaskovic et al., 2012). Six randomised surface-exposed amino acid residues per repeat module takes place in the variable region. Expression of functional DARPins can be performed in *E. coli* with yields reaching ~ 200 mg/l purified protein in simple shake flask cultures (Binz et al., 2003). DARPins have shown to detect positive epidermal growth factor receptor-2 (HER-2) on paraffin-embedded breast cancer tissue sections with similar sensitivity and higher specificity to antibody (p=0.0005) (Theurillat et al., 2010). In another *in vitro* study, anti- HER-2 DARPins showed that binding of two DARPins connected by a short linker, one targeting extracellular subdomain I and the other subdomain IV, causes much stronger cytotoxic effects on the HER2-positive breast cancer cell line BT474 (Jost et al., 2013). To date there is only one report in the literature on DARPins targeted against CEA. The specificity of

CEA-binding DARPins isolated by screening against the N-A1 recombinant domain of CEA was only characterised by immunohistochemical staining on human adenocarcinoma tissue sections (Sainz Pastor, 2008). Therefore, the lack of robust evidence on binding specificity of anti-CEA DARPins in colorectal cancer cells prevented its use in our targeting strategy.

For the purpose of this study, anti-CEA antibodies were readily available as alternative bioreceptors should the Affimer targeting strategy failed. There are a number of monoclonal anti-CEA antibodies against different epitopes on CEA for research purposes (Nap et al., 1992, Hass et al., 1991) while other radio-labeled anti-CEA antibodies are in clinical trials (Wong et al., 2006, Wong et al., 2000). For example, in radioimmunoguided surgery (RIGS), 125I-labeled antibody was given before or during surgery and a hand-held gamma-detecting probe was used to locate tumour tissue (Mayer et al., 2000, Mery et al., 2006, Kim et al., 2005). Anti-CEA Affimers have properties that could be useful for such application. When anti-CEA Affimer was conjugated to the surface of NIR669-dye-dope silica nanoparticle, it was successful at showing tumour-specific fluorescent labelling in three different cell lines of colorectal cancer *in vitro*. The control nanoparticle, bearing a control Affimer, showed negligible fluorescent labelling which indicated specific binding to target and minimal off-target effects. It is possible that an alternative Affimer could be substituted on our nanoparticle to target different tumours that express specific membrane-bound antigens, although this would require characterisation via *in vitro* and *in vivo* studies to guarantee specificity and sensitivity of targeting. The difficulty would be related to identification of a specific tissue marker for targeting with Affimer. Human CEA-family belongs to the immunoglobulin (Ig) superfamily and it is a large trans-membrane

glycoprotein with an apparent molecular weight (MW) ~ 200 kDa of which about 50% comprise carbohydrates (Beauchemin et al., 1987, Hammarström and Baranov, 2001, Hammarström, 1999). The CEA subfamily is very complex involving a large number of genes, which makes it a complicated marker to study (Nap et al., 1992). Since our group had published their work on CEA as being the preferred tissue biomarker for colorectal cancer in 2013, there has been no other published work suggesting an alternative tissue target (Tiernan et al., 2013).

6.2 Characterisation of anti-CEA Affimer

The results of our study suggested that the anti-CEA Affimers are promising bioreceptors and showed excellent specificity to CEA in different applications such as immunoflourescent imaging on tumour cells, direct ELISA, affinity precipitation assays and most importantly as bioreceptors on the surface of functionalised silica nanoparticles for *in vivo* imaging. However, further work needs to be done to distinguish which protein epitopes the anti-CEA Affimers bind to, as there are seven protein domains within CEA. Additionally, investigation of whether the anti-CEA Affimers from three different binders recognise the same, overlapping or different epitopes would be very interesting to explore since each of them contained two unique variable loops.

Linking the anti-CEA Affimer to the surface of functionalised silica nanoparticles in this study highlighted the importance of oriented bioreceptor conjugation as a determinant factor in obtaining sensitive and effective fluorescent imaging. The introduction of a single cysteine residue at the C- terminus of anti-CEA Affimer has allowed site-directed conjugation onto the nanoparticle surface and thereby facilitated specific CEA targeting. It is reasonable to assume that the small size

of anti-CEA Affimer (12 KDa, 3 nm) was advantageous when compared to the monoclonal anti-CEA antibody (150 KDa, 14 nm). The small size of Affimers would increase their density on the surface of nanoparticles and generate more binding sites for targeting CEA. In addition, the small size of Affimers could potentially position the nanoparticle closer to colorectal cancer cell's surface. Initially, three anti-CEA Affimer clones were purified as bioreceptors, but anti-CEA Affimer I expression yield was low and it precipitated upon storage and it was excluded from further analysis. The Affimers are monoclonal and bind to a single epitope but the polyclonal characteristics of antibodies can be mimicked if Affimers are mixed. We showed that bi-Affimer conjugation to silica nanoparticle improved the fluorescent imaging of colorectal cancer cells.

6.3 Theranostic nanoparticles

Nanotherapeutics are designed to overcome the major constraints of conventional medicine such as low solubility and stability, non-adequate pharmacokinetic profiles and side effects. To date, many nanoplatforms have been applied for the delivery of mTHPC, one of the most potent clinically approved photosensitisers. Foslip has been intensively tested in different *in vitro* preclinical models (2D and 3D tumour cell cultures) (Gibot et al., 2014, Gaio et al., 2016, Yakavets et al., 2019a), while complete PDT studies, including biodistribution, pharmacokinetics and PDT efficacy in tumour-bearing *in vivo* animal models are rather sparse (Lassalle et al., 2009, Brezániová et al., 2018). This situation seriously complicates the assessment of the benefits of Foslip-based nanoparticles. We fabricated an anti-CEA Affimer targeted, Foslip-loaded silica nanoparticle that allowed tumour-specific fluorescent labelling and cytotoxicity *in vitro*.

The Foslip-loaded nanoparticle also showed tumour-specific fluorescent labelling in a xenograft mouse model of colorectal cancer using one of the three colorectal cancer cell lines. The dark toxicity of Foslip-loaded nanoparticles was significantly lower than that of free drug and improved selectivity against colorectal cancer cells. Although the *in vivo* study did not assess the photodynamic cytotoxicity of the nanoparticle, due to time limitations, the following observations make the results very powerful. First, anti-CEA Affimer targeted nanoparticles allowed tumour-specific fluorescence in all of the tumour-bearing mice and none of the mice injected with control nanoparticles produced a significant result, all of which suggest a highly sensitive nano-system. Second, the fluorescent signal in the hepatic system was the only observed signal in normal tissues, due to hepatobiliary excretion, indicating that the targeted nanoparticles are specific to the tumour xenograft. Third, the observed fluorescent signal persisted in the tumour tissue beyond 48 hours following injection, indicating stability *in vivo.* The nanoparticle effectively solved the problem of Foslip low tumour localisation, providing easy administration *in vivo*. A common limitation of other nanoparticle-based photosensitisers is poor drug release at the target site. We achieved a reasonable balance between the circulating nanoparticle plasma stability and efficient Foslip fluorescent imaging by tailoring the delivery to the tumour tissue using anti-CEA Affimer. However, due to the variability of processes involved in nanoparticles distribution at various stages (blood circulation, tumour tissue distribution, intracellular accumulation), the parameters adopted for the design of ideal nanoparticles should be extensively investigated.

These findings thus far are possibly the key for translating this work into clinical trials. The major advantage of the system is that silica nanoparticles have low

toxicity profile. Cyanine5.5-doped silica nanoparticles have entered into a phase I clinical trial in metastatic melanoma cancer patients (n=5) in 2014 (Phillips et al., 2014). The near infra-red-dye-doped silica nanoparticles were radiolabelled with 124I for positron emission tomography (PET) imaging of lymph node and functionalised with cyclic arginine–glycine–aspartic acid (cRGDY; targeting bioreceptor for tumour and tumour endothelial cells) peptides for molecular targeting. The functionalised nanoparticles, with diameter of ~ 10 nm, indicated favourable pharmacokinetics and bio-distribution profiles and safety in five patients. The particles were also found to be 20-30 times brighter and more stable than Cy5.5 in solution suggesting excellent biocompatibility for nuclear imaging. The nanoparticles were excreted through the renal system and exhibited low liver uptake at 72 h post intravenous injection. Importantly, no toxic or adverse events attributable to the particles were observed. However, the targeting efficiency of the particles was very poor as only ~0.01% of the injected dose was localised in the tumour site. This was the first report of radiolabelled targeted nanoparticle imaging in humans and helped to establish comprehensive understanding of the biological profiles of the silica nanoparticles *in vivo*. Since the completion of the phase I clinical trial, the same group have functionalised the same nanoparticle with different surface targeting peptides and showed improved tumour localisation in animal models of melanoma and prostate cancers (Chen et al., 2018, Chen et al., 2019).

Foslip is approved for clinical use so translation into clinical trials could potentially be rapid. From the present data, it seems likely that translating an anti-CEA Affimer based fluorescent nanoparticle into a commercial platform is also feasible. This is based on the inexpensive and rapid production of anti-CEA

Affimer using a bacterial expression system for large-scale production, together with simple and cost-effective fabrication of the Affimer-based nanoparticle. For this to be effective, strong bridges must continue to develop between academia, industry, and clinical practice, and the fact that Affimer technology is being commercially developed by Avacta Life Sciences is testament to this. However, there remains a gap in our understanding of the immunogenicity and toxicity profile of Affimers *in vivo*. Investigations into the bio-distribution, systemic clearance and protein-protein interactions in immune competent animals are all important questions yet to be answered.

An interesting recent review on FDA-approved nanomedicines, has shown a steady rise in the number of approval of nano-formulations since 1990s (Bobo et al., 2016). On review of these products, it is evident that the majority of the approved nanomedicine are liposomal- and polymeric nanoparticles-based such as liposomal irinotecan (Ko et al., 2013, Kipps et al., 2017, Wang-Gillam et al., 2019) and Eligard (polymer DL-Lactide-coglycolide)(Braeckman and Michielsen, 2014) for advanced pancreatic and prostate cancers. Liposomal irinotecan has also entered phase II clinical trial for patients with metastatic colorectal cancer and showed acceptable safety profile (Chibaudel et al., 2016).

The number of clinical trials that have been granted investigational new drugs (IND) approval, has also increased in the last decade for micellar, metallic and protein-based particles (Chawla et al., 2010, Libutti et al., 2010, Pottier et al., 2014, Marill et al., 2014) suggesting that more new products are likely to be approved in the near future.

6.4 Limitations

The design of the experiments in this project would benefit from a number of changes. If possible, anti-CEA Affimer sensitivity and specificity to CEA should be tested using immunohistochemical studies on a large cohort of matched normal and malignant human colorectal cancer tissue specimens and lymph nodes to statistically confirm the findings in Chapter 3. The intra-operative lymph node status is arguably the single most important factor in determining the type of resection performed. A preferred model for testing the delivery and fate of anti-CEA Affimer functionalised nanoparticles would be to inject them into the circulation of freshly resected colon cancer specimen and ascertain whether they were present in the tumour tissue or lymph nodes post-injection. Immunohistochemical and immunofluorescence characterisation of mice organs and xenograft would help understanding the fate and bio-distribution of the nanoparticles post-injection.

6.5 Future work

The future prospect for targeted nanoparticles is excellent because of several current promising formulations under preclinical and clinical developments for colorectal cancer which in the near future, and after satisfying the high standards of safety and efficacy for patients required by the FDA, could rapidly enter the market. The next step is to assess the photodynamic therapy efficacy of the nanoparticle in the animal model to ascertain whether our *in vitro* findings can be reproduced *in vivo*. This work is currently in progress with data potentially available in the near future. There is undoubtedly potential for further optimisation of the nanoparticle, and the linkage chemistry to the anti-CEA Affimer. Evaluation on batch-to-batch variation of anti-CEA Affimer for large scale production is

necessary and reproducibility of functionalised nanoparticles in mass production is equally important. Another avenue for research is related to the definition of optimal parameters of photodynamic therapy treatment with Foslip-loaded nanoparticles and toxicology studies on the fully functionalised nanoparticle.

Following this, a larger study using an orthotopic murine model of colorectal cancer, possibly with a metastatic model alongside, would provide the necessary information to inform a first-in-man study. The rapid growth of nanotechnology and advancements in synthetic binding protein production are likely to revolutionise cancer therapies, including PDT. They hold great promise for future targeted drug delivery and medical imaging. All of the above will support the rational administration of precise-targeted nanoformulations containing the most effective drug combination.

References

7 References

ABDELGHANY, S. M., SCHMID, D., DEACON, J., JAWORSKI, J., FAY, F., MCLAUGHLIN, K. M., GORMLEY, J. A., BURROWS, J. F., LONGLEY, D. B. & DONNELLY, R. F. 2013. Enhanced antitumor activity of the photosensitizer meso-tetra (N-methyl-4-pyridyl) porphine tetra tosylate through encapsulation in antibody-targeted chitosan/alginate nanoparticles. *Biomacromolecules,* 14**,** 302-310.

ABDOLAHI, M., SHAHBAZI-GAHROUEI, D., LAURENT, S., SERMEUS, C., FIROZIAN, F., ALLEN, B. J. & MULLER, R. N. 2013. Synthesis and in vitro evaluation of MR molecular imaging probes using J591 mAb-conjugated SPIONs for specific detection of prostate cancer. *Contrast Media Mol Imaging,* 8**,** 175-84.

ABRAHAMSE, H. & HAMBLIN, M. R. 2016. New photosensitizers for photodynamic therapy. *Biochemical Journal,* 473**,** 347-364.

ACPGBI 2007. *Guidelines for the management of colorectal cancer*, Association of Surgeons of Great Britain and Ireland.

AGOSTINIS, P., BERG, K., CENGEL, K. A., FOSTER, T. H., GIROTTI, A. W., GOLLNICK, S. O., HAHN, S. M., HAMBLIN, M. R., JUZENIENE, A. & KESSEL, D. 2011. Photodynamic therapy of cancer: an update. *CA: a cancer journal for clinicians,* 61**,** 250-281.

AHLGREN, S. 2007. Selection of CEA and VEGFR2 Binding Affibody® Molecules Using Phage Display.

AITKEN, D. R., HINKLE, G. H., THURSTON, M. O., TUTTLE, S. E., MARTIN, D. T., OLSEN, J., HAAGENSEN, D. E., JR., HOUCHENS, D. & MARTIN, E. W., JR. 1984. A gamma-detecting probe for radioimmune detection of CEA-producing tumors. Successful experimental use and clinical case report. *Dis Colon Rectum,* 27**,** 279-82.

ALANDER, J. T., KAARTINEN, I., LAAKSO, A., PÄTILÄ, T., SPILLMANN, T., TUCHIN, V. V., VENERMO, M. & VÄLISUO, P. 2012. A review of indocyanine green fluorescent imaging in surgery. *Journal of Biomedical Imaging,* 2012**,** 7.

ALLISON, R. R. & SIBATA, C. H. 2010. Oncologic photodynamic therapy photosensitizers: A clinical review. *Photodiagnosis and Photodynamic Therapy,* 7**,** 61-75.

ANDREW, H., GOSSEDGE, G., CROFT, J., CORRIGAN, N., BROWN, J. M., WEST, N., QUIRKE, P., TOLAN, D., CAHILL, R. & JAYNE, D. G. 2016. Next Generation intraoperative Lymph node staging for Stratified colon cancer surgery (GLiSten): a multicentre, multinational feasibility study of fluorescence in predicting lymph node-positive disease.

ANKERSMIT, M., VAN DER PAS, M., VAN DAM, D. & MEIJERINK, W. 2011. Near infrared fluorescence lymphatic laparoscopy of the colon and mesocolon. *Colorectal Disease,* 13**,** 70-73.

ARNOLD, M. W., SCHNEEBAUM, S., BERENS, A., PETTY, L., MOJZISIK, C., HINKLE, G. & MARTIN, E. W., JR. 1992. Intraoperative detection of colorectal cancer with radioimmunoguided surgery and CC49, a second-generation monoclonal antibody. *Ann Surg,* 216**,** 627-32.

ASHITATE, Y., STOCKDALE, A., CHOI, H. S., LAURENCE, R. G. & FRANGIONI, J. V. 2012. Real-Time Simultaneous Near-Infrared Fluorescence Imaging of Bile Duct and Arterial Anatomy. *Journal of Surgical Research,* In Press, Corrected Proof.

ASHRAF, S. Q., UMANA, P., MOESSNER, E., NTOUROUPI, T., BRUENKER, P., SCHMIDT, C., WILDING, J. L., MORTENSEN, N. J. & BODMER, W. F. 2009. Humanised IgG1 antibody variants targeting membrane-bound carcinoembryonic antigen by antibody-dependent cellular cytotoxicity and phagocytosis. *British Journal of Cancer,* 101**,** 1758-1768.

AZHDARZADEH, M., ATYABI, F., SAEI, A. A., VARNAMKHASTI, B. S., OMIDI, Y., FATEH, M., GHAVAMI, M., SHANEHSAZZADEH, S. & DINARVAND, R. 2016. Theranostic MUC-1 aptamer targeted gold coated superparamagnetic iron oxide nanoparticles for magnetic resonance imaging and photothermal therapy of colon cancer. *Colloids Surf B Biointerfaces,* 143**,** 224-232.

AZZOUZI, A. R., VINCENDEAU, S., BARRET, E., CICCO, A., KLEINCLAUSS, F., VAN DER POEL, H. G., STIEF, C. G., RASSWEILER, J., SALOMON, G., SOLSONA, E., ALCARAZ, A., TAMMELA, T. T., ROSARIO, D. J., GOMEZ-VEIGA, F., AHLGREN, G., BENZAGHOU, F., GAILLAC, B., AMZAL, B., DEBRUYNE, F. M., FROMONT, G., GRATZKE, C., EMBERTON, M. & GROUP, P. C. M. S. 2017. Padeliporfin vascular-targeted photodynamic therapy versus active surveillance in men with low-risk prostate cancer (CLIN1001 PCM301): an open-label, phase 3, randomised controlled trial. *Lancet Oncol,* 18**,** 181-191.

BAGWE, R. P. & KHILAR, K. C. 2000. Effects of intermicellar exchange rate on the formation of silver nanoparticles in reverse microemulsions of AOT. *Langmuir,* 16**,** 905-910.

BAGWE, R. P., MISHRA, B. K. & KHLIAR, K. C. 1999. Effect of chain length of oxyethylene group on particle size and absorption spectra of silver nanoparticles prepared in non-ionic water-in-oil microemulsions. *Journal of Dispersion Science and Technology,* 20**,** 1569-1579.

BAKER, M. 2015. Reproducibility crisis: Blame it on the antibodies. *Nature News,* 521**,** 274.

BALL, D. J., VERNON, D. I. & BROWN, S. B. 1999. Research Note: The High Photoactivity of m-THPC in Photodynamic Therapy. Unusually Strong

Retention of m-THPC by RIF-1 Cells in Culture. *Photochemistry and photobiology,* 69**,** 360-363.

BARA, J. T., BARA, T., BANCU, S., EGYED, I. Z., GURZU, S., BANCU, L., AZAMFIREI, L. & FEHER, A. 2011. Sentinel lymph node mapping in colorectal cancer. *Chirurgia (Bucharest, Romania: 1990),* 106**,** 195-198.

BARATHAN, M., MARIAPPAN, V., SHANKAR, E. M., ABDULLAH, B. J., GOH, K. L. & VADIVELU, J. 2013. Hypericin-photodynamic therapy leads to interleukin-6 secretion by HepG2 cells and their apoptosis via recruitment of BH3 interacting-domain death agonist and caspases. *Cell Death Dis,* 4**,** e697.

BASO, A. O. B. S. A. 2009. Surgical guidelines for the management of breast cancer. *European journal of surgical oncology,* 35**,** S1-S22.

BEAUCHEMIN, N., BENCHIMOL, S., COURNOYER, D., FUKS, A. & STANNERS, C. 1987. Isolation and characterization of full-length functional cDNA clones for human carcinoembryonic antigen. *Molecular and cellular biology,* 7**,** 3221-3230.

BECHET, D., COULEAUD, P., FROCHOT, C., VIRIOT, M.-L., GUILLEMIN, F. & BARBERI-HEYOB, M. 2008. Nanoparticles as vehicles for delivery of photodynamic therapy agents. *Trends in biotechnology,* 26**,** 612-621.

BERLANDA, J., KIESSLICH, T., ENGELHARDT, V., KRAMMER, B. & PLAETZER, K. 2010. Comparative in vitro study on the characteristics of different photosensitizers employed in PDT. *Journal of Photochemistry and Photobiology B: Biology,* 100**,** 173-180.

BETZ, C. S., RAUSCHNING, W., STRANADKO, E. P., RIABOV, M. V., VOLGIN, V. N., ALBRECHT, V., NIFANTIEV, N. E. & HOPPER, C. 2012. Long-term outcomes following foscan®-PDT of basal cell carcinomas. *Lasers in surgery and medicine,* 44**,** 533-540.

BINZ, H. K. & PLÜCKTHUN, A. 2005. Engineered proteins as specific binding reagents. *Current opinion in biotechnology,* 16**,** 459-469.

BINZ, H. K., STUMPP, M. T., FORRER, P., AMSTUTZ, P. & PLÜCKTHUN, A. 2003. Designing repeat proteins: well-expressed, soluble and stable proteins from combinatorial libraries of consensus ankyrin repeat proteins. *Journal of molecular biology,* 332**,** 489-503.

BIPAT, S., GLAS, A. S., SLORS, F. J., ZWINDERMAN, A. H., BOSSUYT, P. M. & STOKER, J. 2004a. Rectal cancer: local staging and assessment of lymph node involvement with endoluminal US, CT, and MR imaging--a meta-analysis. *Radiology,* 232**,** 773-83.

BIPAT, S., GLAS, A. S., SLORS, F. J., ZWINDERMAN, A. H., BOSSUYT, P. M. & STOKER, J. 2004b. Rectal Cancer: Local Staging and Assessment of

Lymph Node Involvement with Endoluminal US, CT, and MR Imaging—A Meta-Analysis 1. *Radiology,* 232**,** 773-783.

BJERNER, J., LEBEDIN, Y., BELLANGER, L., KUROKI, M., SHIVELY, J. E., VARAAS, T., NUSTAD, K., HAMMARSTRÖM, S. & BØRMER, O. P. 2002. Protein epitopes in carcinoembryonic antigen. *Tumor biology,* 23**,** 249-262.

BLUMENTHAL, R. D., HANSEN, H. J. & GOLDENBERG, D. M. 2005. Inhibition of adhesion, invasion, and metastasis by antibodies targeting CEACAM6 (NCA-90) and CEACAM5 (Carcinoembryonic Antigen). *Cancer research,* 65**,** 8809-8817.

BOBO, D., ROBINSON, K. J., ISLAM, J., THURECHT, K. J. & CORRIE, S. R. 2016. Nanoparticle-based medicines: a review of FDA-approved materials and clinical trials to date. *Pharmaceutical research,* 33**,** 2373-2387.

BOOGERD, L. S., HOOGSTINS, C. E., SCHAAP, D. P., KUSTERS, M., HANDGRAAF, H. J., VAN DER VALK, M. J., HILLING, D. E., HOLMAN, F. A., PEETERS, K. C. & MIEOG, J. S. D. 2018. Safety and effectiveness of SGM-101, a fluorescent antibody targeting carcinoembryonic antigen, for intraoperative detection of colorectal cancer: a dose-escalation pilot study. *The Lancet Gastroenterology & Hepatology,* 3**,** 181-191.

BOONSTRA, M. C., TOLNER, B., SCHAAFSMA, B. E., BOOGERD, L. S., PREVOO, H. A., BHAVSAR, G., KUPPEN, P. J., SIER, C. F., BONSING, B. A. & FRANGIONI, J. V. 2015. Preclinical evaluation of a novel CEA-targeting near-infrared fluorescent tracer delineating colorectal and pancreatic tumors. *International journal of cancer,* 137**,** 1910-1920.

BOSSLET, K., LÜBEN, G., SCHWARZ, A., HUNDT, E., HARTHUS, H., SEILER, F., MUHRER, C., KAYSER, K., KLÖPPEL, G. & SEDLACEK, H. 1985. Immunohistochemical localization and molecular characteristics of three monoclonal antibody-defined epitopes detectable on carcinoembryonic antigen (CEA). *International journal of cancer,* 36**,** 75-84.

BRADBURY, A. R. & PLÜCKTHUN, A. 2015. Getting to reproducible antibodies: the rationale for sequenced recombinant characterized reagents. *Protein Engineering, Design and Selection,* 28**,** 303-305.

BRAECKMAN, J. & MICHIELSEN, D. 2014. Efficacy and tolerability of 1-and 3-month leuprorelin acetate depot formulations (Eligard®/Depo-Eligard®) for advanced prostate cancer in daily practice: a Belgian prospective non-interventional study. *Archives of medical science: AMS,* 10**,** 477.

BRENNAN, F. R., SHAW, L., WING, M. G. & ROBINSON, C. 2004. Preclinical safety testing of biotechnology-derived pharmaceuticals. *Molecular biotechnology,* 27**,** 59-74.

BREZÁNIOVÁ, I., ZÁRUBA, K., KRÁLOVÁ, J., ADÁMKOVÁ, H., ULBRICH, P., POUČKOVÁ, P., HRUBÝ, M., ŠTĚPÁNEK, P. & KRÁL, V. 2018. Silica-based nanoparticles are efficient delivery systems for temoporfin. *Photodiagnosis and photodynamic therapy,* 21**,** 275-284.

BROWN, G., RICHARDS, C. J., BOURNE, M. W., NEWCOMBE, R. G., RADCLIFFE, A. G., DALLIMORE, N. S. & WILLIAMS, G. T. 2003. Morphologic predictors of lymph node status in rectal cancer with use of high-spatial-resolution MR imaging with histopathologic comparison. *Radiology,* 227**,** 371-7.

BROWN, S. B., BROWN, E. A. & WALKER, I. 2004. The present and future role of photodynamic therapy in cancer treatment. *The lancet oncology,* 5**,** 497-508.

BUCHHOLZ, J., KASER-HOTZ, B., KHAN, T., BLEY, C. R., MELZER, K., SCHWENDENER, R. A., ROOS, M. & WALT, H. 2005. Optimizing photodynamic therapy: in vivo pharmacokinetics of liposomal meta-(tetrahydroxyphenyl) chlorin in feline squamous cell carcinoma. *Clinical cancer research,* 11**,** 7538-7544.

BUSCH, T. M. 2006. Local physiological changes during photodynamic therapy. *Lasers Surg Med,* 38**,** 494-9.

BYERS, V., PAWLUCYZK, I., BERRY, N., DURRANT, L., ROBINS, R., GARNETT, M., PRICE, M. & BALDWIN, R. 1988. Potentiation of anti-carcinoembryonic antigen immunotoxin cytotoxicity by monoclonal antibodies reacting with co-expressed carcinoembryonic antigen epitopes. *The Journal of Immunology,* 140**,** 4050-4055.

CAHILL, R., ANDERSON, M., WANG, L., LINDSEY, I., CUNNINGHAM, C. & MORTENSEN, N. 2012a. Near-infrared (NIR) laparoscopy for intraoperative lymphatic road-mapping and sentinel node identification during definitive surgical resection of early-stage colorectal neoplasia. *Surgical Endoscopy***,** 1-8.

CAHILL, R. A. 2010. Natural orifice transluminal endoscopic surgery--here and now. *Surgeon,* 8**,** 44-50.

CAHILL, R. A., ANDERSON, M., WANG, L. M., LINDSEY, I., CUNNINGHAM, C. & MORTENSEN, N. J. 2012b. Near-infrared (NIR) laparoscopy for intraoperative lymphatic road-mapping and sentinel node identification during definitive surgical resection of early-stage colorectal neoplasia. *Surgical endoscopy,* 26**,** 197-204.

CAHILL, R. A., RIS, F. & MORTENSEN, N. J. 2011. Near-infrared laparoscopy for real-time intra-operative arterial and lymphatic perfusion imaging. *Colorectal Dis,* 13 Suppl 7**,** 12-7.

CAMPOS-DA-PAZ, M., GARROFEDOREA, J., GALDINO, A. & LACAVA, Z. 2018. Carcinoembryonic Antigen (CEA) and Hepatic Metastasis in

Colorectal Cancer: Update on Biomarker for Clinical and Biotechnological Approaches. *Recent patents on biotechnology*.

CAO, L., DU, P., JIANG, S.-H., JIN, G.-H., HUANG, Q.-L. & HUA, Z.-C. 2008. Enhancement of antitumor properties of TRAIL by targeted delivery to the tumor neovasculature. *Molecular cancer therapeutics,* 7**,** 851-861.

CARBARY-GANZ, J. L., WELGE, W. A., BARTON, J. K. & UTZINGER, U. 2015. In vivo molecular imaging of colorectal cancer using quantum dots targeted to vascular endothelial growth factor receptor 2 and optical coherence tomography/laser-induced fluorescence dual-modality imaging. *Journal of biomedical optics,* 20**,** 096015.

CASTANO, A. P., DEMIDOVA, T. N. & HAMBLIN, M. R. 2004. Mechanisms in photodynamic therapy: part one—photosensitizers, photochemistry and cellular localization. *Photodiagnosis and Photodynamic Therapy,* 1**,** 279-293.

CECIC, I., STOTT, B. & KORBELIK, M. 2006. Acute phase response-associated systemic neutrophil mobilization in mice bearing tumors treated by photodynamic therapy. *Int Immunopharmacol,* 6**,** 1259-66.

CHATTERJEE, D. K., FONG, L. S. & ZHANG, Y. 2008. Nanoparticles in photodynamic therapy: an emerging paradigm. *Advanced drug delivery reviews,* 60**,** 1627-1637.

CHAWLA, S. P., CHUA, V. S., FERNANDEZ, L., QUON, D., BLACKWELDER, W. C., GORDON, E. M. & HALL, F. L. 2010. Advanced phase I/II studies of targeted gene delivery in vivo: intravenous Rexin-G for gemcitabine-resistant metastatic pancreatic cancer. *Molecular Therapy,* 18**,** 435-441.

CHEN, F., MA, K., ZHANG, L., MADAJEWSKI, B., TURKER, M. Z., GALLAZZI, F., CRUICKSHANK, K., ZHANG, X., JENJITRANANT, P. & TOUIJER, K. A. 2019. Ultrasmall Renally Clearable Silica Nanoparticles Target Prostate Cancer. *ACS applied materials & interfaces,* 11**,** 43879-43887.

CHEN, F., ZHANG, X., MA, K., MADAJEWSKI, B., BENEZRA, M., ZHANG, L., PHILLIPS, E., TURKER, M. Z., GALLAZZI, F. & PENATE-MEDINA, O. 2018. Melanocortin-1 receptor-targeting ultrasmall silica nanoparticles for dual-modality human melanoma imaging. *ACS applied materials & interfaces,* 10**,** 4379-4393.

CHEN, L., WANG, Y., CHENG, D., DOU, S., LIU, X., LIU, G., HNATOWICH, D. J. & RUSCKOWSKI, M. 2011. Comparing two TAG-72 binding peptides previously identified by phage display as potential imaging agents. *Nuclear medicine communications,* 32**,** 920.

CHEN, Y. & ZHANG, Y. 2011. Fluorescent quantification of amino groups on silica nanoparticle surfaces. *Analytical and Bioanalytical Chemistry,* 399**,** 2503-2509.

CHENG, Y., SAMIA, A. C., MEYERS, J. D., PANAGOPOULOS, I., FEI, B. & BURDA, C. 2008. Highly efficient drug delivery with gold nanoparticle vectors for in vivo photodynamic therapy of cancer. *Journal of the American Chemical Society,* 130**,** 10643-10647.

CHIBAUDEL, B., MAINDRAULT-GŒBEL, F., BACHET, J. B., LOUVET, C., KHALIL, A., DUPUIS, O., HAMMEL, P., GARCIA, M. L., BENNAMOUN, M. & BRUSQUANT, D. 2016. PEPCOL: a GERCOR randomized phase II study of nanoliposomal irinotecan PEP 02 (MM-398) or irinotecan with leucovorin/5-fluorouracil as second-line therapy in metastatic colorectal cancer. *Cancer medicine,* 5**,** 676-683.

CHO, K., WANG, X., NIE, S. & SHIN, D. M. 2008. Therapeutic nanoparticles for drug delivery in cancer. *Clinical cancer research,* 14**,** 1310-1316.

CHO, Y.-S., YOON, T.-J., JANG, E.-S., HONG, K. S., LEE, S. Y., KIM, O. R., PARK, C., KIM, Y.-J., YI, G.-C. & CHANG, K. 2010. Cetuximab-conjugated magneto-fluorescent silica nanoparticles for in vivo colon cancer targeting and imaging. *Cancer letters,* 299**,** 63-71.

CHONG, G., LEE, F. T., HOPKINS, W., TEBBUTT, N., CEBON, J. S., MOUNTAIN, A. J., CHAPPELL, B., PAPENFUSS, A., SCHLEYER, P. & PAUL, U. 2005. Phase I trial of 131I-huA33 in patients with advanced colorectal carcinoma. *Clinical Cancer Research,* 11**,** 4818-4826.

CISTERNA, B. A., KAMALY, N., CHOI, W. I., TAVAKKOLI, A., FAROKHZAD, O. C. & VILOS, C. 2016. Targeted nanoparticles for colorectal cancer. *Nanomedicine,* 11**,** 2443-2456.

COHADE, C., OSMAN, M., LEAL, J. & WAHL, R. L. 2003. Direct comparison of 18F-FDG PET and PET/CT in patients with colorectal carcinoma. *Journal of Nuclear Medicine,* 44**,** 1797.

COHEN, A. M., MARTIN, E. W., JR., LAVERY, I., DALY, J., SARDI, A., AITKEN, D., BLAND, K., MOJZISIK, C. & HINKLE, G. 1991. Radioimmunoguided surgery using iodine 125 B72.3 in patients with colorectal cancer. *Arch Surg,* 126**,** 349-52.

COMPAGNIN, C., BAÙ, L., MOGNATO, M., CELOTTI, L., MIOTTO, G., ARDUINI, M., MORET, F., FEDE, C., SELVESTREL, F. & ECHEVARRIA, I. M. R. 2009. The cellular uptake of meta-tetra (hydroxyphenyl) chlorin entrapped in organically modified silica nanoparticles is mediated by serum proteins. *Nanotechnology,* 20**,** 345101.

COMPAGNIN, C., MORET, F., CELOTTI, L., MIOTTO, G., WOODHAMS, J. H., MACROBERT, A. J., SCHEGLMANN, D., IRATNI, S. & REDDI, E. 2011. Meta-tetra (hydroxyphenyl) chlorin-loaded liposomes sterically stabilised with poly (ethylene glycol) of different length and density: characterisation, in vitro cellular uptake and phototoxicity. *Photochemical & Photobiological Sciences,* 10**,** 1751-1759.

CONAGHAN, P., ASHRAF, S., TYTHERLEIGH, M., WILDING, J., TCHILIAN, E., BICKNELL, D., MORTENSEN, N. J. & BODMER, W. 2008. Targeted killing of colorectal cancer cell lines by a humanised IgG1 monoclonal antibody that binds to membrane-bound carcinoembryonic antigen. *British journal of cancer,* 98**,** 1217.

CONAGHAN, P. J., MAXWELL-ARMSTRONG, C. A., GARRIOCH, M. V., HONG, L. & ACHESON, A. G. 2010. Leaving a mark: the frequency and accuracy of tattooing prior to laparoscopic colorectal surgery. *Colorectal Disease***,** no-no.

CORTEZ, C., TOMASKOVIC-CROOK, E., JOHNSTON, A. P., SCOTT, A. M., NICE, E. C., HEATH, J. K. & CARUSO, F. 2007. Influence of size, surface, cell line, and kinetic properties on the specific binding of A33 antigen-targeted multilayered particles and capsules to colorectal cancer cells. *Acs Nano,* 1**,** 93-102.

CRUK 2011. Bowel Cancer Statistics. *Key Facts [Online]. Available: http://info.cancerresearchuk.org/cancerstats/types/bowel//incidence.*

DA PAZ, M. C., ALMEIDA SANTOS, M. D. F. M., SANTOS, C. M. B., DA SILVA, S. W., DE SOUZA, L. B., LIMA, E. C. D., SILVA, R. C., LUCCI, C. M., MORAIS, P. C., AZEVEDO, R. B. & LACAVA, Z. G. M. 2012. Anti-CEA loaded maghemite nanoparticles as a theragnostic device for colorectal cancer. *International Journal of Nanomedicine,* 7**,** 5271-5282.

DANHIER, F., FERON, O. & PRÉAT, V. 2010. To exploit the tumor microenvironment: passive and active tumor targeting of nanocarriers for anti-cancer drug delivery. *Journal of controlled release,* 148**,** 135-146.

DANKNER, M. & ROSE, A. A. 2018. Comment on 'Clinical significance of BRAF non-V600E mutations on the therapeutic effects of anti-EGFR monoclonal antibody treatment in patients with pretreated metastatic colorectal cancer: the Biomarker Research for anti-EGFR monoclonal Antibodies by Comprehensive Cancer genomics (BREAC) study'. *British journal of cancer,* 118**,** 1276.

DE VISSCHER, S., WITJES, M., KASCÁKOVÁ, S., ROBINSON, D., STERENBORG, H., ROODENBURG, J. & AMELINK, A. 2010. Non-invasive measurement of photosensitiser concentration using fluorescence differential path-length spectroscopy: validation for different liposomal formulations of m-THPC: Foscan, Foslip and Fospeg. *Head & neck oncology,* 2**,** O46.

DE VISSCHER, S. A., DIJKSTRA, P. U., TAN, I. B., ROODENBURG, J. & WITJES, M. 2013. mTHPC mediated photodynamic therapy (PDT) of squamous cell carcinoma in the head and neck: a systematic review. *Oral oncology,* 49**,** 192-210.

DIENSTMANN, R., SALAZAR, R. & TABERNERO, J. 2015. Personalizing colon cancer adjuvant therapy: selecting optimal treatments for individual patients. *Journal of Clinical Oncology,* 33**,** 1787-1796.

DIGHE, S., BLAKE, H., KOH, M. D., SWIFT, I., ARNAOUT, A., TEMPLE, L., BARBACHANO, Y. & BROWN, G. 2010a. Accuracy of multidetector computed tomography in identifying poor prognostic factors in colonic cancer. *Br J Surg,* 97**,** 1407-15.

DIGHE, S., PURKAYASTHA, S., SWIFT, I., TEKKIS, P., DARZI, A., A'HERN, R. & BROWN, G. 2010b. Diagnostic precision of CT in local staging of colon cancers: a meta-analysis. *Clinical radiology,* 65**,** 708-719.

DOEVENDANS, P. A., DAEMEN, M. J., DE MUINCK, E. D. & SMITS, J. F. 1998. Cardiovascular phenotyping in mice. *Cardiovasc Res,* 39**,** 34-49.

DOLMANS, D. E., FUKUMURA, D. & JAIN, R. K. 2003. Photodynamic therapy for cancer. *Nature reviews cancer,* 3**,** 380-387.

DOUILLARD, J.-Y., SIENA, S., CASSIDY, J., TABERNERO, J., BURKES, R., BARUGEL, M., HUMBLET, Y., BODOKY, G., CUNNINGHAM, D. & JASSEM, J. 2010. Randomized, phase III trial of panitumumab with infusional fluorouracil, leucovorin, and oxaliplatin (FOLFOX4) versus FOLFOX4 alone as first-line treatment in patients with previously untreated metastatic colorectal cancer: the PRIME study. *Journal of clinical oncology,* 28**,** 4697-4705.

EKER, C., MONTAN, S., JARAMILLO, E., KOIZUMI, K., RUBIO, C., ANDERSSON-ENGELS, S., SVANBERG, K., SVANBERG, S. & SLEZAK, P. 1999. Clinical spectral characterisation of colonic mucosal lesions using autofluorescence and δ aminolevulinic acid sensitisation. *Gut,* 44**,** 511-518.

ELJAMEL, M. S. 2008. Brain photodiagnosis (PD), fluorescence guided resection (FGR) and photodynamic therapy (PDT): past, present and future. *Photodiagnosis and photodynamic Therapy,* 5**,** 29-35.

FAERDEN, A. E., SJO, O. H., BUKHOLM, I. R., ANDERSEN, S. N., SVINDLAND, A., NESBAKKEN, A. & BAKKA, A. 2011. Lymph node micrometastases and isolated tumor cells influence survival in stage I and II colon cancer. *Dis Colon Rectum,* 54**,** 200-6.

FAHLGREN, A., BARANOV, V., FRANGSMYR, L., ZOUBIR, F., HAMMARSTROM, M. L. & HAMMARSTROM, S. 2003. Interferon-gamma tempers the expression of carcinoembryonic antigen family molecules in human colon cells: A possible role in innate mucosal defence. *Scandinavian Journal of Immunology,* 58**,** 628-641.

FANG, S. H., EFRON, J. E., BERHO, M. E. & WEXNER, S. D. 2014. Dilemma of stage II colon cancer and decision making for adjuvant chemotherapy. *Journal of the American College of Surgeons,* 219**,** 1056-1069.

FAROKHZAD, O. C. & LANGER, R. 2006. Nanomedicine: developing smarter therapeutic and diagnostic modalities. *Advanced drug delivery reviews,* 58**,** 1456-1459.

FIGUEIREDO, P., BAULETH-RAMOS, T., HIRVONEN, J., SARMENTO, B. & SANTOS, H. A. 2018. The Emerging Role of Multifunctional Theranostic Materials in Cancer Nanomedicine. *Handbook of Nanomaterials for Cancer Theranostics.* Elsevier.

FIGUEREDO, A., COOMBES, M. E. & MUKHERJEE, S. 2008. Adjuvant therapy for completely resected stage II colon cancer. *Cochrane Database Syst Rev***,** CD005390.

FINGAR, V. H., WIEMAN, T. J., WIEHLE, S. A. & CERRITO, P. B. 1992. The role of microvascular damage in photodynamic therapy: the effect of treatment on vessel constriction, permeability, and leukocyte adhesion. *Cancer Res,* 52**,** 4914-21.

FLESHMAN, J., SARGENT, D. J., GREEN, E., ANVARI, M., STRYKER, S. J., BEART, R. W., JR., HELLINGER, M., FLANAGAN, R., JR., PETERS, W. & NELSON, H. 2007. Laparoscopic colectomy for cancer is not inferior to open surgery based on 5-year data from the COST Study Group trial. *Ann Surg,* 246**,** 655-62; discussion 662-4.

FORTINA, P., KRICKA, L. J., GRAVES, D. J., PARK, J., HYSLOP, T., TAM, F., HALAS, N., SURREY, S. & WALDMAN, S. A. 2007. Applications of nanoparticles to diagnostics and therapeutics in colorectal cancer. *Trends in biotechnology,* 25**,** 145-152.

GABIZON, A. A. 2001. Pegylated liposomal doxorubicin: metamorphosis of an old drug into a new form of chemotherapy. *Cancer investigation,* 19**,** 424-436.

GAIO, E., SCHEGLMANN, D., REDDI, E. & MORET, F. 2016. Uptake and photo-toxicity of Foscan®, Foslip® and Fospeg® in multicellular tumor spheroids. *Journal of Photochemistry and Photobiology B: Biology,* 161**,** 244-252.

GAO, D., XU, H., PHILBERT, M. A. & KOPELMAN, R. 2007. Ultrafine hydrogel nanoparticles: synthetic approach and therapeutic application in living cells. *Angewandte Chemie,* 119**,** 2274-2277.

GARY-BOBO, M., HOCINE, O., BREVET, D., MAYNADIER, M., RAEHM, L., RICHETER, S., CHARASSON, V., LOOCK, B., MORÈRE, A. & MAILLARD, P. 2012. Cancer therapy improvement with mesoporous silica nanoparticles combining targeting, drug delivery and PDT. *International journal of pharmaceutics,* 423**,** 509-515.

GAUR, U., SAHOO, S. K., DE, T. K., GHOSH, P. C., MAITRA, A. & GHOSH, P. K. 2000. Biodistribution of fluoresceinated dextran using novel

nanoparticles evading reticuloendothelial system. *International Journal of Pharmaceutics,* 202**,** 1-10.

GIBOT, L., LEMELLE, A., TILL, U., MOUKARZEL, B. A., MINGOTAUD, A.-F. O., PIMIENTA, V. R., SAINT-AGUET, P., ROLS, M.-P., GAUCHER, M. & VIOLLEAU, F. D. R. 2014. Polymeric micelles encapsulating photosensitizer: structure/photodynamic therapy efficiency relation. *Biomacromolecules,* 15**,** 1443-1455.

GOLD, P. & FREEDMAN, S. O. 1965. Specific carcinoembryonic antigens of the human digestive system. *Journal of Experimental Medicine,* 122**,** 467-481.

GOLLNICK, S. O., LIU, X., OWCZARCZAK, B., MUSSER, D. A. & HENDERSON, B. W. 1997. Altered expression of interleukin 6 and interleukin 10 as a result of photodynamic therapy in vivo. *Cancer Res,* 57**,** 3904-9.

GRAFF, C. P., CHESTER, K., BEGENT, R. & WITTRUP, K. D. 2004. Directed evolution of an anti-carcinoembryonic antigen scFv with a 4-day monovalent dissociation half-time at 37 C. *Protein Engineering Design and Selection,* 17**,** 293-304.

GROBMYER, S. R., IWAKUMA, N., SHARMA, P. & MOUDGIL, B. M. 2010. *What is cancer nanotechnology?*, Springer.

GUBALA, V., LE GUEVEL, X., NOONEY, R., WILLIAMS, D. E. & MACCRAITH, B. 2010. A comparison of mono and multivalent linkers and their effect on the colloidal stability of nanoparticle and immunoassays performance. *Talanta,* 81**,** 1833-1839.

GUILLOU, P. J., QUIRKE, P., THORPE, H., WALKER, J., JAYNE, D. G., SMITH, A. M., HEATH, R. M. & BROWN, J. M. 2005a. Short-term endpoints of conventional versus laparoscopic-assisted surgery in patients with colorectal cancer (MRC CLASICC trial): multicentre, randomised controlled trial. *Lancet,* 365**,** 1718-26.

GUILLOU, P. J., QUIRKE, P., THORPE, H., WALKER, J., JAYNE, D. G., SMITH, A. M., HEATH, R. M., BROWN, J. M. & GROUP, M. C. T. 2005b. Short-term endpoints of conventional versus laparoscopic-assisted surgery in patients with colorectal cancer (MRC CLASICC trial): multicentre, randomised controlled trial. *The lancet,* 365**,** 1718-1726.

GYENGE, E. B., DARPHIN, X., WIRTH, A., PIELES, U., WALT, H., BREDELL, M. & MAAKE, C. 2011a. Uptake and fate of surface modified silica nanoparticles in head and neck squamous cell carcinoma. *Journal of nanobiotechnology,* 9**,** 32.

GYENGE, E. B., HIESTAND, S., GRAEFE, S., WALT, H. & MAAKE, C. 2011b. Cellular and molecular effects of the liposomal mTHPC derivative

Foslipos in prostate carcinoma cells in vitro. *Photodiagnosis and photodynamic therapy,* 8**,** 86-96.

HABEEB, A. S. A. 1966. Determination of free amino groups in proteins by trinitrobenzenesulfonic acid. *Analytical biochemistry,* 14**,** 328-336.

HAGGARTY, A., LEGLER, C., KRANTZ, M. J. & FUKS, A. 1986. Epitopes of carcinoembryonic antigen defined by monoclonal antibodies prepared from mice immunized with purified carcinoembryonic antigen or HCT-8R cells. *Cancer research,* 46**,** 300-309.

HAMMARSTRÖM, S. The carcinoembryonic antigen (CEA) family: structures, suggested functions and expression in normal and malignant tissues. Seminars in cancer biology, 1999. Elsevier, 67-81.

HAMMARSTRÖM, S. & BARANOV, V. 2001. Is there a role for CEA in innate immunity in the colon? *Trends in microbiology,* 9**,** 119-125.

HAMY, A., CURTET, C., PAINEAU, J., CHATAL, J. F. & VISSET, J. 1995. Feasibility of radioimmunoguided surgery of colorectal carcinoma using indium 111 CEA specific antibody and simulation with a phantom using 2 steps targetting with bispecific antibody. *Tumori,* 81**,** 103-6.

HARADA, K., HARADA, Y., BEIKA, M., KOIZUMI, N., INOUE, K., MURAYAMA, Y., KURIU, Y., NAKANISHI, M., MINAMIKAWA, T., YAMAOKA, Y., DAI, P., YANAGISAWA, A., OTSUJI, E. & TAKAMATSU, T. 2013. Detection of lymph node metastases in human colorectal cancer by using 5-aminolevulinic acid-induced protoporphyrin IX fluorescence with spectral unmixing. *Int J Mol Sci,* 14**,** 23140-52.

HARITOGLOU, C., GANDORFER, A., SCHAUMBERGER, M., TADAYONI, R. & KAMPIK, A. 2003. Light-absorbing properties and osmolarity of indocyanine-green depending on concentration and solvent medium. *Investigative Ophthalmology & Visual Science,* 44**,** 2722-2729.

HARRISON, E., COULTER, J. A. & DIXON, D. 2016. Gold nanoparticle surface functionalization: mixed monolayer versus hetero bifunctional peg linker. *Nanomedicine,* 11**,** 851-865.

HARTMAN, K. B., WILSON, L. J. & ROSENBLUM, M. G. 2008. Detecting and treating cancer with nanotechnology. *Molecular diagnosis & therapy,* 12**,** 1-14.

HASS, G. M., BOLLING, T. J., KINDERS, R. J., HENSLEE, J. G., MANDECKI, W., DORWIN, S. A. & SHIVELY, J. E. 1991. Preparation of synthetic polypeptide domains of carcinoembryonic antigen and their use in epitope mapping. *Cancer research,* 51**,** 1876-1882.

HATAKEYAMA, K., WAKABAYASHI-NAKAO, K., OHSHIMA, K., SAKURA, N., YAMAGUCHI, K. & MOCHIZUKI, T. 2013. Novel protein isoforms of

carcinoembryonic antigen are secreted from pancreatic, gastric and colorectal cancer cells. *BMC research notes,* 6**,** 381.

HEATH, C. H., DEEP, N. L., SWEENY, L., ZINN, K. R. & ROSENTHAL, E. L. 2012. Use of Panitumumab-IRDye800 to Image Microscopic Head and Neck Cancer in an Orthotopic Surgical Model. *Annals of Surgical Oncology,* 19**,** 3879-3887.

HEINE, M., NOLLAU, P., MASSLO, C., NIELSEN, P., FREUND, B., BRUNS, O. T., REIMER, R., HOHENBERG, H., PELDSCHUS, K. & ITTRICH, H. 2011. Investigations on the usefulness of CEACAMs as potential imaging targets for molecular imaging purposes. *PLoS One,* 6**,** e28030.

HENTZEN, J. E., DE JONGH, S. J., HEMMER, P. H., VAN DER PLAS, W. Y., VAN DAM, G. M. & KRUIJFF, S. 2018. Molecular fluorescence-guided surgery of peritoneal carcinomatosis of colorectal origin: A narrative review. *Journal of surgical oncology*.

HERMANEK, P., HUTTER, R. V., SOBIN, L. H. & WITTEKIND, C. 1999. International Union Against Cancer. Classification of isolated tumor cells and micrometastasis. *Cancer,* 86**,** 2668-73.

HILDERBRAND, S. A. & WEISSLEDER, R. 2010. Near-infrared fluorescence: application to in vivo molecular imaging. *Current Opinion in Chemical Biology,* 14**,** 71-79.

HIRCHE, C., MOHR, Z., KNEIF, S., DONIGA, S., MURAWA, D., STRIK, M. & HÜNERBEIN, M. 2012. Ultrastaging of colon cancer by sentinel node biopsy using fluorescence navigation with indocyanine green. *International journal of colorectal disease,* 27**,** 319-324.

HIRSCH, L. R., STAFFORD, R. J., BANKSON, J. A., SERSHEN, S. R., RIVERA, B., PRICE, R., HAZLE, J. D., HALAS, N. J. & WEST, J. L. 2003. Nanoshell-mediated near-infrared thermal therapy of tumors under magnetic resonance guidance. *Proceedings of the National Academy of Sciences,* 100**,** 13549-13554.

HOI, S. W., WONG, H. M., CHAN, J. Y., YUE, G. G., TSE, G. M., LAW, B. K., FONG, W. P. & FUNG, K. P. 2012. Photodynamic therapy of Pheophorbide a inhibits the proliferation of human breast tumour via both caspase-dependent and -independent apoptotic pathways in in vitro and in vivo models. *Phytother Res,* 26**,** 734-42.

HOOGSTINS, C. E. S., BOOGERD, L. S. F., SIBINGA MULDER, B. G., MIEOG, J. S. D., SWIJNENBURG, R. J., VAN DE VELDE, C. J. H., FARINA SARASQUETA, A., BONSING, B. A., FRAMERY, B., PELEGRIN, A., GUTOWSKI, M., CAILLER, F., BURGGRAAF, J. & VAHRMEIJER, A. L. 2018. Image-Guided Surgery in Patients with Pancreatic Cancer: First Results of a Clinical Trial Using SGM-101, a Novel Carcinoembryonic Antigen-Targeting, Near-Infrared Fluorescent Agent. *Ann Surg Oncol,* 25**,** 3350-3357.

HORLINGS, R. K., TERRA, J. B. & WITJES, M. J. 2015. mTHPC mediated, systemic photodynamic therapy (PDT) for nonmelanoma skin cancers: Case and literature review. *Lasers in surgery and medicine,* 47**,** 779-787.

HSIEH, W. J., LIANG, C. J., CHIEH, J. J., WANG, S. H., LAI, I. R., CHEN, J. H., CHANG, F. H., TSENG, W. K., YANG, S. Y., WU, C. C. & CHEN, Y. L. 2012. In vivo tumor targeting and imaging with anti-vascular endothelial growth factor antibody-conjugated dextran-coated iron oxide nanoparticles. *Int J Nanomedicine,* 7**,** 2833-42.

HUANG, K. W., CHIEH, J. J., LIN, I. T., HORNG, H. E., YANG, H. C. & HONG, C. Y. 2013. Anti-CEA-functionalized superparamagnetic iron oxide nanoparticles for examining colorectal tumors in vivo. *Nanoscale Res Lett,* 8**,** 413.

HUANG, S., LI, R., QU, Y., SHEN, J. & LIU, J. 2009. Fluorescent Biological Label for Recognizing Human Ovarian Tumor Cells Based on Fluorescent Nanoparticles. *Journal of Fluorescence,* 19**,** 1095-1101.

HUGGETT, M. T., JERMYN, M., GILLAMS, A., ILLING, R., MOSSE, S., NOVELLI, M., KENT, E., BOWN, S., HASAN, T. & POGUE, B. 2014. Phase I/II study of verteporfin photodynamic therapy in locally advanced pancreatic cancer. *British journal of cancer,* 110**,** 1698.

HUNDT, W., BRAUNSCHWEIG, R. & REISER, M. 1999a. Evaluation of spiral CT in staging of colon and rectum carcinoma. *European radiology,* 9**,** 78-84.

HUNDT, W., BRAUNSCHWEIG, R. & REISER, M. 1999b. Evaluation of spiral CT in staging of colon and rectum carcinoma. *Eur Radiol,* 9**,** 78-84.

HUTTEMAN, M., CHOI, H. S., MIEOG, J. S., VAN DER VORST, J. R., ASHITATE, Y., KUPPEN, P. J., VAN GRONINGEN, M. C., LOWIK, C. W., SMIT, V. T., VAN DE VELDE, C. J., FRANGIONI, J. V. & VAHRMEIJER, A. L. 2010. Clinical Translation of Ex Vivo Sentinel Lymph Node Mapping for Colorectal Cancer Using Invisible Near-Infrared Fluorescence Light. *Ann Surg Oncol*.

JAIN, A., JAIN, S. K., GANESH, N., BARVE, J. & BEG, A. M. 2010. Design and development of ligand-appended polysaccharidic nanoparticles for the delivery of oxaliplatin in colorectal cancer. *Nanomedicine: Nanotechnology, Biology and Medicine,* 6**,** 179-190.

JAYNE, D., THORPE, H., COPELAND, J., QUIRKE, P., BROWN, J. & GUILLOU, P. 2010a. Five-year follow-up of the Medical Research Council CLASICC trial of laparoscopically assisted versus open surgery for colorectal cancer. *British journal of surgery,* 97**,** 1638-1645.

JAYNE, D. G., THORPE, H. C., COPELAND, J., QUIRKE, P., BROWN, J. M. & GUILLOU, P. J. 2010b. Five-year follow-up of the Medical Research

Council CLASICC trial of laparoscopically assisted versus open surgery for colorectal cancer. *Br J Surg,* 97**,** 1638-45.

JERJES, W., UPILE, T., HAMDOON, Z., ABBAS, S., AKRAM, S., MOSSE, C. A., MORLEY, S. & HOPPER, C. 2011. Photodynamic therapy: The minimally invasive surgical intervention for advanced and/or recurrent tongue base carcinoma. *Lasers in surgery and medicine,* 43**,** 283-292.

JIE, G. F., WANG, L. & ZHANG, S. S. 2011. Magnetic Electrochemiluminescent Fe3O4/CdSe-CdS Nanoparticle/Polyelectrolyte Nanocomposite for Highly Efficient Immunosensing of a Cancer Biomarker. *Chemistry-a European Journal,* 17**,** 641-648.

JOKERST, J. V., LOBOVKINA, T., ZARE, R. N. & GAMBHIR, S. S. 2011. Nanoparticle PEGylation for imaging and therapy. *Nanomedicine,* 6**,** 715-728.

JOOSTEN, J. J. A., STROBBE, L. J. A., WAUTERS, C. A. P., PRUSZCZYNSKI, M., WOBBES, T. & RUERS, T. J. M. 1999. Intraoperative lymphatic mapping and the sentinel node concept in colorectal carcinoma. *British Journal of Surgery,* 86**,** 482-486.

JOSEFSEN, L. B. & BOYLE, R. W. 2012. Unique diagnostic and therapeutic roles of porphyrins and phthalocyanines in photodynamic therapy, imaging and theranostics. *Theranostics,* 2**,** 916.

JOST, C., SCHILLING, J., TAMASKOVIC, R., SCHWILL, M., HONEGGER, A. & PLÜCKTHUN, A. 2013. Structural basis for eliciting a cytotoxic effect in HER2-overexpressing cancer cells via binding to the extracellular domain of HER2. *Structure,* 21**,** 1979-1991.

KAUSHAL, S., MCELROY, M. K., LUIKEN, G. A., TALAMINI, M. A., MOOSSA, A., HOFFMAN, R. M. & BOUVET, M. 2008a. Fluorophore-conjugated anti-CEA antibody for the intraoperative imaging of pancreatic and colorectal cancer. *Journal of gastrointestinal surgery,* 12**,** 1938.

KAUSHAL, S., MCELROY, M. K., LUIKEN, G. A., TALAMINI, M. A., MOOSSA, A. R., HOFFMAN, R. M. & BOUVET, M. 2008b. Fluorophore-conjugated anti-CEA Antibody for the Intraoperative Imaging of Pancreatic and Colorectal Cancer. *Journal of Gastrointestinal Surgery,* 12**,** 1938-1950.

KEENEY, G., JAFRI, S. Z. & MEZWA, D. G. 1989. Computed tomographic evaluation and staging of cecal carcinoma. *Gastrointest Radiol,* 14**,** 65-9.

KELLY, K. A. & JONES, D. A. 2003. Isolation of a colon tumor specific binding peptide using phage display selection. *Neoplasia,* 5**,** 437-444.

KENNEDY, J. C. & POTTIER, R. H. 1992. Endogenous protoporphyrin IX, a clinically useful photosensitizer for photodynamic therapy. *J Photochem Photobiol B,* 14**,** 275-92.

KENT, S. P., RYAN, K. H. & SIEGEL, A. L. 1978. STERIC HINDRANCE AS A FACTOR IN REACTION OF LABELED ANTIBODY WITH CELL-SURFACE ANTIGENIC DETERMINANTS. *Journal of Histochemistry & Cytochemistry,* 26**,** 618-621.

KESSEL, D., LUO, Y., DENG, Y. & CHANG, C. K. 1997. The role of subcellular localization in initiation of apoptosis by photodynamic therapy. *Photochem Photobiol,* 65**,** 422-6.

KIESSLICH, T., BERLANDA, J., PLAETZER, K., KRAMMER, B. & BERR, F. 2007. Comparative characterization of the efficiency and cellular pharmacokinetics of Foscan®-and Foslip®-based photodynamic treatment in human biliary tract cancer cell lines. *Photochemical & Photobiological Sciences,* 6**,** 619-627.

KIJIMA, S., SASAKI, T., NAGATA, K., UTANO, K., LEFOR, A. T. & SUGIMOTO, H. 2014. Preoperative evaluation of colorectal cancer using CT colonography, MRI, and PET/CT. *World J Gastroenterol,* 20**,** 16964-16975.

KIM, J., ROH, S., KOO, K., CHO, Y., KIM, H., YU, C., OH, S., RYU, J., BICKNELL, D. & BODMER, W. 2005. Preclinical application of radioimmunoguided surgery using anti-carcinoembryonic antigen biparatopic antibody in the colon cancer. *European surgical research,* 37**,** 36-44.

KIM, N. K., KIM, M. J., PARK, J. K., PARK, S. I. & MIN, J. S. 2000. Preoperative staging of rectal cancer with MRI: accuracy and clinical usefulness. *Ann Surg Oncol,* 7**,** 732-7.

KIM, S., OHULCHANSKYY, T. Y., PUDAVAR, H. E., PANDEY, R. K. & PRASAD, P. N. 2007. Organically modified silica nanoparticles co-encapsulating photosensitizing drug and aggregation-enhanced two-photon absorbing fluorescent dye aggregates for two-photon photodynamic therapy. *Journal of the American Chemical Society,* 129**,** 2669-2675.

KIM, T.-W., CHUNG, P.-W. & LIN, V. S.-Y. 2010. Facile synthesis of monodisperse spherical MCM-48 mesoporous silica nanoparticles with controlled particle size. *Chemistry of Materials,* 22**,** 5093-5104.

KING, D. S., FIELDS, C. G. & FIELDS, G. B. 1990. A CLEAVAGE METHOD WHICH MINIMIZES SIDE REACTIONS FOLLOWING FMOC SOLID-PHASE PEPTIDE-SYNTHESIS. *International Journal of Peptide and Protein Research,* 36**,** 255-266.

KING, R., TIEDE, C., SIMMONS, K., FISHWICK, C., TOMLINSON, D. & AJJAN, R. 2015. Inhibition of complement C3 and fibrinogen interaction: a potential novel therapeutic target to reduce cardiovascular disease in diabetes. *The Lancet,* 385**,** S57.

KIPPS, E., YOUNG, K. & STARLING, N. 2017. Liposomal irinotecan in gemcitabine-refractory metastatic pancreatic cancer: efficacy, safety and place in therapy. *Therapeutic advances in medical oncology,* 9**,** 159-170.

KIRUI, D. K., REY, D. A. & BATT, C. A. 2010. Gold hybrid nanoparticles for targeted phototherapy and cancer imaging. *Nanotechnology,* 21**,** 105105.

KO, A., TEMPERO, M., SHAN, Y., SU, W., LIN, Y., DITO, E., ONG, A., WANG, Y., YEH, C. & CHEN, L. 2013. A multinational phase 2 study of nanoliposomal irinotecan sucrosofate (PEP02, MM-398) for patients with gemcitabine-refractory metastatic pancreatic cancer. *British journal of cancer,* 109**,** 920-925.

KOIDE, S. & SIDHU, S. S. 2009. The importance of being tyrosine: lessons in molecular recognition from minimalist synthetic binding proteins. *ACS chemical biology,* 4**,** 325-334.

KONAN-KOUAKOU, Y. N., BOCH, R., GURNY, R. & ALLEMANN, E. 2005. In vitro and in vivo activities of verteporfin-loaded nanoparticles. *Journal of controlled release,* 103**,** 83-91.

KOPANSKY, E., SHAMAY, Y. & DAVID, A. 2011. Peptide-directed HPMA copolymer-doxorubicin conjugates as targeted therapeutics for colorectal cancer. *Journal of drug targeting,* 19**,** 933-943.

KORBELIK, M., KROSL, G., KROSL, J. & DOUGHERTY, G. J. 1996. The role of host lymphoid populations in the response of mouse EMT6 tumor to photodynamic therapy. *Cancer Res,* 56**,** 5647-52.

KORBELIK, M., SUN, J. & CECIC, I. 2005. Photodynamic therapy-induced cell surface expression and release of heat shock proteins: relevance for tumor response. *Cancer Res,* 65**,** 1018-26.

KRAMMER, B. & PLAETZER, K. 2008a. ALA and its clinical impact, from bench to bedside. *Photochem Photobiol Sci,* 7**,** 283-9.

KRAMMER, B. & PLAETZER, K. 2008b. ALA and its clinical impact, from bench to bedside. *Photochemical & Photobiological Sciences,* 7**,** 283-289.

KRZYKAWSKA-SERDA, M., DĄBROWSKI, J. M., ARNAUT, L. G., SZCZYGIEŁ, M., URBAŃSKA, K., STOCHEL, G. & ELAS, M. 2014. The role of strong hypoxia in tumors after treatment in the outcome of bacteriochlorin-based photodynamic therapy. *Free Radical Biology and Medicine,* 73**,** 239-251.

KUKOWSKA-LATALLO, J. F., CANDIDO, K. A., CAO, Z., NIGAVEKAR, S. S., MAJOROS, I. J., THOMAS, T. P., BALOGH, L. P., KHAN, M. K. & BAKER, J. R. 2005. Nanoparticle targeting of anticancer drug improves therapeutic response in animal model of human epithelial cancer. *Cancer research,* 65**,** 5317-5324.

KUMAR, R., ROY, I., OHULCHANSKKY, T. Y., VATHY, L. A., BERGEY, E. J., SAJJAD, M. & PRASAD, P. N. 2010. In vivo biodistribution and clearance studies using multimodal organically modified silica nanoparticles. *ACS nano,* 4**,** 699-708.

KUSANO, M., TAJIMA, Y., YAMAZAKI, K., KATO, M., WATANABE, M. & MIWA, M. 2008. Sentinel node mapping guided by indocyanine green fluorescence imaging: A new method for sentinel node navigation surgery in gastrointestinal cancer. *Digestive Surgery,* 25**,** 103-108.

KWAK, J. Y., KIM, J. S., KIM, H. J., HA, H. K., YU, C. S. & KIM, J. C. 2012. Diagnostic value of FDG-PET/CT for lymph node metastasis of colorectal cancer. *World J Surg,* 36**,** 1898-905.

KYLE, S. 2018. Affimer Proteins: Theranostics of the Future? *Trends in biochemical sciences,* 43**,** 230-232.

LAMBERTS, L. E., KOCH, M., DE JONG, J. S., ADAMS, A. L. L., GLATZ, J., KRANENDONK, M. E. G., TERWISSCHA VAN SCHELTINGA, A. G. T., JANSEN, L., DE VRIES, J., LUB-DE HOOGE, M. N., SCHRODER, C. P., JORRITSMA-SMIT, A., LINSSEN, M. D., DE BOER, E., VAN DER VEGT, B., NAGENGAST, W. B., ELIAS, S. G., OLIVEIRA, S., WITKAMP, A. J., MALI, W., VAN DER WALL, E., VAN DIEST, P. J., DE VRIES, E. G. E., NTZIACHRISTOS, V. & VAN DAM, G. M. 2017. Tumor-Specific Uptake of Fluorescent Bevacizumab-IRDye800CW Microdosing in Patients with Primary Breast Cancer: A Phase I Feasibility Study. *Clin Cancer Res,* 23**,** 2730-2741.

LANDSMAN, M. L. J., KWANT, G., MOOK, G. A. & ZIJLSTRA, W. G. 1976. LIGHT-ABSORBING PROPERTIES, STABILITY, AND SPECTRAL STABILIZATION OF INDOCYANINE GREEN. *Journal of Applied Physiology,* 40**,** 575-583.

LASSALLE, H.-P., DUMAS, D., GRÄFE, S., D'HALLEWIN, M.-A., GUILLEMIN, F. & BEZDETNAYA, L. 2009. Correlation between in vivo pharmacokinetics, intratumoral distribution and photodynamic efficiency of liposomal mTHPC. *Journal of controlled release,* 134**,** 118-124.

LEE, H.-C., LING, Q.-D., YU, W.-C., HUNG, C.-M., KAO, T.-C., HUANG, Y.-W. & HIGUCHI, A. 2013. Drug-resistant colon cancer cells produce high carcinoembryonic antigen and might not be cancer-initiating cells. *Drug design, development and therapy,* 7**,** 491.

LEUNG, K. 2012. 99mTc (CO) 3-Anti-carcinoembryonic antigen (CEA) humanized CEA5 graft nanobody. *Molecular Imaging and Contrast Agent Database (MICAD)[Internet].* National Center for Biotechnology Information (US).

LI, L., XIANG, D., SHIGDAR, S., YANG, W., LI, Q., LIN, J., LIU, K. & DUAN, W. 2014. Epithelial cell adhesion molecule aptamer functionalized PLGA-lecithin-curcumin-PEG nanoparticles for targeted drug delivery to human

colorectal adenocarcinoma cells. *International journal of nanomedicine,* 9**,** 1083.

LI, P., WANG, Y., ZENG, F., CHEN, L., PENG, Z. & KONG, L. X. 2011. Synthesis and characterization of folate conjugated chitosan and cellular uptake of its nanoparticles in HT-29 cells. *Carbohydrate research,* 346**,** 801-806.

LI, X. T., SUN, Y. S., TANG, L., CAO, K. & ZHANG, X. Y. 2015. Evaluating local lymph node metastasis with magnetic resonance imaging, endoluminal ultrasound and computed tomography in rectal cancer: a meta-analysis. *Colorectal Disease,* 17**,** O129-O135.

LIBUTTI, S. K., PACIOTTI, G. F., BYRNES, A. A., ALEXANDER, H. R., GANNON, W. E., WALKER, M., SEIDEL, G. D., YULDASHEVA, N. & TAMARKIN, L. 2010. Phase I and pharmacokinetic studies of CYT-6091, a novel PEGylated colloidal gold-rhTNF nanomedicine. *Clinical cancer research,* 16**,** 6139-6149.

LIETO, E., AURICCHIO, A., CARDELLA, F., MABILIA, A., BASILE, N., CASTELLANO, P., ORDITURA, M. & GALIZIA, G. 2018. Fluorescence-Guided Surgery in the Combined Treatment of Peritoneal Carcinomatosis from Colorectal Cancer: Preliminary Results and Considerations. *World journal of surgery,* 42**,** 1154-1160.

LIPKA, J., SEMMLER-BEHNKE, M., SPERLING, R. A., WENK, A., TAKENAKA, S., SCHLEH, C., KISSEL, T., PARAK, W. J. & KREYLING, W. G. 2010. Biodistribution of PEG-modified gold nanoparticles following intratracheal instillation and intravenous injection. *Biomaterials,* 31**,** 6574-6581.

LIU, L., ZHANG, Z. & XING, D. 2011. Cell death via mitochondrial apoptotic pathway due to activation of Bax by lysosomal photodamage. *Free Radic Biol Med,* 51**,** 53-68.

LIU, S., ZHANG, H.-L., LIU, T.-C., LIU, B., CAO, Y.-C., HUANG, Z.-L., ZHAO, Y.-D. & LUO, Q.-M. 2007. Optimization of the methods for introduction of amine groups onto the silica nanoparticle surface. *Journal of Biomedical Materials Research Part A,* 80A**,** 752-757.

LOGAN, R. F. A., PATNICK, J., NICKERSON, C., COLEMAN, L., RUTTER, M. D. & VON WAGNER, C. 2011. Outcomes of the Bowel Cancer Screening Programme (BCSP) in England after the first 1 million tests. *Gut*.

LÖW, K., KNOBLOCH, T., WAGNER, S., WIEHE, A., ENGEL, A., LANGER, K. & VON BRIESEN, H. 2011. Comparison of intracellular accumulation and cytotoxicity of free mTHPC and mTHPC-loaded PLGA nanoparticles in human colon carcinoma cells. *Nanotechnology,* 22**,** 245102.

LU, B., SMYTH, M. R. & OKENNEDY, R. 1996. Oriented immobilization of antibodies and its applications in immunoassays and immunosensors. *Analyst,* 121**,** R29-R32.

LU, J., LIONG, M., ZINK, J. I. & TAMANOI, F. 2007. Mesoporous silica nanoparticles as a delivery system for hydrophobic anticancer drugs. *small,* 3**,** 1341-1346.

MADDAMS, J., UTLEY, M. & MØLLER, H. 2012. Projections of cancer prevalence in the United Kingdom, 2010–2040. *British journal of cancer,* 107**,** 1195-1202.

MARILL, J., ANESARY, N. M., ZHANG, P., VIVET, S., BORGHI, E., LEVY, L. & POTTIER, A. 2014. Hafnium oxide nanoparticles: toward an in vitropredictive biological effect? *Radiation Oncology,* 9**,** 150.

MARKL, B., ROSSLE, J., ARNHOLDT, H. M., SCHALLER, T., KRAMMER, I., CACCHI, C., JAHNIG, H., SCHENKIRSCH, G., SPATZ, H. & ANTHUBER, M. 2012. The clinical significance of lymph node size in colon cancer. *Mod Pathol,* 25**,** 1413-22.

MARSDEN, J. R., NEWTON-BISHOP, J. A., BURROWS, L., COOK, M., CORRIE, P. G., COX, N. H., GORE, M. E., LORIGAN, P., MACKIE, R., NATHAN, P., PEACH, H., POWELL, B. & WALKER, C. 2010. Revised UK guidelines for the management of cutaneous melanoma 2010. *British Journal of Dermatology,* 163**,** 238-256.

MASTER, A. M., LIVINGSTON, M., OLEINICK, N. L. & SEN GUPTA, A. 2012. Optimization of a nanomedicine-based silicon phthalocyanine 4 photodynamic therapy (Pc 4-PDT) strategy for targeted treatment of EGFR-overexpressing cancers. *Molecular pharmaceutics,* 9**,** 2331-2338.

MATSUI, A., WINER, J. H., LAURENCE, R. G. & FRANGIONI, J. V. 2011. Predicting the survival of experimental ischaemic small bowel using intraoperative near-infrared fluorescence angiography. *British Journal of Surgery,* 98**,** 1725-1734.

MATSUMURA, Y. & MAEDA, H. 1986. A New Concept for Macromolecular Therapeutics in Cancer Chemotherapy: Mechanism of Tumoritropic Accumulation of Proteins and the Antitumor Agent Smancs. *Cancer Research,* 46**,** 6387-6392.

MAYER, A., TSIOMPANOU, E., O'MALLEY, D., BOXER, G. M., BHATIA, J., FLYNN, A. A., CHESTER, K. A., DAVIDSON, B. R., LEWIS, A. A. & WINSLET, M. C. 2000. Radioimmunoguided surgery in colorectal cancer using a genetically engineered anti-CEA single-chain Fv antibody. *Clinical Cancer Research,* 6**,** 1711-1719.

MCCARRON, P. A., MAROUF, W. M., QUINN, D. J., FAY, F., BURDEN, R. E., OLWILL, S. A. & SCOTT, C. J. 2008. Antibody targeting of camptothecin-loaded PLGA nanoparticles to tumor cells. *Bioconjugate chemistry,* 19**,** 1561-1569.

MEHES, G., WITT, A., KUBISTA, E. & AMBROS, P. F. 2000. Classification of isolated tumor cells and micrometastasis. *Cancer,* 89**,** 709-711.

MEIER, D., BOTTER, S. M., CAMPANILE, C., ROBL, B., GRÄFE, S., PELLEGRINI, G., BORN, W. & FUCHS, B. 2017. Foscan and foslip based photodynamic therapy in osteosarcoma in vitro and in intratibial mouse models. *International journal of cancer,* 140**,** 1680-1692.

MELANCON, M. P., ZHOU, M. & LI, C. 2011. Cancer theranostics with near-infrared light-activatable multimodal nanoparticles. *Accounts of chemical research,* 44**,** 947-956.

MENG, H., XUE, M., XIA, T., JI, Z., TARN, D. Y., ZINK, J. I. & NEL, A. E. 2011. Use of size and a copolymer design feature to improve the biodistribution and the enhanced permeability and retention effect of doxorubicin-loaded mesoporous silica nanoparticles in a murine xenograft tumor model. *ACS Nano,* 5**,** 4131-44.

MERY, C. M., SHAFI, B. M. & BINYAMIN, G. Molecular imaging and radioimmunoguided surgery. Seminars in pediatric surgery, 2006. Elsevier, 259-266.

MESSMANN, H., KNÜCHEL, R., ENDLICHER, E., HAUSER, T., SZEIMIES, R., KULLMANN, F., BÄUMLER, W. & SCHÖLMERICH, J. 1998. Photodynamic diagnosis of gastrointestinal precancerous lesions after sensitization with 5-aminolevulinic acid. A pilot study. *Deutsche medizinische Wochenschrift (1946),* 123**,** 515-521.

MIDDELBURG, T. A., DE BRUIJN, H. S., TETTERO, L., VAN DER PLOEG VAN DEN HEUVEL, A., NEUMANN, H. A., DE HAAS, E. R. & ROBINSON, D. J. 2013. Topical hexylaminolevulinate and aminolevulinic acid photodynamic therapy: complete arteriole vasoconstriction occurs frequently and depends on protoporphyrin IX concentration in vessel wall. *J Photochem Photobiol B,* 126**,** 26-32.

MOESTA, K. T., EBERT, B., HANDKE, T., RINNEBERG, H. & SCHLAG, P. M. 2000. Fluorescence as a concept in colorectal lymph node diagnosis. *Recent Results Cancer Res,* 157**,** 293-304.

MOGHIMI, S. M., HUNTER, A. C. & ANDRESEN, T. L. 2012. Factors Controlling Nanoparticle Pharmacokinetics: An Integrated Analysis and Perspective. *Annual Review of Pharmacology and Toxicology, Vol 52,* 52**,** 481-503.

MØLGAARD, K., COMPTE, M., NUÑEZ-PRADO, N., HARWOOD, S. L., SANZ, L. & ALVAREZ-VALLINA, L. 2017. Balanced secretion of anti-CEA× anti-CD3 diabody chains using the 2A self-cleaving peptide maximizes diabody assembly and tumor-specific cytotoxicity. *Gene therapy,* 24**,** 208.

MONICI, M. 2005. Cell and tissue autofluorescence research and diagnostic applications. *In:* EL-GEWELY, M. R. (ed.) *Biotechnology Annual Review.* Elsevier.

MOOR, A. C. 2000. Signaling pathways in cell death and survival after photodynamic therapy. *Journal of Photochemistry and Photobiology B: Biology,* 57**,** 1-13.

MORTON, D. L., WEN, D.-R., WONG, J. H., ECONOMOU, J. S., CAGLE, L. A., STORM, F. K., FOSHAG, L. J. & COCHRAN, A. J. 1992. Technical details of intraoperative lymphatic mapping for early stage melanoma. *Archives of surgery,* 127**,** 392-399.

MOWATT, G., N'DOW, J., VALE, L., NABI, G., BOACHIE, C., COOK, J. A., FRASER, C. & GRIFFITHS, T. L. 2011. Photodynamic diagnosis of bladder cancer compared with white light cystoscopy: Systematic review and meta-analysis. *International journal of technology assessment in health care,* 27**,** 3-10.

MROZ, P., SZOKALSKA, A., WU, M. X. & HAMBLIN, M. R. 2010. Photodynamic therapy of tumors can lead to development of systemic antigen-specific immune response. *PLoS One,* 5**,** e15194.

MUGGIA, F. M., HAINSWORTH, J. D., JEFFERS, S., MILLER, P., GROSHEN, S., TAN, M., ROMAN, L., UZIELY, B., MUDERSPACH, L. & GARCIA, A. 1997. Phase II study of liposomal doxorubicin in refractory ovarian cancer: antitumor activity and toxicity modification by liposomal encapsulation. *Journal of Clinical Oncology,* 15**,** 987-993.

MULDER, W. J., STRIJKERS, G. J., HABETS, J. W., BLEEKER, E. J., VAN DER SCHAFT, D. W., STORM, G., KONING, G. A., GRIFFIOEN, A. W. & NICOLAY, K. 2005. MR molecular imaging and fluorescence microscopy for identification of activated tumor endothelium using a bimodal lipidic nanoparticle. *The FASEB journal,* 19**,** 2008-2010.

MULLER, M. G., GEORGAKOUDI, I., ZHANG, Q. G., WU, J. & FELD, M. S. 2001. Intrinsic fluorescence spectroscopy in turbid media: disentangling effects of scattering and absorption. *Applied Optics,* 40**,** 4633-4646.

MULSOW, J., WINTER, D., O'KEANE, J. & O'CONNELL, P. 2003. Sentinel lymph node mapping in colorectal cancer. *British journal of surgery,* 90**,** 659-667.

MURARO, R., WUNDERLICH, D., THOR, A., LUNDY, J., NOGUCHI, P., CUNNINGHAM, R. & SCHLOM, J. 1985. Definition by monoclonal antibodies of a repertoire of epitopes on carcinoembryonic antigen differentially expressed in human colon carcinomas versus normal adult tissues. *Cancer research,* 45**,** 5769-5780.

NAP, M., HAMMARSTRÖM, M.-L., BÖRMER, O., HAMMARSTRÖM, S., WAGENER, C., HANDT, S., SCHREYER, M., MACH, J.-P., BUCHEGGER, F. & VON KLEIST, S. 1992. Specificity and affinity of monoclonal antibodies against carcinoembryonic antigen. *Cancer research,* 52**,** 2329-2339.

NELSON H, S. D., WIEAND HS, FLESHMAN J, ANVARI M, STRYKER SJ, BEART RW JR, HELLINGER M, FLANAGAN R JR, PETERS W, OTA D. 2004. A comparison of laparoscopically assisted and open colectomy for colon cancer. *N Engl J Med,* 350**,** 2050-9.

NILSSON, J., STÅHL, S., LUNDEBERG, J., UHLÉN, M. & NYGREN, P.-Å. 1997. Affinity fusion strategies for detection, purification, and immobilization of recombinant proteins. *Protein expression and purification,* 11**,** 1-16.

NORD, K., GUNNERIUSSON, E., RINGDAHL, J., STÅHL, S., UHLÉN, M. & NYGREN, P.-Å. 1997. Binding proteins selected from combinatorial libraries of an α-helical bacterial receptor domain. *Nature biotechnology,* 15**,** 772-777.

NORD, K., NILSSON, J., NILSSON, B., UHLÉN, M. & NYGREN, P.-Å. 1995. A combinatorial library of an α-helical bacterial receptor domain. *Protein Engineering, Design and Selection,* 8**,** 601-608.

O'NEAL, D. P., HIRSCH, L. R., HALAS, N. J., PAYNE, J. D. & WEST, J. L. 2004. Photo-thermal tumor ablation in mice using near infrared-absorbing nanoparticles. *Cancer letters,* 209**,** 171-176.

O'BRIEN, M., WIGLER, N., INBAR, M., ROSSO, R., GRISCHKE, E., SANTORO, A., CATANE, R., KIEBACK, D., TOMCZAK, P. & ACKLAND, S. 2004. Reduced cardiotoxicity and comparable efficacy in a phase III trial of pegylated liposomal doxorubicin HCl (CAELYX™/Doxil®) versus conventional doxorubicin for first-line treatment of metastatic breast cancer. *Annals of oncology,* 15**,** 440-449.

OFFICE FOR NATIONAL STATISTICS 2010. Colorectal incidence and mortality, 1972 - 2007. Office for National Statistics.

OHANNESIAN, D. W., LOTAN, D., THOMAS, P., JESSUP, J. M., FUKUDA, M., GABIUS, H. J. & LOTAN, R. 1995. CARCINOEMBRYONIC ANTIGEN AND OTHER GLYCOCONJUGATES ACT AS LIGANDS FOR GALECTIN-3 IN HUMAN COLON-CARCINOMA CELLS. *Cancer Research,* 55**,** 2191-2199.

OHULCHANSKYY, T. Y., ROY, I., GOSWAMI, L. N., CHEN, Y., BERGEY, E. J., PANDEY, R. K., OSEROFF, A. R. & PRASAD, P. N. 2007. Organically modified silica nanoparticles with covalently incorporated photosensitizer for photodynamic therapy of cancer. *Nano letters,* 7**,** 2835-2842.

ORTNER, M., EBERT, B., ZUMBUSCH, K., NOLTE, D., FUSCO, V., WEBER, J., WIRTH, J., FLEIGE, B., DIETEL, M. & RINNEBERG, H. 1997. Endoscopic detection of dysplasia in ulcerative colitis using delayed laser-induced fluorescence spectroscopy. *Endoscopy,* 29**,** E35.

OUKKAL, M., DJILAT, K., HADJAM, R., MAHGOUN, M., BENTABAK, K., GRABA, A., SMAIL, N., KACI, N. A., AHMED, R. B. & BOUZID, K. 2010.

Treatment of advanced and/or metastatic colorectal cancer with bevacizumab in combination with oxaliplatin-based chemotherapy (Folfox7 regimen). *Bulletin du cancer,* 97**,** 469-474.

OWENS III, D. E. & PEPPAS, N. A. 2006. Opsonization, biodistribution, and pharmacokinetics of polymeric nanoparticles. *International Journal of Pharmaceutics,* 307**,** 93-102.

PACIOTTI, G. F., MYER, L., WEINREICH, D., GOIA, D., PAVEL, N., MCLAUGHLIN, R. E. & TAMARKIN, L. 2004. Colloidal gold: a novel nanoparticle vector for tumor directed drug delivery. *Drug delivery,* 11**,** 169-183.

PARK, J.-H., GU, L., VON MALTZAHN, G., RUOSLAHTI, E., BHATIA, S. N. & SAILOR, M. J. 2009. Biodegradable luminescent porous silicon nanoparticles for in vivo applications. *Nature materials,* 8**,** 331-336.

PAULSSON, J., SJÖBLOM, T., MICKE, P., PONTÉN, F., LANDBERG, G., HELDIN, C.-H., BERGH, J., BRENNAN, D. J., JIRSTRÖM, K. & ÖSTMAN, A. 2009. Prognostic significance of stromal platelet-derived growth factor β-receptor expression in human breast cancer. *The American journal of pathology,* 175**,** 334-341.

PAVONI, E., FLEGO, M., DUPUIS, M. L., BARCA, S., PETRONZELLI, F., ANASTASI, A. M., D'ALESSIO, V., PELLICCIA, A., VACCARO, P. & MONTERIÙ, G. 2006. Selection, affinity maturation, and characterization of a human scFv antibody against CEA protein. *BMC cancer,* 6**,** 41.

PEER, D., KARP, J. M., HONG, S., FAROKHZAD, O. C., MARGALIT, R. & LANGER, R. 2007a. Nanocarriers as an emerging platform for cancer therapy. *Nature nanotechnology,* 2**,** 751.

PEER, D., KARP, J. M., HONG, S., FAROKHZAD, O. C., MARGALIT, R. & LANGER, R. 2007b. Nanocarriers as an emerging platform for cancer therapy. *Nat Nano,* 2**,** 751-760.

PENG, H.-P., LEE, K. H., JIAN, J.-W. & YANG, A.-S. 2014. Origins of specificity and affinity in antibody–protein interactions. *Proceedings of the National Academy of Sciences,* 111**,** E2656-E2665.

PERRAULT, S. D., WALKEY, C., JENNINGS, T., FISCHER, H. C. & CHAN, W. C. W. 2009. Mediating Tumor Targeting Efficiency of Nanoparticles Through Design. *Nano Letters,* 9**,** 1909-1915.

PETRI, A., YOVA, D., ALEXANDRATOU, E., KYRIAZI, M. & RALLIS, M. 2012. Comparative characterization of the cellular uptake and photodynamic efficiency of Foscan® and Fospeg in a human prostate cancer cell line. *Photodiagnosis and photodynamic therapy,* 9**,** 344-354.

PHILLIPS, E., PENATE-MEDINA, O., ZANZONICO, P. B., CARVAJAL, R. D., MOHAN, P., YE, Y., HUMM, J., GÖNEN, M., KALAIGIAN, H. &

SCHÖDER, H. 2014. Clinical translation of an ultrasmall inorganic optical-PET imaging nanoparticle probe. *Science translational medicine,* 6**,** 260ra149-260ra149.

POTTIER, A., BORGHI, E. & LEVY, L. 2014. New use of metals as nanosized radioenhancers. *Anticancer Research,* 34**,** 443-453.

POVOSKI, S. P., HATZARAS, I. S., MOJZISIK, C. M., ARNOLD, M. W., HINKLE, G. H., HITCHCOCK, C. L., YOUNG, D. C. & MARTIN, E. W. 2012. Antigen-directed cancer surgery for primary colorectal cancer: 15-year survival analysis. *Annals of surgical oncology,* 19**,** 131-138.

RAHBARI, N. N., BORK, U., MOTSCHALL, E., THORLUND, K., BUCHLER, M. W., KOCH, M. & WEITZ, J. 2012. Molecular detection of tumor cells in regional lymph nodes is associated with disease recurrence and poor survival in node-negative colorectal cancer: a systematic review and meta-analysis. *J Clin Oncol,* 30**,** 60-70.

RAINA, M., SHARMA, R., DEACON, S., TIEDE, C., TOMLINSON, D., DAVIES, A., MCPHERSON, M. & WÄLTI, C. 2015. Antibody mimetic receptor proteins for label-free biosensors. *Analyst,* 140**,** 803-810.

RAWAL, S. & PATEL, M. M. 2019. Threatening cancer with nanoparticle aided combination oncotherapy. *Journal of Controlled Release*.

REGULA, J., MACROBERT, A., GORCHEIN, A., BUONACCORSI, G., THORPE, S., SPENCER, G., HATFIELD, A. & BOWN, S. 1995. Photosensitisation and photodynamic therapy of oesophageal, duodenal, and colorectal tumours using 5 aminolaevulinic acid induced protoporphyrin IX--a pilot study. *Gut,* 36**,** 67-75.

REINTGEN, D., CRUSE, C. W., WELLS, K., BERMAN, C., FENSKE, N., GLASS, F., SCHROER, K., HELLER, R., ROSS, M. & LYMAN, G. 1994. The orderly progression of melanoma nodal metastases. *Annals of surgery,* 220**,** 759.

RODRIGUEZ-BIGAS, M. A., MAAMOUN, S., WEBER, T. K., PENETRANTE, R. B., BLUMENSON, L. E. & PETRELLI, N. J. 1996. Clinical significance of colorectal cancer: metastases in lymph nodes < 5 mm in size. *Ann Surg Oncol,* 3**,** 124-30.

ROJNIK, M., KOCBEK, P., MORET, F., COMPAGNIN, C., CELOTTI, L., BOVIS, M. J., WOODHAMS, J. H., MACROBERT, A. J., SCHEGLMANN, D. & HELFRICH, W. 2012. In vitro and in vivo characterization of temoporfin-loaded PEGylated PLGA nanoparticles for use in photodynamic therapy. *Nanomedicine,* 7**,** 663-677.

ROLLVÉN, E., ABRAHAM-NORDLING, M., HOLM, T. & BLOMQVIST, L. 2017. Assessment and diagnostic accuracy of lymph node status to predict stage III colon cancer using computed tomography. *Cancer Imaging,* 17**,** 3.

ROLLVEN, E., HOLM, T., GLIMELIUS, B., LORINC, E. & BLOMQVIST, L. 2013. Potentials of high resolution magnetic resonance imaging versus computed tomography for preoperative local staging of colon cancer. *Acta Radiol,* 54**,** 722-30.

ROY, I., OHULCHANSKYY, T. Y., PUDAVAR, H. E., BERGEY, E. J., OSEROFF, A. R., MORGAN, J., DOUGHERTY, T. J. & PRASAD, P. N. 2003. Ceramic-based nanoparticles entrapping water-insoluble photosensitizing anticancer drugs: A novel drug− carrier system for photodynamic therapy. *Journal of the American Chemical Society,* 125**,** 7860-7865.

SAINZ PASTOR, N. 2008. *Generation and characterisation of designed ankyrin repeat proteins for targeting carcinoembryonic antigen.* UCL (University College London).

SAITO, R., KRAUZE, M. T., BRINGAS, J. R., NOBLE, C., MCKNIGHT, T. R., JACKSON, P., WENDLAND, M. F., MAMOT, C., DRUMMOND, D. C. & KIRPOTIN, D. B. 2005. Gadolinium-loaded liposomes allow for real-time magnetic resonance imaging of convection-enhanced delivery in the primate brain. *Experimental neurology,* 196**,** 381-389.

SANTRA, S., ZHANG, P., WANG, K. M., TAPEC, R. & TAN, W. H. 2001. Conjugation of biomolecules with luminophore-doped silica nanoparticles for photostable biomarkers. *Analytical Chemistry,* 73**,** 4988-4993.

SARPARANTA, M., BIMBO, L. M., RYTKÖNEN, J., MÄKILÄ, E., LAAKSONEN, T. J., LAAKSONEN, P. I., NYMAN, M., SALONEN, J., LINDER, M. B. & HIRVONEN, J. 2012. Intravenous delivery of hydrophobin-functionalized porous silicon nanoparticles: stability, plasma protein adsorption and biodistribution. *Molecular pharmaceutics,* 9**,** 654-663.

SARTORE-BIANCHI, A., MARSONI, S. & SIENA, S. 2018. Human epidermal growth factor receptor 2 as a molecular biomarker for metastatic colorectal cancer. *JAMA oncology,* 4**,** 19-20.

SAVARY, J.-F., GROSJEAN, P., MONNIER, P., FONTOLLIET, C., WAGNIERES, G., BRAICHOTTE, D. & VAN DEN BERGH, H. 1998. Photodynamic therapy of early squamous cell carcinomas of the esophagus: a review of 31 cases. *Endoscopy,* 30**,** 258-265.

SAVARY, J.-F., MONNIER, P., FONTOLLIET, C., MIZERET, J., WAGNIÈRES, G., BRAICHOTTE, D. & VAN DEN BERGH, H. 1997. Photodynamic therapy for early squamous cell carcinomas of the esophagus, bronchi, and mouth with m-tetra (hydroxyphenyl) chlorin. *Archives of Otolaryngology–Head & Neck Surgery,* 123**,** 162-168.

SCHMIDT, M. M., THURBER, G. M. & WITTRUP, K. D. 2008. Kinetics of anti-carcinoembryonic antigen antibody internalization: effects of affinity, bivalency, and stability. *Cancer Immunology Immunotherapy,* 57**,** 1879-1890.

SENGE, M. O. & BRANDT, J. C. 2011. Temoporfin (Foscan®, 5, 10, 15, 20-tetra (m-hydroxyphenyl) chlorin)—a second-generation photosensitizer. *Photochemistry and photobiology,* 87**,** 1240-1296.

SEYDACK, M. 2005. Nanoparticle labels in immunosensing using optical detection methods. *Biosensors and Bioelectronics,* 20**,** 2454-2469.

SHA, F., SALZMAN, G., GUPTA, A. & KOIDE, S. 2017a. Monobodies and Other Synthetic Binding Proteins for Expanding Protein Science. *Protein Science*.

SHA, F., SALZMAN, G., GUPTA, A. & KOIDE, S. 2017b. Monobodies and other synthetic binding proteins for expanding protein science. *Protein Science,* 26**,** 910-924.

SHABARUDDIN, F. H., CHEN, L.-C., ELLIOTT, R. A. & PAYNE, K. 2013. A systematic review of utility values for chemotherapy-related adverse events. *Pharmacoeconomics,* 31**,** 277-288.

SHAHZAD, M. M., MANGALA, L. S., HAN, H. D., LU, C., BOTTSFORD-MILLER, J., NISHIMURA, M., MORA, E. M., LEE, J.-W., STONE, R. L. & PECOT, C. V. 2011. Targeted delivery of small interfering RNA using reconstituted high-density lipoprotein nanoparticles. *Neoplasia (New York, NY),* 13**,** 309.

SHAMSUDDIN, S. 2019. Biosensors for detection of colorectal cancer. *University of Leeds*

SHARMA, M., MALIK, R., VERMA, A., DWIVEDI, P., BANOTH, G. S., PANDEY, N., SARKAR, J., MISHRA, P. R. & DWIVEDI, A. K. 2013. Folic acid conjugated guar gum nanoparticles for targeting methotrexate to colon cancer. *Journal of biomedical nanotechnology,* 9**,** 96-106.

SHI, Q., TAO, Z., YANG, H., FAN, Q., WEI, D., WAN, L. & LU, X. 2017. PDGFRβ-specific affibody-directed delivery of a photosensitizer, IR700, is efficient for vascular-targeted photodynamic therapy of colorectal cancer. *Drug delivery,* 24**,** 1818-1830.

SHIA, J., KLIMSTRA, D. S., NITZKORSKI, J. R., LOW, P. S., GONEN, M., LANDMANN, R., WEISER, M. R., FRANKLIN, W. A., PRENDERGAST, F. G. & MURPHY, L. 2008. Immunohistochemical expression of folate receptor α in colorectal carcinoma: patterns and biological significance. *Human pathology,* 39**,** 498-505.

SHINOZAKI, E., YOSHINO, T. & TSUCHIHARA, K. 2018. Reply toComment onClinical significance of BRAF non-V600E mutations on the therapeutic effects of anti-EGFR monoclonal antibody treatment in patients with pretreated metastatic colorectal cancer: the Biomarker Research for anti-EGFR monoclonal Antibodies by Comprehensive Cancer genomics (BREAC) study". *British journal of cancer,* 118**,** 1278.

SIEGAL, R., DESANTIS, C. & JEMAL, A. 2014. Colorectal cancer statistics 2014. *CA Cancer J Clin,* 64**,** 104-117.

SLAMON, D. J., LEYLAND-JONES, B., SHAK, S., FUCHS, H., PATON, V., BAJAMONDE, A., FLEMING, T., EIERMANN, W., WOLTER, J. & PEGRAM, M. 2001. Use of chemotherapy plus a monoclonal antibody against HER2 for metastatic breast cancer that overexpresses HER2. *New England Journal of Medicine,* 344**,** 783-792.

SMITH, N., BEES, N., BARBACHANO, Y., NORMAN, A., SWIFT, R. & BROWN, G. 2007. Preoperative computed tomography staging of nonmetastatic colon cancer predicts outcome: implications for clinical trials. *British journal of cancer,* 96**,** 1030.

SOLTESZ, E. G., KIM, S., KIM, S. W., LAURENCE, R. G., DE GRAND, A. M., PARUNGO, C. P., COHN, L. H., BAWENDI, M. G. & FRANGIONI, J. V. 2006. Sentinel lymph node mapping of the gastrointestinal tract by using invisible light. *Annals of Surgical Oncology,* 13**,** 386-396.

SOSTER, M., JURIS, R., BONACCHI, S., GENOVESE, D., MONTALTI, M., RAMPAZZO, E., ZACCHERONI, N., GARAGNANI, P., BUSSOLINO, F., PRODI, L. & MARCHIO, S. 2012. Targeted dual-color silica nanoparticles provide univocal identification of micrometastases in preclinical models of colorectal cancer. *International Journal of Nanomedicine,* 7**,** 4797-4807.

SOURIS, J. S., LEE, C.-H., CHENG, S.-H., CHEN, C.-T., YANG, C.-S., HO, J.-A. A., MOU, C.-Y. & LO, L.-W. 2010. Surface charge-mediated rapid hepatobiliary excretion of mesoporous silica nanoparticles. *Biomaterials,* 31**,** 5564-5574.

STAR, W. M., MARIJNISSEN, H. P., VAN DEN BERG-BLOK, A. E., VERSTEEG, J. A., FRANKEN, K. A. & REINHOLD, H. S. 1986. Destruction of rat mammary tumor and normal tissue microcirculation by hematoporphyrin derivative photoradiation observed in vivo in sandwich observation chambers. *Cancer Res,* 46**,** 2532-40.

STORHOFF, J. J., LUCAS, A. D., GARIMELLA, V., BAO, Y. P. & MÜLLER, U. R. 2004. Homogeneous detection of unamplified genomic DNA sequences based on colorimetric scatter of gold nanoparticle probes. *Nature biotechnology,* 22**,** 883.

STUMMER, W., PICHLMEIER, U., MEINEL, T., WIESTLER, O. D., ZANELLA, F., REULEN, H.-J. & GROUP, A.-G. S. 2006. Fluorescence-guided surgery with 5-aminolevulinic acid for resection of malignant glioma: a randomised controlled multicentre phase III trial. *The lancet oncology,* 7**,** 392-401.

SUN, D., BLOOMSTON, M., HINKLE, G., AL-SAIF, O. H., HALL, N. C., POVOSKI, S. P., ARNOLD, M. W. & MARTIN, E. W. 2007. Radioimmunoguided surgery (RIGS), PET/CT image-guided surgery,

and fluorescence image-guided surgery: Past, present, and future. *Journal of surgical oncology,* 96**,** 297-308.

SUN, L., WU, H. & GUAN, Y.-S. 2008. Colonography by CT, MRI and PET/CT combined with conventional colonoscopy in colorectal cancer screening and staging. *World journal of gastroenterology,* 14**,** 853.

SWARTLING, J., HÖGLUND, O. V., HANSSON, K., SÖDERSTEN, F., AXELSSON, J. & LAGERSTEDT, A.-S. 2016. Online dosimetry for temoporfin-mediated interstitial photodynamic therapy using the canine prostate as model. *Journal of biomedical optics,* 21**,** 028002.

TADA, D. B. & BAPTISTA, M. S. 2015. Photosensitizing nanoparticles and the modulation of ROS generation. *Frontiers in chemistry,* 3**,** 33.

TAGHAVI, S., RAMEZANI, M., ALIBOLANDI, M., ABNOUS, K. & TAGHDISI, S. M. 2017. Chitosan-modified PLGA nanoparticles tagged with 5TR1 aptamer for in vivo tumor-targeted drug delivery. *Cancer letters,* 400**,** 1-8.

TAMASKOVIC, R., SIMON, M., STEFAN, N., SCHWILL, M. & PLÜCKTHUN, A. 2012. Designed ankyrin repeat proteins (DARPins): from research to therapy. *Methods in enzymology.* Elsevier.

TAN, K., KAWAMURA, Y., MIZOKAMI, K., SASAKI, J., TSUJINAKA, S., MAEDA, T., NOBUKI, M. & KONISHI, F. 2010. Distribution of the first metastatic lymph node in colon cancer and its clinical significance. *Colorectal disease,* 12**,** 44-47.

TANEJA, S. S. 2017. Re: Padeliporfin Vascular-Targeted Photodynamic Therapy versus Active Surveillance in Men with Low-Risk Prostate Cancer (CLIN1001 PCM301): An Open-Label, Phase 3, Randomised Controlled Trial. *J Urol,* 198**,** 255-257.

THEURILLAT, J.-P., DREIER, B., NAGY-DAVIDESCU, G., SEIFERT, B., BEHNKE, S., ZÜRRER-HÄRDI, U., INGOLD, F., PLÜCKTHUN, A. & MOCH, H. 2010. Designed ankyrin repeat proteins: a novel tool for testing epidermal growth factor receptor 2 expression in breast cancer. *Modern Pathology,* 23**,** 1289-1297.

THOMAS, P., TOTH, C. A., SAINI, K. S., JESSUP, J. M. & STEELE JR, G. 1990. The structure, metabolism and function of the carcinoembryonic antigen gene family. *Biochimica et Biophysica Acta (BBA)-Reviews on Cancer,* 1032**,** 177-189.

THOMPSON, W. M., HALVORSEN, R. A., FOSTER, W. L., JR., ROBERTS, L. & GIBBONS, R. 1986. Preoperative and postoperative CT staging of rectosigmoid carcinoma. *AJR Am J Roentgenol,* 146**,** 703-10.

TIEDE, C., BEDFORD, R., HESELTINE, S. J., SMITH, G., WIJETUNGA, I., ROSS, R., ALQALLAF, D., ROBERTS, A. P., BALLS, A. & CURD, A.

2017. Affimer proteins are versatile and renewable affinity reagents. *Elife,* 6**,** e24903.

TIEDE, C., TANG, A. A., DEACON, S. E., MANDAL, U., NETTLESHIP, J. E., OWEN, R. L., GEORGE, S. E., HARRISON, D. J., OWENS, R. J. & TOMLINSON, D. C. 2014a. Adhiron: a stable and versatile peptide display scaffold for molecular recognition applications. *Protein Engineering, Design and Selection,* 27**,** 145-155.

TIEDE, C., TANG, A. A., DEACON, S. E., MANDAL, U., NETTLESHIP, J. E., OWEN, R. L., GEORGE, S. E., HARRISON, D. J., OWENS, R. J. & TOMLINSON, D. C. 2014b. Adhiron: a stable and versatile peptide display scaffold for molecular recognition applications. *Protein Engineering Design and Selection,* 27**,** 145-155.

TIERNAN, J. & JAYNE, D. 2017. Antigen-Directed Cancer Surgery for Primary Colorectal Cancer: 15-Year Survival Analysis. *Annals of surgical oncology,* 24**,** 609-609.

TIERNAN, J., PERRY, S., VERGHESE, E., WEST, N., YELURI, S., JAYNE, D. & HUGHES, T. 2013. Carcinoembryonic antigen is the preferred biomarker for in vivo colorectal cancer targeting. *British journal of cancer,* 108**,** 662.

TIERNAN, J. P., INGRAM, N., MARSTON, G., PERRY, S. L., RUSHWORTH, J. V., COLETTA, P. L., MILLNER, P. A., JAYNE, D. G. & HUGHES, T. A. 2015. CEA-targeted nanoparticles allow specific in vivo fluorescent imaging of colorectal cancer models. *Nanomedicine,* 10**,** 1223-1231.

TIVNAN, A., ORR, W. S., GUBALA, V., NOONEY, R., WILLIAMS, D. E., MCDONAGH, C., PRENTER, S., HARVEY, H., DOMINGO-FERNANDEZ, R., BRAY, I. M., PISKAREVA, O., NG, C. Y., LODE, H. N., DAVIDOFF, A. M. & STALLINGS, R. L. 2012. Inhibition of Neuroblastoma Tumor Growth by Targeted Delivery of MicroRNA-34a Using Anti-Disialoganglioside GD(2) Coated Nanoparticles. *Plos One,* 7.

TIWARI, D. K., TANAKA, S., INOUYE, Y., YOSHIZAWA, K., WATANABE, T. M. & JIN, T. 2009. Synthesis and Characterization of Anti-HER2 Antibody Conjugated CdSe/CdZnS Quantum Dots for Fluorescence Imaging of Breast Cancer Cells. *Sensors (Basel),* 9**,** 9332-64.

TORCHILIN, V. 2008. Multifunctional pharmaceutical nanocarriers: development of the concept. *Multifunctional Pharmaceutical Nanocarriers.* Springer.

TORRE, L. A., BRAY, F., SIEGEL, R. L., FERLAY, J., LORTET-TIEULENT, J. & JEMAL, A. 2015. Global cancer statistics, 2012. *CA: a cancer journal for clinicians,* 65**,** 87-108.

TROMBERG, B. J., KIMEL, S., ORENSTEIN, A., BARKER, S. J., HYATT, J., NELSON, J. S., ROBERTS, W. G. & BERNS, M. W. 1990. Tumor

oxygen tension during photodynamic therapy. *J Photochem Photobiol B,* 5**,** 121-6.

UK, C. R. 2011. Cancer Research UK.

VAN DER PAS, M. H., ANKERSMIT, M., STOCKMANN, H. B., SILVIS, R., VAN GRIEKEN, N. C., BRIL, H. & MEIJERINK, W. J. 2013. Laparoscopic sentinel lymph node identification in patients with colon carcinoma using a near-infrared dye: description of a new technique and feasibility study. *Journal of Laparoendoscopic & Advanced Surgical Techniques,* 23**,** 367-371.

VAN DER PAS, M. H., MEIJER, S., HOEKSTRA, O. S., RIPHAGEN, I. I., DE VET, H. C., KNOL, D. L., VAN GRIEKEN, N. C. & MEIJERINK, W. J. 2011. Sentinel-lymph-node procedure in colon and rectal cancer: a systematic review and meta-analysis. *The lancet oncology,* 12**,** 540-550.

VAN DER ZAAG, E. S., BOUMA, W. H., TANIS, P. J., UBBINK, D. T., BEMELMAN, W. A. & BUSKENS, C. J. 2012. Systematic review of sentinel lymph node mapping procedure in colorectal cancer. *Annals of surgical oncology,* 19**,** 3449-3459.

VAN LEEUWEN-VAN ZAANE, F., DE BRUIJN, H. S., VAN DER PLOEG-VAN DEN HEUVEL, A., STERENBORG, H. J. & ROBINSON, D. J. 2014. The effect of fluence rate on the acute response of vessel diameter and red blood cell velocity during topical 5-aminolevulinic acid photodynamic therapy. *Photodiagnosis Photodyn Ther,* 11**,** 71-81.

VAN SCHELTINGA, A. G. T. T., VAN DAM, G. M., NAGENGAST, W. B., NTZIACHRISTOS, V., HOLLEMA, H., HEREK, J. L., SCHRODER, C. P., KOSTERINK, J. G. W., LUB-DE HOOG, M. N. & DE VRIES, E. G. E. 2011. Intraoperative Near-Infrared Fluorescence Tumor Imaging with Vascular Endothelial Growth Factor and Human Epidermal Growth Factor Receptor 2 Targeting Antibodies. *Journal of Nuclear Medicine,* 52**,** 1778-1785.

VARGAS, A., LANGE, N., ARVINTE, T., CERNY, R., GURNY, R. & DELIE, F. 2009. Toward the understanding of the photodynamic activity of m-THPP encapsulated in PLGA nanoparticles: correlation between nanoparticle properties and in vivo activity. *Journal of drug targeting,* 17**,** 599-609.

VEIT-HAIBACH, P., KUEHLE, C. A., BEYER, T., STERGAR, H., KUEHL, H., SCHMIDT, J., BÖRSCH, G., DAHMEN, G., BARKHAUSEN, J. & BOCKISCH, A. 2006. Diagnostic accuracy of colorectal cancer staging with whole-body PET/CT colonography. *Jama,* 296**,** 2590-2600.

VISWANATH, B., KIM, S. & LEE, K. 2016. Recent insights into nanotechnology development for detection and treatment of colorectal cancer. *International Journal of Nanomedicine,* 11**,** 2491.

VITTAR, N. B., AWRUCH, J., AZIZUDDIN, K. & RIVAROLA, V. 2010. Caspase-independent apoptosis, in human MCF-7c3 breast cancer cells, following photodynamic therapy, with a novel water-soluble phthalocyanine. *Int J Biochem Cell Biol,* 42**,** 1123-31.

VROUENRAETS, M. B., VISSER, G. W., SNOW, G. B. & VAN DONGEN, G. A. 2003. Basic principles, applications in oncology and improved selectivity of photodynamic therapy. *Anticancer Res,* 23**,** 505-22.

WAGNER, A., DENZER, U. W., NEUREITER, D., KIESSLICH, T., PUESPOECK, A., RAUWS, E. A., EMMANUEL, K., DEGENHARDT, N., FRICK, U. & BEUERS, U. 2015. Temoporfin improves efficacy of photodynamic therapy in advanced biliary tract carcinoma: A multicenter prospective phase II study. *Hepatology,* 62**,** 1456-1465.

WANG, H., RAJAGOPAL, S., REYNOLDS, S., CEDERBERG, H. & CHAKRABARTY, S. 1999. Differentiation-promoting effect of 1-O (2 methoxy) hexadecyl glycerol in human colon cancer cells. *Journal of Cellular Physiology,* 178**,** 173-178.

WANG-GILLAM, A., HUBNER, R. A., SIVEKE, J. T., VON HOFF, D. D., BELANGER, B., DE JONG, F. A., MIRAKHUR, B. & CHEN, L.-T. 2019. NAPOLI-1 phase 3 study of liposomal irinotecan in metastatic pancreatic cancer: Final overall survival analysis and characteristics of long-term survivors. *European Journal of Cancer,* 108**,** 78-87.

WEINBERG, W. C., FRAZIER-JESSEN, M. R., WU, W. J., WEIR, A., HARTSOUGH, M., KEEGAN, P. & FUCHS, C. 2005. Development and regulation of monoclonal antibody products: challenges and opportunities. *Cancer and metastasis reviews,* 24**,** 569-584.

WEISSLEDER, R. & NTZIACHRISTOS, V. 2003. Shedding light onto live molecular targets. *Nat Med,* 9**,** 123-128.

WEST, N. P., MORRIS, E. J., ROTIMI, O., CAIRNS, A., FINAN, P. J. & QUIRKE, P. 2008a. Pathology grading of colon cancer surgical resection and its association with survival: a retrospective observational study. *The lancet oncology,* 9**,** 857-865.

WEST, N. P., MORRIS, E. J., ROTIMI, O., CAIRNS, A., FINAN, P. J. & QUIRKE, P. 2008b. Pathology grading of colon cancer surgical resection and its association with survival: a retrospective observational study. *Lancet Oncol,* 9**,** 857-65.

WONG, J. Y., CHU, D. Z., WILLIAMS, L. E., LIU, A., ZHAN, J., YAMAUCHI, D. M., WILCZYNSKI, S., WU, A. M., YAZAKI, P. J. & SHIVELY, J. E. 2006. A phase I trial of 90Y-DOTA-anti-CEA chimeric T84. 66 (cT84. 66) radioimmunotherapy in patients with metastatic CEA-producing malignancies. *Cancer biotherapy & radiopharmaceuticals,* 21**,** 88-100.

WONG, J. Y., CHU, D. Z., YAMAUCHI, D. M., WILLIAMS, L. E., LIU, A., WILCZYNSKI, S., WU, A. M., SHIVELY, J. E., DOROSHOW, J. H. & RAUBITSCHEK, A. A. 2000. A phase I radioimmunotherapy trial evaluating 90yttrium-labeled anti-carcinoembryonic antigen (CEA) chimeric T84. 66 in patients with metastatic CEA-producing malignancies. *Clinical cancer research,* 6**,** 3855-3863.

WU, C.-H., KUO, Y.-H., HONG, R.-L. & WU, H.-C. 2015. α-Enolase–binding peptide enhances drug delivery efficiency and therapeutic efficacy against colorectal cancer. *Science translational medicine,* 7**,** 290ra91-290ra91.

WU, H., HUO, Q., VARNUM, S., WANG, J., LIU, G., NIE, Z., LIU, J. & LIN, Y. 2008. Dye-doped silica nanoparticle labels/protein microarray for detection of protein biomarkers. *Analyst,* 133**,** 1550-1555.

WU, J., MA, R., CAO, H., WANG, Z., JING, C., SUN, Y., ZHANG, Y., YANG, Z., HOFFMAN, R. M. & TANG, J. 2013. Intraoperative Imaging of Metastatic Lymph Nodes Using a Fluorophore-conjugated Antibody in a HER2/neu-expressing Orthotopic Breast Cancer Mouse Model. *Anticancer Research,* 33**,** 419-424.

XIE, X., LI, F., ZHANG, H., LU, Y., LIAN, S., LIN, H., GAO, Y. & JIA, L. 2016. EpCAM aptamer-functionalized mesoporous silica nanoparticles for efficient colon cancer cell-targeted drug delivery. *European Journal of Pharmaceutical Sciences,* 83**,** 28-35.

YAKAVETS, I., MILLARD, M., LAMY, L., FRANCOIS, A., SCHEGLMANN, D., WIEHE, A., LASSALLE, H.-P., ZORIN, V. & BEZDETNAYA, L. 2019a. Matryoshka-type liposomes offer the improved delivery of temoporfin to tumor spheroids. *Cancers,* 11**,** 1366.

YAKAVETS, I., MILLARD, M., ZORIN, V., LASSALLE, H.-P. & BEZDETNAYA, L. 2019b. Current state of the nanoscale delivery systems for temoporfin-based photodynamic therapy: Advanced delivery strategies. *Journal of Controlled Release*.

YAN, F. & KOPELMAN, R. 2003. The Embedding of Meta-tetra (Hydroxyphenyl)-Chlorin into Silica Nanoparticle Platforms for Photodynamic Therapy and Their Singlet Oxygen Production and pH-dependent Optical Properties¶. *Photochemistry and photobiology,* 78**,** 587-591.

YANG, B., LI, Y., WEN, R., JIANG, Z., ZHANG, Y., LAI, D. & CHEN, S. 2015. [Application of carbon nanoparticles labeled lymph node staining in curative laparoscopic resection for colorectal carcinoma]. *Zhonghua wei chang wai ke za zhi= Chinese journal of gastrointestinal surgery,* 18**,** 549-552.

YANG, S.-J., LIN, F.-H., TSAI, K.-C., WEI, M.-F., TSAI, H.-M., WONG, J.-M. & SHIEH, M.-J. 2010. Folic acid-conjugated chitosan nanoparticles

enhanced protoporphyrin IX accumulation in colorectal cancer cells. *Bioconjugate chemistry,* 21**,** 679-689.

YANG, Z., LIU, Z., ALLAKER, R., REIP, P., OXFORD, J., AHMAD, Z. & RENG, G. 2013. A review of nanoparticle functionality and toxicity on the central nervous system. *Nanotechnology, the Brain, and the Future.* Springer.

YAZAKI, P. J., KASSA, T., CHEUNG, C.-W., CROW, D. M., SHERMAN, M. A., BADING, J. R., ANDERSON, A.-L. J., COLCHER, D. & RAUBITSCHEK, A. 2008. Biodistribution and tumor imaging of an anti-CEA single-chain antibody–albumin fusion protein. *Nuclear medicine and biology,* 35**,** 151-158.

YAZAKI, P. J., LEE, B., CHANNAPPA, D., CHEUNG, C.-W., CROW, D., CHEA, J., POKU, E., LI, L., ANDERSEN, J. T. & SANDLIE, I. 2012. A series of anti-CEA/anti-DOTA bispecific antibody formats evaluated for pre-targeting: comparison of tumor uptake and blood clearance. *Protein Engineering, Design & Selection,* 26**,** 187-193.

YEUNG, T. M., WANG, L. M., COLLING, R., KRAUS, R., CAHILL, R., HOMPES, R. & MORTENSEN, N. J. 2018. Intraoperative identification and analysis of lymph nodes at laparoscopic colorectal cancer surgery using fluorescence imaging combined with rapid OSNA pathological assessment. *Surgical endoscopy,* 32**,** 1073-1076.

YOO, H. S. & PARK, T. G. 2004. Folate-receptor-targeted delivery of doxorubicin nano-aggregates stabilized by doxorubicin–PEG–folate conjugate. *Journal of controlled release,* 100**,** 247-256.

YOO, J. O. & HA, K. S. 2012. New insights into the mechanisms for photodynamic therapy-induced cancer cell death. *Int Rev Cell Mol Biol,* 295**,** 139-74.

YOON, T. J., KIM, J. S., KIM, B. G., YU, K. N., CHO, M. H. & LEE, J. K. 2005. Multifunctional nanoparticles possessing a “magnetic motor effect” for drug or gene delivery. *Angewandte Chemie International Edition,* 44**,** 1068-1071.

YU, Z., PAN, W., LI, N. & TANG, B. 2016. A nuclear targeted dual-photosensitizer for drug-resistant cancer therapy with NIR activated multiple ROS. *Chemical science,* 7**,** 4237-4244.

ZALBA, S., CONTRERAS, A. M., HAERI, A., TEN HAGEN, T. L., NAVARRO, I., KONING, G. & GARRIDO, M. J. 2015. Cetuximab-oxaliplatin-liposomes for epidermal growth factor receptor targeted chemotherapy of colorectal cancer. *Journal of Controlled Release,* 210**,** 26-38.

ZENG, H., SUN, M., ZHOU, C., YIN, F., WANG, Z., HUA, Y. & CAI, Z. 2013. Hematoporphyrin monomethyl ether-mediated photodynamic therapy selectively kills sarcomas by inducing apoptosis. *PLoS One,* 8**,** e77727.

ZHAO, X. J., HILLIARD, L. R., MECHERY, S. J., WANG, Y. P., BAGWE, R. P., JIN, S. G. & TAN, W. H. 2004. A rapid bioassay for single bacterial cell quantitation using bioconjugated nanoparticles. *Proceedings of the National Academy of Sciences of the United States of America,* 101**,** 15027-15032.

ZOU, P., XU, S., POVOSKI, S. P., WANG, A., JOHNSON, M. A., MARTIN, E. W., SUBRAMANIAM, V., XU, R. & SUN, D. 2009a. Near-Infrared Fluorescence Labeled Anti-TAG-72 Monoclonal Antibodies for Tumor Imaging in Colorectal Cancer Xenograft Mice. *Molecular Pharmaceutics,* 6**,** 428-440.

ZOU, P., XU, S., POVOSKI, S. P., WANG, A., JOHNSON, M. A., MARTIN JR, E. W., SUBRAMANIAM, V., XU, R. & SUN, D. 2009b. Near-infrared fluorescence labeled anti-TAG-72 monoclonal antibodies for tumor imaging in colorectal cancer xenograft mice. *Molecular pharmaceutics,* 6**,** 428-440.